Monte Carlo simulation and characterisation of phase formation in Pt-based alloy thin films

by

Richard Anthony Harris

M.Sc. (Physics)

A thesis submitted for the fulfillment of the requirements for the degree

PHILOSOPHIAE DOCTOR

in the

Department of Physics
Faculty of Natural and Agricultural Science

at the

University of the Free State
Bloemfontein

June 2010

Supervisor: Prof. J.J. Terblans

Co-Supervisor: Prof. H.C. Swart

In Memory Of

Frikkie Grobler, Tossie Nel, Natie Terblanche, Charl Terblance, Geoffry Harris

Acknowledgements

The author wishes to express his thanks and gratitude to the following people:

- My Heavenly Father. Though I am painfully aware of my sins and failures, Your love for me remains unconditional.
- Prof. Koos Terblans. Thank you for your patience, kindness, tolerance and guidance in these last years. Thank you for many informative discussions.
- Prof. Hendrik Swart. Thank you for your friendly support helpful discussions and guidance in these last years.
- Mr. Heinrich Joubert for a lot of advice on computer modelling and software programming.
- Mr. Shaun Cronje for assistance in various areas of this study, especially experimental.
- Ms. Liza Coetsee for assistance with the PHI 700 nano-probe.
- The personnel of the Physics Department, UFS, for numerous informative discussions.
- My parents, siblings and family for their unending love and support.

Keywords

Ambient gasses
Chemical potential
Diffusion
Droplets
Electron beam – physical vapour deposition (EB-PVD)
Monte Carlo method
Nickel based super alloys
Phases
Platinum based super alloys
Pulsed laser deposition (PLD)
Simulation
Stoichiometric transfer
Thin films

Abstract

From Icarus' mythical flight to escape Crete to manned space flight to the moon, mankind's dream to fly has impacted this world immensely. Technological advancements made in metallurgy and alloy development has played a huge role in realizing this dream. Developing materials and superalloys with higher melting temperatures and greater strength has allowed for the design of the modern turbine jet engines. Economical and (today more than ever) environmental concerns continue to provide ample motivation for operating the engines at ever increasing temperatures, thereby improving the thermodynamic efficiency and reducing pollutant emissions. One of the most aggressive man made environments is that of the high pressure turbine section of a modern gas turbine engine. During operation, after combustion, highly oxidizing gas enters the turbine. This happens at temperatures exceeding 200 °C above the melting point of the superalloy turbine blade. Newer generations of civil aircraft will have turbine entry temperatures (TET) that will exceed 1800 K at take-off. Increased power and improved fuel consumption remains a continuing demand in modern aero-gas turbine engines as this result in an increase in TET. One strategy to achieve this goal is by coating the turbine blades with a thin film composed of alloy material. These films can be engineered to have specific heat-resistant, oxidation-resistant properties. Two coating techniques that show promise in achieving these goals are pulsed laser ablation (PLD) and electron beam physical vapour deposition (EB-PVD). These techniques are investigated in this study in particular of platinum-aluminium alloys. The appearances of droplets on the thin film surface that arise due to the pulsed laser ablation technique itself are investigated. A suitable technique to minimize the appearance of these droplets by using ambient gas and ambient gas pressure is discussed. The stoichiometric transfer of material from the target to a substrate was also investigated. A lot of insight into engineering these types of coatings can be gained from computer simulations of the processes governing the diffusion of the individual elements making up the superalloy. Therefore, in this study, a chemical potential Monte Carlo (CPMC) model was developed to simulate diffusion of platinum-aluminium binary alloys. The change in microstructure during diffusion as the pure elements diffuse into each other to form an alloy with a specific composition is investigated. In the model, data structures, search algorithms and a random number generator were developed and employed in an object-orientated code

to simulate the diffusion of binary metals during annealing. Several simulations were performed at different compositions. The results are compared to experimentally-measured elemental maps of EB-PVD prepared thin film samples.

Samevatting

Sedert Icarus se mitiese vlug om van Kretense af te ontsnap tot die meer onlangse bemande ruimte ruise na die maan het die mensdom se droom om te kan vlieg die wêreld geweldig beïnvloed en verander. Tegnologiese ontwikkeling in mettalurgie en allooi ontwikkeling het 'n groot rol gespeel om hierdie droom te verwesenlik. Die ontwikkeling van materiale en super allooie met hoër smeltpunte en beter drywingsvermoëns het 'n groot rol gespeel in die ontwerp van die moderne turbine vliegtuig enjins. Ekonomiese en omgewings faktore is vandag die grootste motiveerder om hierdie enjins teen selfs hoër temperature te laat werk. Hierdeur word die termodinamiese effektiwiteit verhoog en die emissie van afvalstowwe verlaag. Een van die aggresiefste mensgemaakte omgewings is in die höe druk turbine seksie van 'n moderne gasturbine enjin. Hier word hoogs oksiderende gasse oor die turbine laat vloei teen temperature wat 200 °C hoër is as die smeltpunt van die super allooi turbine lemme. Van die nuwer generasie van siviele vliegtuie sal turbine ingangs-temperature (TIT) hê wat hoër is as 1800 K wanneer die vliegtuig opstyg. Daarom is die verhoging in drywing en verbetering in brandstof verbruiking van vliegtuie 'n vereiste in moderne gas turbine enjins. Een van die strategiëe wat gebruik word om hierdie doelwit te bereik is om die turbine lemme te bedek met 'n dunfilm wat bestaan uit 'n allooi material. Hierdie dun films kan so ontwerp word dat dit spesifieke hitte-bestande en oksidasie-bestande eienskappe het. Twee van die beddekkingstegnieke wat belowend lyk om hierdie doelwitte te bereik is gepulseerde laser deponering (PLD) en elektron bundel fisiese damp deponering (EB-PVD). In hierdie studie word hierdie tegnieke ondersoek in spesifiek op platinum-alluminium allooie. Films wat met gepulseerde laser deponering vervaardig word het klein druppel-vormige deeltjies op die oppervlakte. Hierdie druppels sowel as 'n gepaste tegniek om die voorkoms van druppels op die dun film oppervlakte te minimeer (deur middel van die verandering van die atmosfeer druk en tipe gas in die atmosfeer) is ondersoek. Die stoigiometriese oordrag van die materiaal van die teiken na die substraat is ook ondersoek. Die stoichiometriese oordrag van materiaal vanaf 'n teiken na 'n substraat word ook ondersoek. Baie insig oor hoe om deklagies te ontwerp kan bekom word deur middel van rekenaar simmulasies van die diffusie prossesse in die super allooie. Gevolglik is 'n chemiese-potensiaal Monte Carlo model (CPMC) ontwerp en gebruik om diffusie in platinum-alluminium binêre allooie te simmuleer. Met behulp van

hierdie model kan die verandering in die mikrostruktuur tydens diffusie van die suiwer elemente van ‘n binêre allooi ondersoek word. In die model is data strukture, soek algoritmes en ‘n ewekansige getal generator ontwikkel en gebruik in ‘n voorwerp-georiënteerde omgewing. Die model is gebruik om die diffusie van binêre allooie tydens verhitting te ondersoek. Verskeie simmulasies is gedoen teen verskillende element samestellings. Die resultate is vergelyk met eksperimenteel gemete element-kaarte van Pt/Al dun films wat met EB-PVD voor berei is.

Index

Chapter 1: Introduction . . . . pg. 15
1.1) Goals of this study . . . . pg. 16
1.2) Layout of thesis . . . . pg. 17
References . . . . pg. 18

Chapter 2: Turbines and Alloys. . . . . pg. 19
Introduction. . . . . pg. 19
2.1) Turbines and super alloys: a brief history. . . . . pg. 19
2.2) Ni and Pt -based super alloys. . . . . pg. 22
2.3) The platinum group metals as alloying constituents:
Basic strengthening effects. . . . . pg. 26
2.4) Corrosion resistance. . . . . pg. 26
2.5) Oxidation resistance. . . . . pg. 28
2.6) Summary. . . . . pg. 28
References. . . . . pg. 30

Chapter 3: Pulsed Laser Deposition (PLD) . . . . .pg. 34
Introduction. . . . . pg. 34
3.2) Basic setup. . . . . pg. 35
3.3) Droplet formation. . . . . pg. 37
3.4) Ambient gasses. . . . . pg. 39
References. . . . . pg. 40

Chapter 4: Electron Beam – Physical Vapour Deposition (EB-PVD) pg. 43
Introduction. . . . . pg. 43
4.1) Physical vapour deposition (PVD) processes. . . . . pg. 44
4.2) Advantages and disadvantages of PVD process. . . . . pg. 46
4.3) The physics of evaporation: evaporation rate . . . . pg. 46
4.4) Electron beam – physical vapour deposition setup. . . . . pg. 48
4.5) Summary. . . . . .pg. 49
References. . . . . pg. 50

Chapter 5: Diffusion and Monte Carlo. . . . . .pg. 52
Introduction. . . . . pg. 53
5.1) Early diffusion models: the laws of Fick. . . . . pg. 54
5.1.1) Fick's first law: the rate of diffusion. . . . . pg. 55
5.1.2) Fick's second law. . . . . pg. 57
5.2) Mechanisms of diffusion. . . . . .pg. 57
5.2.1) Ring diffusion. . . . . pg. 57
5.2.2) Vacancy diffusion. . . . . pg. 58
5.2.3) Interstitial diffusion. . . . . pg. 59
5.3) The Monte Carlo method and random numbers. . . . . pg. 60
Introduction to Monte Carlo. . . . . .pg. 60
5.3.1) Illustration of the Monte Carlo method. . . . . pg. 61
5.3.2) Random number generators. . . . . pg. 63
5.3.3) "True" random numbers *vs*. pseudorandom numbers. . . . . pg. 64

5.3.4) Mersenne Twister. . . . . pg. 65
References. . . . . pg. 67

Chapter 6: Chemical Potential Monte Carlo Model. . . . . pg. 69
Introduction. . . . . pg. 69
6.1) Chemical potential. . . . . pg. 69
6.2) Regular solution model (RSM) . . . . . pg. 72
6.3) Interaction coefficient. . . . . pg. 75
6.4) Relation between μ and G_{mole} via regular solution model. . . . . pg. 76
6.5) Basic hypothesis and general equilibrium conditions. . . . . pg. 77
6.6) Bulk equilibrium conditions. . . . . pg. 78
6.7) The CPMC model and the change in "microscopic" μ. . . . . pg. 80
6.7.1) Crystal setup. . . . . pg. 80
6.7.2) Atomic motion through diffusion. . . . . pg. 82
6.8) Software flow chart. . . . . pg. 86
References. . . . . pg. 87

Chapter 7: PLD Results. . . . . pg. 88
Introduction. . . . . pg. 88
7.1) Preparation of Pt_{84}:Al_{11}:Cr_3:Ru_2 samples. . . . . pg. 89
7.2) Stoichiometric transfer of target material. . . . . pg. 90
7.3) Sample characterisation. . . . . pg. 92
7.3.1) Thin films from the annealed Pt_{84}:Al_{11}:Cr_3:Ru_2 target. . . . . pg. 92
7.3.2) Thin films from the unannealed Pt_{84}:Al_{11}:Cr_3:Ru_2 target. . . . . pg. 98
7.3.3) Conclusion. . . . . pg. 103
7.4) The effect of ambient gas and gas pressure on PLD thin films. . . . . pg. 103
7.4.1) Imaging via secondary electron microscopy (SEM) . . . . . pg. 104
7.4.2) Atomic force microscopy (AFM) . . . . . pg. 110
7.4.3) Discussion. . . . . pg. 114
7.4.4) Conclusion. . . . . pg. 116
References. . . . . pg. 117

Chapter 8: PVD and Simulation Results. . . . . pg. 118
Introduction. . . . . pg. 118
8.1) Experimental setup and procedures. . . . . pg. 118
8.1.1) Diffusion barrier for thin films: wet oxidation. . . . . pg. 119
8.1.2) Calculation of at.% for the thin films. . . . . pg. 121
8.1.3) Preparation of the thin films: EB-PVD. . . . . pg. 121
8.1.4) Annealing of the thin films. . . . . pg. 122
8.1.5) Characterisation of the thin films. . . . . pg. 123
8.2) Simulation setup. . . . . pg. 124
8.3) Results and discussion. . . . . pg. 126
8.4) Time evolution . . . . . pg. 154
8.5) Summary. . . . . pg. 159
References. . . . . pg. 161

Chapter 9: Comparison to other models. . . . . pg. 162
Introduction . . . . . pg. 162
9.1) Introduction to phase-field modelling . . . . . pg. 162
9.2) Phase-field modelling of microstructure evolution . . . . . pg. 163

9.3) The CPMC model in its proper perspective . . . . pg. 166
9.4) Summary . . . . pg. 168
References. . . . . pg. 170

Chapter 10: Conclusion. . . . . pg. 171
Future work . . . . pg. 173

Appendix A. . . . . .pg. 175

List of Tables and Figures

List of Figures

Chapter 2 . . . . .Figure 1 . . . . .pg. 24

Chapter 3 . . . . .Figure 1. . . . . pg. 36
Figure 2. . . . . pg. 37
Figure 3. . . . . pg. 38

Chapter 4 . . . . .Figure 1. . . . . pg. 48

Chapter 5 . . . . .Figure 1. . . . . pg. 53
Figure 2. . . . . pg. 56
Figure 3. . . . . pg. 58
Figure 4. . . . . pg. 59
Figure 5. . . . . pg. 60
Figure 6. . . . . pg. 61
Figure 7. . . . . pg. 63
Figure 8. . . . . pg. 66

Chapter 6 . . . . .Figure 1. . . . . pg. 72
Figure 2. . . . . pg. 81
Figure 3. . . . . pg. 81
Figure 4. . . . . pg. 82
Figure 5. . . . . pg. 83
Figure 6. . . . . pg. 84
Figure 7. . . . . pg. 85
.
Chapter 7 . . . . .Figure 1. . . . . pg. 93
Figure 2. . . . . pg. 93
Figure 3. . . . . pg. 94
Figure 4. . . . . pg. 94
Figure 5. . . . . pg. 95
Figure 6. . . . . pg. 97
Figure 7. . . . . pg. 100
Figure 8. . . . . pg. 100
Figure 9. . . . . pg. 101
Figure 10. . . . . .pg. 101
Figure 11. . . . . .pg. 102

Figure 12. . . . . .pg. 102

Figure 13. . . . . .pg. 104
Figure 14. . . . . .pg. 105
Figure 15. . . . . .pg. 106
Figure 16. . . . . .pg. 107

Figure 17. . . . . .pg. 108
Figure 18. . . . . .pg. 109
Chapter 7 (continue) . . . . Figure 19. . . . . .pg. 110
Figure 20. . . . . .pg. 111
Figure 21. . . . . .pg. 112
Figure 22. . . . . .pg. 113
Figure 23. . . . . .pg. 114
Figure 24. . . . . .pg. 115

Chapter 8 . . . . .Figure 1. . . . . pg. 126
Figure 2. . . . . pg. 127
Figure 3. . . . . pg. 128
Figure 4. . . . . pg. 128
Figure 5. . . . . pg. 129
Figure 6. . . . . pg. 129
Figure 7. . . . . pg. 129
Figure 8. . . . . pg. 130
Figure 9. . . . . pg. 131
Figure 10. . . . . .pg. 131
Figure 11. . . . . .pg. 133
Figure 12. . . . . .pg. 134
Figure 13. . . . . .pg. 134
Figure 14. . . . . .pg. 135
Figure 15. . . . . .pg. 136
Figure 16. . . . . .pg. 138
Figure 17. . . . . .pg. 138
Figure 18. . . . . .pg. 139
Figure 19. . . . . .pg. 140
Figure 20. . . . . .pg. 141
Figure 21. . . . . .pg. 141
Figure 22. . . . . .pg. 142
Figure 23. . . . . .pg. 143
Figure 24. . . . . .pg. 144
Figure 25. . . . . .pg. 145
Figure 26. . . . . .pg. 145
Figure 27. . . . . .pg. 146
Figure 28. . . . . .pg. 147
Figure 29. . . . . .pg. 148
Figure 30. . . . . .pg. 148
Figure 31. . . . . .pg. 149
Figure 32. . . . . .pg. 150
Figure 33. . . . . .pg. 151
Figure 34. . . . . .pg. 152
Figure 35. . . . . .pg. 152
Figure 36. . . . . .pg. 153
Figure 37. . . . . .pg. 154
Figure 38. . . . . .pg. 155
Figure 39. . . . . .pg. 157
Figure 40. . . . . .pg. 158

Chapter 9 . . . . Figure 1. . . . . pg. 169

Appendix A. Figure A.1. . . . . pg. 175
Figure A.2 . . . . pg. 176

List of Tables

Chapter 2 . . . . Table 1. . . . . pg. 27

Chapter 7 . . . . Table 1. . . . . pg. 89
Table 2. . . . . pg. 91
Table 3. . . . . pg. 98

Chapter 8 . . . . Table 1. . . . . pg. 120
Table 2. . . . . pg. 123

Chapter 1

Introduction

Although flying has become a conventional method of transportation by now, it is hard to imagine that a mere 70 years ago, in the early 1940's, jet-powered flight was seen as nothing more than science-fiction. Back then scientists realized that materials used in parts of the engine would not be able to survive more than a few hundred hours' relatively modest temperatures. Ten years later however, jet fighters were put in combat over Korea and at the end of the 1960's commercial jets were accepted and the commercial aviation market overtook the military one by the end of the 1980's [1].

Improvement in engine materials certainly played a key role in this aviation progression. Economical and (today more than ever) environmental concerns continue to provide ample motivation for operating the engines at ever increasing temperatures, thereby improving the thermodynamic efficiency and reducing pollutant emissions. The quest for higher temperatures was dominated by materials and processes developments in the earlier decades of jet-engine manufacturing. Major steps were the use of the superalloy, considerable advancements in casting technologies and the cooling system for turbine blades which allowed service temperatures to be increased by 20 °C or more. However, although alloy improvement has been a key issue over the last 3 decades, recent times have seen a shift in focus to that of coating systems, which have allowed an increase of gas temperature of up to 110 °C [1].

One of the most aggressive man made environments is that of the high pressure turbine section of a modern gas turbine engine. During operation, after combustion, highly oxidizing gas enters the turbine. This happens at temperatures 200 °C above the melting point of the superalloy turbine blade. Newer generations of civil aircraft will have turbine entry temperatures (TET) that will exceed 1800 K at take-off [2]. Increased power and improved fuel consumption remains a continuing demand in modern aero-gas turbine engines as this result in an increase in TET. These increases in TETs, with the associated increases in turbine component operating temperatures, have been made possible in the past largely due to the continuing development of

nickel base superalloys with higher temperature capability and improvements in component air cooling technology. However, as TETs in aero gas turbines continue to increase, improved cooling technology or higher temperature capability superalloy alloy materials will no longer suffice. [2].

Another route that enables turbine components to operate at higher TETs is to insulate the metal surface from the hot combustion gas, reducing actual metal temperature. This is an attractive proposition and was the basis for the development of thermal barrier coatings some 25 years ago.

Coatings in gas turbines serve a variety of purposes, whether in jet engines, land-based power generation turbines or marine engines. A first requirement to operate turbines at higher temperatures was, of course, improved strength. Unfortunately, these conditions also mean several oxidation/corrosion problems, and to make things worse, the improvement in mechanical properties of the base alloys was made at the expense of environmental resistance [2].

1.1) Goals for this study

The goals of this study are three fold:

- Investigate two different coating-techniques, pulsed laser ablation (PLD) and physical vapour deposition (PVD), to grow binary metallic thin films. These films consist of platinum and aluminium. A study into the characteristics of thin films grown via PLD could reveal any detrimental effects to the resulting thin films.

- The design and implementation of a theoretical model with the purpose of being able to predict the resulting structure and depth profiles of metallic binary thin films that are heat treated.

- Obtaining experimental data (through EB-PVD) to verify or disprove the theoretical model.

1.2) Layout of thesis

Chapter 2 gives a background and overview of the platinum-based alloys.

Chapter 3 discusses the pulsed laser ablation (PLD) coating technique.

Chapter 4 gives a background and short overview of the physical vapour deposition processes.

Chapter 5 describes the general theory of diffusion and in particular the laws of Fick which are derived. It is shown how these laws are used to describe diffusion kinetics. An overview of the Monte Carlo technique is also given. This technique is used in the development of the chemical potential Monte Carlo (CPMC) model presented in this study.

Chapter 6 discusses in detail the thermodynamics of binary alloys and the influence of the chemical potential on such systems. The regular solution model is also discussed and an equation for the interaction energy is derived. Equilibrium conditions for alloy atoms in a bulk system are derived from the regular solution model. The chemical potential Monte Carlo model is then derived and discussed. A flowchart of the developed software for the CPMC is shown.

Chapter 7 describes the experimental setup and results from the PLD study.

Chapter 8 describes the experimental setup and results from the EB-PVD- grown thin films. These experimentally measured results are compared to the theoretical simulation results.

Chapter 9 gives an overview of phase-field modelling (developed in the same time period as this study) and compares CPMC to phase-field simulations.

Chapter 10: a conclusion is drawn on the PLD experimental results, EB-PVD experimental results as well as the theoretical model results.

References

1. ***Coatings for Turbine Blades***, ***Sourmail T.***, Available Online: June 2006 at: http://www.msm.cam.ac.uk/phase/trans/2003/Superalloys/coatings/index.html.

2. **Wing R.,** Materials World, Volume 10, (2000).

Chapter 2

Turbines and Alloys

Introduction

Platinum-based alloys are being developed for high temperature and special applications for good corrosion and oxidation resistance. The microstructures are similar to those of nickel-based superalloys, and comprise of Pt_3Al particles in a Pt-based matrix [1].

2.1) Turbines and superalloys: a brief history

The superalloys are high-temperature materials which display exceptional resistance to mechanical and chemical degradation at temperatures close to their melting points [2]. They are based upon nickel but usually contain significant amounts of 4 other elements and more, including chromium and aluminium.

These alloys have had a unique impact since their first appearance in the 1950s as an alloy used in aero engines which power the modern civil aircraft [3] and later in land based turbine systems for electricity generation [6]. The superalloys are employed in the very hottest sections of the turbines. Here these alloys are also exposed to the heaviest of loads and therefore the utmost importance is placed on assuring the integrity of the components fabricated from them [4]. Therefore the development of the superalloys has been inherently linked to the history of the jet engine for which they were designed. Further improvements in temperature capability are now being actively sought for the engines to power the two-decked Airbus A380 and the Boeing 787 Dreamliner, to name just two examples [2, 5]. Since fuel economy is improved and carbon emissions are reduced by higher operating conditions, research in this has

attracted much attention [7]. For the next generation of ultra-efficient power generation systems new developments in superalloys are an essential requirement. For the next 25 years, the world's installed power generation capacity is expected to double [2, 8], due to the rapidly growing economies and populations of the developing countries. Thus improving the superalloys is important for the world.

One of the key factors to consider when designing a gas turbine engine is the choice of the turbine entry temperature (TET) [9, 10]. This is the temperature of the hot gases entering the turbine arrangement. Inside the turbine the temperature falls as mechanical work is extracted from the gas stream [2]. For this reason the conditions at turbine entry can be considered to be the most demanding on the nickel-based superalloys from which they are made. Thus if the TET can be raised, the performance of the engine can be greatly improved [11]. In the last 54 years since their conception, this has provided the incentive to improve the temperature capability of these superalloys. The success of this endeavour can be judged from the way in which the TET of the large civil aero engine has increased since Whittle's first engine of the 1940s [12]. A 700 °C improvement in a 70 year period has been achieved [2].

The turbine entry temperature varies greatly during a typical flight cycle. It is largest during the take-off and climb to cruising altitude. For power-generating applications, turbines experience fewer start-up/power-down cycles but very much longer periods of operation. During these periods of time the TET tends to be rather constant.

The high pressure turbine section of a modern gas turbine engine operates in very aggressive environments [13 - 15]. Following combustion, highly oxidizing gases enter the turbine at a temperature more than 200 °C above the melting point of the superalloy turbine blade. In the new generation of civil aircraft, turbine entry temperature (TET) on take-off will exceed 1800 K [16]. The only reason turbine components survive under these conditions is due to the massive amount of cooling air blown through them, maintaining actual metal temperature below the superalloy melting point.

The continuing demand for increased power and improved specific fuel consumption in modern aero gas turbine engines has resulted in a progressive increase in TETs over the last 30 to 40 years [17; 18]. This trend is expected to continue into the foreseeable future, as even more powerful large aero-engines are developed. These increases in TETs, with the associated increases in turbine component operating temperatures, have been made possible in the past largely due to the continuing development of nickel based superalloys with higher temperature capability and improvements in component air cooling technology. However, as TETs in aero-gas turbines continue to increase; this requirement will not be able to be realized through improved cooling technology or higher temperature capability superalloy materials.

Another route that enables turbine components to operate at higher TETs is to insulate the metal surface from the hot combustion gas, reducing actual metal temperature [19]. This is an attractive proposition and was the basis for the development of thermal barrier coatings some 25 years ago [20].

The current state-of-the-art thermal barrier coatings use electron beam physical vapour deposition (EB-PVD) and are favoured for use in gas turbine engines due to their increased strain tolerance, improved erosion resistance and better surface finish. The evolution of the gas turbine engine has relied in large part on the development of improved materials, and this is especially true in the field of high pressure turbines. Temperature capability increases in this area have been possible thanks to improvements in nickel based superalloy materials but, with the development of high rhenium content single crystal materials, this technology is now reaching its end.

In an effort to protect the turbine blades from these extremely high temperature gases; the thermal barrier coating (TBC) system has been implemented. The TBC system primarily consists of four layers: the ceramic top-coat, the thermally grown oxide (TGO), the bond coat, and the substrate. The ceramic top-coat is the layer that provides thermal insulation for the blade. It has a very low thermal conductivity and has been designed using point defects to withstand thermal cycles. This layer is typically made of Y_2O_3 which is stabilized with ZrO_2, or YSZ for short. The thermal conductivity for this layer at a temperature of 1000 °C is 2.3 W/ (M*K) which is one of lowest conductivity of all the ceramics. In addition YSZ has a very high melting

point (2700 °C) which makes it perfect for this application. Furthermore in an effort to reduce stresses in this material, cracks and porosity are intentionally incorporated into the material to make it highly compliant (elastic modulus of 50 GPa) and strain tolerant. The next two layers are the bond coat and the thermally grown oxide (TGO). The TGO layer was not intended but was created when the ceramic top-coat reacts with the bond coat in very high temperatures. This layer is about 1 – 10 μm thick and is engineered to form as α-Al_2O_3 and that its growth is slow, uniform, and defect free. The bond coat falls above the supperalloy and is about 75-150 μm thick. It is an oxidation-resistant metallic layer and is primary used to hold the ceramic top coat to the substrate. This layer is typically made of Ni and Pt and in some cases can consist of more than one layer having different composition. The final layer, which is the substrate is usually a nickel or cobalt based supperalloy which is air cooled by hollow channels inside the turbine blade. This supperalloy may also contain additional elements to improve specific properties such as high temperature strength, ductility, oxidation resistance, hot corrosion resistance and castability.

Thermal barrier coatings with reduced thermal conductivity and increased temperature capability are the only way of meeting the demands of increasing TETs in gas turbine engines. With a growing need for aircraft to be more efficient and environmentally friendly, coatings are essential for future gas turbine engine development [21].

2.2) Ni and Pt -based superalloys

The mechanical properties of nickel based superalloys can be optimized by tailoring alloy chemistry and micro-structural features through refined special practices and process control [22]. Nickel based superalloys are complex alloys with various micro structural features that contribute to the mechanical properties of the material. These features include among others the grain size, grain boundary morphology as well as the γ' size to name a few. One of the most important features is the grain size. It greatly influences strength, creep, fatigue crack initiation and the growth rate of cracks [23]. For this reason grain size control and optimization is one of the primary goals when turbine disc components are being manufactured. A great deal of work has

been done to develop predictive tools for recrystallization and grain growth of numerous nickel-based superalloys [24 - 28]. As these efforts are an ongoing process it will be a vital part of alloy and process design in the future. The control of γ' size and distribution is just as important in nickel-based superalloy materials. This is so because precipitation of the γ' phase is the main method of strengthening for these high-temperature alloys [29, 30]. This phase is primarily controlled through heat treatment, making this processing step vital to all superalloy components [31 – 39]. The heat treatment of nickel-based superalloys has and continues to be a topic of great interest [40]. Cooling rates, growth rates and γ' nucleation rates demonstrate the intricacy of these engineered materials. For example the high cooling rates from the solution heat-treatment cycle promote fine γ' formation which leads to high tensile and creep strengths. The chemical composition of the alloy also plays an important role in γ' formation size, morphology, and stability through specific phase chemistry and lattice mismatch issues. Another micro-structural feature that impacts turbine-performance is the grain-boundary morphology. Engineering the morphologies of grain boundaries has a great potential for improving material performance. Efforts to develop wavy or serrated grain boundaries have shown improvements in creep and rupture capabilities [41–50].

The three main advantages of using single crystal turbine blades over the conventionally cast and directionally solidified components are [55,56]:

- Elimination of grain boundaries transverse to the principal tensile stress axis has reduced grain boundary cavitations and cracking, resulting in greatly enhanced creep ductility,
- Elimination of grain boundaries made strengthening elements, such as carbon and hafnium redundant. This has facilitated heat treatment and allowed for the further optimization of the alloy chemistry to increase of the high temperature capability.

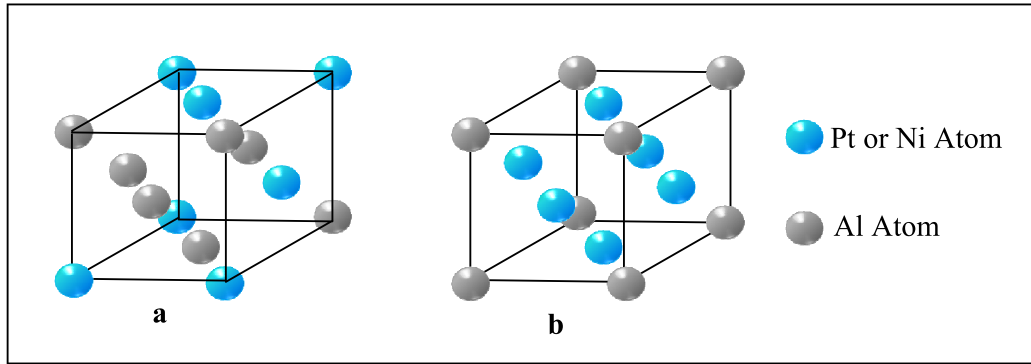

Figure 1: (a) Disordered FCC structure (b) Ordered $L1_2$ structure.

- The preferred <001> crystallographic solidification direction, which coincides with the minimum in Young's modulus and is oriented parallel to the component axis minimizes the thermal stresses developed on engine start-up and shut-down, this has dramatically improved the thermal fatigue resistance of the turbine hot gas path components.

Nickel-based superalloys have excellent mechanical properties because they have a microstructure comprising of many small, strained-coherent particles in a softer matrix. The strengthening originates from dislocations being slowed down as they negotiate the small ordered particles. Additionally, there is a solid solution strengthening in the Ni-matrix. Although these alloys are used at relatively high temperatures, coarsening does not occur because the surface energy itself is very small. This is because the particle structure is very closely related to that of the matrix. Both are based on the face centred cubic structure: the matrix has a random FCC structure, and the particles have an $L1_2$ ordered structure (where the Ni-atoms are located at the faces of the cubic unit cell and the Al- atoms at the corners.) The lattice misfit between these structures is very small and renders the surface energy negligible.

The Ni-based superalloys have virtually reached their temperature limit for operation in turbine engines. However, there is a need to further increase the operational temperatures of these engines to achieve greater thrust, reduced fuel consumption and lower pollution. Thus, there is interest in developing a whole new suite of similar

structured alloys based on a metal with a higher melting point which can be used at temperatures of 1300 °C.

Platinum has been selected as the base material for these alloys because of its similarity to Ni in FCC structure and similar chemistry: similar phases to Ni_3Al could be used to give similar mechanisms as found in the Ni-based superalloys.

The important differences are the higher melting point (1769 °C for platinum compared to 1455 °C for nickel) and improved corrosion resistance. Although platinum-based alloys are unlikely to replace all Ni-based superalloys on account of both higher price and higher density, it is likely that they can be used for the highest application temperature components.

Economic and ecological considerations are promoting the development of aircraft gas turbines and rocket engines with increased operation temperatures. Currently precipitation hardened Ni-based superalloys are predominant in high performance applications, i.e. at high temperatures and stresses. A further increase of the operation temperature of these alloys appears to be difficult, since in some applications they are already exposed to temperatures up to 90% of the melting temperature of the base metal Ni [51]. Beyond this point the alloy strength decreases rapidly because of the progressive dissolution of the hardening Ni_3Al precipitates.

Since the mid-1990s, the platinum group metals Ir, Rh and Pt have been the subjects of rising interest as base elements for new high and ultra high temperature alloys [52]. For potential use at temperatures up to 1300 °C, precipitation hardened Pt-base alloys are being developed. The main advantages of Pt as base material are its superior corrosion and oxidation resistance. However, pure Pt is very soft and ductile. Therefore, the highly successful strengthening of Ni-base superalloys by $L1_2$-ordered particles coherently embedded in face-centred cubic matrix is being mimicked in Pt-base alloys.

2.3) The Platinum Group Metals as Alloying Constituents: Basic Strengthening Effects

Refractory alloying elements play a key role in the high temperature strength of modern superalloys. The platinum group metals are very effective solid solution strengtheners to a basic nickel 20 wt% chromium austenite. At the lower temperature of 800 °C, platinum is almost equivalent, on an at.% basis, to tungsten (which has a similar density) while molybdenum and tantalum are more effective in their solid solution strengthening capabilities. However, at the higher temperatures of 1000 °C and 1200 °C, the platinum group metals and particularly platinum show a clear advantage, even over tantalum and molybdenum [53]. This strengthening effect also manifests itself in terms of creep strength. The creep strengths of Pt-based alloys at the very high temperature of 1300°C are higher than those of the Ni- and Co-based superalloys, whose precipitates dissolve in this high-temperature regime, resulting in loss of strength. A general observation can be made that platinum-enriched alloys tend to show superior creep properties over their conventional counterparts at higher temperatures.

2.4) Corrosion Resistance

The presence of contaminants in the combustion gases of turbine engines accelerates corrosive attack of superalloys. This happens particularly in the temperature range 650 °C to 950°C. Especially alumina-forming alloys are prone to this attack. When platinum is added to RJM1020- and RJM1030- alloys corrosion resistance is dramatically enhanced (RJM1020 and RJM1030 are 10 weight percent platinum alloys compositionally similar to the conventional alloys Mar-M200 and Mar-M007, respectively.

Alloy	Cr	Co	W	Ti	Al	Nb	C	B	Zr	Mo	Hf	Ta	Pt
RJM1020	9	10	12.5	2	5	1.8	0.15	0.015	0.05	0	0	0	balance
RJM1030	8	10	0.1	1	6	0.1	0.1	0.015	0.075	6	1.3	4.25	balance

Table 1: Composition of RJM1020 and RHM1030 superalloys. All concentrations are in at.%.

Even over Mar-M200 and Mar-M007- alloys in crucible sulphidation tests at 925 °C (Mar-M200 and Mar-M007 are nickel-based superalloys strengthened by a solid solution of W, Co and Cr, and by precipitates of $Ni_3(Ti,Al)$ and carbides). In these tests specimens are immersed in a molten 10% NaCl, 90% Na_2SO_4 mixture. This enhanced corrosion resistance occurs for both alumina- and chromia-forming alloys.

For the Mar-M200 alloy and its platinum-enriched equivalent RJM1020 tested under salt shower conditions it was shown [54] that platinum considerably enhances corrosion resistance over the whole temperature range of hot sulphidation corrosion. This occurred for long test durations. The salt shower test [54] is a laboratory test designed to simulate the hot sulphidation conditions seen in gas turbine environments.

The effect of platinum in promoting considerably enhanced corrosion resistance is also seen under other very aggressive high temperature environments where aggressive species other than sulphur are present. Therefore, by careful alloy design, it is possible to construct platinum containing alloys that show not only excellent corrosion resistance in these difficult environments but also satisfactory creep strength at temperatures. At these temperatures the useful alloys are those growing protective alumina-rich oxide scales.

High temperature hot corrosion (HTHC) tests (by L.A. Cornish et al.) that were conducted at 950°C for 540 hours showed that Pt-based alloys displayed far superior corrosion properties compared to coated and uncoated benchmark Ni-based superalloys [57].

2.5) Oxidation Resistance

Studies have shown that platinum group metal additions to superalloys do not greatly affect the isothermal oxidation rates. Under the more severe cyclic oxidation conditions, the improvement in oxide spallation characteristics is considerable. The cyclic oxidation test consists of one hourly cycles [53]. The specimen is annealed for 40 minutes at 1000 °C. This is followed by rapid cooling to, and maintaining at, room temperature for 20 minutes. Then by rapidly re-inserting the test samples into the hot furnace another cycle is started. The cycle is repeated as desired. The platinum alloys (RJM1020 and RJM1030) have a considerable improvement in cyclic oxidation behaviour, compared to the inherently good alloy Mar- M007.

Oxidation tests (by P.J. Hill et al.) on ternary Pt-Al-Z, Pt-Ti-Z, Pt-Ta-Z and Pt-Nb-Z (where Z can be Ni, Ru or Re) showed that alloys containing Al have considerably better oxidation properties than the other systems. This is because a protective Al-oxide film forms in the Pt–Al–Z systems, as opposed to internal oxidation in alloys not containing Al. It seems likely that alloying with Al will be essential in order to develop an oxidation- resistant alloy [58]. The formation of this Aluminium oxide was also observed in this study and will be discussed further in Chapter 8.

2.6) Summary

The concept of the use of platinum, and the other platinum group metals as alloys and alloying constituents have been described and shown to promote a considerable enhancement in oxidation and corrosion properties in nickel-based superalloys. For this reason platinum enriched and platinum based superalloys are being studied and developed for specific industrial and aerospace application. This is done by increasing efforts to tailor alloys with specific combinations of properties. These alloys have much to offer in industrial applications where corrosion resistance in high temperature environments is an important materials selection criterion. Application fields such as coal conversion and combustion and the petrochemical areas, for example, suggest themselves as candidates for platinum group metal alloys [53]. For

this reason the study of the diffusion process that governs a Pt-based binary alloy (in a thin film system) is investigated in this study. The aim is to provide a better understanding of this process through computer simulations. This will allow for the tailoring of alloys with specific combinations of properties.

References

1. **Cornish L.A., Süss R., Chown L.H., Taylor S., Glaner L., Douglas A. and Prins S.N.,** *International Platinum Conference 'Platinum Adding Value': The South African Institute of Mining and Mettalurgy*, (2004).
2. **Reed R.C**., *The Superalloys: Fundamentals and Applications,* New York, Cambridge University Press, (2006), pg.1-3.
3. **Totten G.E., MacKenzie D.S.,** *Handbook of Aluminium: alloy production and materials manufacturing*, Volume 2, New York, Marcel Dekker Inc, (2003), pg. 442-443.
4. **Donachie M.J., Donachie S.J**., *Superalloys: a technical guide, 2nd edn*, Materials Park Ohio, ASM International, (2002), pg. 15-17.
5. **Winstone M.R., Partridge A., Brooks J.W.,** *Proceedings of the Institution of Mechanical Engineers, Part L: Journal of Materials: Design and Application*, Professional Engineering Publishing, Volume 215, Nr. 2, (2001), pg. 63-73.
6. **Furrer D., Fecht H.,** *Journal of Minerals, Metals and Materials Society*, Volume 51, Nr. 1, (1999), pg. 14-17.
7. **Staley J.T. and Lege D.J.,** *Journal de Physique 111*, Volume 3, (1993), pg. 179-190.
8. ***The High Octane Economy***, Available Online March 2009, http://www.compassonbusiness.com/index2.php?option=com_content&do_pdf=1&id=186.
9. **Esgar J.B. and Reynolds R.A.,** *Technical Evaluation Report on AGARD Technical Meeting on High Temperature Turbines*, AGAFD Conference Proceedings No. 73, (1971).
10. ***Superalloy Explained***, Available Online March 2009 at http://www.madabout-kitcars.com/kitcar/kb.php?aid=438.
11. **Miller S.,** *Interdisciplinary Science Reviews*, Volume 20, Nr. 4, (13), (1995), pg. 117-129.
12. **Whittle F.,** *The early history of the Whittle jet propulsion gas turbine, James Clayton Memorial Lecture*, 1945, Available online April 2009:

http://presidentschoice.imeche.org.uk/NR/rdonlyres/B86DBAD0-204A-4B59-8FC1-9E39BABBA262/0/jc12.pdf.

13. **Gurrappa I.**, *Surface and Coatings Technology*, Volume 139, Issues 2-3, (2001) pg. 272-293.
14. **Carter T. J.,** *Engineering Failure Analysis*, Volume 12, Issue 2, (2005), pg. 237-247.
15. **DeMasi-Marcin J.T. and Gupta D.K.,** Surface *and Coatings Technology*, Volumes 68-69, (1994), pg. 1-9.
16. **Papamoschou D.,** *Journal of Propulsion and Power*, Volume 20, No. 2, (2004).
17. **Meetham G.W.**, *Materials & Design*, Volume 9, Issue 4, (1988) pg. 213-219.
18. **Boyce M.P.,** *Gas Turbine Engineering Handbook, 3^{d} edn.*, Burlington USA, Elsevier, pg. 15-17.
19. **DeMasi-Marcin J.T. and Gupta D.K.,** Surface *and Coatings Technology*, Volumes 68-69, (1994) pg. 10-11.
20. **Clarke D.R. and Phillpot S.R.,** *Materials Today*, Volume 8, Issue 6, (2005) pg. 22-29.
21. **Wing R.,** *White hot technology - a turbine revolution*, Materials World, (2000).
22. **Shen G. and Furrer D.,** *Proceedings of the 4th International Precision Forging Conference,* Columbus, OH, (1998).
23. **Chang K.M., Henry M.F. and Benz M.G.,** *Journal of Materials*, Volume 42, Issue 12, (1990), pg. 29–35.
24. **Balaji et al.**, *Proceedings of the North American Forging Technology Conference* (1994).
25. **Shen G., Semiatin S.L., and Shivpuri R.,** *Metalurgical and Materials Transactions A,* 26A.
26. **Shen G, Rollins J., and Furrer D., R.D. Kissinger et. al. (Eds),** *Superalloys 1996,* Warrendale, PA: TMS, (1996), pg. 613– 620.
27. **Furman T. and Shankar R.,** *Advanced Materials and Processes*, (1998), pg.45.
28. **Muralidharan G. and Thompson R.G.,** *Scripta Materiala,* Volume 36, Issue 7 (1997), pg. 755–761.

29. **Stoloff N.S., (Eds) Sims C., Stoloff N., and Hagel W.,** *Superalloys II,* New York, John Wiley & Sons, (1987), pg. 61–96.

30. **Nembach E. and Neite G.,** *Progress in Materials Science,* Volume 29, (1985), pg. 177–319.

31. **Ricks R.A., Porter A.J., and Ecob R.C.,** *Acta Materiala.,* Volume 31, (1983), pg. 43–53.

32. **Muller L., Glatzel U. and Feller-Kniepmeier M.,** *Acta Meta Materriala,* Volume 40, Issue 6, (1992), pg. 1321–1327.

33. **Svetlov I.L.,** *Scripta Materiala.,* Volume 26, (1992), pg. 1352–1358.

34. **Gayrand N.,** *Journal De Physique IV, Colloque C7,* Volume 3, (1993), pg. 271–276.

35. **Bhowal P.R., Wright E.F., and Raymond E.L.,** *Metallurgical and Materials Transactions A,* Volume 21A, (1990), pg. 1709–1717.

36. **Macia M.L. and Sanders T.H., Jr.,** *Proceedings of the 2nd International Conference on Heat-Resistant Materials,* Materials Park, Ohio, ASM, (1995), pg. 163–170.

37. **Klepser C.A.,** *Scripta Metalurgica.,* Volume 33, Issue 4, (1995), pg. 589–596.

38. **Schirra J.J. and Goetschius S.H., (Eds) Antolovich S.D. et. al.**, *Superalloys 1992,*.Warrendale, PA, TMS, (1992), pg. 437–446.

39. **Van Der Molen E.H., Oblak J.M., and Kriege O.H.,** *Metallurgical and Materials Transactions,* Volume 2, (1971), pg. 1627–1633.

40. **Wallis R.A.,** *AGARD Conference Proceedings No. 426*, Cesme, Turkey, NATO, (1987).

41. **Chang M., Koul A.K., and Cooper C, (Eds) R.D. Kissinger et. al.,** *Superalloys 1996,* Warrendale, PA, TMS, (1996), pg. 677- 985.

42. **Y. Zhang and F.D.S. Marquis, (Eds) R.D. Kissinger et. al.,** *Superalloys 1996,* Warrendale, PA, TMS, (1996), pg. 391 – 399.

43. **Wahi R.P.,** *Acta Materialia,* Volume 45, Issue 8, (1997), pg. 3143–3154.

44. **Myagawa O. et. al.,** *Proceedings of the Third International Symposium on Metallurgy and Manufacturing of Superalloys, Warrendale*, PA, TMS, (1976), pg. 245–254.

45. **Koul A.K. and Thamburaj R.,** *Metallurgical and Materials Transactions A,* Volume 16A, (1985), pg. 17–26.

46. **Koul A.K. and Gessinger G.H.,** *Acta Metallurgica.,* Volume 31, Issue 7, (1983), pg. 1061–1069.

47. **Larson J.M. and Floreen S.,** *Metallurgical and Materials Transactions. A,* Volume 8A, (1977), pg.51–55.

48. **Yoshiba M.,** *Proceedings of the Fifth International Conference on Creep of Materials* (1992), pg. 51–59.

49. **Merrick H.F. and Floreen S.,** *Metallurgical and Materials Transactions A,* Volume 9A, (1978), pg. 231–236.

50. **Henry M.F.,** *Metallurgical and Materials Transactions A,* Volume 24A (1993), pg. 1733–1743.

51. **Süss R., Freund D, Völkl R, Fischer B, Hill PJ, Ellis P et. al.,** *Material Science and Engineering. A*, Volume 338, (2002), pg. 1331.

52. **Yamabe Y, Koizumi Y, Murakami H, Ro Y, Maruko T, et. al.,** *Scripta Materiala*, Volume 35, (1996), pg. 211.

53. **Corti C. W., Coupland D. R. and Selman G. L.,** *Platinum Metals Review,* Volume 24, (1980), pg. 1.

54. **Norman P. L. and Harston J. D., (Eds.) Hart A. B. and Cutler A. J. B.,** *"Deposition and Corrosion in Gas Turbines"*, New York, Applied Science Publications., (1973), pg. 260.

55. **Onyszko A., Kubiak K., Sieniawski J.**, *Journal of Achievements in materials and Manufacturing Engineering*, Volume 32, Issue 1, (2009), pg. 66 – 69.

56. **Reed R.C.,** *The superalloys: Fundamentals and Applicaion*, Cambridge University Press, Cambridge, (2006).

57. **Cornish L.A., Suss R., Volkl., Wenderoth M., Vorberg S., Fischer B., Glatzel U., Douglas A., Chown L.H., Murakumo T., Preussner J., Lupton D., Glaner L., Maledi N.B., Potgieter J.H., Sephton M., Williams G.,** *SAIMM Symposium Series*, S45, (2006) pg. 81-90.

58. **Hill P.J., Biggs T., Ellis P., Hohls J., Taylor S., Wolff I.M.,** *Materials Science and Engineering,* Volume A301, (2001), pg. 167–179.

Chapter 3

Pulsed Laser Deposition

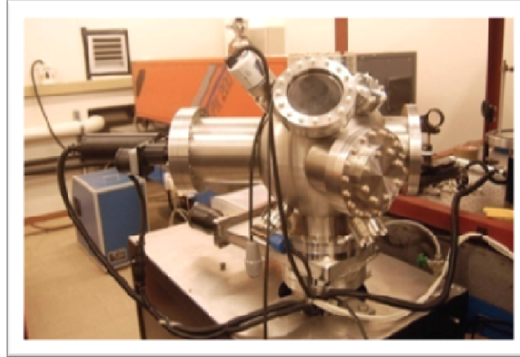

Introduction

In recent years there has been an enormous upsurge of interest in pulsed laser deposition (PLD) of thin films [1 - 6]. The main reason for this is because of its very successful application to high-temperature superconducting material (like $YBa_2Cu_3O_7$) (7, 8). The technique has been applied to a wide range of materials [9 - 15]. Kools has pointed out that metal films were first deposited by PLD in 1969 and that by 1978 the technique had been tried for more than half the metals in the periodic table [7].

Laser ablation can be used to create coatings by ablating the coating material from a source and letting it deposit on the surface to be coated; this is a special type of physical vapor deposition and can create coatings from materials that cannot readily be evaporated any other way. This process is used to manufacture some types of high temperature superconductors [16-18].

The process involves using a pulsed (10 - 30ns) laser to vaporize the surface of a solid target, and condensing the vapor onto a suitable substrate. The very rapid and intense heating leads to the congruent removal of the target constituents. PLD is now being used to prepare thin solid films of a wide range of materials including metals, semiconductors, insulators and superconductors [19].

Since PLD appeared as a promising thin film fabrication technique, both its advantages and drawbacks have continuously been discussed in the technical and scientific literature [20-25]. The characteristic behaviors of pulsed laser deposition of metallic alloys are: high deposition rates of up to 3nm/s above an ablation threshold of about 5 J/cm^2 a nearly congruent transfer between target and film and droplets on the film surface [26].

The congruent removal of target material can be exploited in the deposition of intermetallic compound and metal alloy materials. Since the deposition rate is typically less than one monolayer per laser pulse, it would seem that the technique is well suited for the preparation of thin film multilayers, where the period can be as small as 1 nm [27].

The quality of thin films obtained by PLD is often reduced by the simultaneous deposition of particulates. The main reason for the formation of particulates is the gradual degradation of the target surface which is the consequence of repetitive ablation [28-31]. In this chapter the physical mechanism of ablation and the drawback of the formation of droplets will be discussed.

3.1) Basic Setup

Laser ablation is the process of removing material from a solid or liquid surface by irradiating it with a laser beam. At low laser flux/fluence, the material is heated by the absorbed laser energy and evaporates or sublimates. At high laser flux, the material is converted to a plasma. The depth over which the laser energy is absorbed and the amount of material removed by a single laser pulse depends on the material's optical properties and laser wavelength.

Laser pulses can vary over a very wide range of duration (milliseconds to femtoseconds) and fluxes [32]. The experimental set-up is simple (see Figure 1), but the ablation process itself is extremely complex involving the interaction between the laser and a solid target material, plasma formation and the transport of material across the vacuum to the substrate.

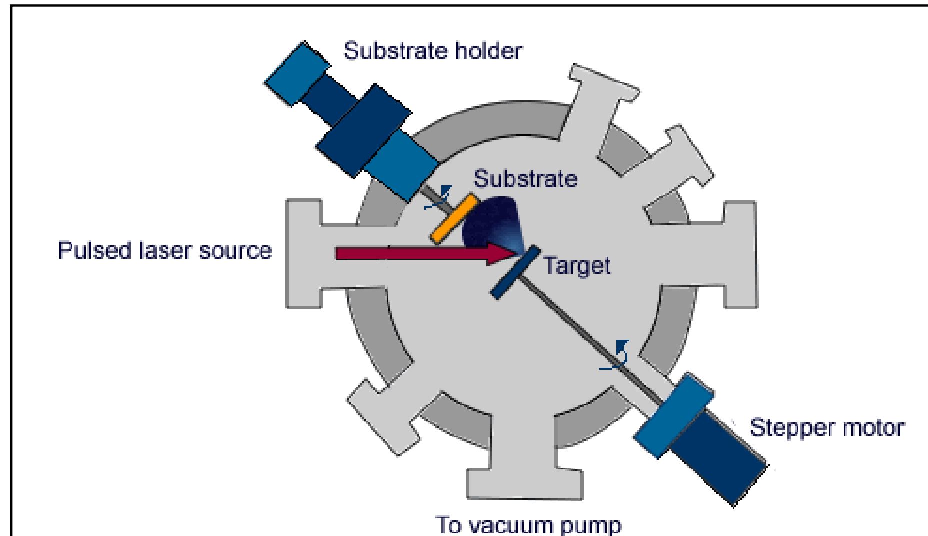

Figure 1: Experimental setup of the PLD system.

A high powered laser is focused onto a rotating target within a vacuum chamber. The extreme energy of the focused beam is absorbed by the small target surface area causing the breakdown of chemical bonds within the targeted region. This causes a few surface layers of the target to be ejected in the form of an ablation plume (see Figure 2) The components of these layers (ions, atoms or clusters), travel at extreme speed through the vacuum chamber until they impinge on the surface of the rotating substrate. The properties and composition of the plume may evolve in this short time as a result of collisions between the particles within the plume and interaction between the plume and the laser.

When the ablated material hits the substrate surface at high impact energies (typically 100 eV) the particles stick to the surface with reasonably high adhesion, and are compressed, forming a continuous film. Further laser pulses ablate more material and gradually the thickness of the film increases from a few atomic layers to microns. Other surface modification processes can take place during the process such as implantation or sputtering. PLD deposited films are not as dense as those deposited by other techniques such as magnetron sputtering that deposit coatings atom by atom [33].

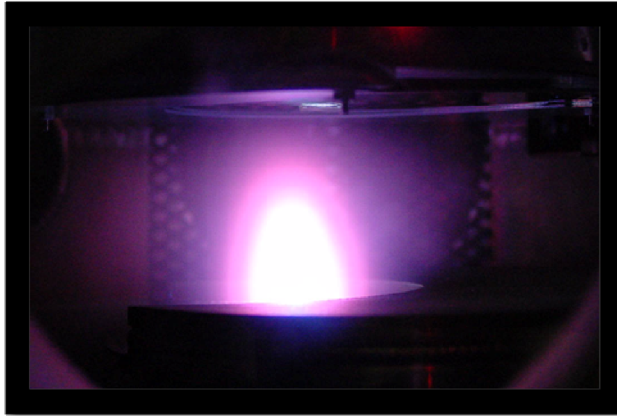

Figure 2: Plume formation after laser ablation of the target.

The laser-target interactions are sensitively dependent both on the nature and condition of the target material, and on the laser pulse parameters (wavelength, intensity, fluence, and pulse duration). Subsequent laser-plume interactions are also dependent on the properties of the laser radiation, while the evolution and propagation of the plume are sensitive to collisions and thus to the quality of the vacuum under which the ablation is conducted and/or the presence of any background gas. Obviously, the ultimate composition and velocity distribution (or distributions, in the case of a multi-component ablation plume) of the ejected material is likely to be reflected in the detailed characteristics of any deposited film.

Specific attention has been given to the role played by the ambient gas (He, Ar, N_2 and O_2) and its influence on the droplet minimization.

3.2) Droplet Formation

One of the major benefits of using PLD to grow thin films is the congruent removal of target material. This makes the technique suitable for the preparation of compound- and alloy- films [27]. This stoichiometric transfer [38] between target and substrate during PLD (above an ablation threshold of about 3-6 J/cm2) is of particular interest in this study where the platinum-based superalloy, Pt_{84}:Al_{11}:Cr_3:Ru_2, is deposited as a thin film, preserving its specifically engineered properties. Thus it is important that there is no change in the microstructure between the target and the deposited thin film during PLD.

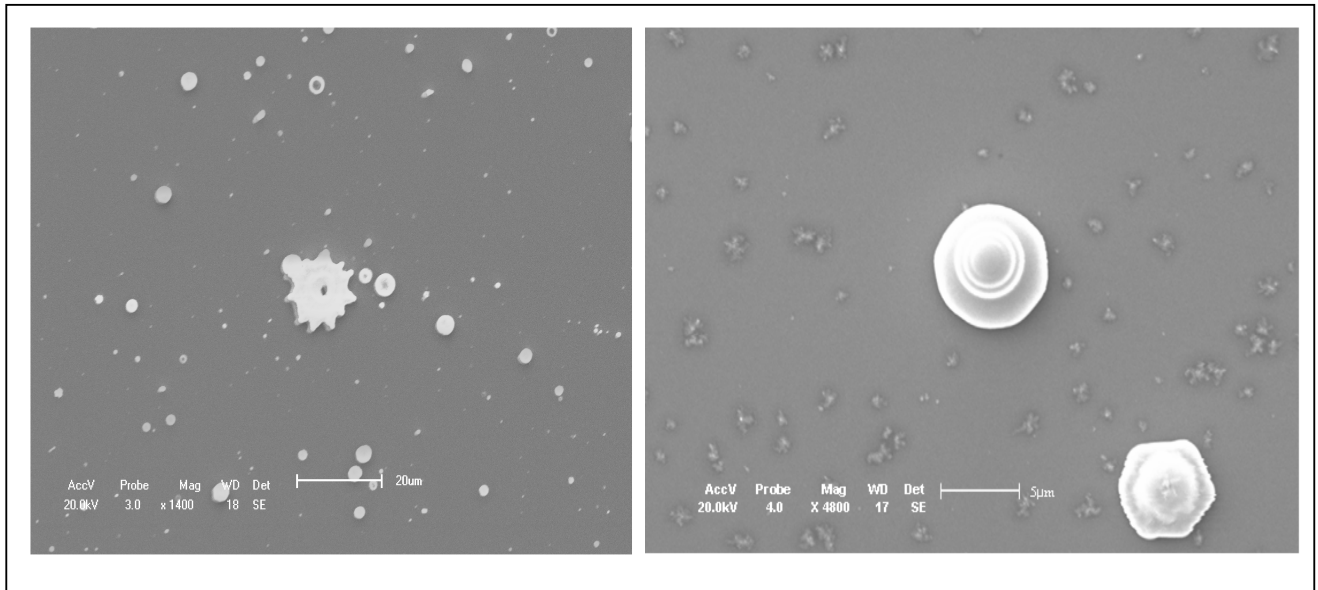

Figure 3: SEM micrograph in SE-mode of pulsed laser ablation induced droplets are clearly seen on these two Pt-alloy thin films.

In many cases when thin films are prepared by PLD it is found that the films are contaminated to varying degrees by particulates [35-38]. Figure 3 gives an example of these particulates for Pt-based alloy thin films deposited with PLD. The various shapes and sizes of these circular shaped droplets can be seen. For ceramic materials loosely bound particulates in the target can be detached by the pressure pulse associated with the ablation. In metals the contamination usually has the appearance of solidified droplets, and seems to arise from hydrodynamic expulsion of a molten layer on the surface of the target. However the detailed mechanism for the droplet formation is still controversial although much effort has been devoted to clarify the mechanism [39-41]. There are reports on a wide variety of experimental techniques to minimize the droplet density, and these are surveyed by Van de Riet et al. In the paper [42] it is pointed out that the size and quantity of droplets correlates closely with the laser induced surface roughness on the target, and measures taken to reduce the surface roughness of the target also minimize the amount of droplets on the thin films. The droplet velocity distributions for a variety target materials have been measured [43] and found to be in the range 100-200 ms^{-1}, which is much slower that the velocities of the ions and atoms in the vapor. Thus it is possible to construct a mechanical filter to transmit the vapor but not the droplets. Using a pallet rotating at 500 Hz and synchronized to the laser pulse a 100-fold reduction in droplet density has been demonstrated [27].

The occurrence of these droplets can be understood by the strong heating of a thin surface layer of the target during the laser pulse, where temperatures of typically up to 5000 K are reached, and a tearing off of columnar structures and balls formed on the target surface [26]. The simulated behavior of droplets in a PLD system with a starting position at the center of the target and with initial speed of 20 km/s shows that by increasing the mass, the particles tend to have smoother trajectories and become harder to deflect from their trajectories. Thus a stronger deviation angle may be possible for lighter particles, driven into the deposition area by the plume fine particles [44].

3.3) Ambient gasses

Laser deposited metallic films and alloys prepared under vacuum conditions at room temperature show significant differences in structure and microstructure compared to films produced by conventional deposition methods [26, 45]. These differences are caused by the kinetic energy of the ablated atoms and ions. Collisions with the inert gas atoms are expected to change the energy distribution of the ablated ions [45].

It is well known [46, 47] that ablation under high pressure atmospheres results in the formation of a shock wave which then propagates through the background gas towards the substrate accompanying the plume plasma. However, during propagation of the plume, interactions may occur (between the plume and shockwave) and the velocities and trajectories of ablated species can be modified which result in a change of the plasma parameters. Therefore, the study of laser ablation plasmas in the presence of a background gas has great importance [46]. The expansion dynamics of an ablation plume is strongly affected by the presence of background inert gas that leads to observable changes of plume shape and velocity, associated to scattering by gas atoms and to the development of a shock wave [48-50]. Briefly, during the motion of the plume between the target and the substrate the ablated particles in the expanding plume are scattered by gas atoms and transfer to them a fraction of their kinetic energy [48]. It turns out that the reaction between the ejected particles and the ambient molecules are enhanced in the shock front [39].

References

1. **Douglas C.B, Hubler G.K., (Eds.),** *Pulsed Laser Deposition of Thin Films*, New York, Wiley-VCH,(2003), pg. 648.
2. **Fan X. M., Lian J. S., Guo Z. X. and Lu H. J.**, *Applied Surface Science,* Volume 239, Issue 2, (2005), pg. 176-181.
3. **Douglas C.B. and Hubler G.K. (Eds.),** *Pulsed Laser Deposition*, New York: John Wiley and Sons, (1994), pg. 511.
4. **Venakatesan T, Wu X. D., Inam A., and Wachtman J. B**., *Applied Physics Letters* Volume 52, (l988), pg. ll93.
5. **Miller J. C. (Ed.),** *Laser Ablation*, Berlin/Heidelberg: Springer Series in Materials Science, (1994).
6. **Cheung J. T. and Sankur H.,** *Review Solid State Material. Science*, Volume 15, (1988), pg. 63 - 109.
7. **Kools, J., Hubler C.A. (Ed.),** *Pulsed Laser Deptosition of Thin Films*, New York : Wiley, (1994).
8. **Venkatesan T. and Green S. M.,** *Feature article in The Industrial Physicist: "Pulsed Laser Deposition: Thin Films in a Flash*", American Institute of Physics, (1996), pg. 22-24.
9. **Miller J.C. and HagIund R.F., Jr**.**(Eds.)**, *Laser Ablation*, Berlin, Springer (1991).
10. **Fogarassy E. and Lazare S. (Eds.)**, *Laser Ablation of Electronic Materials,* North-Holland, Amsterdam, (1992).
11. **Gutfeld R.J. and Dreyfus R.W.,** *Applied Physics Letters*, Volume 54, (1989), pg.1212.
12. **Dyer P.E.,** *Applied Physics Letters*, Volume 55, (1988), pg. 1630.
13. **Mehlman G., Burkhalter P.G., Horwitz J.S., Newman D.A.,** *Journal of Applied. Physics*, Volume 74, (1993), pg. 53.
14. **Dreyfus R.W.,** *Journal of Applied Physics*, Volume 69, (1991), pg. 1721.
15. **Phipps C.R. et. al.,** *Journal of Applied Physics*, Volume 64, (1988), 1083.
16. **Krebs H.U., Weisheit M., Faupel J., et. al.,** *Advances in Solid State Physics,* Volume 43, (2003), pg. 505 - 517.
17. ***Pulsed laser deposition (PLD) of thin films***: Available online April 2009: http://ap.polyu.edu.hk/apakhwon/lecture_notes/Thin_Films3.pdf.

18. ***Pulsed Laser Deposition of Dielectric and Ferroelectric Thin Films***: Available online June 2009: http://www.ceramics.nist.gov/programs/thinfilms/PLD.html.
19. **Haglund, J. M.** *Laser Ablation.* Berlin, Springer, (1991).
20. ***Main Advantages of PLD***, Available online June 2009: http://www.physandtech.net/3.htm.
21. **Jackson T. J., Palmer S. B.,** *Journal of Physics D: Applied. Physics*, Volume 27, (1994) pg. 1581.
22. **Paschotta R.,** *Encyclopedia of Laser Physics and Technology, Vol. 1*, Weinheim, Wiley-VCH Verlag GmbH & Co, KGaA, (2008).
23. **Quanhe Bao, Chuanzhong Chen, Diangang Wang, Qianmao Ji and Tingquan Lei,** *Applied Surface Science*, Volume 252, Issue 5, (2005), pg. 1539-1544.
24. **Willmott P. R., Huber J. R.,** *Reviews of Modern Physics*, Volume 72, Issue 1, (2000), pg. 315 – 328.
25. **Frumar M., Frumarova B., Nemec P., Wagner T., Jedelsky J. and Herdlicka M.,** *Journal of Non-Crystalline Solids,* Volume 352, Issue 6-7, (2006), pp 544-561.
26. **Krebs, H.U.,** *Applied Surface Sience*, Volume 86, (1995), pp. 86-89.
27. **Lunney, J.G.,** *Applied Surface Science*, Volume 86, (1995), pg.79-85.
28. **Chen, L., C. A. Hubler (Ed.).,** *Pulsed Laser Deposition of Thin Films, "Particulates generated by pulsed laser ablation"*, New York, Wiley, (1994), pg. 167-198.
29. **Ang L.K., Lau Y. Y., Gilgenbach R. M., Spindler H. L., Lash J. S. and Kovaleski S. D.,** *Journal of Applied Physics*, Volume 83, Nr 8, (1998), pg. .4466-4471.
30. **Schou J.,** *Applied Surface Science*, Volume 255, (2009) pg. 5191–5198.
31. **Chang-Hoon Kim, In-Tae Kim, Kug-Sun Hong, Taek-Sang Hahn, Sang-Sam Choi,** *Thin Solid Films*, Volume 358, (2000) pg. 223 – 228.
32. **Wang Y. C., Chen J. W., Lin H. C., Hwang C. C.,** *Journal of Heat Transfer*, Volume 131, Issue 3, (2009), pg. 33112.
33. ***PVD-Coatings***. Available Online March 2007: http://www.pvd-coatings.co.uk/theory-of-pvd-coatings-pulsed-laser-ablation.htm.

34. **Craciun V., Elders J., Gardeniers J. G. E. and Boyd I.W.,** *Applied Physics Letters*, Volume 65, Issue 23, (1994), pg. 2963 - 2965.
35. **Pechen E.V., Varlashkin A. V., Krasnosvobodtsev S. I., Brunner B., and Renk K. F.,** *Applied Physics Letters*, Volume 66, (1995), pg. 264 - 266.
36. **Michael N., Ashfold R., Claeyssens F., Fuge G.M. and Henley S.J.,** *Chemical Society Review,* Volume 33, (2004), pg. 23 – 31.
37. **Shen J., Zheng Gai, Kirschner J.,** *Surface Science Reports*, Volume 52, Issues 5-6, (2004), pg. 163-218.
38. **Kantor Z., Szorenyo T., Toth Z., Simon A., and Gombos L.,** *Applied Surface Science,* Volumes 138-139, (1999), pg. 599-604.
39. **Atsushi Masuda,** *Materials Science and Engineering B*, Volume 41, (1996), pg. 161-165.
40. **Lichtenwalner, D.,** *Journal of Applied Phyics*, Volume 74, (1993), pg. 7497.
41. **Watanabe, T.,** *Journal of Applied Physics*. Volume 78, (1995) pg. 2029.
42. **Van de Riet E., Nillesen C. M. and Dieleman J.,** *Journal of Applied Physics*, Volume 74, (1993) pg. 2008.
43. **Dupendant H., Gavigan J. P., Givord D., Lienard A., Rebouillat J. A. and Souche Y.,** *Applied Surface Science*, Volume 43 (1989) pg. 369.
44. **Marcu, A.,** *Applied Surface Science*, Volume 248, (2005), pg. . 466-469.
45. **Sturm, Kai.,** *Applied Surface Science.* Volumes 154-155, (2000), pg. 462-466.
46. **Escobar-Alarcon, L.,** *Applied Surface Science*, Volumes 197-198, (2002), pg. 192-196.
47. **Geohegan, D.,** *Applied Physics Letters,* Volume 60, (1992), pg 2732-2734.
48. **Bailini, A.,** *Applied Surface Science,* Volume 252, (2006), pg. 4364-4367.
49. **Wood, R.F.,** *Applied Surface Science,* Volume 151, (1998), pg. 127-129.
50. **Geohegan, D.B.,** *Applied Physics Letters,* Volume 72, (1998) pg. 2987.

Chapter 4

Electron Beam - Physical Vapour Deposition

Introduction

In recent years, thin film science has grown world-wide into a major research area. The importance of coatings and the synthesis of new materials for industry have resulted in a tremendous increase of innovative thin film processing technologies. Currently, this development goes hand-in-hand with the explosion of scientific and technological breakthroughs in microelectronics, optics and nanotechnology [1]. These films are essential for a multitude of production areas, such as thermal barrier coatings and wear protections. This enhances the service life of tools and protects materials against thermal and atmospheric influences. Presently, rapidly changing needs for thin film materials and devices are creating new opportunities for the development of new materials and technologies. Therefore, basic research activities will be necessary in the future, to increase knowledge, understanding, and to develop predictive capabilities for relating fundamental physical and chemical properties to the microstructure and performance of thin films in various applications. In basic research, special model systems are needed for quantitative investigations of the relevant and fundamental processes in thin film materials science. In particular, these model systems enable the investigation of i.e. nucleation and growth processes, solid state reactions, the thermal and mechanical stability of thin film systems and phase boundaries. Results of combined experimental and theoretical investigations are a prerequisite for the development of new thin film systems and the tailoring of their microstructure and performance.

During surface engineering the properties of the surface and near-surface region is being changed in a advantageous way. Surface engineering can be accomplished in two ways: either an overlay process or a surface modification process [2] . In overly

processes a material is added to the surface and the underlying material (substrate) is covered and not detectable on the surface. A surface modification process changes the properties of the surface but the substrate material is still present on the surface. For example, in aluminium anodization, oxygen reacts with the anodic aluminium electrode of an electrolysis cell to produce a thick oxide layer on the aluminium surface [3].

An atomistic film deposition process is one in which the overlay material is deposited atom-by-atom [5] . The resulting film can range from single crystal to amorphous, fully dense to less than fully dense, pure to impure, and thin to thick. Generally the term "thin film" is applied to layers which have thicknesses on the order of several microns or less and may be as thin as a few atomic layers. Often the properties of thin films are affected by the properties of the underlying material (substrate) and can vary throughout the thickness of the film [3]. Thicker layers are generally called coatings [6]. Atomistic deposition process can be done in vacuum, plasma, gaseous or electrolytic environment.

4.1) Physical Vapour Deposition (PVD) Processes

Physical vapour deposition (PVD) processes (often just called thin film processes) are atomistic deposition processes in which material is vaporized from a solid or liquid source in the form of atoms or molecules, transported in the form of a vapour through a vacuum or low pressure gaseous (or plasma) environment to the substrate where it condenses [3]. Typically, PVD processes are used to deposit films with thicknesses in the range of a few nanometers to thousands of nanometers; however they can also be used to form multilayer coatings, graded composition deposits, very thick deposits and freestanding structures. The substrates can range in size from very small to very large such as the 25×30 cm^2 glass panels used for architectural glass. The substrates can range in shape from flat to complex geometries such as watchbands and tool bits. Typical PVD deposition rates are 10 to 1000 Å (1 to 10 nanometers) per second [7 - 10].

PVD processes can be used to deposit films of elements and alloys as well as compounds using reactive deposition processes. In reactive deposition processes,

compounds are formed by the reaction of depositing material with the ambient gas environments such as nitrogen or with co-depositing material.

The main categories of PVD processing are vacuum evaporation, sputter deposition and ion planting [3]. In this study the focus fall on vacuum deposition.

Vacuum deposition which is sometimes called vacuum evaporation is a PVD process in which material from a thermal vaporization source reaches the substrate with little or no collision with gas molecules in the space between the source and substrate [3]. The trajectory of the vaporized material is “line-of-sight”. The vacuum environment also provides the ability to reduce gaseous contamination in the deposition system to a low level. Typically; vacuum deposition takes place in the gas pressure range of 10^{-5} Torr to 10^{-9} Torr depending on the level of gaseous contamination that can be tolerated in the deposition system.

The thermal vaporization rate can be very high compared to other vaporization methods [4]. The material vaporized from the source has a composition which is in proportion the relative vapour pressures of the material in the molten source material. Thermal evaporation is generally done using thermally heated sources such as tungsten wire coils or by high energy electron beam heating of the source material itself [3]. Generally the substrates are mounted at an appreciable distance away from the evaporation source to reduce radiant heating of the substrate by the vaporization source.

Vacuum deposition is used to form optical interference coatings [11], mirror coatings, decorative coatings, and permeation barrier films on flexible packaging materials, electrically conducting films, wear resistant coatings and corrosion protective coatings.

4.2) Advantages and disadvantages of PVD process

Some of the advantages of the PVD process are [12 - 14]:

- Materials can be deposited with improved properties compared to the substrate material.
- Almost any type of inorganic material can be used as well as some kinds of organic materials.
- The process is more environmentally friendly than processes such as electroplating.
- The almost unlimited variation in the chemical composition of the coating material.
- The deposition of compounds like nitrides, carbides etc.
- The deposition of materials like carbon or diamond.
- Provides distinctive coatings of a unique columnar microstructure for gas turbine components. This in turn leads to superior strain and thermo shock tolerant behaviour of the coatings due to their columnar microstructure [8].

Some of the disadvantages of the PVD process are [12 - 14]:

- It is a line of sight technique meaning that it is extremely difficult to coat undercuts and similar surface features.
- High capital cost (for coating large structures).
- Some processes operate at high vacuums and temperatures requiring skilled operators.
- Processes requiring large amounts of heat require appropriate cooling systems.
- The rate of coating deposition is usually quite slow.

4.3) The physics of evaporation: evaporation rate

Early attempts to quantitatively interpret evaporation phenomena are associated with the names of Hertz and Knudsen and, later, Langmiur [15]. Based on experimentation on the evaporation of mercury, Hertz in 1882 observed that evaporation rates were:

1) Not limited by insufficient heat supplied to the surface of the molten evaporant.

2) Proportional to the difference between the equilibrium pressure, P_e, of Hg at the given temperature and the hydrostatic pressure, P_h, acting on the evaporant.

He concluded that a liquid has a specific ability to evaporate at a given temperature. Furthermore, the maximum evaporation rate is attained when the number of vapour molecules emitted corresponds to that required to exert the equilibrium vapour pressure while none return. These ideas led to the basic equation for the rate of evaporation from both liquid and solid surfaces [16]:

$$\Phi_e = \frac{\alpha_e N_A (P_e - P_h)}{(2\pi MRT)^{1/2}} \tag{1.1}$$

Where Φ_e is the evaporation flux in number of atoms (or molecules) per unit area, per unit time and α_e is the coefficient of evaporation, which has a value between 0 and 1. When $\alpha_e = 1$ and P_h is zero, the maximum evaporation rate is realized. An expression for the maximum value of Φ_e is

$$\Phi_e = \frac{3.513 \times 10^{22}}{(MT)^{1/2}} P_e \tag{1.2}$$

This is measured in molecules/cm^2-s. When P_e is expressed in torr, a useful variant of this formula is [16]

$$\Gamma_e = 5.84 \times 10^{-2} (M / T)^{1/2} P_e \quad \text{g/cm}^2\text{-s} \tag{1.3}$$

Where Γ_e is the mass evaporation rate. At a pressure of 10^{-2} torr, a typical value of Γ_e for many elements is approximately 10^{-4} grams per second per cm^2 of evaporant area. The key variable influencing evaporation rates is temperature since it has a profound effect on equilibrium vapour pressures.

4.4) Electron beam – physical vapour deposition setup

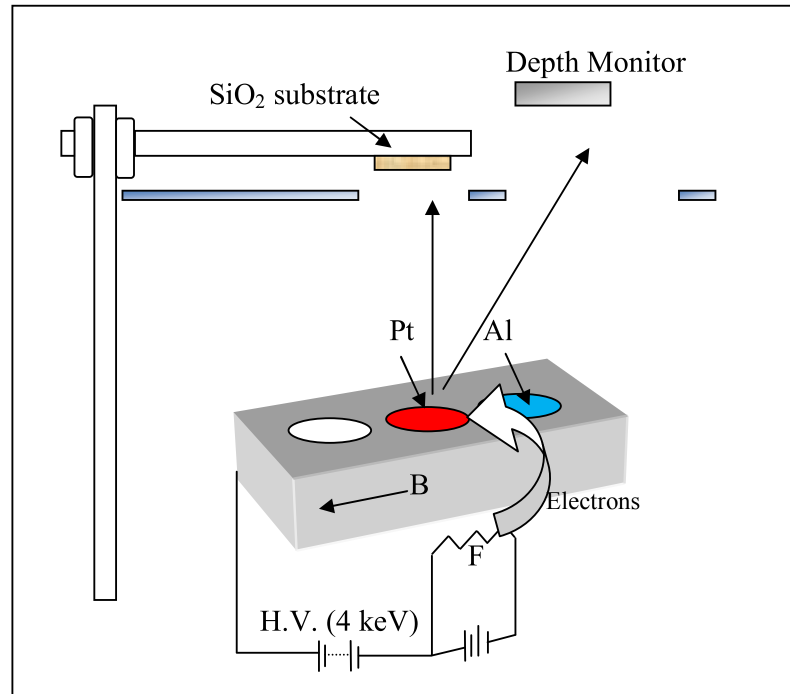

Figure 1: Schematic representation of electron beam - physical vapour deposition.

In the electron beam – physical vapour deposition system an electrical current is sent through a wolfram filament (F) (Figure 1). The filament is heated due to the flow of the current to the point where electrons are being released. These electrons are then accelerated via an electrical potential of 4 keV. Emitted electrons are accelerated towards an anode with very high speed. (approaching 40000 km/sec at 4 keV). A combination of the electrical field and a magnetic field (B) is then used to reflect the electrons towards a crucible where the target materials are placed. This setup is referred to as a "magnetic lens". In this study the target materials were Pt and Al. These high energy electrons then heat up these pure elements, individually. This happens because the kinetic energy of the electrons are transfered to thermal energy; resulting in a very high temperature. (For example if the velocity approaches 60000 km/sec a temperature of 5000 to 6000 °C can be created when bombarding target material [4]). This is done up to the point of evaporation. The vapour is then deposited onto the substrates and thin film layers start growing atomistically; i.e. monolayer by monolayer. In this study the substrates used were SiO_2.

The thickness of the deposited thin film is measured via a quartz-crystal which is placed in such a manner inside the vacuum chamber that the vapour is deposited on the substrates as well as on the crystal. The natural/resonant vibration frequency of the crystal changes with an increase in the thickness of the deposited layer. This allows for the determination of the thickness of the ensuing layer. The Z-ratio is a parameter that corrects the frequency change to a thickness transfer function for the effects of acoustic impedance mismatch between the crystal and the coated material. The acoustic impedance (Z) of a material is defined as the product of density (p) and acoustic velocity (V) of that material. (Z = pV). Acoustic impedance is important in the determination of acoustic transmission and reflection at the boundary of two materials having different acoustic impedance. The Z-ratio is therefore the ratio of the acoustic impedance of quartz (105 g/cm^2 s) to that of the selected material. Because the flow of material from a deposition is not uniform it is necessary to account for flux differences between the deposition meter's sensor and any samples. This is accounted for by the tooling factor, which can be experimentally established.

4.5) Summary

It is no understatement to say that thin-film growth techniques have, in the past four decades, fundamentally changed both condensed matter physics and everyday life. Well established thin-film technologies are used to grow the integrated circuits in our computers, cell phones, and palm pilots, while novel effects in thin films continue to be discovered and explored by both solid-state physicists and optical physicists. Many of the techniques used to grow thin films are related, and many involve physics and technology of marvellous subtlety.

In EB-PVD processes the material to be deposited is vaporized and all the atoms and ions evaporated from the target pass through the space between source and substrate in a line-of-sight flight. These atoms and ions are deposited on the surface by a condensation process. In this process the films and coatings grow on an atomic scale allowing for precise control of thin film thickness by controlling the film growth rate (in the order of 1 to 1000s of Å/s). This allows for a precise control of the composition of the deposited films when multi-layers are evaporated onto the substrate in sequence. This is an important requirement in this study.

References

1. **Siegel R. W., Hu E. H., Roco M. C.,** *WTEC panel report on R& D status and trends in nanoparticles, nanostructured materials and nanodevices, Workshop,* (1997), Available online September 2009 at: http://itri.loyola.edu/nano/us_r_n_d/toc.htm.
2. **Kennedy D. M., Xuey Y. and Mihaylovaz E.,** *The Engineers Journal*, Volume 59 (2005), pg.287-292.
3. **Mattox Donald M.,** *Handbook of physical vapour deposition (PVD) processing: film formation*, Noyes Publications, New Jersey.
4. ***Eta Film Technology Inc.***: Available online October 2009 at: http://www.etafilm.com.tw/PVD_Thermal_Evaporation_Deposition.html.
5. **Huang H., Gilmer G. H. and De la Rubia T. D.,** *Journal of Applied Physics*, Volume 84, Issue 7, (1998), pg. 3636 – 3650.
6. **Hollstein F., Wiedemann R. and Scholz J.,** *Surface and Coatings Technology,* Volume 162, Issue 2-3, (2003), pg. 261-268.
7. **Marcus S.D., Foster R.F.,** *Thin Solid Films*, Volume 236, Issue 1-2, (1993), pg. 330-333.
8. **Schulz U., Schmücker**, *Materials Science and Engineering A*, Volume 276, Issue 1-2 (2000), pg. 1-8.
9. **Navinsek B., Panjan P.,** *Surface and Coatings Technology*, Vol 59, Issue 1-3, (October 1993) pg. 244-248.
10. **Reinhold E., Botzler P. and Deus C.,** *Surface and Coatings Technology*, Volume 120-121, (1999), pg. 77-83.
11. ***Kolzer, Vacuum Deposition Process,*** Available online December 2008 at: http://www.kolzer.com/files /vacuum_deposition_guide.PDF.
12. **Saenger K. L.,** *Advance Materials Processes*, Volume 3, No.1, (1993), pg. 1-24.
13. **Jehn H.A.,** *Surface and Coatings Technology*, Volume 112, (1999), pg. 210-216.
14. **Azom Materials**, *Azom.com*, Available online February 2010 at: http://www.azom.com/Details.asp?ArticleID=1558.
15. **Glang, R.,** *Handbook of Thin Film Technology,* L.I. Maissel and R.Glang, eds., McGraw-Hill, New York, (1970).

16. **Ohring Milton,** *Materials science of thin films, deposition & structure, 2nd edn.* Academic Press, New Jersey, (2002).

Chapter 5
Diffusion and Monte Carlo

Introduction

Diffusion is the movement of atoms within a material [1]. Atoms move in a predictable fashion to eliminate concentration differences and produce a homogeneous, uniform composition [2]. This movement is most often from a region of high concentration (high energy) to a region of low concentration (low energy). The diffusion process will continue until the total energy of the system is minimized [2], resulting in a uniform distribution of atoms. Many of the treatments that are performed on materials require diffusion [3, 4]; for example the heat treatment of metals, the solidification of materials, the manufacture of ceramics and the manufacture of transistors and solar cell all require diffusion to take place.

This chapter serves as a summary for existing diffusion theories and to give the necessary background knowledge regarding diffusion and diffusion mechanisms. These processes are important to understand for the developed Chemical Potential Monte Carlo method developed in this study.

5.1) Early Diffusion Models: The Laws of Fick

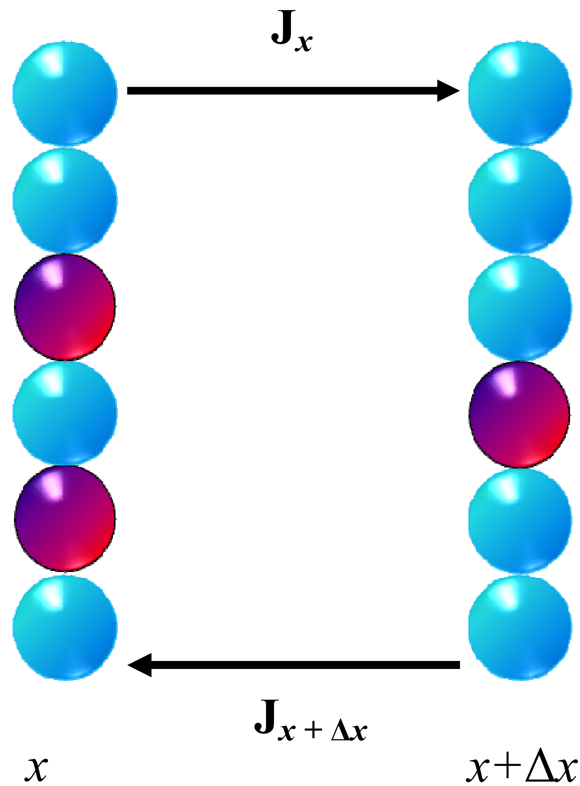

Figure 1: Atomic flux in the derivation of Fick's first law.

The only way in which concentration differences in a solid can be achieved or dispersed is through diffusion. Thus a relation exists between the atomic motion and the diffusion coefficient. This section provides a derivation of Fick's first law. The diffusion coefficient will be described in terms of the jump frequency and jump distance of atoms.

5.1.1) Fick's First Law: the Rate of Diffusion

In a crystal where all the diffusing atoms are of the same element, the diffusion coefficient (D) will be independent of concentration [5]. To see this let the concentration of impurity atoms per unit area at position x be N_x and $N_{x+\Delta x}$ at $x+\Delta x$, as shown in Figure 1. This derivation is done assuming diffusion is limited to nearest neighbour exchanges.

Let the mean jump frequency of the atoms be ρ. That means that, at any given moment, an atom jumps ρ times per second. Then the flux of atoms moving from layer x to layer $x+\Delta x$ is given by [5, 6]

$$J_x = \frac{1}{2}\rho N_x \tag{5.1}$$

An equation for atoms moving from layer $x+\Delta x$ to x can be expressed:

$$J_{x+\Delta x} = \frac{1}{2}\rho N_{x+\Delta x} \tag{5.2}$$

The net flux (from $x+\Delta x$ to x), from Figure 1 and equations (5.1) and (5.2), will be

$$J = J_{x+\Delta x} - J_x = \frac{1}{2}\rho(N_{x+\Delta x} - N_x) \tag{5.3}$$

By multiplying equation (5.3) with $\frac{\Delta x^2}{\Delta x^2}$, the flux in terms of concentration per unit volume and the concentration gradient can be expressed as:

$$\begin{aligned} J &= \frac{1}{2}\rho\left(\Delta x^2\right)\frac{\left(N_{x+\Delta x} - N_x\right)}{\Delta x \Delta x} \\ &= \frac{1}{2}\rho\left(\Delta x^2\right)\frac{\Delta N}{\Delta x \Delta x} \end{aligned} \tag{5.4}$$

Let ΔC be the change in concentration. Then $\left(\frac{\Delta N}{\Delta x}\right)$ in equation (5.4) can be replaced with ΔC:

$$J = -\frac{1}{2}\rho(\Delta x)^2 \frac{\partial C}{\partial x} = -D\frac{\partial C}{\partial x} \quad (5.5)$$

with $D = -\frac{1}{2}\rho(\Delta x)^2$. This equation (5.5) is Fick's first law [6, 7], for a one-dimensional system. For a 3-dimensional setup, the diffusion coefficient will be [7]

$$D = \frac{1}{6}\rho\left(\Delta x\right)^2 \quad (5.6)$$

5.1.2) Fick's Second Law

Fick's first law was setup for the ideal situation where the diffusing species were all from the same element. However in most practical situations the concentration will change with both distance *and* time. Therefore steady-state conditions are not established. Therefore Fick's first law can no longer be used. Having this in mind it can be seen that it is important to determine how the concentration of atoms, at any point in a material, varies with *time*. Consider a volume of material. Let it have a unit area *A* and a thickness δx, as shown in Figure 2. $J_1 A\delta t$ will be and expression for the number of atoms that diffuse into the volume in a small time interval δt [9]. The number of atoms that leave the volume in the same time interval is $J_2 A\delta t$. Therefore a change in the number of atoms can be expressed as

$$\begin{aligned} \Delta N &= J_1 A\delta t - J_2 A\delta t \\ &= (J_1 - J_2)A\delta t \end{aligned} \quad (5.7)$$

By dividing ΔN by the volume $A\delta x$ the concentration of atoms in the volume can be found:

$$\begin{aligned} \frac{\Delta N}{A\delta x} = \delta C &= \frac{\left(J_1 - J_2\right)A\delta t}{A\delta x} \\ &= (J_1 - J_2)\frac{\delta t}{\delta x} \end{aligned} \quad (5.8)$$

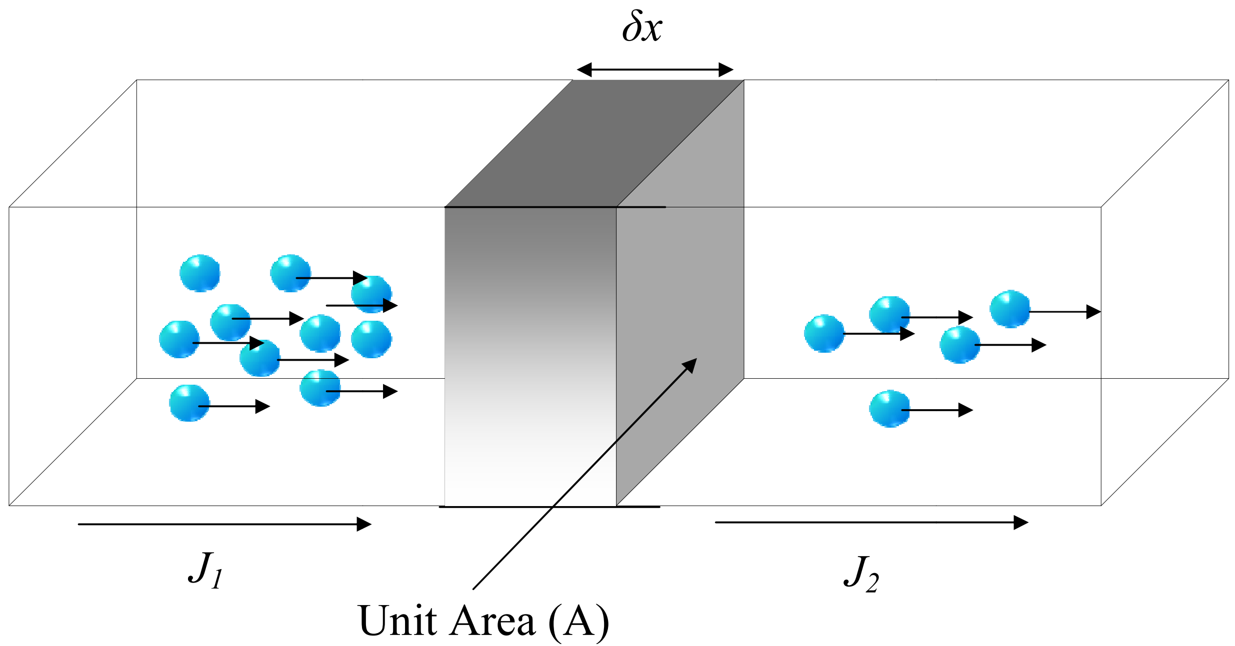

Figure 2: Flux of atoms through a unit area. The number of atoms that leave the infinitesimal volume is lower than the amount that enters this same volume. The difference in flux of atoms is used to derive Fick's second law.

The change in the concentration with time can be found from equation (5.8):

$$\frac{\delta C}{\delta t} = (J_1 - J_2)\frac{1}{\delta x} \tag{5.9}$$

Consider now that the width of the volume δx is very small. Therefore the flux leaving the volume is given by

$$J_2 = J_1 + \frac{\partial J}{\partial x}\partial x \tag{5.10}$$

Inserting equation (5.10) into equation (5.9) leads to the continuity equation [9]

$$\frac{\partial C}{\partial t} = \frac{\partial J}{\partial x} \tag{5.11}$$

By now substituting Fick's first law (equation (5.5)) into equation (5.11) the following expression is obtained:

$$\frac{\partial C}{\partial t} = \frac{\partial}{\partial x}\left(D \frac{\partial C}{\partial x} \right) \tag{5.12}$$

D is assumed to be constant and if variations in the concentration are ignored and. Thus equation (5.12) becomes [9]

$$\frac{\partial C}{\partial t} = D \frac{\partial^2 C}{\partial x^2} \tag{5.13}$$

This is Fick's second law. This shows the physical meaning of the diffusion coefficient; it relates the diffusion distance and time.

5.2) Mechanisms of diffusion

In metals, the most important types of diffusion that can take place are interstitial, vacancy and ring diffusion. The diffusion coefficient is influenced by these types of diffusion as well as the size of the atom and whether the diffusion is defect related.

5.2.1) Ring diffusion

When the atoms are large enough a direct exchange rather than interstitial movement can take place. This is known as ring diffusion. The lattice will then undergo deformation and this deformation energy dictates the type of diffusion process that will take place. This distortion or deformation of the lattice is comparable to an interstitial mechanism for solvent atoms. However because the energy required to execute such a distortion is very high, the probability of this type of mechanism to take place, is not very high [10]. If three or four atoms were to take part in the exchange, the distortion would be considerably less [10, 11]. There is however very little evidence that this diffusion mechanism takes place [11]. Figure 3 shows the graphical representation of ring diffusion.

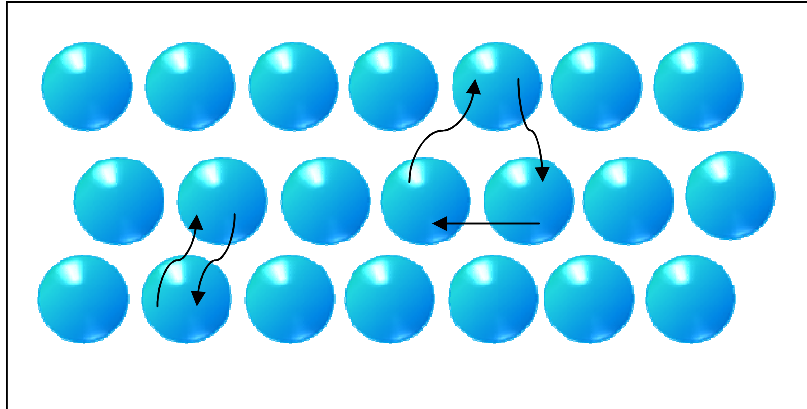

Figure 3: An example of ring diffusion.

5.2.2) Vacancy diffusion

As the name implies, this diffusion type depends on the availability of vacancies in the crystal lattice. Lattice vacancies occur in small equilibrium concentrations [12], but their contribution to the diffusion process is nevertheless important. For diffusion to take place, vacancies are required in the crystal lattice. The amount of vacancies in a lattice can be calculated from [12]

$$N_v = N_0 e^{\left(\frac{-E_v}{RT}\right)} \tag{5.14}$$

Here N_0 represents the amount of lattice positions in the crystal and E_v is the vacancy formation energy. In this type of diffusion the atoms in the crystal move *via* vacancies. This is shown in Figure 4.

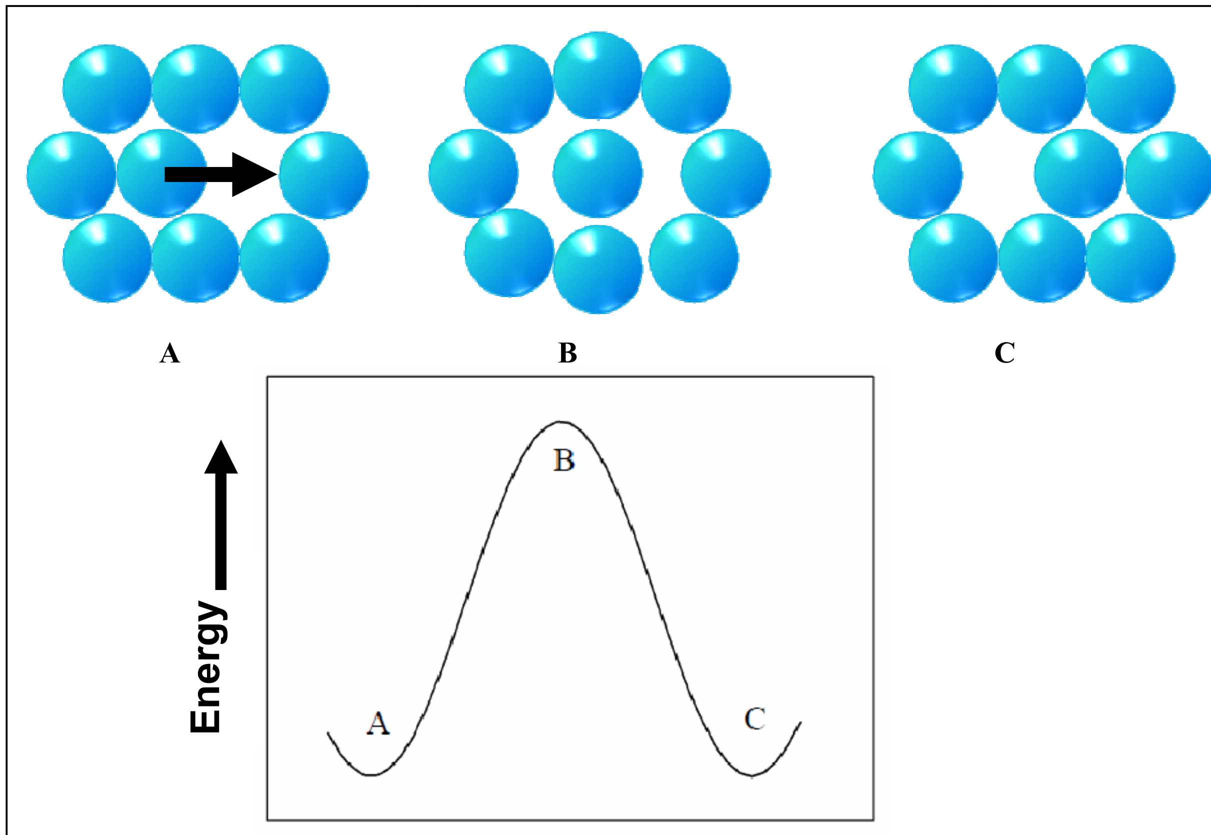

Figure 4: Vacancy diffusion: the potential barrier (when the diffusing atom moves from A to B to C) is also shown.

5.2.3) Interstitial diffusion

When interstitial diffusion takes place, the crystal is deformed (shown in Figure 5) as the diffusing atoms move interstitially. Although similar to vacancy diffusion the difference is that interstitial diffusion is favoured by small atoms. Thus it does not deform the crystal significantly. Therefore the activation energy for interstitial diffusion is less than that for vacancy diffusion because there is no energy required to form vacancies (ΔH_v).

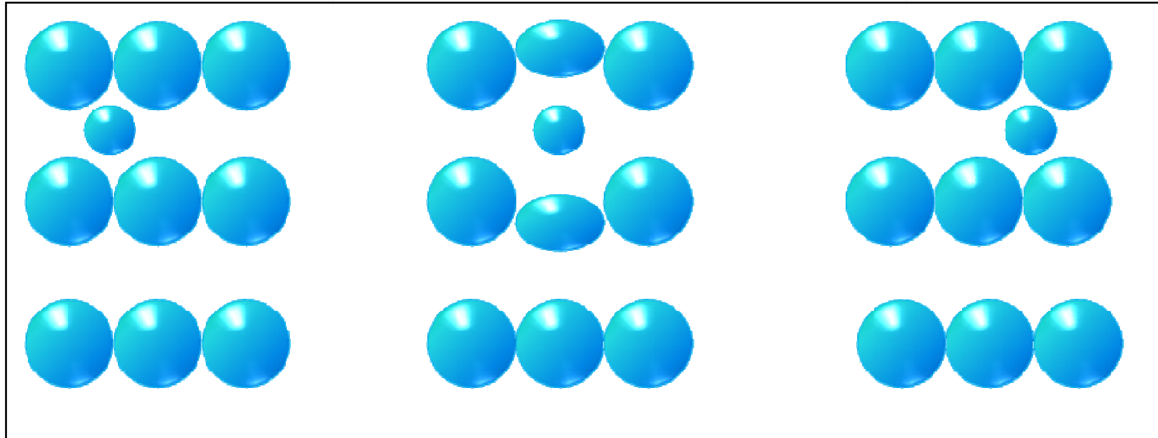

Figure 5: Interstitial diffusion: the energy required to move an interstitial atom is less than the energy required to move an atom through a vacancy mechanism.

5.3) The Monte Carlo Method and Random Numbers

Introduction to Monte Carlo

The Monte Carlo Method is a statistical technique utilizing random quantities to find approximate solutions of mathematical or physical problems [13].

N. Metropolis and S. Ulam published an article in 1949 entitled: "*The Monte Carlo Method*". This is widely accepted as the first paper linking the Monte Carlo name to the use of random quantities [14]. This article is by no means the first implementation of random numbers to solve statistical problems. An experiment recorded in the Bible (1 Kings 7:23 and 2 Chronicles 4:2) reveals that π was deduced by comparing the circumference and width of columns in King Solomon's temple. Random quantities are certainly not a recent invention [15]. The "Monte Carlo" name has its origins in the city of Monte Carlo, Monaco, which became famous for the gambling establishment in the city. Mathematically seen, the roulette wheel is a perfect random number generator as can be constructed by mechanical means [19].

With the advent of modern computers in the first half of the 20th century, the Monte Carlo method evolved into a powerful numerical technique with wide ranging applications in scientific circles [15]

The Monte Carlo method provides approximate solutions to a variety of mathematical problems by performing statistical sampling experiments on a computer. It employs a random number generator to sample a probability density function and predict the possible outcome of a certain event, described by this density function.

5.3.1) Illustration of the Monte Carlo method

Consider the approximation of the value of π as an example to illustrate the use of the Monte Carlo method. In Figure 6 a unit circle is shown lying within a square with sides of length 2. Choose a random point (x, y), with x € [0, 1] and y € [0, 1]. The probability that this random point lies inside the upper right quarter of the unit circle (indicated by the shaded area) is given by the proportion between the area of the unit circle and the upper right square:

$$P(x^2 + y^2 < 1) = \frac{A_{circle}}{A_{square}} = \frac{\pi / 4}{2^2 / 4} = \pi / 4 \tag{5.15}$$

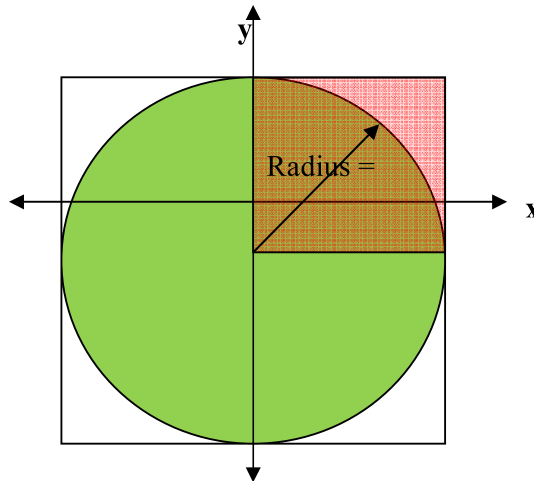

Figure 6: The value for π is approximated using the Monte Carlo method. The square has sides of length 2 with the unit circle inside. The approximation uses the ratio of random points that lie inside the quarter circle to the total number of randomly chosen points.

If n random points are chosen and m of those points lie inside the unit circle, the probability that any random point lies inside the circle is given by:

$$P(x^2 + y^2 < 1) = m / n \tag{5.16}$$

And therefore the value of π can be approximated by the following expression:

$$\pi = \frac{4m}{n} \tag{5.17}$$

It can thus be seen that by increasing the number of random points (increasing the odds, so to speak), n, the approximation of π becomes more accurate. This is shown in Figure 7 where the approximation of π is shown for a different number of random points each time. The value for π was sampled 5 different times for each set of random points. A small number of random points lead to a greater variation in the outcome. However, as the number of random points increases, the values vary less and the accuracy of the approximation increases. When 10^6 random points are used the value for π is approximated as 3.142 which is the mean of 5 samples.

Thus by increasing the number of samples (tests), the accuracy of the simulation also increases. But this also leads to an increase in the computational time. This increase is linear with the number of samples. There exists therefore a trade-off between the accuracy of the approximation and the computational time.

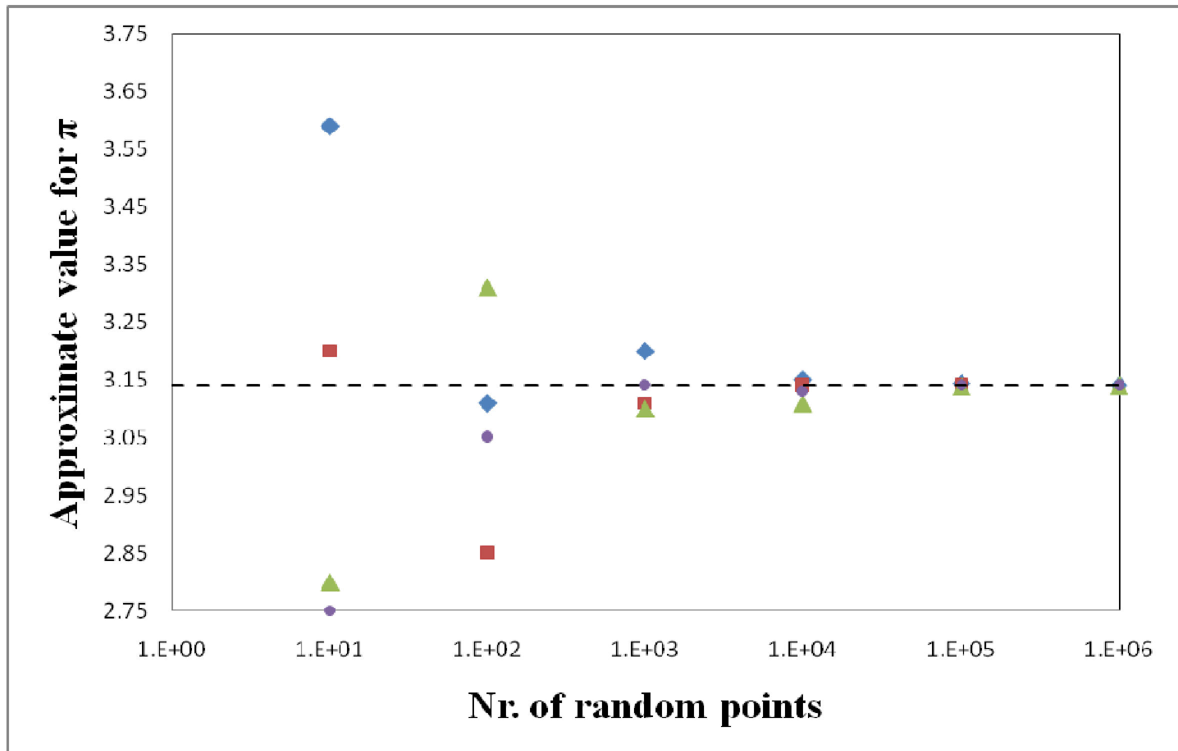

Figure 7: The value of π approximated by using the Monte Carlo method. The accuracy of the approximation increases as the number of random points is increased.

5.3.2) Random Number Generators

A random number generator (RNG) is a computational or physical device (like the roulette wheel) designed to generate a sequence of numbers or symbols that lack any pattern, i.e. appear random [18]. Computer-based systems for random number generation are widely used, but often fall short of this goal, thought they may meet some statistical tests for randomness intended to ensure that they do not have any easily discernible patters. Methods for generating random results have existed since ancient times, including the dice, coin flipping, the shuffling of playing cards and many other techniques.

The many applications of randomness have led to many different methods for generating random data. These methods may vary as to how unpredictable or statistically random they are, and how quickly they can generate random numbers.

Before the advent of computational random number generators, generating large amount of sufficiently random numbers required a lot of work. Results would sometimes be collected and distributed as *random number tables* [15].

5.3.3) "True" random numbers *vs*. pseudorandom numbers

Two methods exist to generate random numbers: the measurement of some physical phenomena that is expected to be random and the use of computational algorithms that produce long sequences of apparently random results. These apparently random results are in fact completely determined by a shorter initial value, known as a *seed* or *key*. The latter type is often called *pseudorandom number generators*.

A mathematical operation is needed to generate numbers by numbers. It is also known that generating true random numbers is a notoriously difficult problem [16]. True random numbers can however be generated by numbers through algorithmic processes without any mathematical operation. To execute the algorithm, only memory and counting ability are required. This implies that the world has about 6.5 billion living random number generators [17].

A single number as well as pseudorandom numbers can be generated by numbers with the help of a mathematical operation through algorithmic process [20]. Although there is no mathematical proof that random numbers cannot be generated by any classical algorithm, it is widely believed that random numbers can only be generated by using random events. Von Neumann first ruled out [20] the possibility of generating random numbers by any mathematical operation. But he did not rule out the generation of random numbers by any algorithmic technique. In fact, it is easy to generate random numbers by using quantum algorithm [21]. In case of quantum algorithm, numbers are not generated by numbers; intrinsic randomness of quantum systems is exploited to generate random numbers.

5.3.4) Mersenne Twister

In 1997 Makoto Matsumoto and Takuji Nishimura [22 - 24] developed the Mersenne twister. The Mersenne twister is a pseudorandom number generator based on a matrix linear recurrence over a finite binary field F_2. It provides for fast generation of very high-quality pseudorandom numbers, having been designed specifically to rectify many of the flaws found in older algorithms.

The commonly used variant of the Mersenne Twister, MT19937, has the following desirable properties:

- It was designed to have a period of 2^{19937} -1 (The creators of the algorithm proved this property). Compare this, for example with the native MATLAB version. It has a period of 2^{1492} [19]. In practice, there is little reason to use larger ones, as most applications do not require 2^{19937} unique combinations (2^{19937} is approximately 4.315425 x 10^{6001}).
- It has a very high order of dimensional equi-distribution. This implies that there is negligible serial correlation between successive values in the output sequence.
- It passes numerous tests for statistical randomness, including the Diehard test [22, 23, 25]. It passes most, but not all, of the even more stringent TestU01 Crush randomness test.

Figure 8 shows a so-called “parking lot” test on two different random number generators. The top graph is an example of a “bad” generator because it exhibits a striped pattern while the bottom graph is an example of a “good” generator. The random number generator created for the Chemical Potential Monte Carlo model using the Mersene Twister algorithm as basis is also used to create the bottom graph.

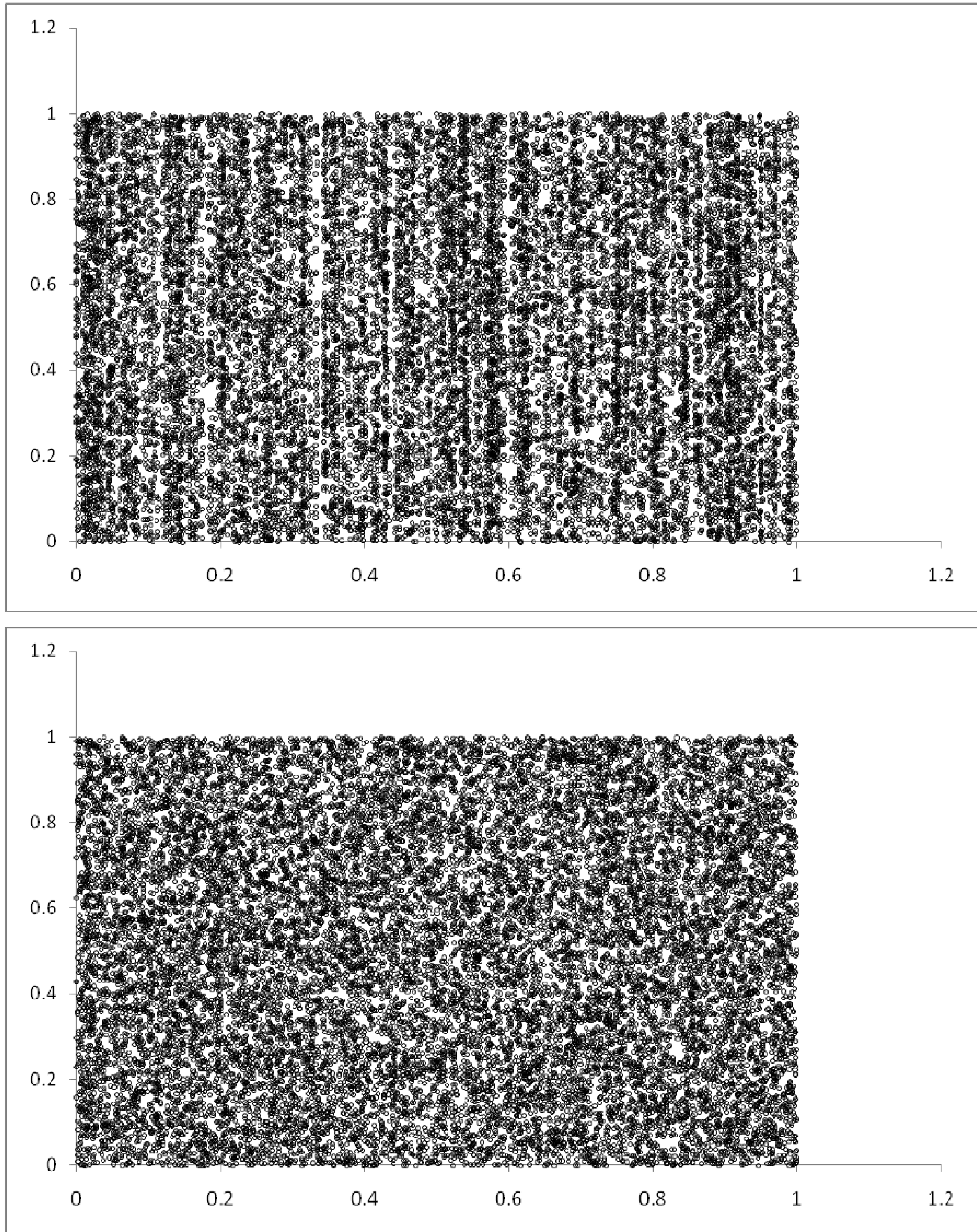

Figure 8: The top graph is an example of a "bad" generator because it exhibits a striped pattern; the bottom graph is an example of a "good" generator.

References

1. ***Diffusion, Atom or Molecule Random Movements***, Available Online March 2009: http://scientificinquiry.suite101.com/article.cfm/diffusion_definition_characteristics_properties.
2. **Askeland D.R.,** *The Science and Engineering of Materials, Third S.I. Edition.* Cheltenham, UK, Stanley Thornes (Publishers) Ltd., (1998).
3. **Leyland A., Lewis D. B., Stevenson P. R. and Matthews A.,** *Surface and Coatings Technology,* Volume 62, Issue 1-3, (1993), pg. 608-617.
4. **Tsoukalas D., Tsamis C. and Norm P.,** *Journal of Applied Physics*, Volume 89, Issue 12, (2001) pg. 7809 – 7813.
5. **Borg R. J., Dienes G. J.,** *An Introduction to Solid State Diffusion.* Boston, Boston Acedemic Press, (1998).
6. **Du Plessis, J.,** *Diffusion and Defect Data, Solid State Phenomena - Part B Volume 11.* Brookfiled USA, Sci-Tech Publications, (1990).
7. **Du Plessis J., Viljoen P. E., Van Wyk G. N.,** *Surface Science*, Volume 244, (1991), pg. 277-284.
8. **B. Tuck.,** *Introduction to diffusion in semiconductors.*: IEE Monograph Series 16, Peter Peregrinus Ltd, (1974).
9. **Porter D. A., Easterling K. E.,** *Phase Transformations in Metals and Alloys,* Chapman & Hall, (1981).
10. **Shewmon P. G.,** *Diffusion in Solids,* McGraw-Hill Book Company, (1963).
11. **Tuck B.,** *Introduction to diffusion in semiconductors,* IEE Monograph Series 16, Peter Peregrinus Ltd, (1974).
12. **Omar M. A.,** *Elementary solid state physics: principles and applications, 1st edn.* Addison-Wesley, (1975).
13. **Binder K., Heermann D. W.,** *Monte Carlo Simulation and Statistical Physics: An Introduction*, Berlin Heidelberg, Springer-Verlag, (2002), pg. 1 – 10.
14. **Sobol I. M.,** *The Monte Carlo Method.* Chicago, The University of Chicago Press, (1974).

15. **Joubert H. D.,** *A Monte Carlo Program for simulating segregation and diffusion utlizing chemical potential calculations, M.Sc.* Bloemfontein, (2004).

16. **Fischer V., Drutarovsky M.,** *Cryptographic Hardware and Embedded Systems – CHES 2002*, Berlin Heidelberg, Springer (2003), pg. 415 – 430.

17. **Maltoni D., Maio D., Jain A. K., Prabhakar S.,** *Handbook of fingerprint recognition 2nd edition*, London, Springer Verlag, (2009) pg.1.

18. **Banks J. (Ed.),** *Simulation: principles, methodology, advances, applications and practice,* Danvers MA, John Wiley & Sons Inc., (1998), pg. 93 – 96.

19. **Greeff A. P.,** *A Monte Carlo simulation of the effect of a ZnO layer on the cathodoluminescence generated in a ZnS phosphor powder, PhD,* Bloemfontein, (2001).

20. **Von Neumann J., (Ed.) Taub A. H.,** *John von Neumann, Collected Works (Various Techniques Used in Connection with Random Digits),* MacMillan, (1963).

21. **Chuang I, Nielsen M. A.,** *Quantum Computation and Quantum Information, 2nd Edition*. Cambridge, Cambridge university press.

22. **Mersenne Twister.** *Wikipedia, the free encyclopedi,* Available online July 2008 at: http://en.wikipedia.org/wiki/Mersenne_Twister.

23. **Matsumoto M., Nishimura T.,** *ACM Transactions on Modelling and Computer Simulation*, Volume 8, Issue 1, (1998), pg. 3 – 30.

24. **Saito M., Matsumoto M.,** Monte *Carlo and Quasi-Monte Carlo Methods 2006*, Berlin Heidelberg, Springer, (2007), pg. 607-622.

25. **Hübscher R.,** *What's in a prerequisite*, Available online June 2008 at: http://citeseerx.ist.psu.edu/viedoc/download?doi-10.1.1.17.8660&rep=rep1& type=pdf.

Chapter 6

Chemical Potential Monte Carlo Model

Introduction

The chemical potential of a system can be viewed as the rate of change of the total Gibbs free energy of the system when holding the temperature and the pressure constant, and an infinitesimal amount of the component *i* is added to the system without changing the number of moles of the other components *j*.

In this chapter the definition of the chemical potential will be explained extensively. Its application in the regular solution model (RSM) will be discussed because it leads to the equilibrium equations of atoms in a solid.

6.1) Chemical Potential

In the physical sciences, a phase is a region of space (in a thermodynamic system), throughout which all physical properties of a material are essentially uniform. A system can exist in an equilibrium state as a single homogeneous phase or as a heterogeneous mixture of several homogeneous phases, each of which has its characteristic temperature (T), energy (E) and entropy (S). The relationship between these quantities (T,E,S) and the atoms comprising the system is statistical in nature and is difficult if not impossible to describe in detail. Nevertheless, it is possible to use the principles of statistical thermodynamics to describe certain phase transformations in solids in terms of the energies of these phases.

The first to analyze transformations on this basis was J. Willard Gibbs [1] who obtained the relation

$$G = E - TS + PV \tag{5.18}$$

where G is called the *Gibbs free energy*, E is the internal energy of the system, S is the entropy, T is the temperature (on the absolute scale), P is the pressure and V is the volume.

In general, a system tends to be in the state that has the *minimum free energy*. This follows from the first and second laws of thermodynamics. At low temperatures atoms attempt to form a structure that has the lowest possible internal energy [1]. The internal energy is inversely proportional to the coordination number of the constituent atoms. This is consistent with the tendency of atoms in ionic and metallic compounds to surround themselves with as large a number of other atoms as possible [1].

A homogeneous open system is a system which consists of a single phase and allows mass transfers across its boundaries. The energy of such a system will depend not only on the variables necessary to study a closed system (such as pressure and temperature), but also on the variables necessary to describe its size and composition. To analyze the system, it is convenient to choose as independent variables its entropy, its volume and the numbers of moles n_i of its components:

$$E = E(S,V,n_i) \tag{5.19}$$

The perfect differential of E may be written:

$$dE = \left(\frac{\partial E}{\partial S}\right)_{V,n_i} dS + \left(\frac{\partial E}{\partial V}\right)_{S,n_i} dV + \sum \left(\frac{\partial E}{\partial n_i}\right)_{S,V,n_j} dn_i \tag{5.20}$$

The first two partial derivatives may be easily identified. Since the composition is kept constant (all n_i), they are identical to the partial derivatives $\left(\partial E / \partial S\right)_V$ and $\left(\partial E / \partial V\right)_S$ of a closed system. Thus

$$dE = T\ dS - P\ dV + \sum \left(\frac{\partial E}{\partial n_i}\right)_{S,V,n_j} dn_i \tag{5.21}$$

The last partial derivative is called the chemical potential of component i and is represented by μ_i. Equation (5.21) then becomes

$$dE = T\ dS - P\ dV + \sum_i \mu_i\ dn_i \tag{5.22}$$

Note now the definition of the following: enthalpy (H),

$$H = E + PV \tag{5.23}$$

the Helmholtz free energy (A),

$$A = E - TS \tag{5.24}$$

and the Gibbs free energy (G), equation (5.18), the following relations are derived from (5.22):

$$dH = T\ dS + V\ dP + \sum_i \mu_i\ dn_i \tag{5.25}$$

$$dA = -S\ dT - P\ dV + \sum_i \mu_i\ dn_i \tag{5.26}$$

$$dG = -S\ dT + V\ dP + \sum_i \mu_i\ dn_i \tag{5.27}$$

The chemical potential μ_i may thus be defined by any of the following partial derivatives:

$$\mu_i = \left(\frac{\partial E}{\partial n_i}\right)_{S,V,n_j} = \left(\frac{\partial H}{\partial n_i}\right)_{S,P,n_j} = \left(\frac{\partial A}{\partial n_i}\right)_{T,V,n_j} = \left(\frac{\partial G}{\partial n_i}\right)_{T,P,n_j} \tag{5.28}$$

Thus: the chemical potential of a system can be viewed as the rate of change of the total Gibbs free energy of the system when holding the temperature and the pressure constant, and an infinitesimal amount of the component *i* is added to the system without changing the number of moles of the other components *j*.

6.2) Regular Solution Model (RSM)

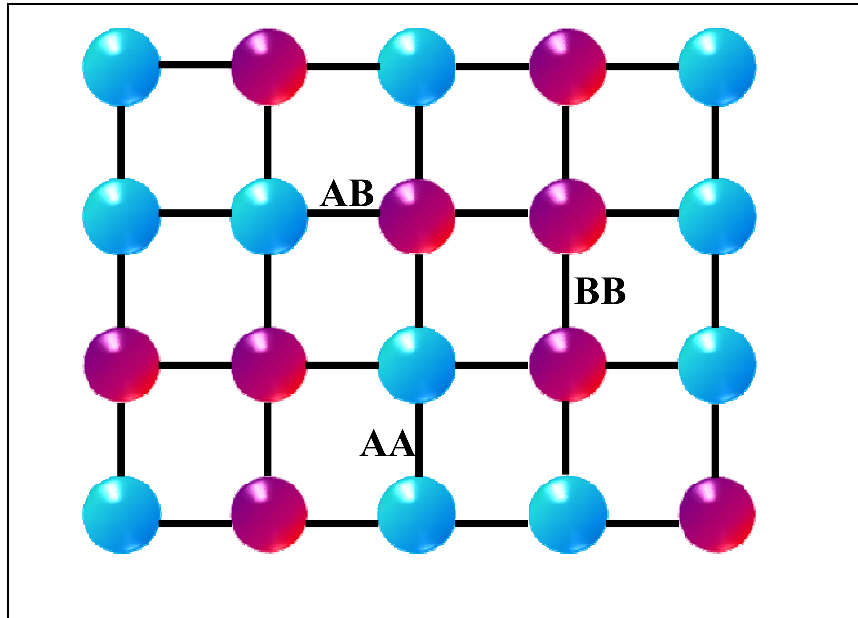

Figure 1: Interatomic bonds in a solid solution.

Hildebrand [2] developed the regular solution model which is a statistical model based on the following three assumptions:

1. Atoms are randomly distributed over positions in a three-dimensional lattice;
2. No vacancies exist;
3. The energy of the system may be expressed as the sum of pair wise interactions between neighbouring atoms.

Consider a binary alloy composed of N_A atoms of component A and N_B components of atom B. Three types of interatomic bonds are present (shown in Figure 1.):

1. $A-A$ bonds of N_{AA} pairs each with an energy γ_{AA};
2. $B-B$ bonds of N_{BB} pairs each with an energy γ_{BB};
3. $A-B$ bonds of N_{AB} pairs each with an energy γ_{AB}.

By now only counting the closest neighbours, the coordination number, Z, is defined as the number of closest neighbours of A or B, because each atom A is included in Z pairs AA of AB. The summation over all A atoms is given by

$$ZN_A = 2N_{AA} + N_{AB} \tag{5.29}$$

The factor 2 for N_{AA} is because each atom A is counted twice for the AA pairs. Similarly for atoms of type B,

$$ZN_B = 2N_{BB} + N_{AB} \tag{5.30}$$

Accordingly the total energy of the lattice is given by

$$E = N_{AA}\gamma_{AA} + N_{BB}\gamma_{BB} + N_{AB}\gamma_{AB} \tag{5.31}$$

By now making N_{AA} and N_{BB} the subjects of equations (5.29) and (5.30) respectively and substituting that into equation(5.31), the following is obtained.

$$E = \frac{1}{2}ZN_A\gamma_{AA} + \frac{1}{2}ZN_B\gamma_{BB} + N_{AB}\left[\gamma_{AB} - \frac{1}{2}\left(\gamma_{AA} + \gamma_{BB}\right)\right] \tag{5.32}$$

Through equation (5.29) it is seen that the expression $\frac{1}{2}ZN_A$ represents the total number of AA pairs in the pure solution of A before any mixing with component B. The expression $\frac{1}{2}ZN_A\gamma_{AA}$ therefore represents the total energy E_A of the N_A atoms of component A before mixing. The same argument holds for element B. The expression for the total energy may thus be written as:

$$E = E_A + E_B + N_{AB}\left[\gamma_{AB} - \frac{1}{2}\left(\gamma_{AA} + \gamma_{BB}\right)\right] \tag{5.33}$$

The parameter ω_{AB} is defined as the difference between the A-B bond energy and the average of the A-A and B-B bond energies:

$$\omega_{AB} = \gamma_{AB} - \frac{1}{2}\left(\gamma_{AA} + \gamma_{BB}\right) \tag{5.34}$$

By substituting (5.34) into (5.33) the following is obtained:

$$E = E_A + E_B + N_{AB}\omega_{AB} \tag{5.35}$$

Atoms are randomly distributed in the lattice and no vacancies exist (assumption 2 of the Regular Solution Model) therefore the probability of finding an atom *A* in position *i* is proportional to the fraction $X_A = N_A / N$, where N is the total number of atoms. Similarly, the probability of finding an atom B at a position *i + 1* is proportional to the fraction $X_B = N_B / N$. Therefore the probability of finding the pair AB at position *i*, *i + 1* is given by $X_A X_B$. If no distinction is made between AB and BA the probability becomes $2X_A X_B$. The total number N_{AB} of AB pairs in the solution can be expressed as

$$N_{AB} = \left(\frac{1}{2}ZN\right)\left(2X_A X_B = Z\frac{N_A N_B}{N}\right) \tag{5.36}$$

To calculate the Gibbs free energy of such a system it is first necessary to find the partition function *C* (3) which is defined as

$$C = \sum_i g_i \exp\left(\frac{-E_i}{kT}\right) \tag{5.37}$$

where g_i is the degeneracy of the distribution of atoms corresponding to energy of E_i. The degeneracy $g = g_i$ is given by

$$g = \frac{N!}{N_A! N_B!} \tag{5.38}$$

For the single value energy E

$$\begin{aligned} C &= g \exp\left(\frac{-E_i}{kT}\right) \\ &= \frac{N!}{N_A! N_B!} \exp\left[\frac{-\left(E_A + E_B + \frac{ZN_A N_B}{N}\omega_{AB}\right)}{kT}\right] \end{aligned} \tag{5.39}$$

For the solid solution the Gibbs free energy G may be expressed as

$$G = H = -kT\ lnQ \tag{5.40}$$

Thus

$$G = -kT\ ln\frac{N!}{N_A!N_B!} + E_A + E_B + \frac{ZN_AN_B}{N}\omega_{AB} \tag{5.41}$$

Which simplifies using the Stirling approximation of $ln\ x! = x\ ln\ x\ -\ x$ to

$$G = E_A + E_B + kT\left(N_A ln\frac{N_A}{N} + N_B ln\frac{N_B}{N} \right) + \frac{ZN_AN_B}{N}\omega_{AB} \tag{5.42}$$

The molar Gibbs free energy of a binary system is therefore given by

$$\begin{aligned} G_{mole} &= \frac{N_0 G}{N} \\ &= X_A G_A + X_B G_B + RT\left(X_A lnX_A + X_B lnX_B \right) + \Omega_{AB} X_A X_B \end{aligned} \tag{5.43}$$

Where

$$G_A = \frac{1}{2}ZN_0\gamma_{AA} = \frac{1}{2}Z\varepsilon_{AA} \tag{5.44}$$

$$G_B = \frac{1}{2}ZN_0\gamma_{BB} = \frac{1}{2}Z\varepsilon_{BB} \tag{5.45}$$

$$\Omega_{AB} = ZN_0\omega_{AB} = Z\left(\varepsilon_{AB} - \frac{1}{2}\left(\varepsilon_{AA} + \varepsilon_{BB} \right) \right) \tag{5.46}$$

N_0 is Avogadro's number, ε_{AB} is the interaction energy per mole between atoms *A* and *B*, ε_{AA} and ε_{BB} are the interaction energies per mole of two *A* atoms and two *B* atoms respectively. It is clear that the interaction parameter Ω_{AB} is defined in energy per mole in contrast with ω_{AB} which is defined in energy per atom pair.

6.3) Interaction coefficient

As can be seen from equation (5.46) the interaction coefficient Ω_{AB} is the difference between the bonding energy of unlike atoms (*A* and *B*) and the arithmetic mean of the bonding energies between like atoms (*A-A* and *B-B*). The interaction coefficient Ω_{AB} may be either positive (attractive) or negative (repulsive) (4). If atoms *A* and *B* have a greater affinity for each other than for other atoms like themselves, then Ω_{AB} is

negative. When like atoms have a greater affinity for each other than for unlike atoms, Ω_{AB} is positive [11, 12].

6.4) Relation between μ and G_{mole} via regular solution model

As was seen in section 6.1 there is a relation between the Gibbs free energy (G_{mole}) of a closed system and the chemical potential, μ. To expand the chemical potential further in terms of the concentration (X) of element *A* and *B*, an appropriate solution model should be used [3].

Consider the equation (5.43) and the definition of the chemical potential for the binary system where

$$X_A + X_B = 1 \tag{5.47}$$

as given by C.H.P. Lupis [3]

$$\mu = \mu_0 + (1 - X)\frac{\partial G_{mole}}{\partial X} \tag{5.48}$$

Where μ_0 is the standard chemical potential for the element under consideration in the bulk [5]. The chemical potential of element A in the regular solution model is then

$$\begin{aligned} \mu_A &= \mu_0^A + (1 - X_A)\frac{\partial G_{mole}}{\partial X_A} \\ &= \mu_0^A + RT \ln X_A + \Omega_{AB}(X_B)^2 \end{aligned} \tag{5.49}$$

And the same for element *B*:

$$\begin{aligned} \mu_B &= \mu_0^B + (1 - X_B)\frac{\partial G_{mole}}{\partial X_B} \\ &= \mu_0^B + RT \ln X_B + \Omega_{AB}(X_A)^2 \end{aligned} \tag{5.50}$$

By using the identities from equation (5.47)

$$X_A = 1 - X_B \text{ and } X_B = 1 - X_A \tag{5.51}$$

μ_A and μ_B may now be written in terms of element *A* and *B* alone respectively:

$$\mu_A = \mu_0^A + RT \ln X_A + \Omega_{AB}(1 - X_A)^2 \quad (5.52)$$

And $$\mu_B = \mu_0^B + RT \ln X_B + \Omega_{AB}(1 - X_B)^2 \quad (5.53)$$

The regular solution model is the simplest one for describing the interactions between atoms; some refinements to the regular solution model were made by Guggenheim [6]. Other models that have a larger degree of sophistication is the central atom model [7] and other statistical models addressing interstitial solutions [8]. All these expressions contain interaction parameters similar to the Ω's. In most cases thermodynamic information in a system is limited and the regular solution model's description should be a satisfactory starting point.

6.5) Basic hypothesis and general equilibrium conditions

As a point of departure the following definition is used for diffusion of solute atoms between two bulk phases in contact: "the redistribution of solute atoms between phase 1 (consisting of atoms *A*) and phase 2 (consisting of atoms *B*) such that the total energy of the crystal is minimized [1]. This basic definition can be extended further to avoid any ambiguities:

1. The crystal is regarded as a closed system consisting of two bulk phases (*A* and *B*) in contact, which are both open systems, allowing for transfer of atoms *A* into *B* and vice versa.
2. The contact region is finite and the bulk is infinite in size.
3. Atoms may be exchanged between the two phases until the energy of the crystal is minimized.

Consider a closed system consisting of *p* phases. The equilibrium condition is given by [1]

$$\left(\delta E\right)S,V,ni = \sum_{\nu=1}^{p} \delta E^{\nu} \geq 0 \quad (5.54)$$

That means the total energy, *E*, of the crystal as a whole is a minimum. This term may be expanded as

$$\delta E^{\nu} = T^{\nu}\delta S - P^{\nu}\delta V^{\nu} + \delta G^{\nu} \tag{5.55}$$

With T^{ν} the temperature, S^{ν} the entropy, P^{ν} the pressure and V^{ν} the volume of phase ν. The Gibbs free energy is denoted by G. If the temperature and pressure is the same for all the phases it may be shown that equation (5.54) reduces to

$$\left(\delta E\right)_{n_i} = \left(\delta G\right)_{n_i} \geq 0 \tag{5.56}$$

It is thus sufficient to consider the behaviour of the Gibbs free energy G (instead of the total energy E) under the condition of constant temperature and pressure. The advantage of this formulation is that the Gibbs free energy may be expanded in terms of the chemical potentials of the various constituents and that the equilibrium conditions may then be expressed as a function of the chemical potential terms.

6.6) Bulk equilibrium conditions

The Gibbs free energy G for the phase *v* consisting of *m* components is:

$$G_{\nu} = \sum_{i=1}^{m} n_i^{\nu} \mu_i^{\nu} \tag{5.57}$$

Where n_i^{ν} is the number of moles of species *i* in the phase ν and μ_i^{ν} is the chemical potential of species *i* in phase ν.

Consider a crystal divided into *N + 1* subsystems. Let each of these subsystems represent one phase (see Figure 6).

The change in the Gibbs free energy can be calculated when atoms of species *i* move from subsystem *j+1* to subsystem *j*. The Gibbs free energy of the subsystems involved, *j+1* and *j*, consisting of an alloy containing *m* different components can be deduced from equation (5.57) to be

$$G = \sum_{i}^{m} n_i^{j} \mu_i^{j} + \sum_{i}^{m} n_i^{j+1} \mu_i^{j+1} \tag{5.58}$$

Where n_i^j is the number of moles of species *i* in the jth subsystem, μ_i^j is the chemical potential of species *i* in the jth subsystem etc. Thus it is clear that the change in the

Gibbs free energy (if there is an exchange between atoms between the two subsystems) is equal to

$$\begin{aligned}\delta G &= \sum_i^m \left(\delta n_i^j \mu_i^j + n_i^j \delta\mu_i^j \right) + \sum_i^m \left(\delta n_i^{j+1} \mu_i^{j+1} + n_i^{j+1} \delta\mu_i^{j+1} \right) \\ &= \left[\sum_i^m \delta n_i^j \mu_i^j + \sum_i^m \delta n_i^{j+1} \mu_i^{j+1} \right] + \left[\sum_i^m n_i^j \delta\mu_i^j + \sum_i^m n_i^{j+1} \delta\mu_i^{j+1} \right]\end{aligned} \tag{5.59}$$

By now applying the well-known Gibbs-Duhem relation $\left(\sum_i n_i \delta\mu_i = 0 \right)$ to the expression in the second square brackets in equation (5.59) the expression reduces to (9)

$$\delta G = \sum_i^m \left(\delta n_i^j \mu_i^j + \delta n_i^{j+1} \mu_i^{j+1} \right) \tag{5.60}$$

If the atomic flux is from subsystem *j+1* to *j*, if follows from the conservation of atoms that

$$\delta n_i^j = -\delta n_i^{j+1} \tag{5.61}$$

Therefore, equation (5.60) becomes

$$\begin{aligned}\delta G &= \sum_i^m \delta n_i^j \left(\mu_i^j - \mu_i^{j+1} \right) \\ 0 &\le \sum_i^m \delta n_i^j \left(\mu_i^j - \mu_i^{j+1} \right)\end{aligned} \tag{5.62}$$

This implies that

$$\left(\mu_i^j - \mu_i^{j+1} \right) = 0 \tag{5.63}$$

or

$$\mu_i^j = \mu_i^{j+1} \quad \text{for } i = 1, 2, ..., m \tag{5.64}$$

This last relation (equations (5.63) and(5.64)) is the equilibrium condition for two bulk phases in contact expressed in terms of the chemical potential.

6.7) The CPMC model and the change in "microscopic" μ

In this section the Monte Carlo model that uses chemical potential calculations to simulate the diffusion of two metals into each other and the resulting microstructure is described. The calculation routine is initiated with the selection of a random atom inside a crystal matrix. The chemical potentials, derived in the previous sections, are calculated and then determine the direction of motion available to the selected atom. With the use of the equations for chemical potential, (5.52) and (5.53), as well as the conditions for equilibrium, (5.64), the *chemical potential Monte Carlo model* developed in this study will now be described.

6.7.1) Crystal Setup

Consider a crystal consisting of two thin films in contact, Figure 2. Thin film A consists out of a metal with element A and thin film B consists out of a metal with element B. The crystal packing is depicted in Figure 3. *For this model a FCC crystal arrangement was used, because both Pt and Al have a FCC crystal structure. This is also one of the limitations of the current model.* This setup thus makes the software specifically applicable to the Pt/Al system as well as any other system that has an FCC crystal structure. (This is so because the amount of nearest neighbours and next nearest neighbours would be the same as long as the system has a FCC crystal structure). In this arrangement each atom (for example atom A in Figure 3) is surrounded by 6 nearest neighbour atoms (the atoms labelled 1 to 6 in red) and 12 next nearest neighbour atoms (the atoms labelled form 7 to 18 in black). A "microscopic" system (area) within the extended crystal matrix can be identified as this arrangement of 19 atoms, Figure 4. The crystal can be divided into *N* "microscopic" subsystems as depicted in Figure 4 and Figure 5 (it is to be understood that with "microscopic" it is not meant 10^{-6} meter, but rather just "very small", for lack of a better descriptive word). The "size" of these subsystems can be chosen to be very large (to include the entire crystal as nearest neighbour- and next nearest neighbour- atoms for atom A) or extremely small (to include only the 6 nearest neighbour atoms of atom A, as it is depicted in Figure 4). The larger this subsystem (area) is chosen, the more accurate the

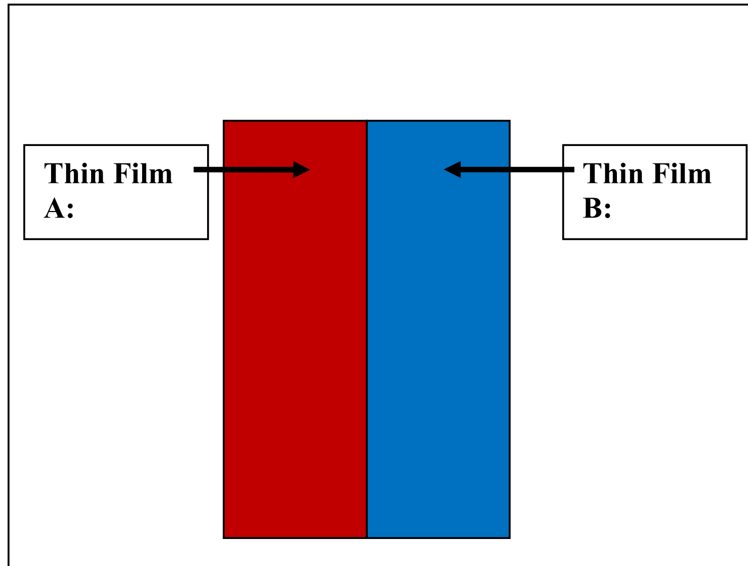

Figure 2: Two thin films in contact consisting out of elements A and B.

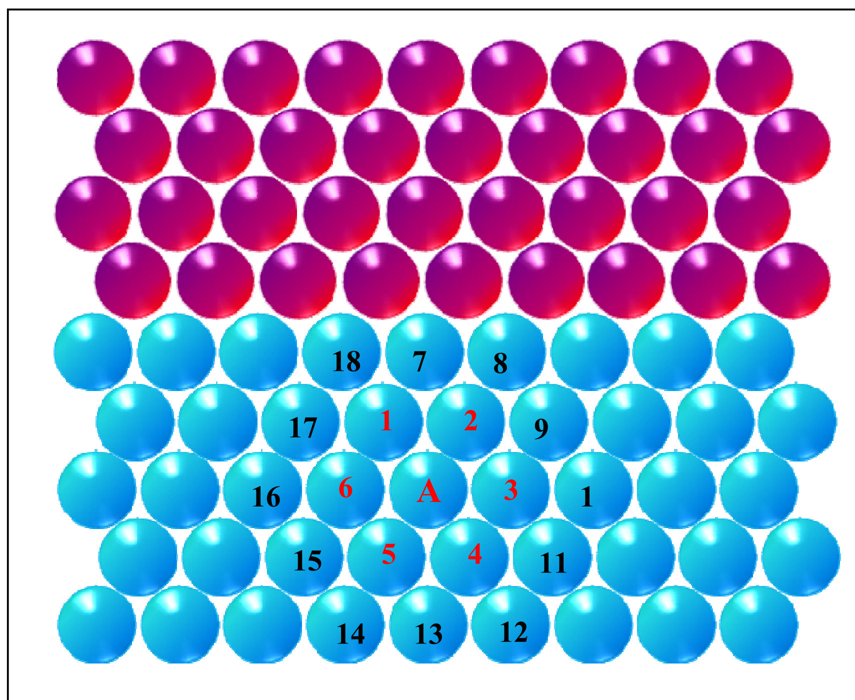

Figure 3: FCC crystal packing for the chemical potential Monte Carlo model.

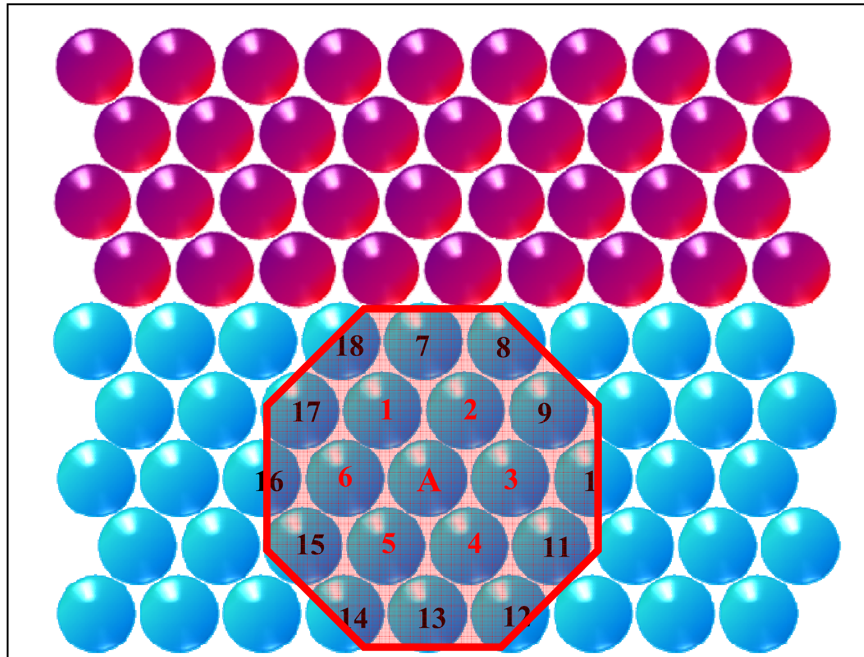

Figure 4: "Microscopic" sub-system identified within the crystal matrix consisting of 19 atoms.

resulting simulation will be. However, this is done at the expense of calculation and simulation time. Therefore a trade off exist between accuracy and simulation time. For this model, the size of the "microscopic" subsystem was chosen to consist out of the 6 nearest neighbour atoms and the 12 next nearest neighbour atoms as depicted in Figure 4.

6.7.2) Atomic motion through diffusion

Through a random number generator a random atom *A* (Figure 5 and 6) in the crystal is chosen and put up for evaluation, i.e. to evaluate whether a "jump" to position 1, 2, 3, 4, 5 or 6 is permitted or not, as depicted in Figure 6. Thus, an atom is only allowed to trade places with one of its 6 nearest neighbour atom. Equations (1.35) and (1.36) are used to determine the direction of atomic motion. At first the chemical potential of the area with the atom *A* at the centre is calculated. After this, the random atom *A* is allowed to trade places with its 6 nearest neighbours respectively. With each trade, six new "microscopic" areas are defined. Each of these areas has random atom *A* at the centre. For example, in Figure 5 random atom *A* trades places with its neighbour atom *1*. The original area for which the "microscopic" chemical potential was calculated is marked in red and the new area is marked in blue. The chemical potential for each of these six new areas are also calculated using equations (1.35) and (1.36).

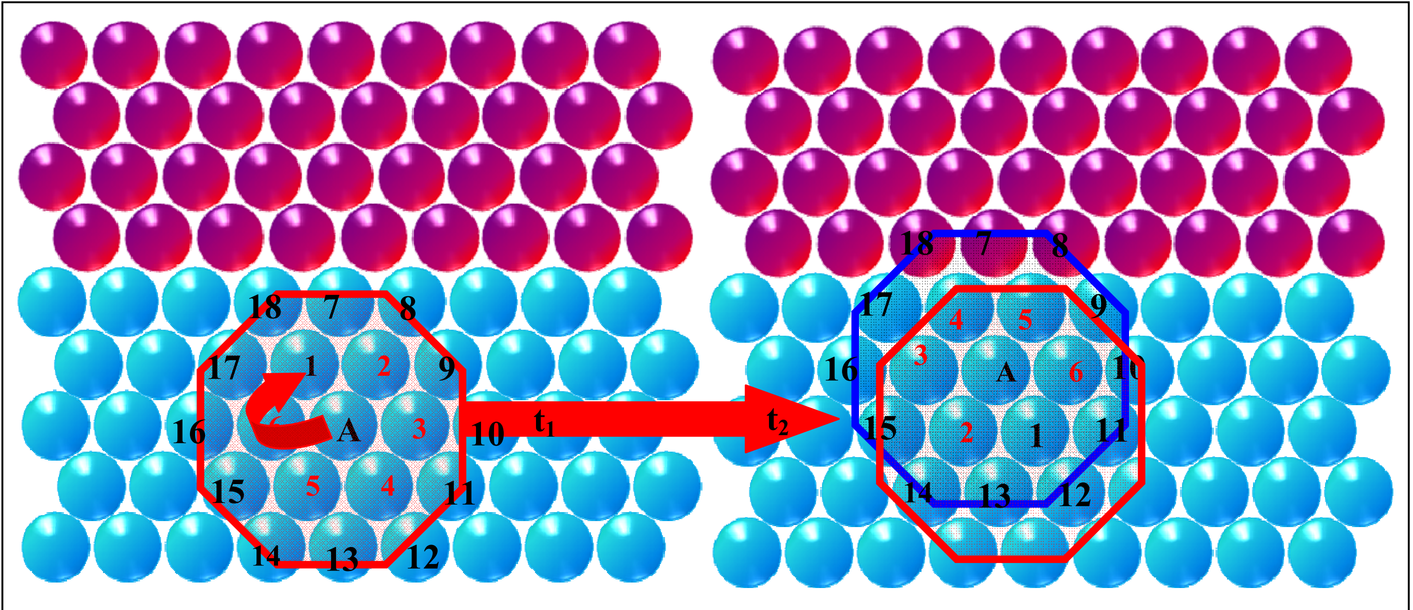

Figure 5: The left crystal shows the "microscopic" area before atom A and atom 1 are allowed to trade places; at time = t_1. The right crystal shows the new "microscopic" area (in blue) after the atom exchange at time = t_2.

Each of the six possible moves possesses a certain probability that an exchange in that particular direction can take place. The probability is calculated from the energy change for a particular atomic exchange. Since the change in the chemical potential represents the change in energy, the probability of motion (p_i) is given by [10, 13, 14]:

$$p_i = e^{\frac{\Delta\mu_i(t_1 \to t_2)}{RT}} \tag{5.65}$$

Where t_2 is the time of the chemical potential ***after*** the exchange and t_1 is the time of the chemical potential ***before*** the exchange, R is the Gas constant and T is the temperature.

Since only nearest neighbours are considered, i (in equation (1.48)) can assume any value in the interval $1 \leq i \leq 6$ with i an integer.

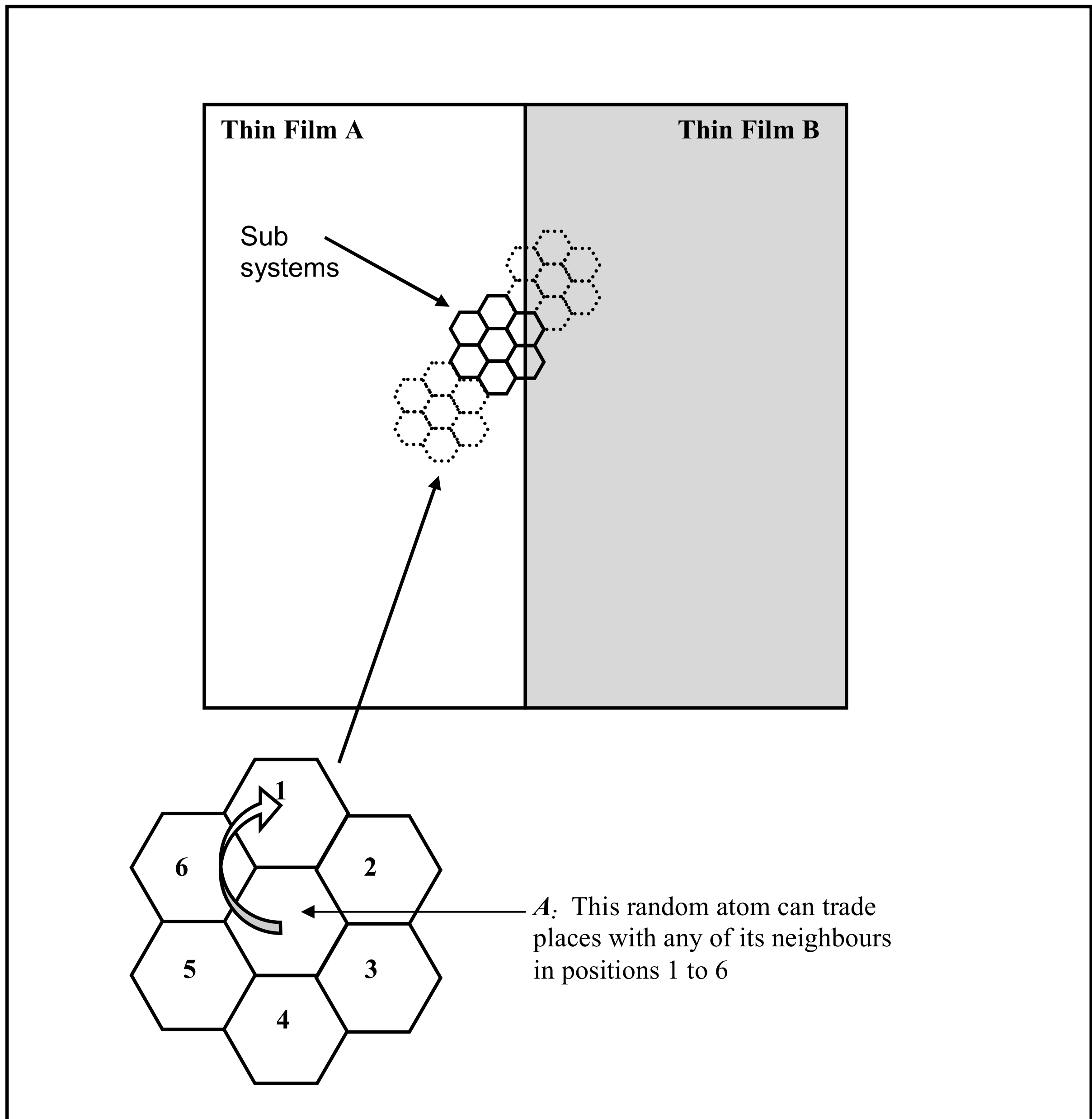

Figure 6: The double layer thin film system is divided into $j+1$ sub systems. The minimizing of the chemical potential of each sub system is used to make a decision on which Monte Carlo jump (1-6) is more favourable.

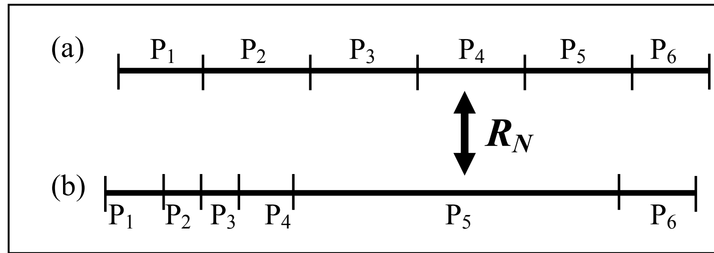

Figure 7: Representations of two probability scales used to determine the direction of motion.

These probabilities can be combined to form a normalized probability scale between 0 and 1 that dynamically changes as atoms are chosen at random in the crystal. Two possible permutations of the probability scale are shown in Figure 7.

To determine the direction of atomic motion, a random number (R_N) in the interval $0 \leq R_N \leq 1$ is chosen. An arbitrary random number is indicated in Figure 7. In Figure 7 (a), the random number falls in the interval assigned to an exchange with atom *4*. However in Fig. 7 (b), an exchange with atom *5* results in a much larger decrease in energy, and thus the probability for this exchange is very high. In this case the randomly selected atom R_A will exchange with atom *5*. In practice this means the following: a jump has the highest possibility of occurring if the microscopic chemical potential of *both* the sub systems involved will be lowered (the one from which the atom comes, and the one to which the atom is jumping). A jump has a much lower probability of occurring if either one of the two sub systems' chemical potentials are raised. If the chemical potentials of the two sub systems involved are neither raised nor lowered then the probability of atom R_N remaining in its current position is the highest. Thus, an exchange between particles will continue to take place as long as the equilibrium condition, equation (1.47) is not satisfied.

At any point during the simulation the diffusion process can thus be stopped (before equation (1.47) is satisfied) and a "snapshot" in time of the particular microstructure can be obtained.

6.8) Software Flow Chart

The following flow chart describes the construct of the software that was designed in the programming language Visual Basic 6.0.

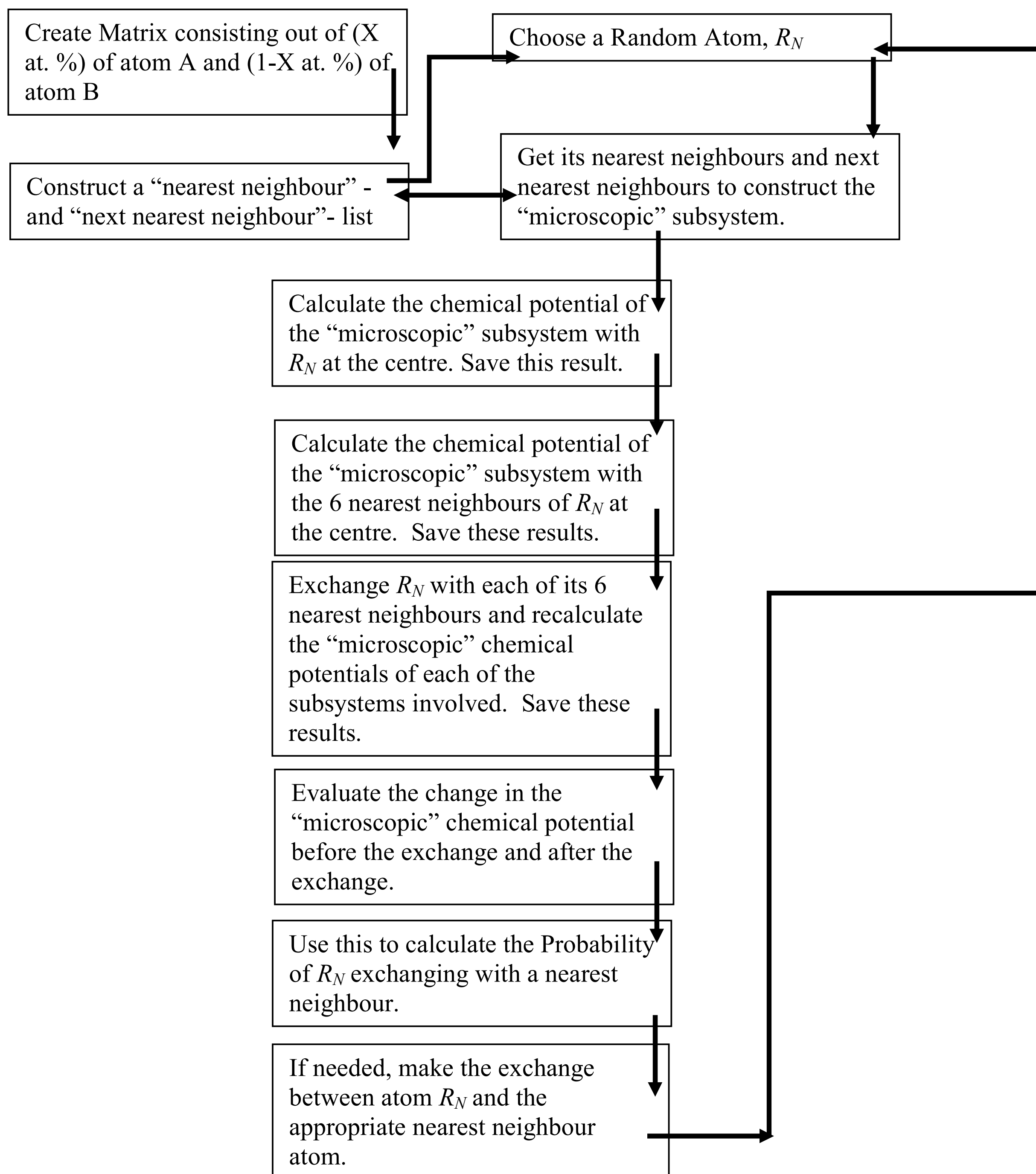

References

1. **Du Plessis J.,** *Surface Segregation.* Brookfield, Sci Tech Publications Ltd, (1990).
2. **Scott J. H. and Hildebrand R.L.,** *The Solubility of Nonelectrolytes, 3rd edn.* New York : Van Nostrand Reinhold, (1950).
3. **Lupis C. H. P.,** *Chemical Thermodynamics of Materials.* Amsterdam, North-Holland, (1983).
4. **Du Plessis J., Van Wyk G. N.,** *Chapter 2: Equilibrium Segregation.*
5. **Joubert H. D., Swart H. C., Terblans J. J.,** *Surface and Interface Analysis.* Volume 37, (2005), pg. 1027-1030.
6. **Guggenheim E. A.,** *Mixtures,* Oxford, Oxford University Press, (1952).
7. **Eyring H.,** *Journal of Chemistry and Physics*, Volume 4, (1936), pg. 283.
8. **Kirkaldy G. R., and Purdy J. S.,** *Canadian Journal of Physics*, Volume 40, (1962), pg. 202.
9. **Du Plessis J. and Van Wyk G. N.,** *Journal of Phyisics and Chemistry of Solids*, Volume 49, (1988), pg. 1441.
10. **Omar M. A.,** *Elementary solid state physics: principles and applications, 1st edn.*, Addison-Wesley, (1975**).**
11. **Du Plessis J., van Wyk G. N.,** *Journal of the Physical Chemicstry of Solids,* Vol. 50, Issue 3, (1989), pg.237.
12. **Du Plessis J.,** *Solid State Phenomena – Part B, Volume 11,* Brookfield, Sci-Tech Publications, (1990).
13. **Du Plessis J., van Wyk G. N.,** *Journal of the Physical Chemistry of Solids*, Vol. 49, Issue 12, (1988), pg. 1441.
14. **Du Plessis J.,** *Applied Surface Science,* Vols. 70 – 71, (1993), pg. 303.

Chapter 7

PLD Results

Introduction

Pulsed laser deposition (PLD) is a highly flexible technique for the fabrication of thin films, and may in principle be applied to all solid materials including metals, refractory metals and rare earths. The characteristic behaviour of pulsed laser deposition (at 248 nm) of metallic alloys includes the following. Firstly high deposition rates of up to 3 nm/s above an ablation threshold of about 5 J/cm^2 is observed during PLD. Another characteristic is the nearly congruent transfer between target and film (hence a stoichiometric transfer of ablated material). Droplets on the film surface are also a very important characteristic of PLD.

The stoichiometric transfer between target and substrate during PLD are of particular interest in this study where the platinum-based superalloy, Pt_{84}:Al_{11}:Cr_3:Ru_2, is deposited as a thin film, preserving its specifically engineered properties of greater specific strength (than it's counter part Ni-based alloys) and improved corrosion and oxidation resistance. Thus it is important that there is no change in the microstructure between the target and the deposited thin film during PLD. However, one of the major problems of PLD is the roughening of the target and hence the formation of macroscopic droplets (up to some μm in size) on the growing films. The droplet formation is however dependant on the base pressure of the background gas. In this chapter it will be shown how the density and size of the droplets can be controlled during PLD. The stoichiometric transfer of a Pt-based superalloy target to a substrate will also be discussed.

7.1) Preparation of Pt_{84}:Al_{11}:Cr_3:Ru_2 samples

		Pt	Al	Cr	Ru
	at.%	84	11	3	2
Ideal	**wt%**	1.9249 g	0.0341 g	0.0179 g	0.0232 g
Target 1	**wt%**	1.9258 g	0.0351 g	0.0176 g	0.0237 g
Target 2	**wt%**	1.9255 g	0.0349 g	0.0177 g	0.0240 g

Table 1: Composition of the superalloy sample.

Platinum, aluminium, chromium and ruthenium, all in powder form, was weighed in order to form the above mentioned ratio of elements. Table 1 gives an indication of these ratios. The ideal ratios, i.e. that which is required to form the exact composition of Pt_{84}:Al_{11}:Cr_3:Ru_2, and that which could actually be achieved, is shown in this table.

These elemental powders were then melted in a button arc furnace to form the superalloy. The button arc furnace was evacuated to a pressure of 15 millibar, in order to reduce the oxygen and atmospheric gas content of the chamber. The chamber was then backfilled with an inert Argon gas, and the carbon tip was warmed via a 20 A current. The powders were melted to form two lumps of $5 \times 5 \times 5$ mm^3. It was expected that these lumps would have a homogenous composition. *Target 1* was annealed at 1350 ºC for 96 hours [1]. This was done to give the alloy the cubic $L1_2$ – Pt_3Al intermetallic phase inside the Pt-matrix. Thin films were then grown via PLD using this second target as source to investigate the stoichiometric transfer of target material to the thin film substrate. *Target 2* was kept unannealed and used to grow the thin films via PLD to investigate the effect of the ambient gas and the ambient gas pressure on the droplet formation.

7.2) Stoichiometric transfer of target material

For this experiment the PLD-system at the Council for Scientific and Industrial Research (CSIR)'s National Laser Centre (NLC) was used. This system is equipped with a Krypton-fluoride (KrF) laser which has a wavelength of 248 nm. Unfortunately, the existing setup does not allow for a great range of different fluences. As a matter of fact, the only controlled way in which the fluence can be changed, is by adjusting the focusing lens, and thus by altering the laser spot size. However, in the case of a very small target, as in the present case, this leads to missing the target all together, or hitting the target holder, and thus evaporating some of this material.

Twenty nine thin film samples were prepared. Table 2 shows the various parameters and observations made, during this process. For every thin film prepared the vacuum chamber was pumped to a pressure of 2.1×10^{-5} Torr and then backfilled with various atmospheres (as noted in the table) to maintain a certain pressure inside the chamber. The laser was then pulsed at a frequency of between 8 and 10 Hz for various time durations, as noted in the table, and the superalloy was vaporized and condensed onto the substrate. A Si (1 0 0) substrate at room temperature was used.

Sample	Time (min)	Nr. Of Pulses	Frequency (Hz)	Pressure (Torr)	Gas
1Test	4.16	2500	10	8.5×10^{-6}	Vacuum
1	13.33	8000	10	9×10^{-6}	Vacuum
2	8.33	5000	10	9×10^{-6}	Vacuum
3	8.33	5000	10	9×10^{-6}	Vacuum
4	8.33	5000	10	9×10^{-6}	Vacuum
5	8.33	5000	10	9×10^{-6}	Vacuum
6	8.33	5000	10	3.0×10^{-5}	Vacuum
13	11.6	7000	10	1×10^{-3}	Argon
14	11.6	7000	10	$1.7x10^{-4}$	Argon
15	11.6	7000	10	1.8×10^{-2}	Argon
16	11.6	7000	10	1.1×10^{-1}	Argon
17	11.6	7000	10	1.3	Argon
18	11.6	7000	10	4.5	Argon
28	20	12000	10	3.5×10^{-6}	Argon
14.1	20	12000	10	1.4×10^{-4}	Argon
13.1	20	12000	10	3.7×10^{-3}	Argon
15.1	20	12000	10	2.9×10^{-2}	Argon
16.1	20	12000	10	3.1×10^{-1}	Argon
17.1	20	12000	10	1.00	Argon
19	20	12000	10	3.3×10^{-4}	Oxygen
20	20	12000	10	2.6×10^{-3}	Oxygen
21	20	12000	10	2.6×10^{-2}	Oxygen
22	20	12000	10	1.2×10^{-1}	Oxygen
23	20	12000	10	1.2	Oxygen
24	20	12000	10	3.6×10^{-4}	Nitrogen
25	20	12000	10	2.9×10^{-3}	Nitrogen
26	20	12000	10	1.4×10^{-2}	Nitrogen
27	20	12000	10	4.0×10^{-1}	Nitrogen
29	20	12000	10	1.1	Nitrogen

Table 2: PLD parameters for 29 samples.

7.3) Sample Characterisation

Samples were imaged by means of Scanning Electron Microscopy (SEM) (Shimadzu SSX-550) with both a Secondary Electron Detector (SED) and a Backscattered Electron Detector (BSED). X-ray photoelectron spectroscopic depth profiling (XPS) was also done, to determine whether or not there was a stoichiometric transfer of target material to the Si (1 0 0) substrate. Energy Dispersive X-ray Spectroscopy (EDS) was also done.

One of the goals of this study was to investigate whether or not a specifically engineered and prepared alloy target (in this case with the composition Pt_{84}:Al_{11}:Cr_3:Ru_2) could be transported onto a substrate to grow a thin film of the exact same stoichiometry. In order to achieve this goal the following questions are addressed: do the droplets have the same stoichiometry as the rest of the thin film? And does the thin film have the same stiochiometry as the target material? To answer these question the samples prepared as listed in table 2 were characterised via secondary electron microscopy (SEM) and energy dispersive spectroscopy (EDS) as well as X-ray photoelectron spectroscopic depth profiling (XPS-depth profiling). The goal was to compare the secondary electron images of the target and the PLD-grown thin films. After this was done to identify differences (if there are any) and then to identify the stoichiometry of the thin film through EDS and XPS.

7.3.1) Thin films from the annealed Pt_{84}:Al_{11}:Cr_3:Ru_2 target

Droplets were the main feature visible on the prepared films. These droplets varied in size, shape and number-density. This section reports on the transfer of material from the specifically engineered *Target 1* to the Si (1 0 0)-substrate. *Target 1* (annealed at 1350 ºC) showed very clear phases of Pt_3Al in the Pt-matrix (dark areas in Figure 1). It is this microstructure that is sought to be preserved onto the thin films.

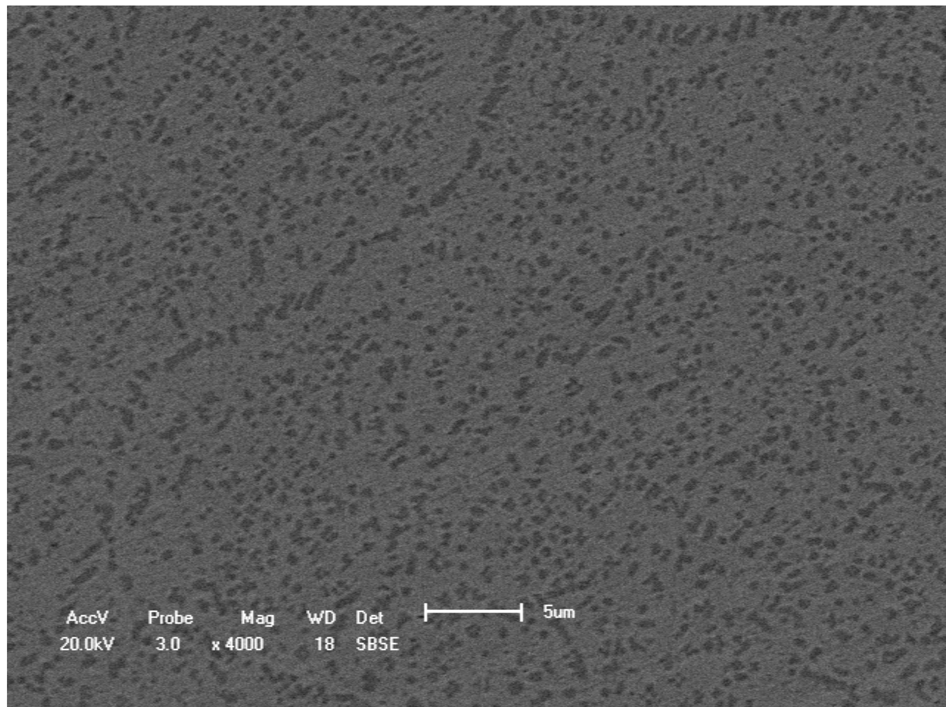

Figure 1: SEM micrograph in SBSE mode of Pt_3Al-phases (the darker areas) in the Pt-matrix (the lighter area) on the target. It is this specifically engineered property that is sought to be preserved onto the thin films. (AccV. 20.0 kV, Probe size 3.0, Magnification ×4000, WD 18).

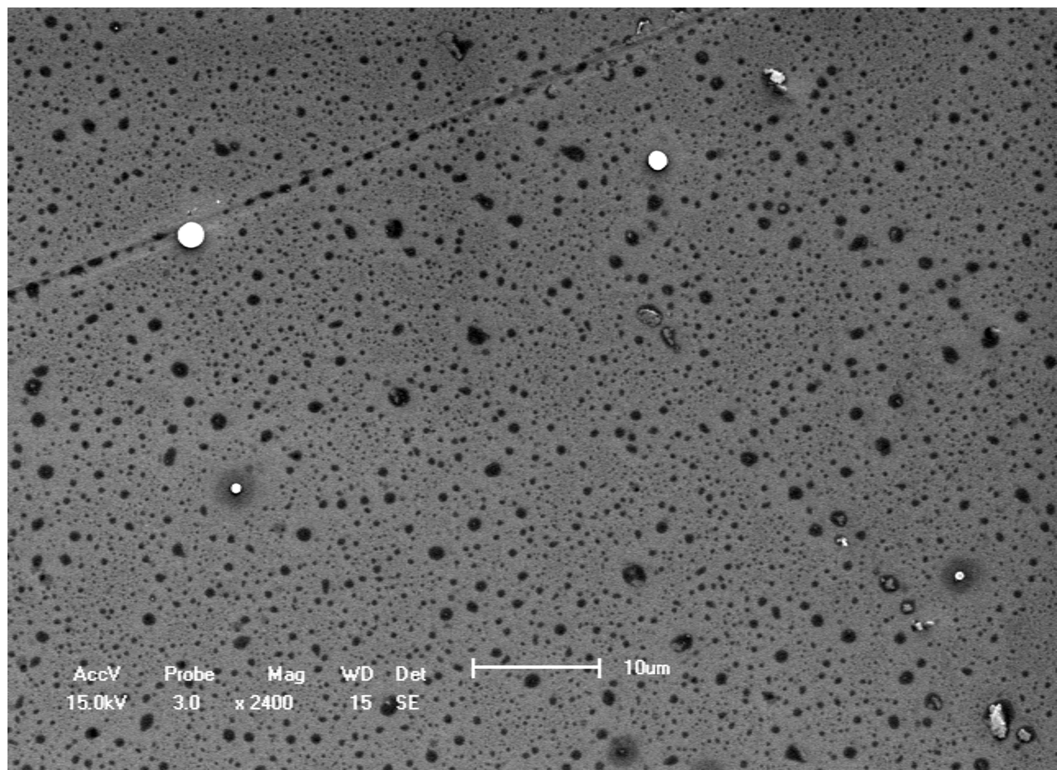

Figure 2: SEM micrograph in SED mode of sample 14.1. (AccV. 15.0 kV, Probe size 3.0, Magnification ×2400, WD 15).

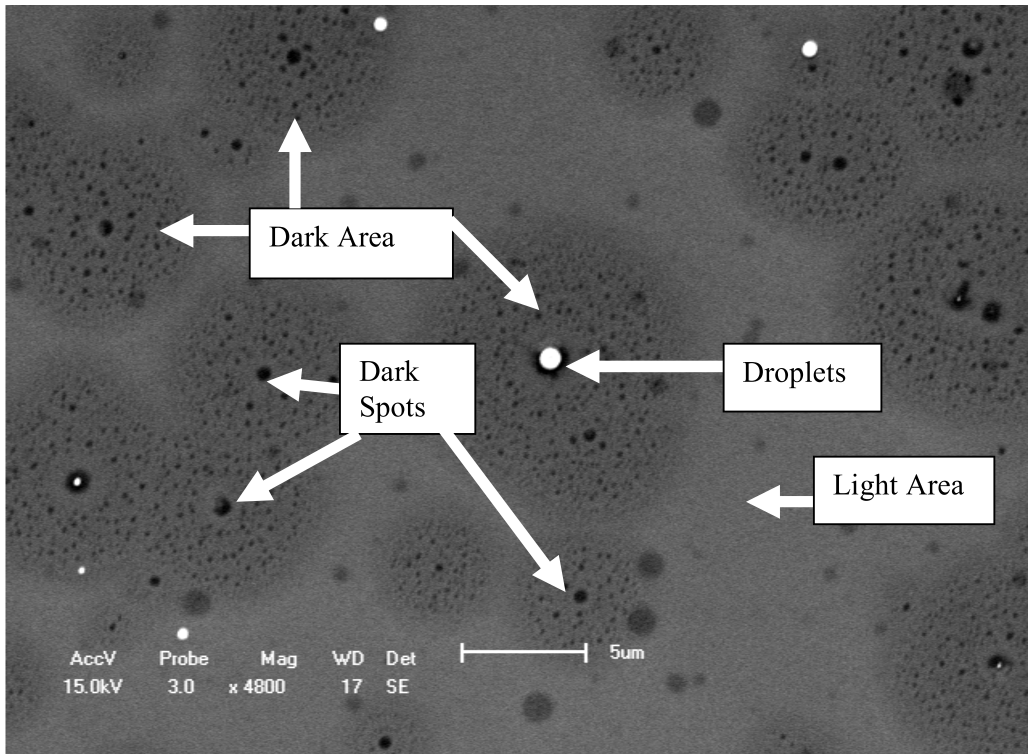

Figure 3: SEM micrograph in SED mode of four different "areas" identified for characterisation. (AccV. 15.0 kV, Probe size 3.0, Magnification ×4800, WD 17).

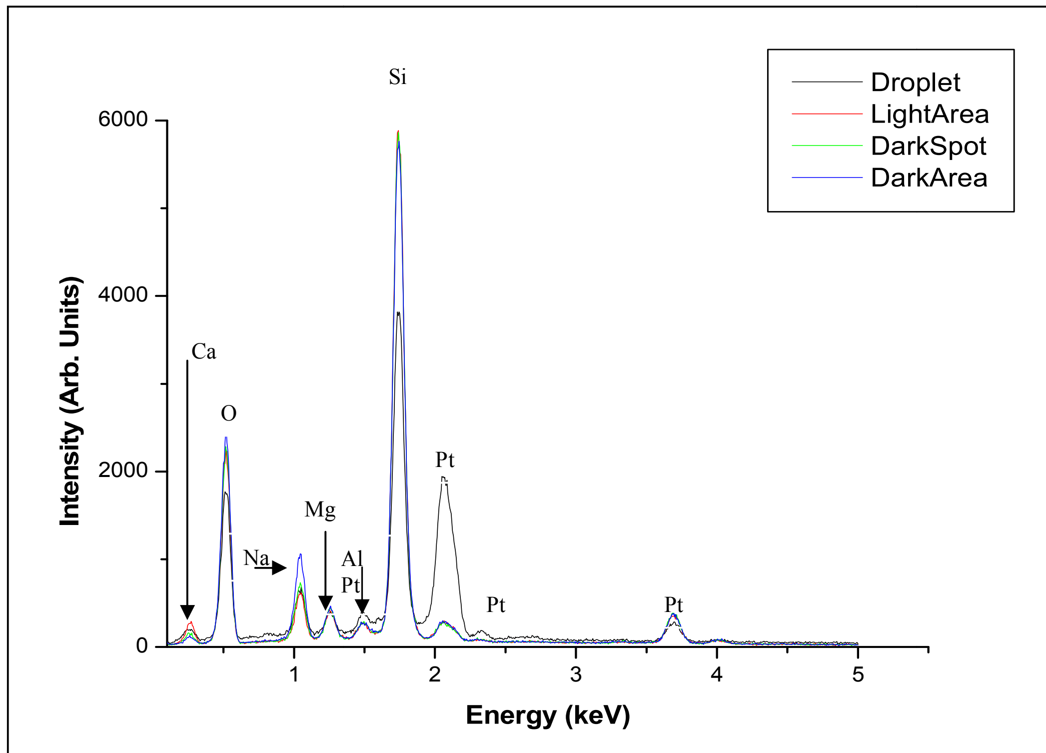

Figure 4: EDS spectra (combined) for different areas.

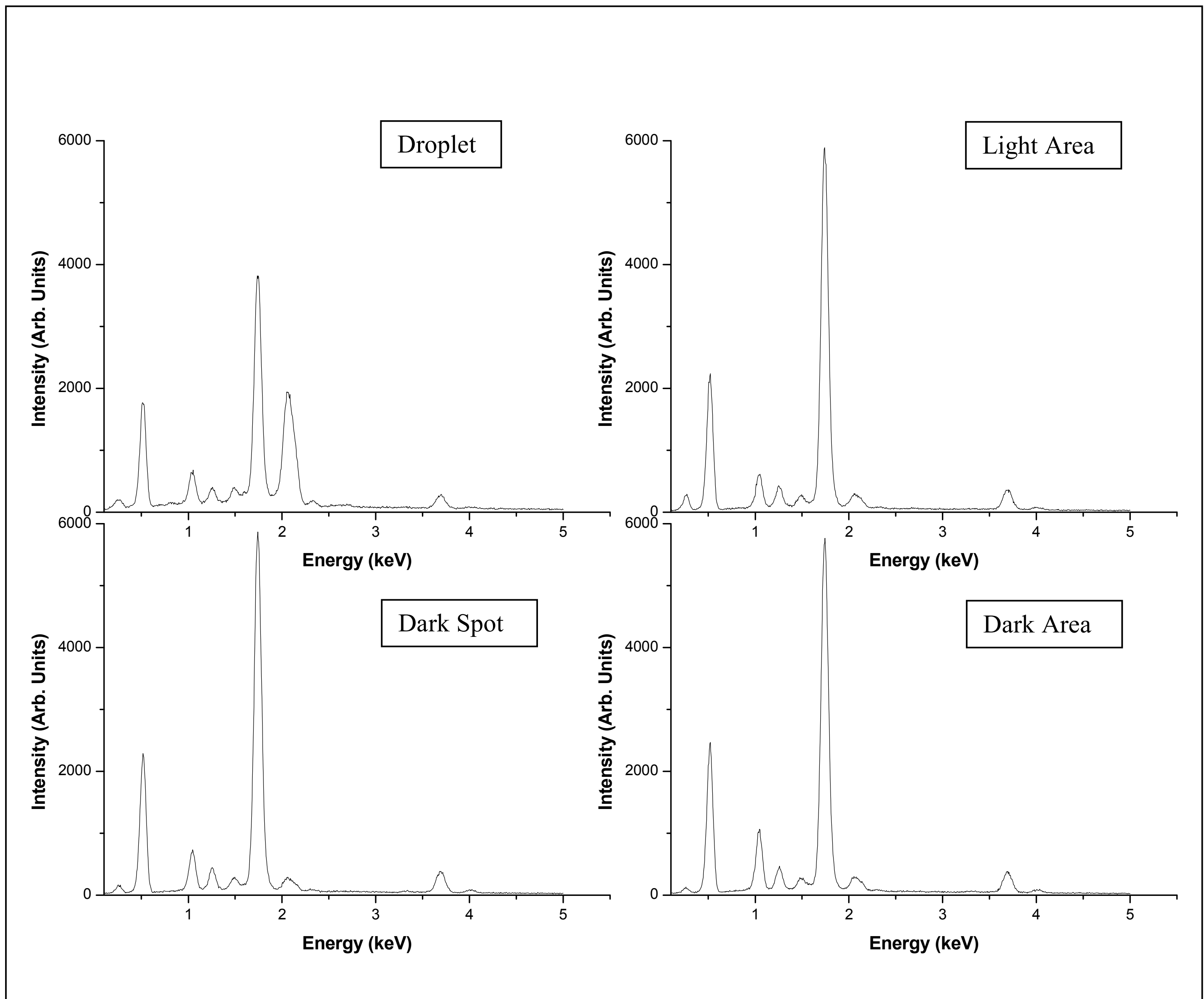

Figure 5: EDS spectra for different areas.

Figure 2 and 3 shows SEM micrographs for two of the thin films grown with the above mentioned target. (The other thin film micrographs look similar). It was expected that the thin film surface should look the same as the target surface (Figure 1). However, as can clearly be seen in Figure 2, this is not the case. It appears as if the transfer of material from the target to the substrate under the specific conditions listed in Table 2 was not stoichiometeric because the darker areas in Figure 1, corresponding to the Pt_3Al phase in the Pt-matrix, are not observed in the micrograph of Figure 2. Four different areas (as labelled in Figure 3) were identified on the thin film surfaces for EDS analysis: dark area, light area, dark spot and droplet.

EDS was employed to see if a difference in the composition of these areas could be found. Figures 4 and 5 show these results:

From Figure 4 and 5 it is clear that the silicon peak intensity is very large at all the different areas. This peak originates from the substrate itself. It is also clear that (except for the droplets) the different areas do not appear to have any difference in stoichiometric composition for the Pt and Al peaks. It was expected that the droplets would have more material in it than the thin film, since it is physically thicker and in the order of micrometers, compared to the thin film thickness of a few nanometers, Figure 6. Therefore there is a difference in the Si-and Pt-peaks intensities for the droplet and the other thin film areas. But it is concluded that these areas do not have different stoichiometric compositions.

To investigate whether there was a congruent transfer between target material and the thin film X-ray photoelectron spectroscopic depth-profiling was done. Figure 6 shows this depth profile. The Pt at.% that was transferred from the Pt-based superalloy target was between 80 at.% and 89 at.%. This averages to ± 84 at.%. This was also the composition of the target material. However the Al composition averaged to 4 at.% and the Cr to between 2 and 1 at.%. This was different to the target alloy composition. (Al 11 at.%, Cr 3 at.% and Ru 2 at.%). It was also observed that there was a relatively large oxygen presence in the PLD-prepared thin films. Therefore it is concluded that there was no stoichiometric transference of the annealed *Target 1* material to the PLD prepared thin films.

The question arises: to what degree does the heating of the target by the laser change the original alloy stoichiometry and microstructure, since, in practice the alloy is given a 2nd heat treatment through the laser beam. For this reason the unannealed Pt-based alloy was used as a target in a second experiment.

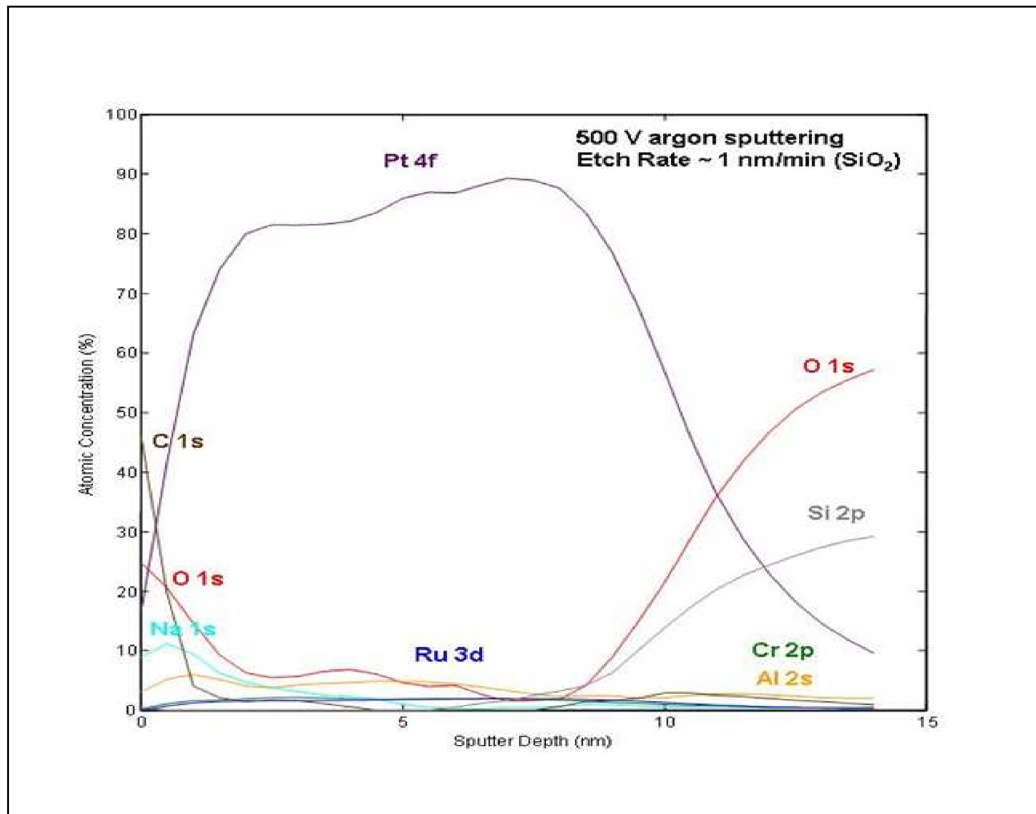

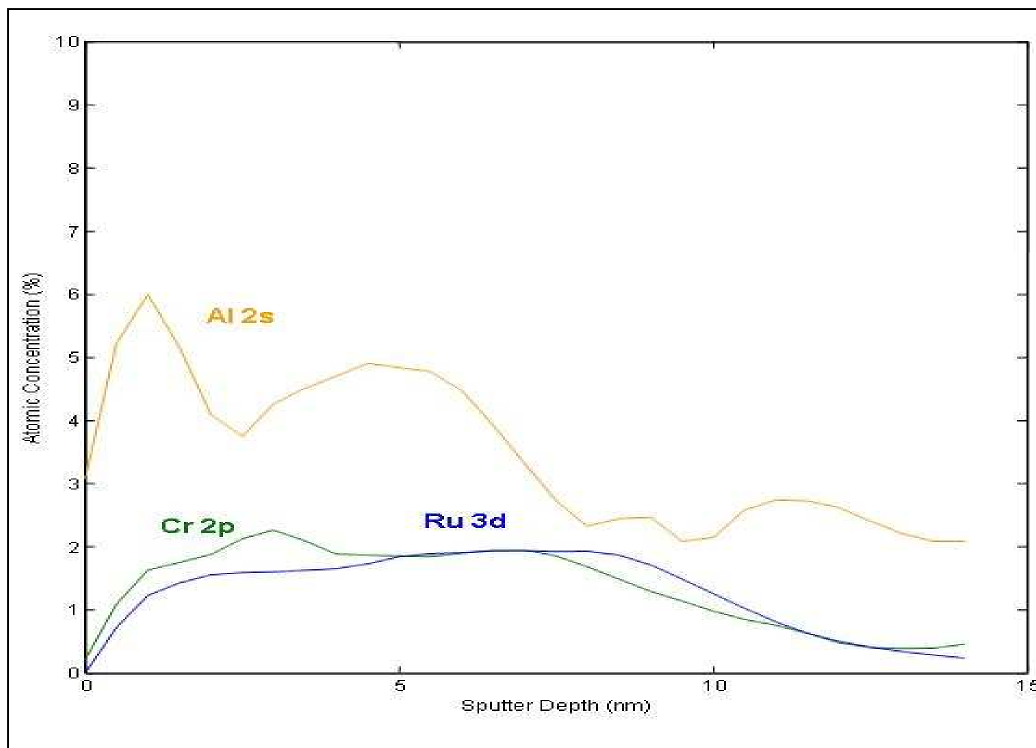

Figure 6: XPS depth profile of thin films prepared from the annealed *Target 1*: Pt_{84}:Al_{11}:Cr_3:Ru_2.

7.3.2) Thin films from the unannealed Pt_{84}:Al_{11}:Cr_3:Ru_2 target

Pressure (Torr)	Gas	Observations
2.1×10^{-5}	None	No plume was observed. Large particles seemed to be sputtered from the target area and deposited onto the substrate.
2.5×10^{-3}	N_2	No plume was observed; however it appeared as if the colour of the substrate changed, relative to that of unused Si substrates.
1.8	N_2	A plume did form and was spherical in shape.
1.8	Ar	A plume did form, but it did not have any distinct shape.
1.8	O_2	A spherical plume did form

Table 3: Ambient gasses and gas pressure for four samples prepared *via* PLD using *Target 2*.

A KrF laser was used having a wavelength of λ = 248 nm and a power supply of 26 kV.

For every thin film prepared the vacuum chamber was pumped to a pressure of 2.1×10^{-5} Torr and then backfilled with various gasses (as noted in the table) to maintain a certain pressure inside the chamber. A substrate temperature of 600 °C was used. The laser was then pulsed at a frequency of 8 Hz for various time durations (Table 2) and the superalloy was vaporized and condensed onto the substrate. A Si (1 0 0) substrate was used. The very high pressure systems (1.8 Torr) allowed for plume formation.

The Pt-based alloy target and thin films were then characterized with X-ray diffraction (XRD). Figure 7 shows the XRD-spectrum of the unannealed alloy *Target 2*. The blue lines indicate the expected peak positions for Pt_3Al. The red lines indicate the expected peak position for Pt. Figures 8 to 11 shows the XRD spectrum for the **thin films** from the unannealed *Target 2*. On the thin film XRD-spectra the Pt_3Al peak positions have been indicated. These thin films were done in different ambient gasses and the effect of this will be discussed in the next section. A comparison between the unannealed *Target 2* XRD spectrum and the resulting thin

film's XRD spectra show no correlation at all. Therefore it is concluded that no stoichiometric transfer between the unannealed Pt-based *Target 2* and thin films could be achieved in this manner.

However, a comparison between XRD spectra of these thin films (prepared from the unannealed *Target 2*), Figures 8 to 11, and the XRD spectrum of the annealed *Target 1*, Figure 12, **does** show a correlation. The Pt_3Al peak positions present in the annealed *Target 1* XRD spectrum at 33.7°, 40° and 47° are all also present in the thin films' XRD spectra (the films prepared from unannealed *Target 2*). The Si (1 0 0) substrate has a peak that lies at 70°, but, because its intensity is so large (relative to the Pt_3Al and Pt peaks) it is not shown on these graphs. It is therefore concluded that the heat of the laser beam gave the unannealed *Target 2* a sufficient heat treatment to transform the resulting thin film microstructure to be similar to that of the specifically engineered alloy of *Target 1*. The transferred films therefore have the same stoichiometry as the annealed *Target 1*. Thus, in this manner, a congruent transfer between target and substrate could be achieved.

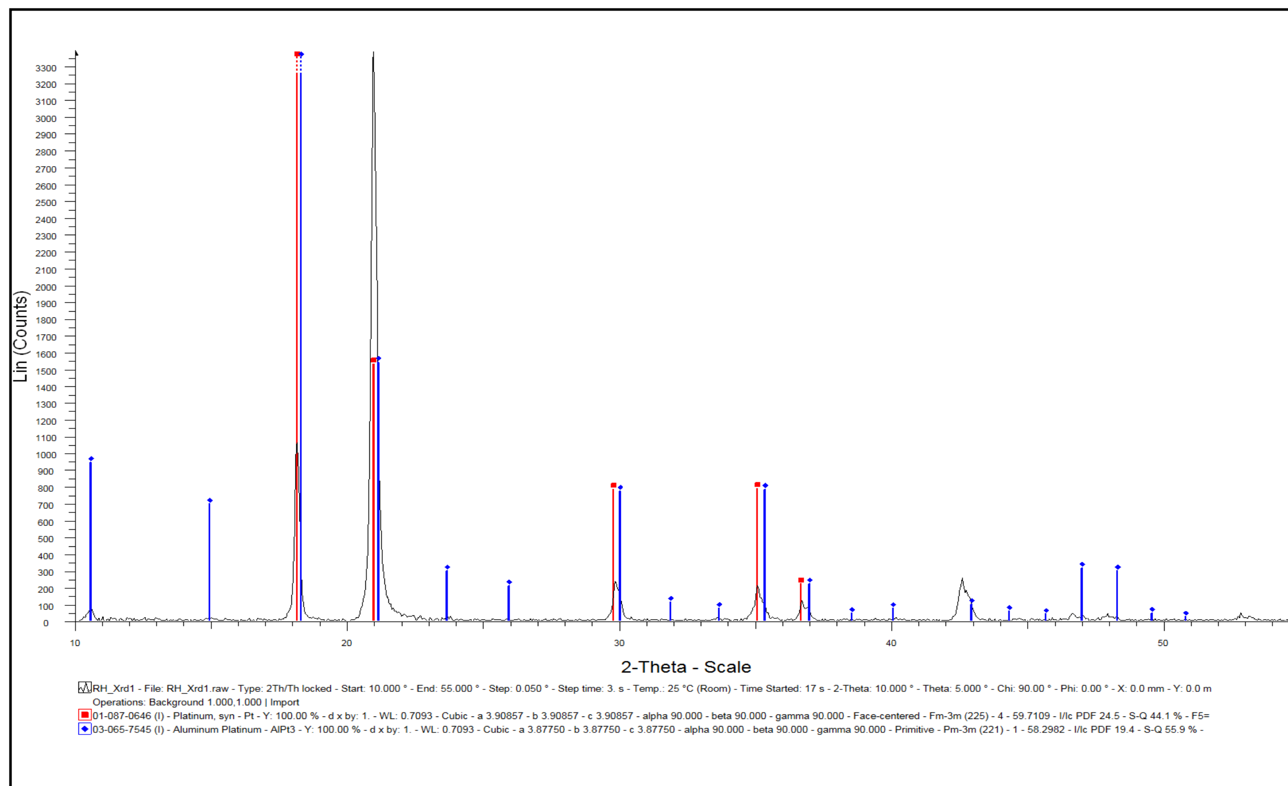

Figure 7: XRD spectrum of *Target 2*: Pt_{84}:Al_{11}:Cr_3:Ru_2-unannealed.

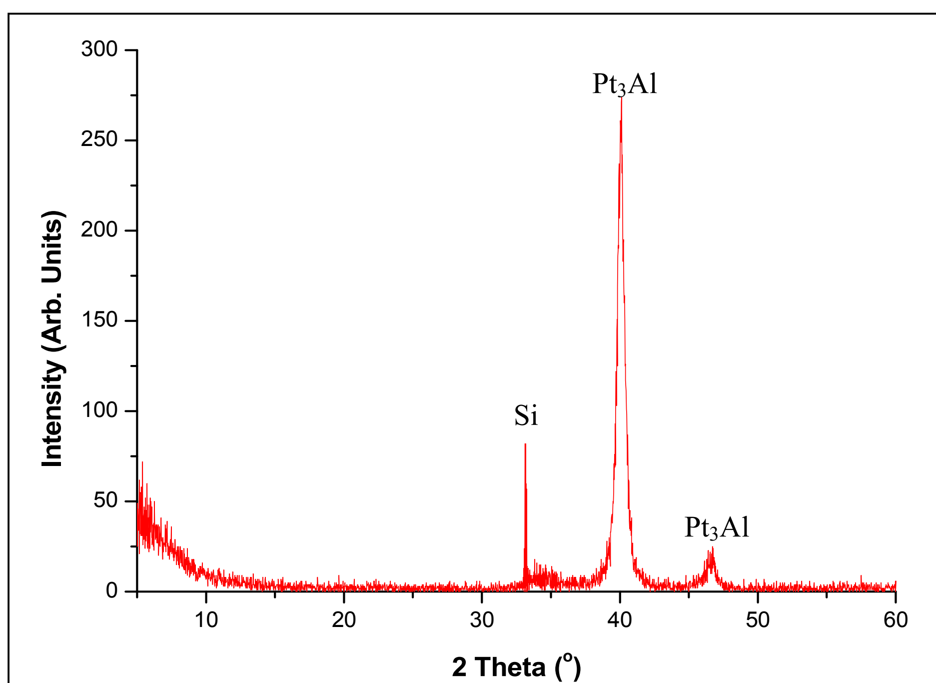

Figure 8: XRD spectrum for Sample B prepared in a high pressure N_2 atmosphere.

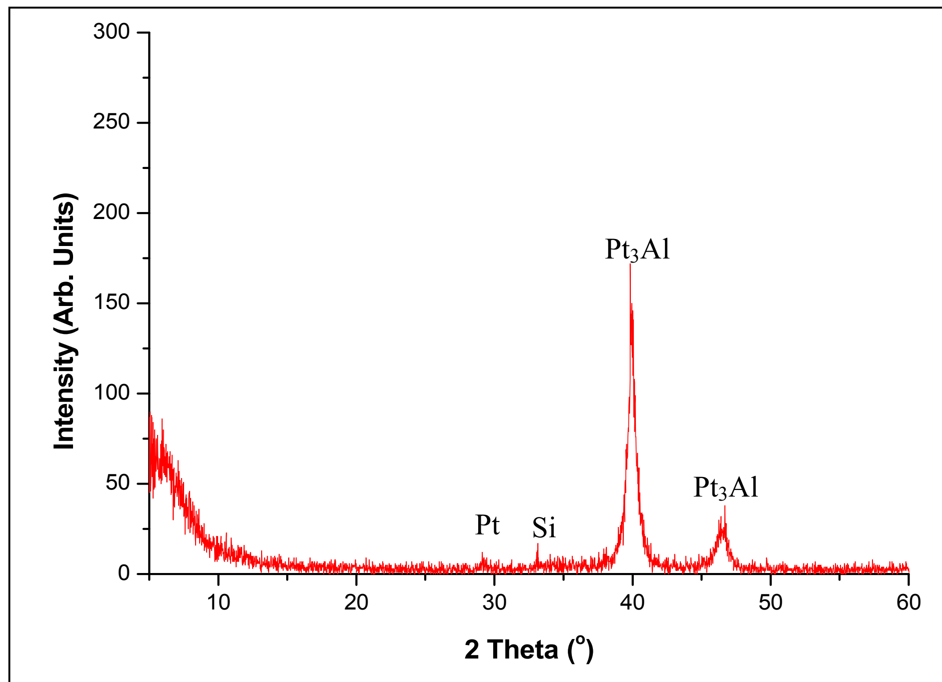

Figure 9: XRD spectrum for Thin Film C prepared in a low pressure N_2 atmosphere.

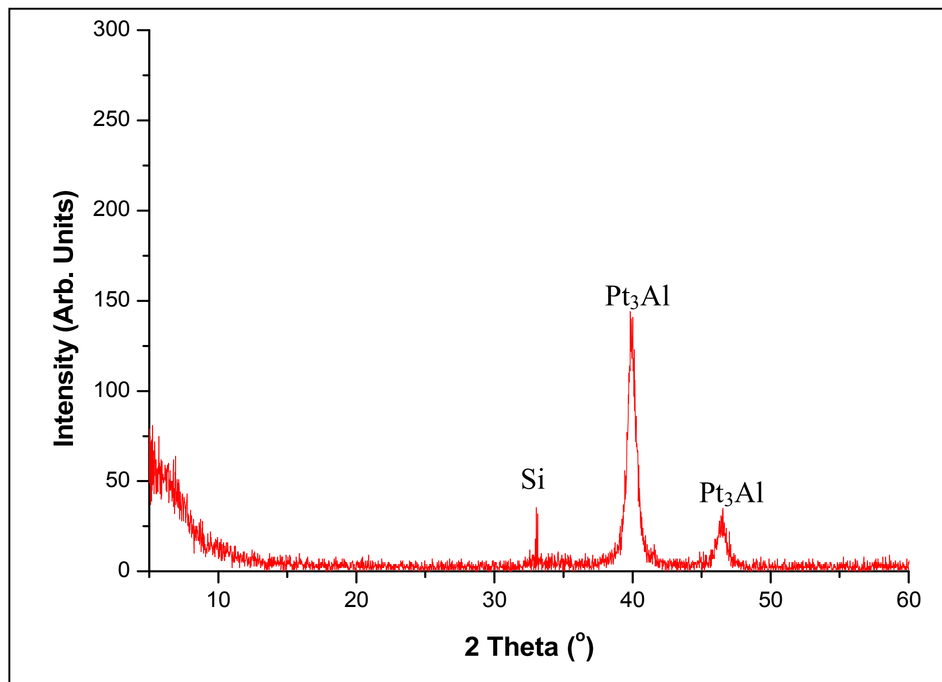

Figure 10: XRD Spectrum for Thin Film D prepared in an Ar atmosphere.

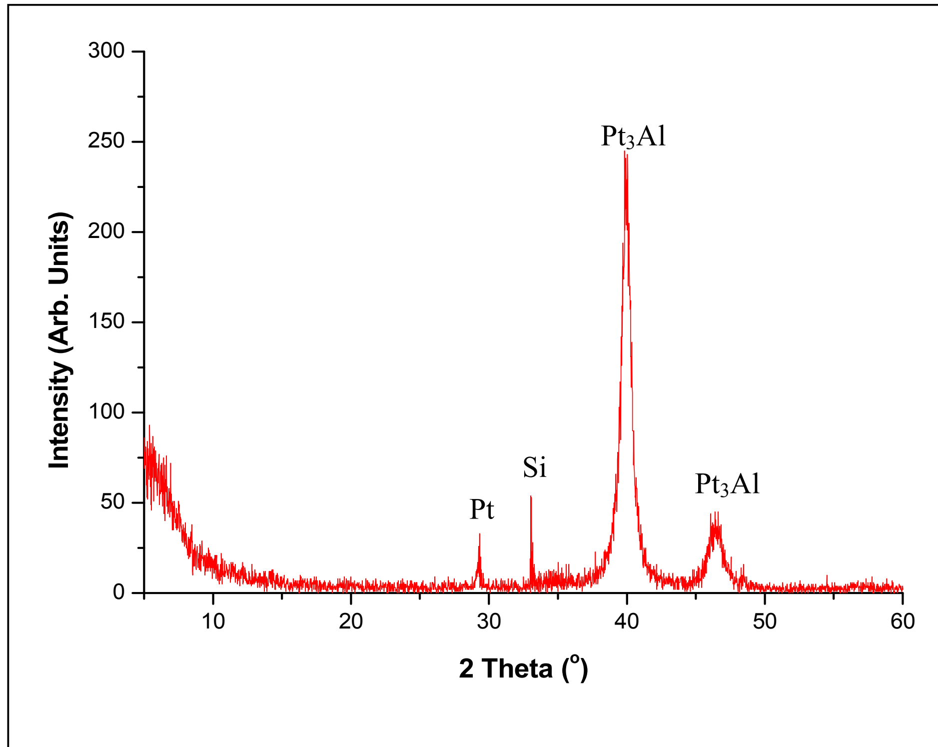

Figure 11: XRD Spectrum for Thin Film E prepared in an O_2 atmosphere.

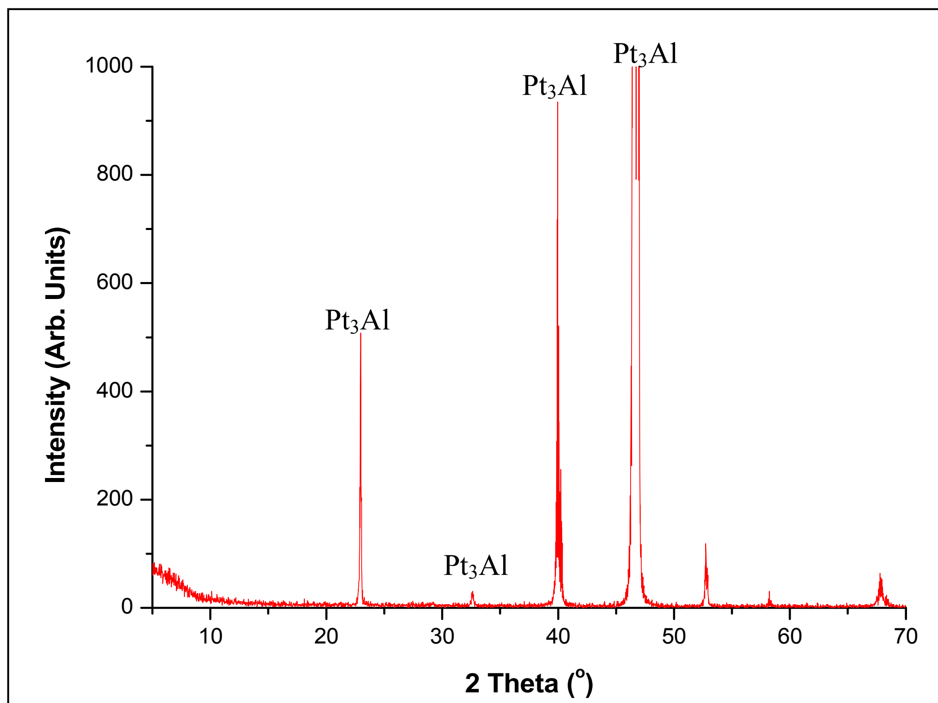

Figure 12: XRD Spectrum of annealed Pt-based alloy *Target 1*.

7.3.3) Conclusion

A specifically engineered Pt-based alloy *Target 1*, was given a heat treatment to have a microstructure of fine Pt_3Al particulates inside the Pt-matrix. This *Target 1* was used to grow thin films with the same stoichiometry and microstructure as the target. However, no stoichiometric transfer could be achieved (as was observed from SEM micrographs and XPS depth profiling). A second, unannealed target of the same composition, *Target 2*, was then used to grow thin films. Again, no stoichiometric transfer could be observed in the thin films (by comparing XRD images of *Target 2* with the resulting thin films).

However a comparison between the XRD spectra of the thin films prepared from *Target 2*, and the XRD spectrum of *Target 1*, revealed a remarkable correlation. This suggests that the laser beam is giving the unannealed target a sufficient heat treatment. Therefore the resulting thin films from *Target 2* (transferred to the substrate via PLD) have the same stoichiometry and microstructure as that of the annealed *Target 1*. In this manner thin films having the same stoichiometry and microstructure as the specifically engineered alloy *Target 1* could be grown via PLD. This is the case even though no *direct* congruent transfer between target and substrate could be achieved.

7.4) The effect of ambient gas and gas pressure on PLD thin films

On both types of thin films discussed above (from *Target 1* and *Target 2*) droplets were the main feature. These droplets varied in size, shape and number-density. Since it is envisaged to grow smooth thin films of the Pt-based alloy, these droplets were an unwanted feature on the thin films. Therefore a method was sought to reduce their appearance. To do this, an investigation into the effect of the ambient gas and ambient gas pressure on the formation of these droplets were carried out. The samples were imaged by means of Scanning Electron Microscopy (SEM) (Shimadzu SSX-550) with both a Secondary Electron Detector (SED) and a Backscattered Electron Detector (BSED). Atomic Force Microscopy (AFM) and Scanning Auger Microscopy (SAM) were also done. With the SEM – micrographs the large scale structure of these thin films were investigated with particular focus on the droplets

that formed on the surface. The droplet density per unit area was determined from the SAM micrographs. With AFM the nano-structure of the various thin films was characterized with particular focus on the particle density per unit area on thus much smaller scale.

7.4.1) Imaging via Secondary Electron Microscopy (SEM)

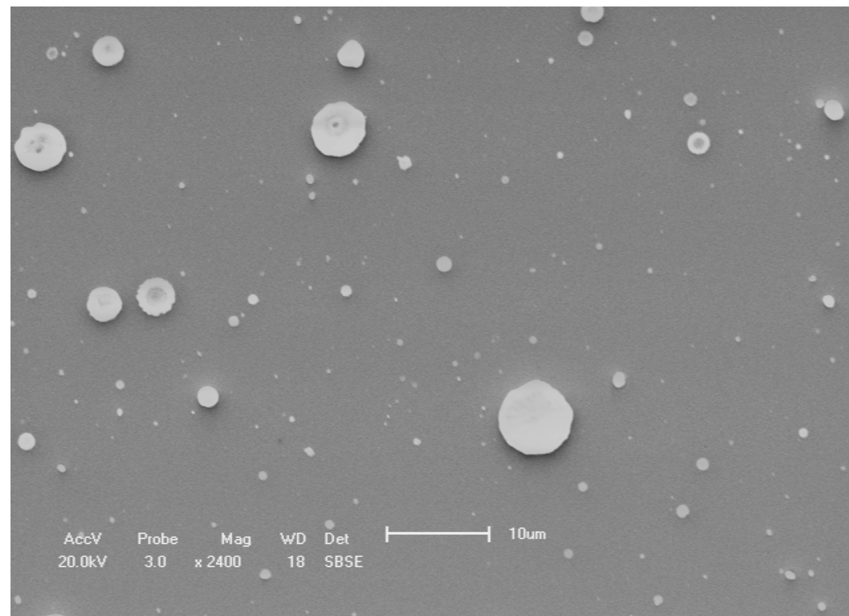

Figure 13: SEM image in SBSE-mode of droplets formed in vacuum. (AccV. 20.0 kV, Probe size 3.0, Magnification ×2400, WD 18).

Droplets were the main feature visible on the prepared thin films. These droplets formed on these films differed in size, shape and number-density and it is believed that both the ambient gas and gas-pressure was the main contributors to this. From literature we know that the fluence and substrate temperature would also play a crucial role in the droplet formation [8-10]. Since these droplets might have a detrimental effect on the envisaged thin-films to be used as coatings for turbine blades, it would be useful if their growth could be controlled. Figure 13 shows some of the different droplets.

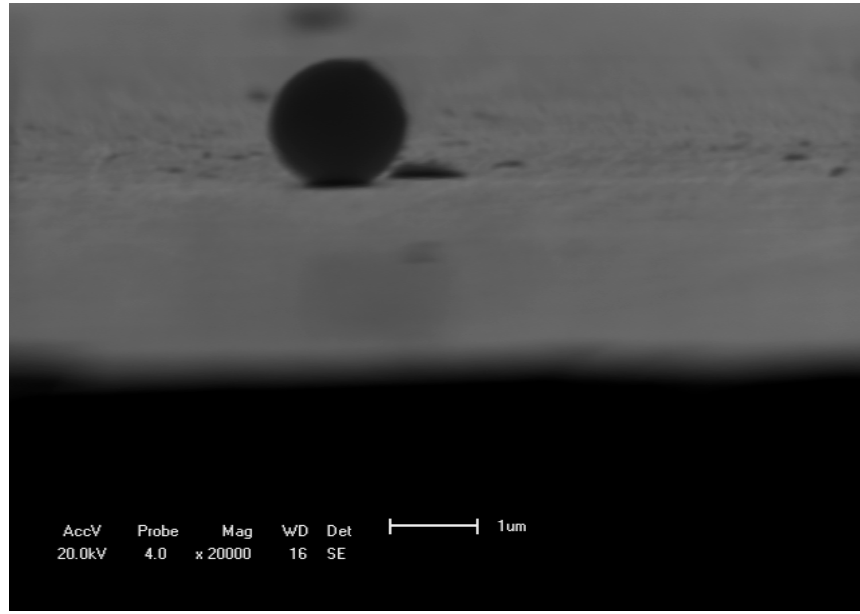

Figure 14: SEM image in SED-mode at 90º angle of droplet formed in oxygen. (AccV. 20.0 kV, Probe size 4.0, Magnification ×20 000, WD 16).

In Figure 13 numerous droplets can be seen. Notice the number density per 20 × 20 micron on this image was relatively large and will be discussed shortly. What is important to note in Figure 13 is the shape of these droplets (circular) as well as the various sizes, ranging from less than one micron up to about 5 micron. Figure 14 shows a 90° side view and from this micrograph it can be seen that these droplets are not just circular but are in fact spherical in shape.

Roughening of the target is clearly visible in Figure 15. This roughening is the main cause for the formation of droplets (up to some micrometer in size) on the growing films. The major problem with films grown with PLD is the formation of droplets caused by the splashing of target material on the substrate. There is considerable evidence that the droplet formation is preceded by the formation of wavelike structures on the ablated target surface [2]. There are two main types of surface structures resulting from laser irradiation (ablation). The first type is of small scale, on the order of the laser-light wavelength. In general it is more dependent on the surface condition, such as the optical properties of the material. The second type of target surface structures has a scale much larger than the laser-light wavelength. These large surface

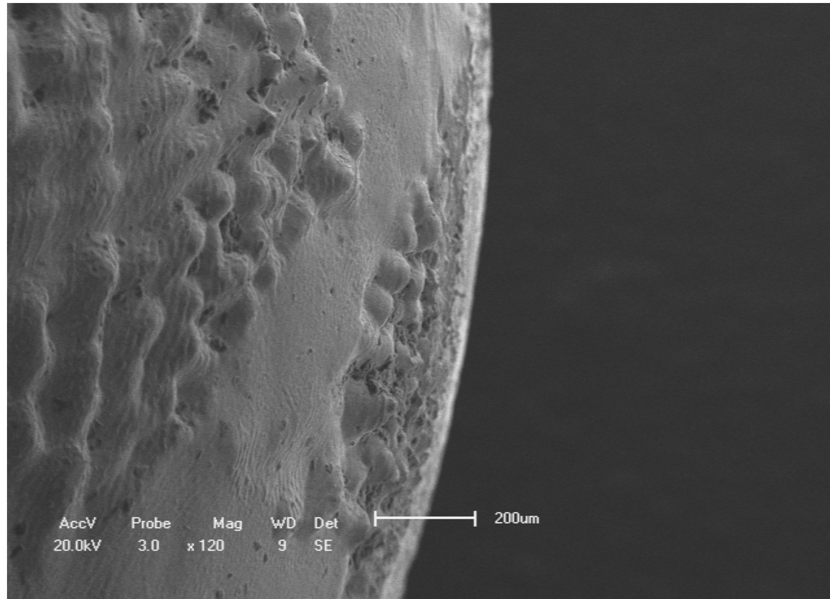

Figure 15: Target roughening as viewed by SEM in SED-mode. (AccV. 20.0 kV, Probe size 3.0, Magnification ×120, WD 9)

structures [2 - 4] appear when the laser fluence is above the damage threshold and the target is heated beyond the vapour phase to the plasma state. The fairly regular wavelike patterns look much like the wind driven surface wave in a pond (see Figure 3). In this study, the molten Pt-Al target plays the role of ''water,'' and the ''wind'' comes from expansion of the high pressure plasma plume. The large surface structures occur when the surface waves coming from the centre of the laser spot are splashed and solidified at the edge.

During the deposition, the surface of the target is modified with cumulative laser beam irradiation and, as a result, forms a cone-like structure [6]. As this irregular surface structure is formed, the effective laser energy density incident on the target decreases, and if it becomes less than the threshold, then a non-stoichiometric deposition occurs. In addition, the inhomogeneities of the target surface in the area of incident laser beam induce a difference in the ablation rate leading to a surface roughening of the target through the appearance of the droplets [7]. Commonly the sintered target has a very rough and grainy surface and internal voids, and with laser incidence, the weakly connected areas like grain boundaries are likely to be preferentially ablated.

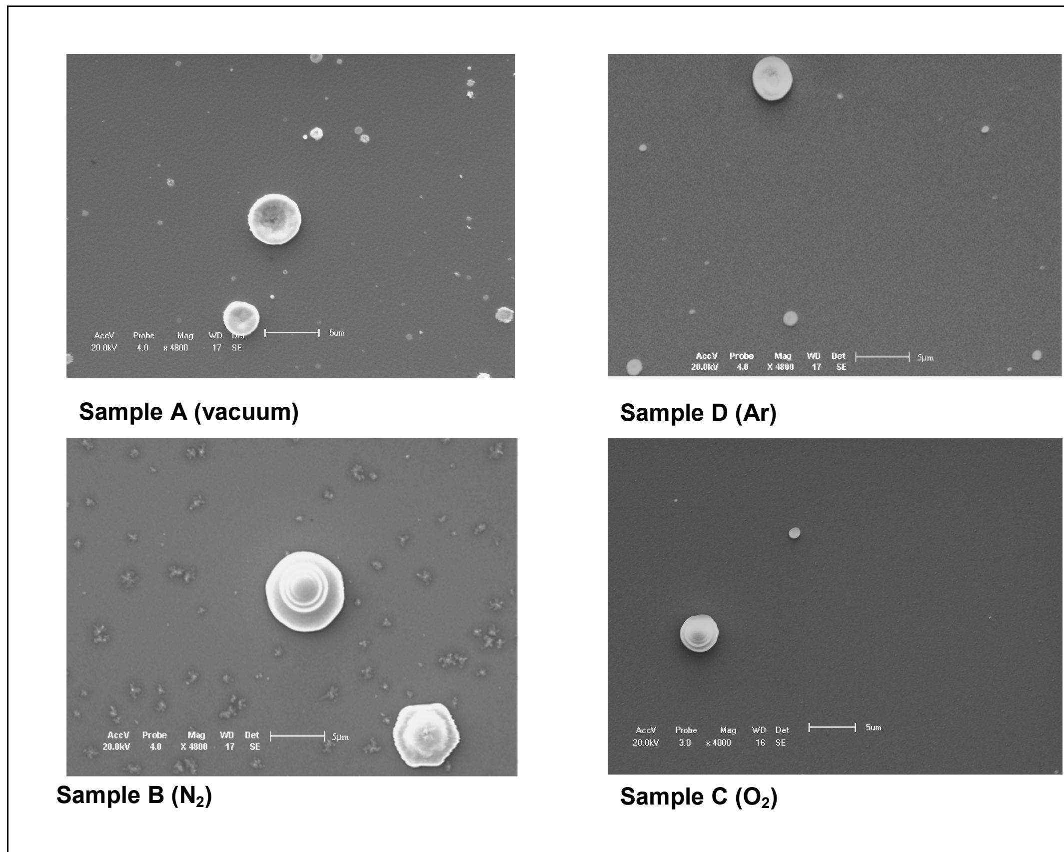

Figure 16: SEM micrographs in SED mode of samples A, B, C and D prepared in vacuum, N_2, O_2 and Ar atmospheres respectively (the scale bar shows 5 μm).

From Figure 16 it is observed that the thin film surfaces prepared in a N_2-atmosphere and in vacuum are much more cluttered with finer droplets (less than 5 μm in diameter) than those films prepared in the Ar and O_2 atmospheres. It is also seen that there are more large (5 μm and larger) droplets in the vacuum and N_2 prepared films that for the Ar and O_2 films. Since these large droplets (5 μm and larger) appeared to be in the minority for this specific experiment, the focus was on the formation of these smaller droplets. The question was to what degree do the ambient-gas influence the formation of smaller (less than 1μm) particles? Using the Heyn-method [8] the number of particles (less than 1μm) per unit area was determined and the results are presented in Figure 17. The droplet size distribution for the various ambient-gases was also determined and the results displayed in Figure 18.

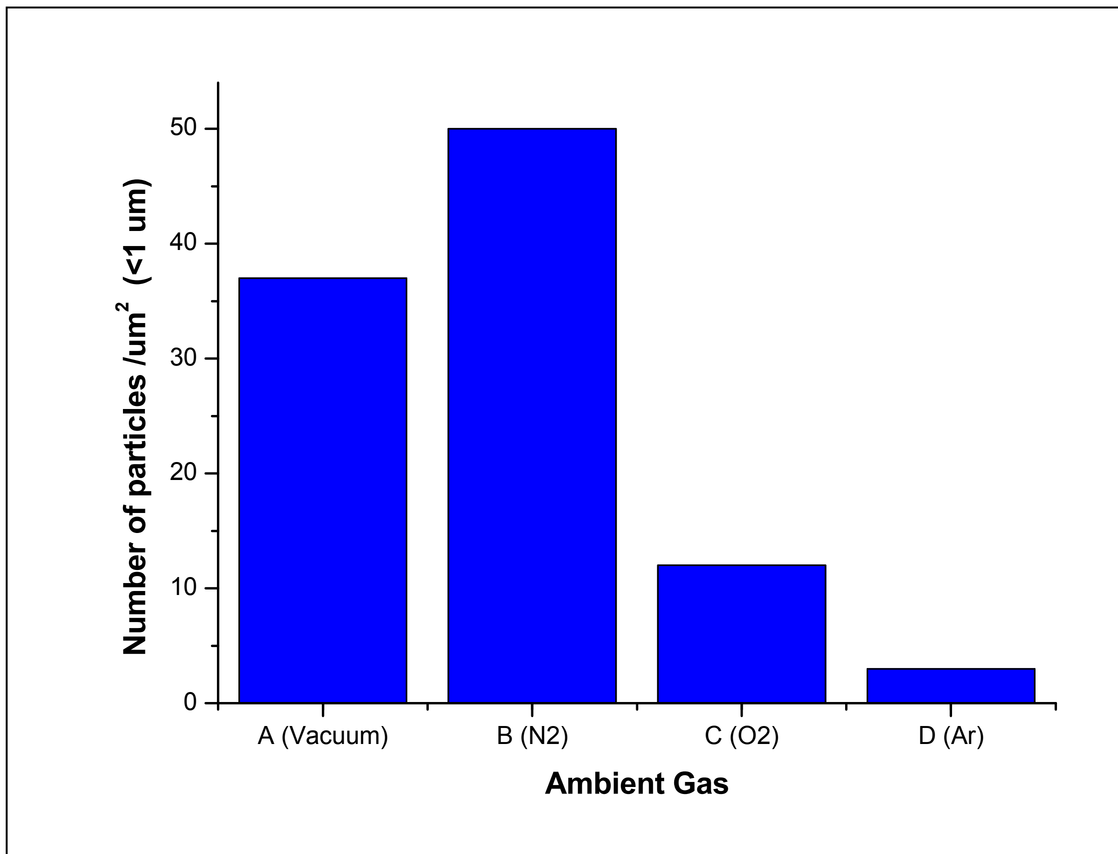

Figure 17: Number of Particles/ μm^2 (<1 μm) for different ambient gases.

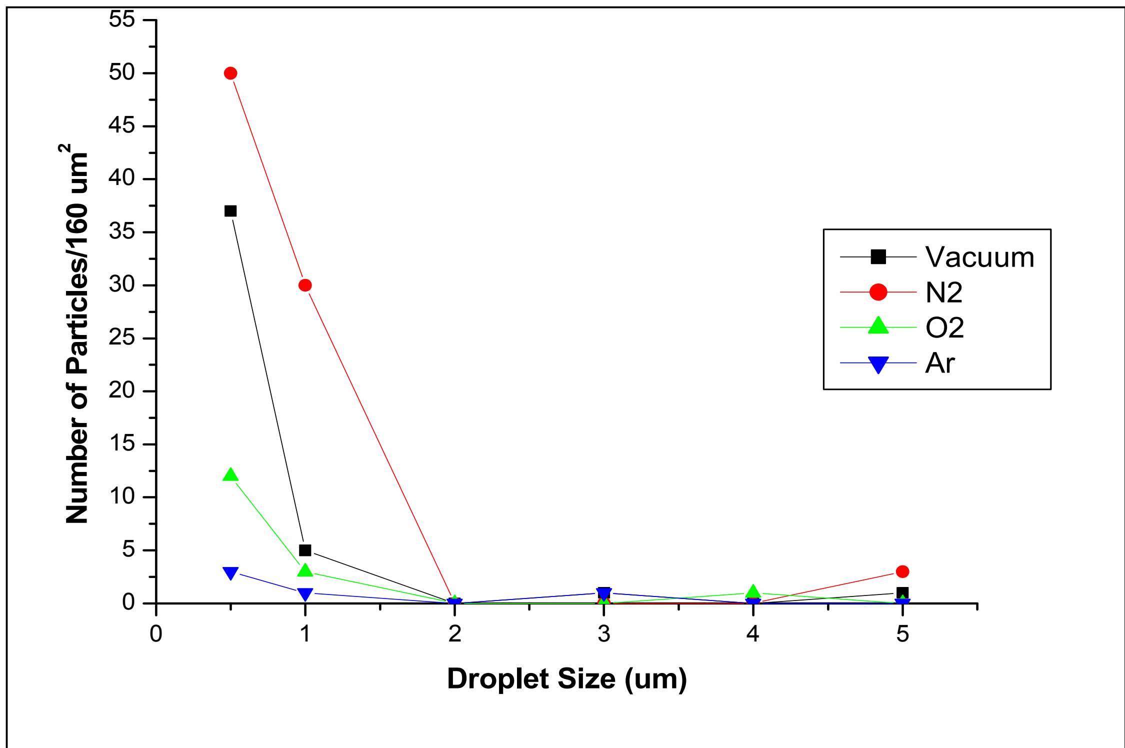

Figure 18: Number of particles/160 μm^2 vs. droplet size for various ambient gases.

Consider first the droplet size for films prepared in the vacuum. It is clear from Figure 16 that quite a large number of small droplets (< 1 μm in diameter) appear on the thin film surface, giving these films a rough surface. This is also the case for the films prepared in a nitrogen ambient gas. However for the nitrogen-films the surface is even rougher since even more small particles (from 1 μm and smaller) are present. When this is compared to the thin films prepared in O_2 and Ar ambient gasses the following is observed. Less small droplets are present for O_2 and the least for those films prepared in Ar. From this it is concluded that, on the microscopic scale, argon gives the "cleanest" surfaces with the least number of large and smaller droplets. The reasons why this is so will be discussed in section 7.4.3

7.4.2) Atomic Force Microscopy (AFM)

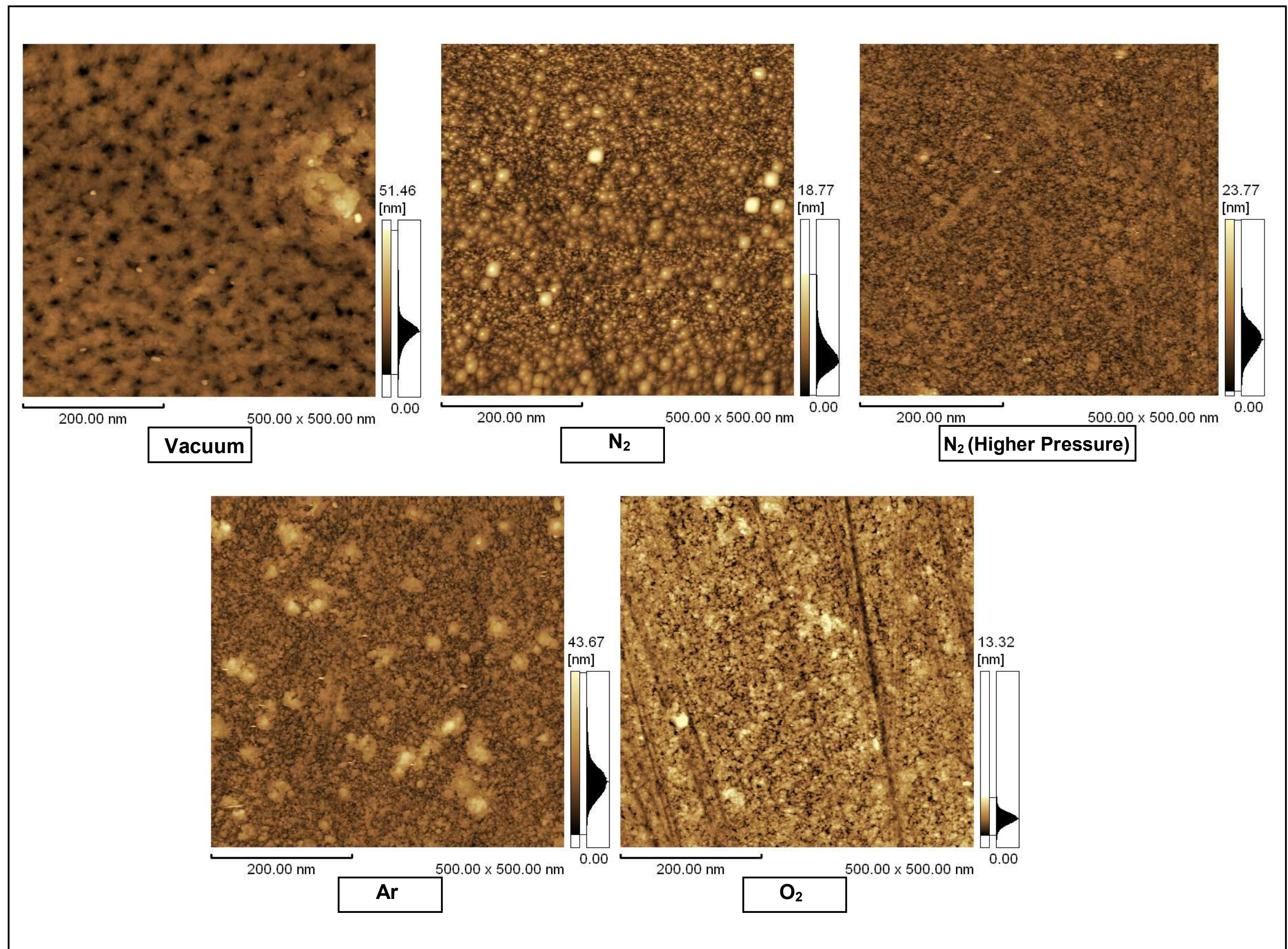

Figure 19: AFM images of a 500 × 500 nm^2 area, showing clearly the influence of both the ambient gasses and the different ambient gas pressures.

The formation of the thin films was then further investigated via a Shimadzu SPM-9600 AFM at the University of the Free State (UFS). A 500 × 500 nm^2 area was scanned in contact mode at a scan rate of 1 Hz for each of the various films. The Heyn-method was employed again and particle densities were obtained. Figure 20 gives an example of how the Heyn-method was employed for a smaller 50 × 50 nm area. Four lines are drawn (via the AFM software) (line A-B, C-D, E-F and G-H) across the 50 × 50 nm area and the software gives the topography of the sample across those lines. The various particle sizes can be obtained from these topographical graphs and the number of particles intercepting the line can be obtained.

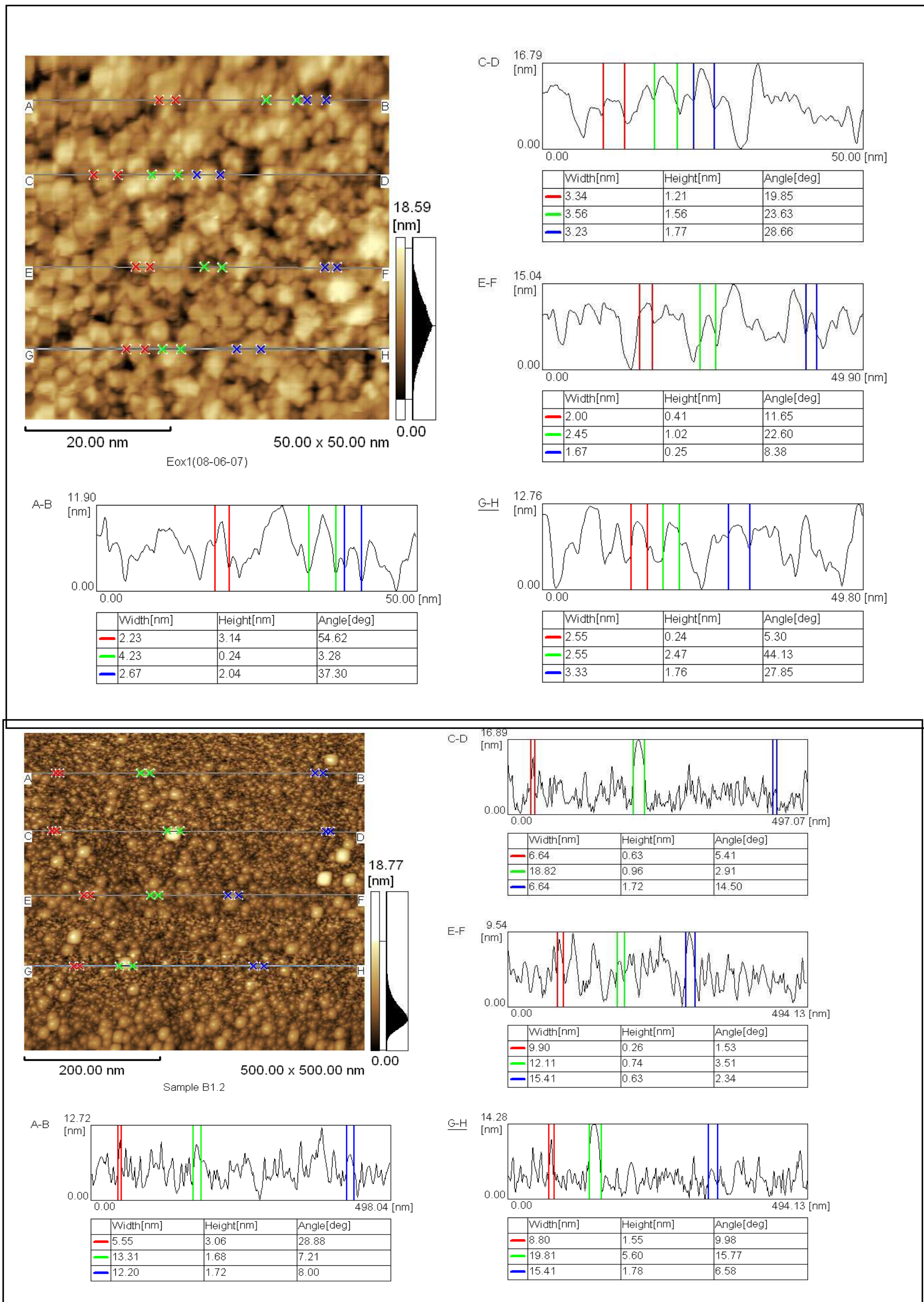

Figure 20: Example of the implementation of the Heyn-method for two different samples, one with a courser and the other a finer structure.

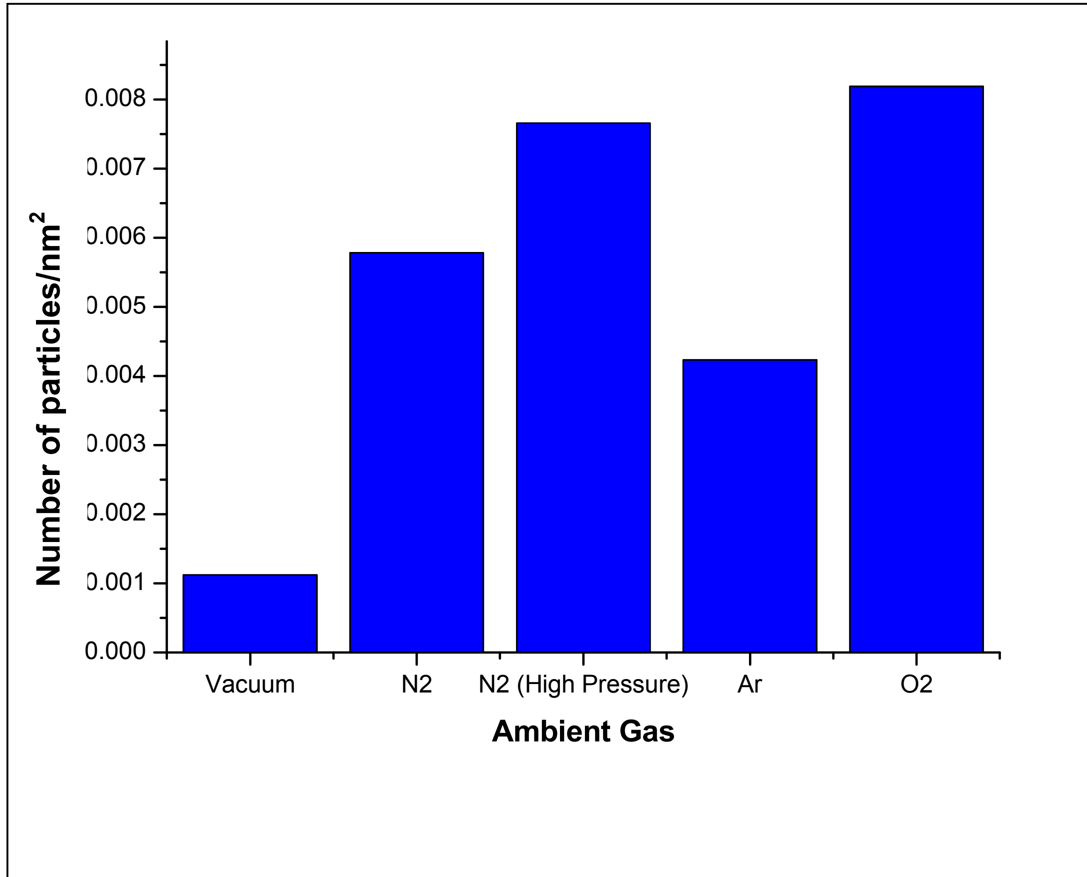

Figure 21: Particle density for different ambient gasses in a 500 × 500 nm^2 area.

As an example consider the topographical graph of the A-B line for the first AFM image from Figure 20. The particle between the red cross-hairs has a height of 3.14 nm and a width of 2.23 nm. By now counting the number of particles intercepting the line an average particle density per 50 nm can be obtained. Figure 19 shows the obtained AFM images for the films for a 500 × 500 nm area. The particle density per unit area was then determined and the results are shown in Figure 21. The particle density is the smallest for the vacuum-setup and not the argon-setup. However, this is the case because of clustering, as is clearly visible for the vacuum-setup (Figure 19). Though some clustering for the argon-setup is also visible, it is less than for the vacuum, and the particles are finer than for the other samples. This will be explained later in more detail. Images were obtained for an even smaller area (50 × 50 nm^2) to see if the above results are also valid on this smaller scale. Figure 22 shows these images.

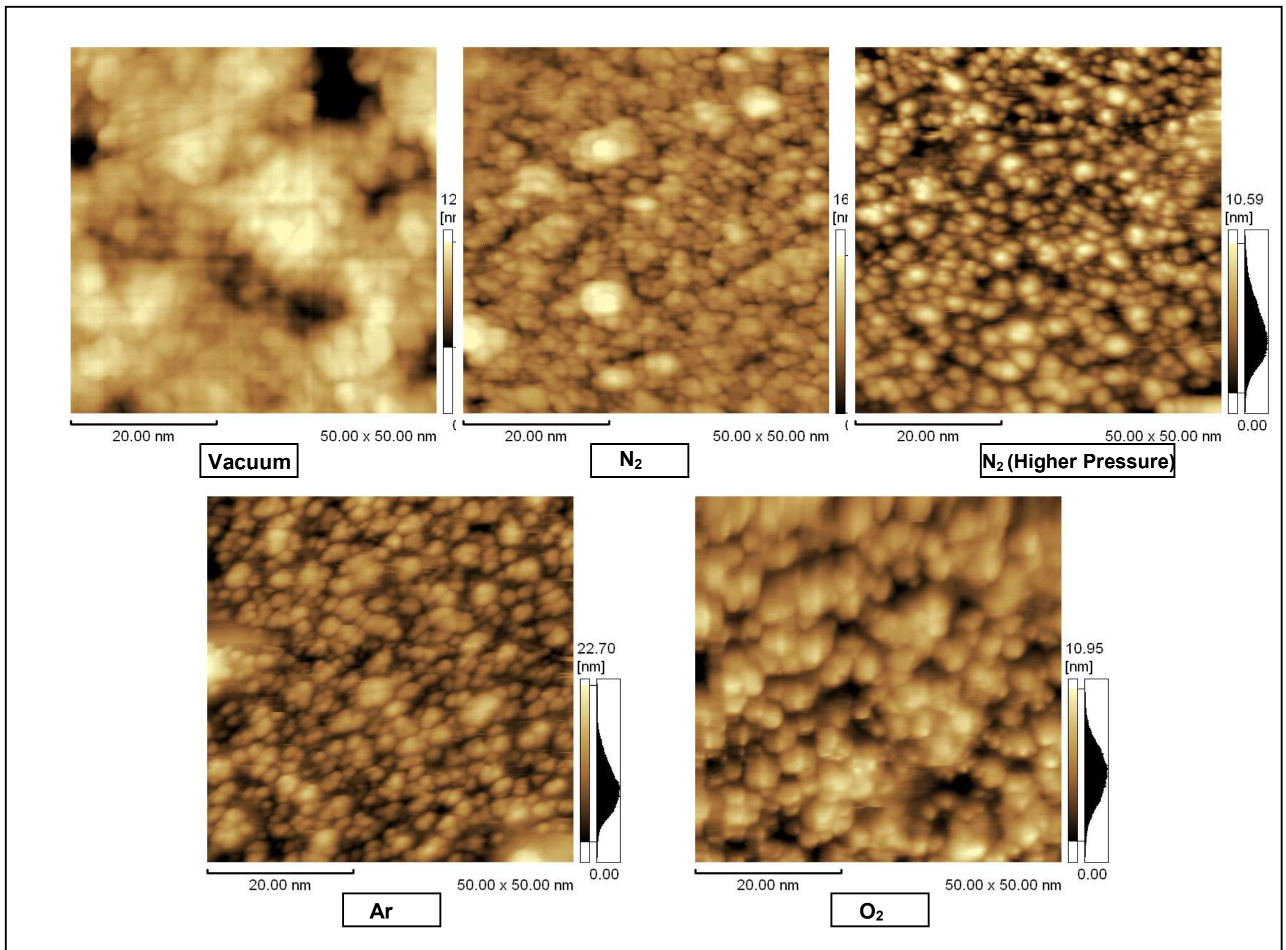

Figure 22: AFM images for 50 × 50 nm^2 areas.

The clustering in the vacuum conditions is clearly seen in this image. It also seems as if the thin films grown in the N_2- and Ar-ambient gasses have the most clearly defined particles. By using the Heyn-method [8], the particle size distribution is shown in Figure 23. From this it is clear that the Nitrogen-ambient gas setup led to the smallest particles (finest particles) at a high pressure (1.8 Torr).

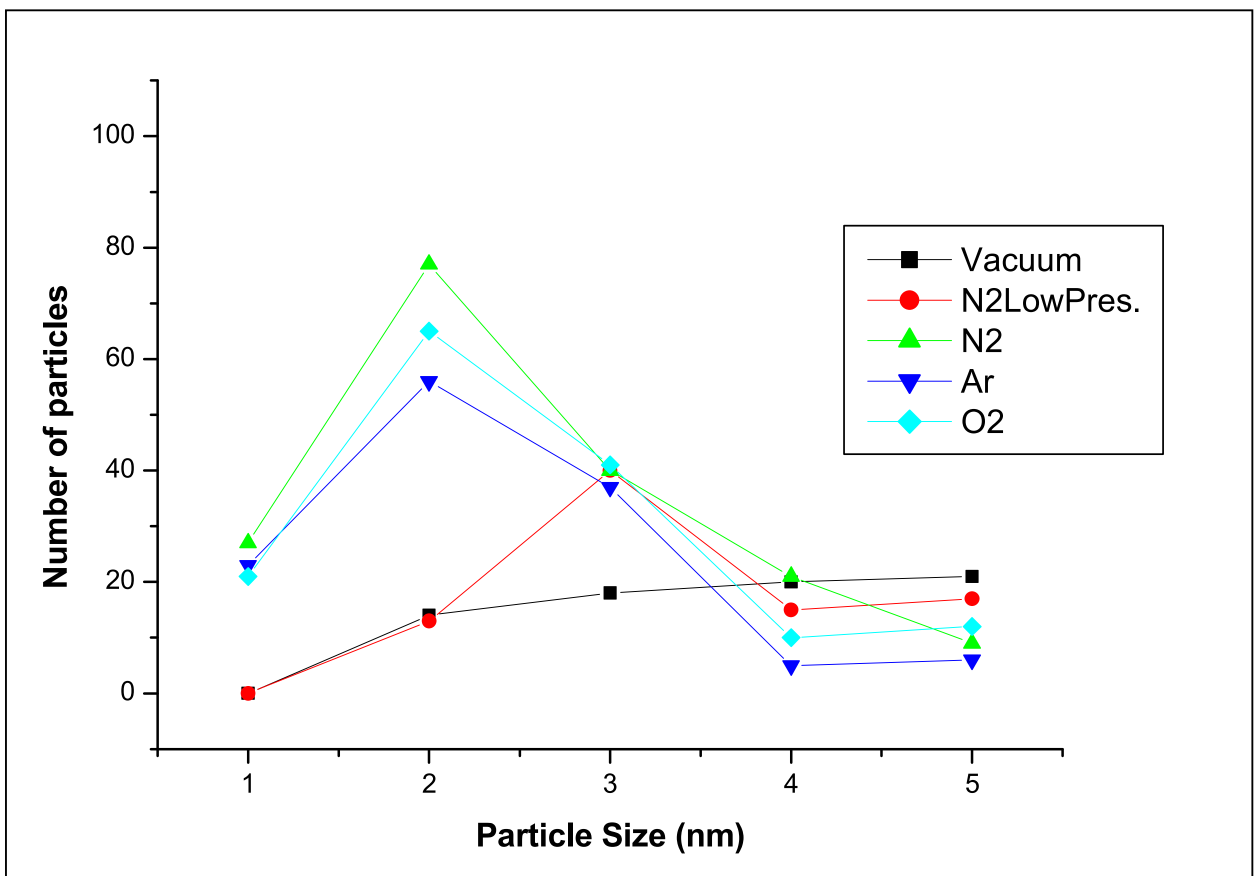

Figure 23: Particle Size Distribution for an area of 50 × 50 nm^2.

7.4.3) Discussion

Assume the Ar gas atoms are in rest relative to the ablated ions and atoms, which are much faster (the ablated ions are faster by a factor of 30 compared to the Ar and the atoms by a factor of 5). A dense cloud of ablated particles moves through an almost static diluted arrangement of Ar atoms.

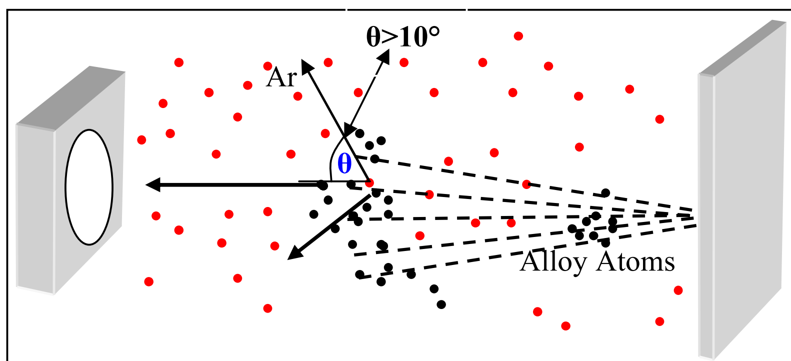

Figure 24: A cloud of ablated particles moves through an arrangement of Ar atoms.

The ions that collide with Ar atoms as well as the Ar atoms themselves are scattered out of the flight path of the ablated material between target and substrate. Since the mass of an Ar atom is sufficiently high for a large scattering angle, about 90% of all scattering angles are larger than 10º [9]. Thus, the scattered ions are not deposited onto the substrate. As the colliding Ar atoms are also removed from the flight path, the following slower ions and atoms fly through a significantly reduced Ar atom density and have a higher probability to reach the substrate. Thus: faster ions are scattered and not deposited, but open a channel for the deposition of the slower particles [10].

However by decreasing the mass of the ambient gas atoms (from Ar to O_2 to N_2), the scattering angle also decreases, allowing more of the fast moving particles to be deposited onto the substrate. Thus more material reaches the substrate, and hence larger particles are formed since clustering takes place.

An increase in ambient gas pressure leads to the roughening of the film surface (other than the droplets). The ejected particles are cooled and lose their kinetic energy by collisions with the atoms/molecules in the ambient gas during the flight process. Thus the morphology of the film surface changes to be rough due to the solidification of the smaller particles immediately after reaching the film.

In other words fewer particles coalesce and hence more particles are spread out over the surface of the substrate, explaining the increase in number of particles at higher ambient gas pressures.

The decrease of droplet density in the film by the increase in ambient-gas pressure can be explained by the above cooling model, resulting in a reduced sticking coefficient of the droplets on the film surface [10]. An increase in ambient gas pressure leads to a decrease in droplet density at a constant substrate temperature.

Thus to summarize: an increase in ambient gas pressure leads to film surface roughening and increase in number of smaller particles. An increase of ambient gas atomic mass leads to a decrease in number of deposited particles because less material reaches the substrate surface.

7.4.4) Conclusion

The influence of the ambient gas and gas pressure definitely place a crucial role in the formation of droplets, as well as in the finer microstructure of the grown thin film. To what degree these droplets influence the phase formation and transformation from the target to the substrate is worth investigating in the future. It would also be useful to investigate whether these droplets will be detrimental or constructive in the final application of these thin film coatings. From this study is was showed how the ambient gas and ambient gas pressure can increase or decrease (to a degree) the amount of droplets, as well as the film's particle- size and -density by varying the ambient gasses as well as the ambient gas pressure.

References

1. **L. A. Cornish et al.** *Journal of Mining and Metallurgy,* Volume 38 (3-4) B, (2002), pg. 197 – 204.
2. **Spindler H. L., Gilgenbach R. M. and Lash J. S.,** *Applied Physics Letters*, Volume 68, (1996), pg. 3245.
3. **Akhmanov S. A., Emel'yanov V. I., Koroteev N. I., and Seminogov V. N**., *Soviet Physics Uspekhi*, Volume 28, (1985), pg. 1084.
4. **Bostanjoglo O. and Nick T.,** *Journal of Applied Physics*, Volume 79, (1996), pg. 8725.
5. **Bauerle D.,** *Laser Processing and Chemistry,* Berlin, Springer, (1996), pg. 409.
6. **Mao X. and Russo R. E.,** *Applied Physics A: Solids and Surfaces*, Volume 64, (1997), pg.1.
7. **Mele A., Guidoni A. G., Kelly R., Miotello A., Orlando S., Teghil R., and Flamini C.,** *Nuclear Instruments and Methods in Physics Research B*, Volume 116, (1996), pg. 257.
8. **Van der Voort G. F., McCall J. J. and Steele J. H., Jr., (Eds.),** *Grain Size measurement, Practical Applications of Quantitative Metallography*, ASTM STP 839, Philadelphia, American Society for Testing and Materials, (1984), pg..85-131.
9. **Strum K. et. al.,** *Applied Surface Science*, Volumes 154-155 ,(2000), pg. 462-466.
10. **Yonezawa Y.,** *Applied Surface Science*, Volumes 127-129, (1998), pg. 639-644.

Chapter 8

PVD and Simulation Results

Introduction

The development of the CPMC model is discussed in chapter 6. In this chapter a direct comparison is made between the experimentally measured thin film structures and the simulated predicted structures of a binary thin film system. This is done by comparing elemental maps of binary thin films with the simulation results. Simulated depth profiles are also compared to experimentally measured depth profiles.

8.1) Experimental setup and procedures

In order to grow binary thin films, the following procedure was followed. Appropriate substrates had to be obtained. At first Si and glass substrates were used, however unwanted silicates (Al and Pt) formed during the annealing process. Since the purpose was to compare the theoretically modelled results with the experimental results, the presence of the silicates was unwanted. For this reason an oxide barrier was introduced in the form of a SiO_2 layer on top of the Si (1 0 0) substrates. A 4000 Å oxide layer (determined by the colour of the substrate as violet-red) was grown on top of a silicon (Si (1 0 0)) substrate. The wet oxidation process was used for the oxidation process. The Al and Pt two-layer thin films were deposited on top of the SiO_2 substrate. This was done with physical vapour deposition (PVD). These samples were then annealed at the appropriate temperatures and annealing times in a vacuum furnace at a pressure of 10^{-6} to 10^{-7} Torr. These samples were analyzed in a nano-scanning auger microprobe (*PHI 700*). Depth profiles and elemental maps at

different sputter depths were obtained. These elemental maps and depth profiles were then compared to the simulated results.

8.1.1) Diffusion barrier for thin films: wet oxidation

SiO_2 is a high-quality electrical insulator and can be used as a barrier material during diffusion in order to prevent diffusion into the silicon substrate or vice versa. Wet and dry oxidations are used for growing an oxide onto silicon [1].

The reaction for wet oxidation is as follows:

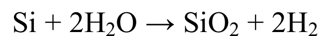

$$Si + 2H_2O \rightarrow SiO_2 + 2H_2$$

In order to prepare the silicon dioxide substrates the following procedure was followed. The silicon wafers were properly cleaned with acetone inside an ultrasonic bath. These are then placed inside a Lindberg-vacuum-furnace, preheated to 1000°C. Oxygen is then bubbled through distilled boiling water and the oxygen and vapour are allowed to pass over the silicon wafers. To grow an oxygen layer of between 4000 and 5000 Å, the silicon wafer is exposed to the water-oxygen-vapour for an hour at a temperature of 1000 °C. A rough measure of the thickness of the oxide film can be made by observing the change in colour of the silicon surface. A colour chart for SiO_2 shows different oxide layer thicknesses corresponding to different colours [2]. This is due to the optical interference in the oxide that reflects back certain light frequencies depending on the thickness of the oxide layer. A change in hue from a silver mirror surface to a violet surface signifies the growth of the oxide to the order of between 4000 and 5000 Å (see Table 1).

Thickness (µm)	**Colour**	**Order**
0.05	Tan	I
0.07	Brown	
0.10	Dark violet to red-violet	
0.12	Royal Blue	
0.15	Light Blue to metallic blue	
0.17	Metallic to yellow-green	
0.20	Light gold to yellow	
0.22	Gold	
0.25	Orange to melon	
0.27	Red-violet	
0.30	Blue to violet-blue	
0.31	Blue	
0.32	Blue to blue-green	
0.34	Light green	
0.35	Green to yellow-green	
0.36	Yellow-green	II
0.37	Green-yellow	
0.39	Yellow	
0.41	Light orange	
0.42	Carnation pink	
0.44	Violet-red	
0.46	Red-violet	
0.47	Violet	
0.48	Violet-blue	
0.49	Blue	
0.50	Blue-green	
0.52	Green (broad)	
0.54	Yellow-green	
0.56	Green-yellow	III
0.57	Yellowish	
0.58	Light orange	
0.60	Carnation pink	
0.63	Violet-red	
0.68	Bluish	
0.72	Blue-green to green	IV
0.77	Yellowish	
0.80	Orange	

Table 1: Colour chart for SiO_2 films under daylight fluorescent light.

8.1.2) Calculation of at.% for the thin films

To show (as an example) the calculation algorithm the thickness ratio between the Pt and Al layers for $Pt_{50}Al_{50}$ is calculated as follows:

$$\mathrm{Pt}_{50}\mathrm{Al}_{50} = \mathrm{Pt}_1 : \mathrm{Al}_1 \tag{5.66}$$

$$\frac{\mathrm{Pt}_{\mathrm{Atoms}}}{\mathrm{Al}_{\mathrm{Atoms}}} = \frac{\left(\dfrac{\rho_{\mathrm{Pt}} A h_{\mathrm{Pt}}}{M_r(\mathrm{Pt})}\right)}{\left(\dfrac{\rho_{\mathrm{Al}} A h_{\mathrm{Al}}}{M_r(Al)}\right)} = \frac{\rho_{\mathrm{Pt}} h_{\mathrm{Pt}} M_r(Al)}{\rho_{\mathrm{Al}} h_{\mathrm{Al}} M_r(\mathrm{Pt})} \tag{5.67}$$

Since the area of the substrate remains the same, the area terms cancel out and the only relevant parameters are the molar mass, M_r, density, ρ and the thickness or height of the layers, h. Thus by inserting these parameters (Mr_{Al}= 26.982 g/mol, Mr_{Pt} = 195.08 g/mol, ρ_{Pt}= 21.45 g/cm^3 and ρ_{Al} = 2.699 g/cm^3) a ratio between the Pt height/thickness and Al height/thickness can easily be found.

8.1.3) Preparation of the thin films: electron beam - physical vapour deposition

After the growth of the SiO_2 substrates, the substrates were mounted in a PVD vacuum system. For these particular experiments, the vacuum chamber was evacuated to a pressure of 10^{-6} to 10^{-7} Torr. A current between 100 to 250 mA was passed through the wolfram filament to release the electrons as discussed in chapter 4. The reason for the variation of this current was in order to control the emission current and hence the deposition rate. The deposition rate varied between 1 to 2 Å/s for the Pt and 10 to 20 Å/s for the Al. The Al deposition rate was more difficult to control, since Al is much more volatile than Pt. (The heat of vaporization for Pt is 469

kJ/mol compared to the much lower 294 kJ/mol for Al). These target materials were then evaporated onto the SiO_2 substrates and the thicknesses monitored via the thickness monitor. The parameters programmed into the thickness monitor for the two elements were as follows. Al: Bulk density = 2.7g/cm^3, Z-ratio = 1.08. Pt: Bulk density = 21.4 g/cm^3, Z-ratio = 0.245. The order in which these films were deposited was: SiO_2-substrate/Al film/Pt film. The various thicknesses of the Pt and Al layers (resulting in different Pt-Al binary thin film compositions) are listed in table 2.

8.1.4) Annealing of the thin films

After the Al and Pt thin films were deposited onto the SiO_2 substrates the samples were placed inside the Lindberg-vacuum-furnace. The furnace was evacuated to a pressure of between 10^{-6} to 10^{-7} Torr. The Pt-Al binary thin films were then annealed at various annealing times and temperatures as listed in Table 2.

After removing the samples from the vacuum furnace adhesion problems rendered most of these samples useless. The moment that the samples were exposed to the atmosphere the thin film layers (Al and Pt) peeled off from the SiO_2 substrate rendering most of the samples useless for depth profiling. The thin films listed in Table 2, however, had no adhesion problems. However the oxide barrier did play a detrimental role. It was observed that Al affinity to the underlying oxide layer caused it to diffuse rapidly into the SiO_2. This resulted in the original composition (reported in Table 2) ***being altered***. Consequently the results reported here focus only on the following three systems: $Pt_{25}Al_{75}$, $Pt_{55}Al_{45}$ and $Pt_{63}Al_{37}$. There was a lowering of the Al concentration due to the loss of the Al into the oxide. This, inversely, leads to an increase in the Pt concentration.

Composition	Annealing temperatures (°C)	Annealing times at each temperature (min)	Pt thickness (Å)	Al thickness (Å)
$Pt_{25}Al_{75}$	350, 400, 500, 550	49, 16, 4	500	1649
$Pt_{30}Al_{70}$	350, 400, 500, 550	49, 16, 4	500	1283
$Pt_{35}Al_{65}$	350, 400, 500, 550	49, 16, 4	500	1020
$Pt_{50}Al_{50}$	350, 400, 500, 550	49, 16, 4	500	550

Table 2: Matrix of prepared thin film samples.

.

8.1.5) Characterisation of the thin films

The thin films obtained after annealing were characterized with the PHI 700 nano-probe. Depth profiles as well as elemental micrographs were obtained. The following parameters were used during the measurement of the thin films:

- Electron gun: Beam voltage = 10 kV
  Filament current = 2.34 A
  Beam current =10 nA
  Emission current = 246.3 μA
- Ion gun: Emission Current = 15 mA
  Raster Area = 2 × 2 mm
  Beam Voltage = 2 kV
  Ion beam current = 2 μA
  Sputter Rate for SiO_2: 8.5 nm/min
- Lenses: 1st condenser = 74%
  2nd condenser = 73.85%
  Objective = Bend 3.45%
- Energy Analyzer: Time constant: 50 ms per step; 1 eV per step; 10 sweeps
- Multiplier voltage: 2200 V

8.2) Simulation Setup

In order to calculate the expected structures for the various thin films a matrix of 320 × 320 constituents were setup. Both larger and smaller matrices could be created, but it was found that this matrix size gives accurate results without compromising on an increase in calculation time. This matrix consisted of two different elements: Pt and Al. The ratios of these two different elements are simply the concentration of the Pt and Al in the experimental thin films. An appropriate nearest neighbour and next nearest neighbour list was then setup. This was done by creating an algorithm to find each atoms neighbour and nearest neighbour in the entire matrix. This list was stored. It is used during the calculation of the "microscopic" chemical potential as discussed in section 6.8 of chapter 6.

The main goal of the CPMC-model is to minimize the energy across the entire matrix. Thus the derivative of the following equation was set equal to 0:

$$\mu_A = \mu_0^A + RT \ln X_A + \Omega_{AB}(1 - X_A)^2 \tag{5.68}$$

Thus:

$$\frac{\partial \mu_A}{\partial X_A} = 0 \tag{5.69}$$

Then:

$$\begin{aligned} \frac{\partial \mu_A}{\partial X_A} &= 0 + \left[0(1 - X_A)^2 + 2\Omega_{AB}(1 - X_A)\right] + \frac{RT}{X_A} \\ &= 0 + [0 + 2\Omega_{AB} - 2\Omega_{AB}(X_A)] + \frac{RT}{X_A} \\ &= 2\Omega_{AB} - 2\Omega_{AB} X_A + \frac{RT}{X_A} \end{aligned} \tag{5.70}$$

As an example consider $X_A = 0.75$. Which Ω_{AB} will minimize the chemical potential?

$$
\begin{aligned}
0 &= 2\Omega_{AB} - 2\Omega_{AB}(0.75) + \frac{RT}{0.75} \\
\Omega_{AB} &= (22.17)T
\end{aligned}
\tag{5.71}
$$

with T in Kelvin.

Thus, for each concentration X_A, across all possible temperatures, T, a Ω_{AB} value can be found that minimized the energy, μ. These Ω_{AB} values are then used in order to simulate the binary thin film diffusion and phase formation.

Figure 1 shows the various values for the interaction energy and annealing temperature used in the simulations for each of the different Pt concentrations. The results of these simulations and the experimentally measured depth profiles and elemental maps are presented in section 8.3.

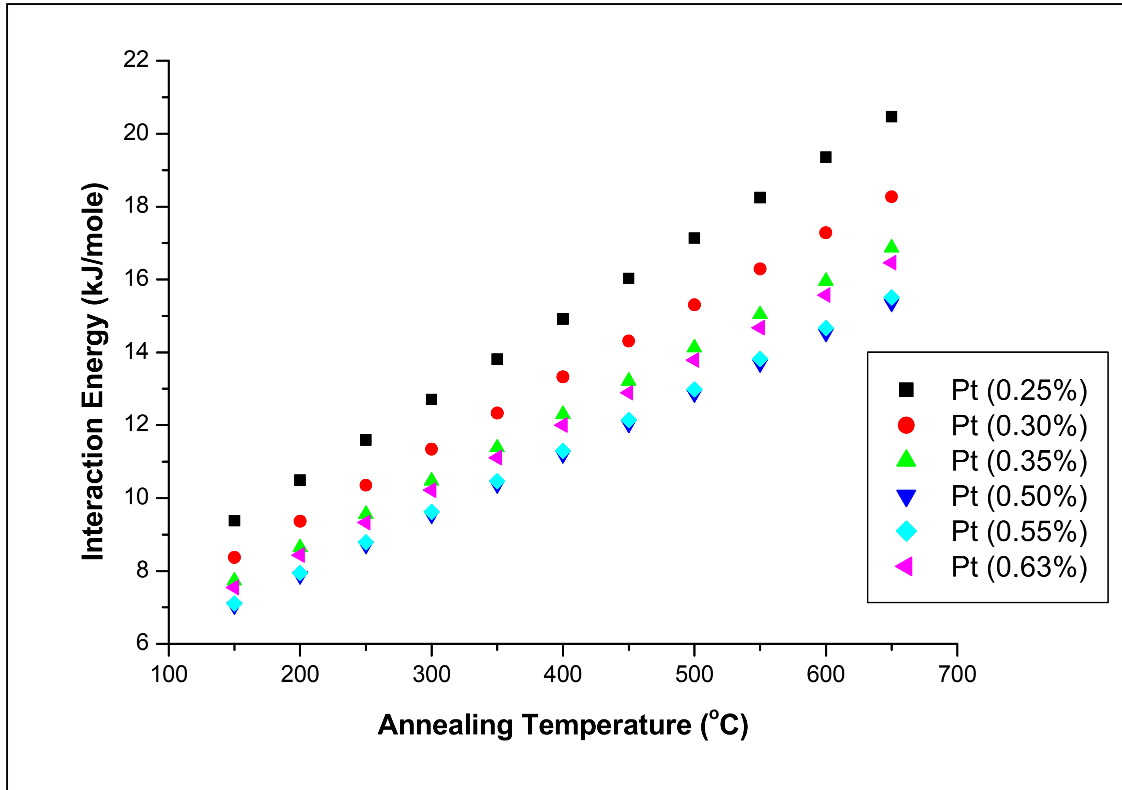

Figure 1: The various values for the interaction energy and annealing temperature used in the simulations are shown for each of the different Pt concentrations.

8.3) Results and Discussion

First a **very general** comparison is made between microstructures found in literature and CPMC simulated microstructures to see if the proposed CPMC has any value. Consider a predicted microstructure for an alloy at the solidification point. For example consider the Pb/Sn system. Pb has an FCC crystal structure and Sn has a tetragonal crystal structure. In specific it has a diamond cubic structure which is in the Fd3m space group, which follows the face-centered cubic bravais lattice. This can be viewed as a stretching of the face-centered cubic lattice. Thus both these elements follow an FCC packing in 2 dimensions. This is similar to the conditions of the software and crystal packing of the CPMC model, as it will have the same number of nearest neighbours and next nearest neighbours as the Pt/Al system for which the software was designed.

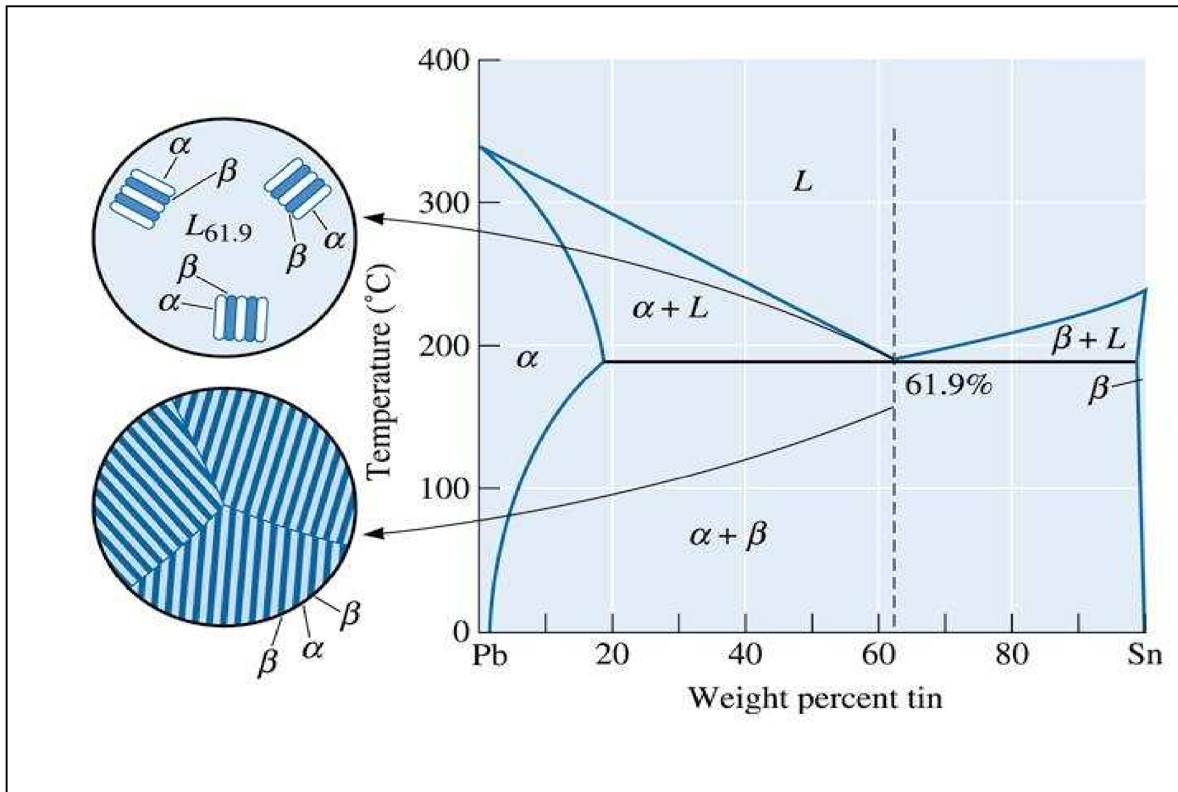

Figure 2: Solidification and microstructure of the alloy Pb-61.9% Sn [3].

Therefore the model can (in general) be used to for the Pb/Sn system. In the Pb/Sn system (at solidification) a lamellar structure consisting of two solid phases in intimate contact is formed, as can be seen from Figure 2 [3].

By considering the diffusion of a bulk Al, 1000 Å Pt thin film at the solidification point, the predicted microstructure by the CPMC simulation leads to the same lamellar structure as can be seen from Figure 3. This can be compared to a photomicrograph [3] as seen in Figure 4.

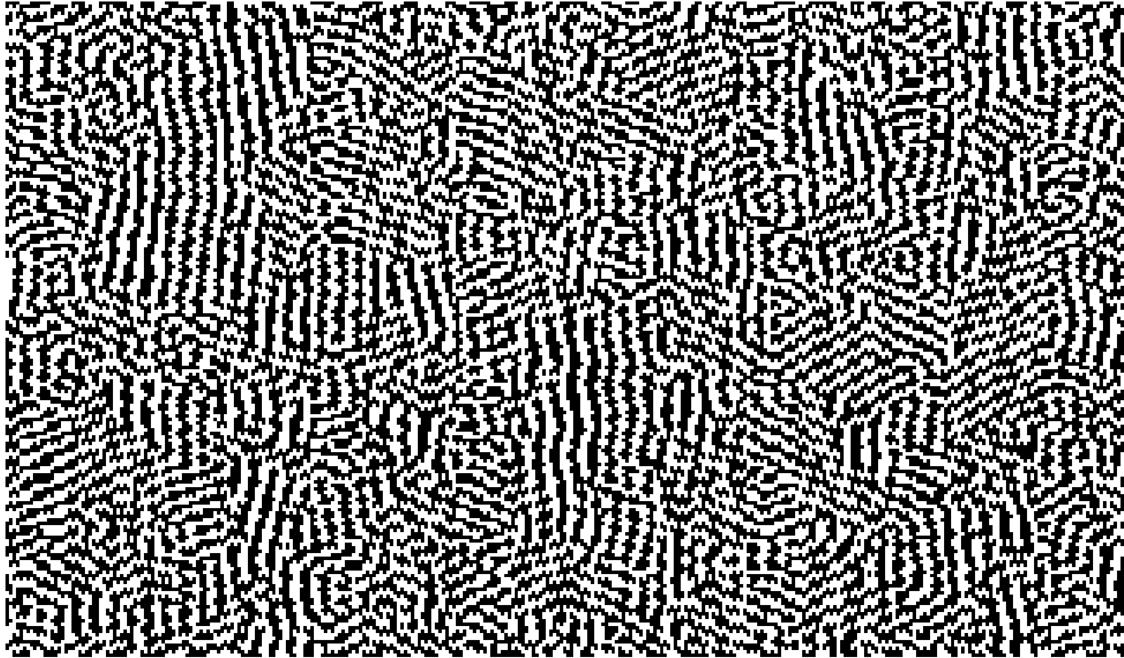

Figure 3: Lamellar structure as predicted by CPMC for a bulk Al, 1000 Å Pt thin film system.

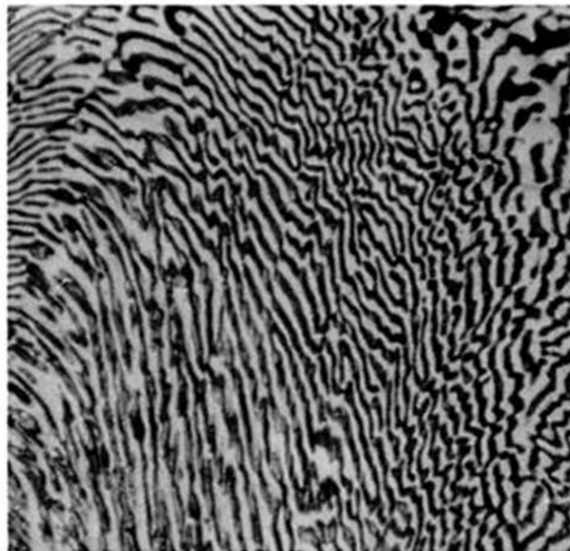

Figure 4: Photomicrograph of the Lead-Tin microstructure [3].

From this it can be seen that the predicted microstructure compares considerably well with the measured microstructure at the solidification point. By now varying the interaction parameter the following microstructures is predicted:

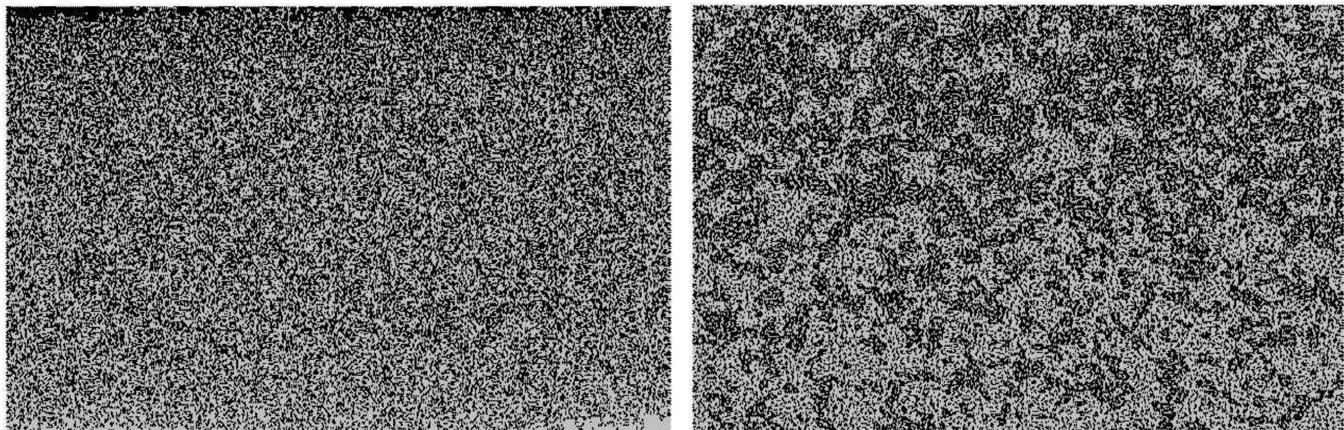

Figure 5: Ω_{12} = 7 kJ/mole (left) and Ω_{12} = 7.5 kJ/mole (right).

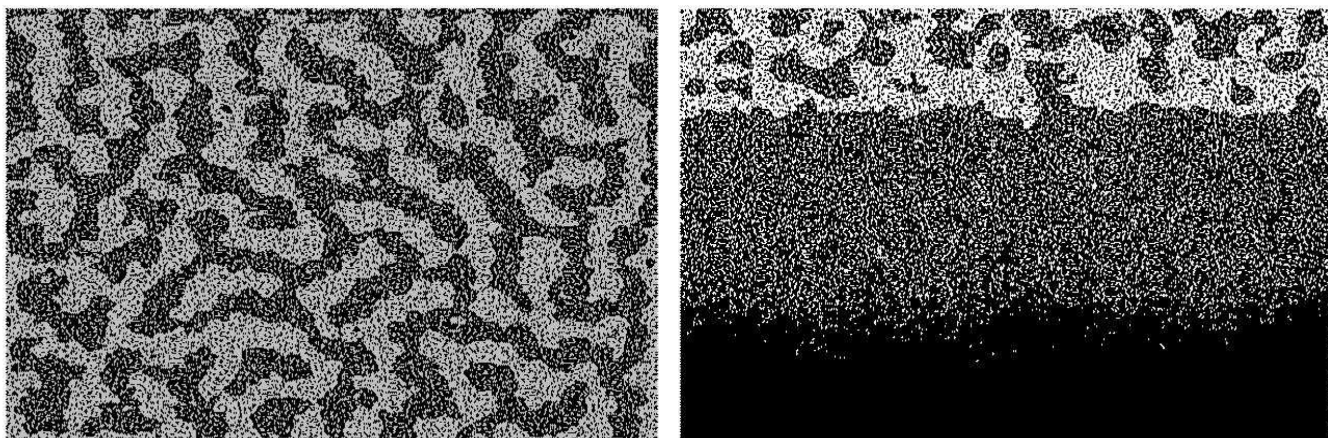

Figure 6: Ω_{12} = 7.8 kJ/mole (left) and Ω_{12} = 8.0 kJ/mole (right)

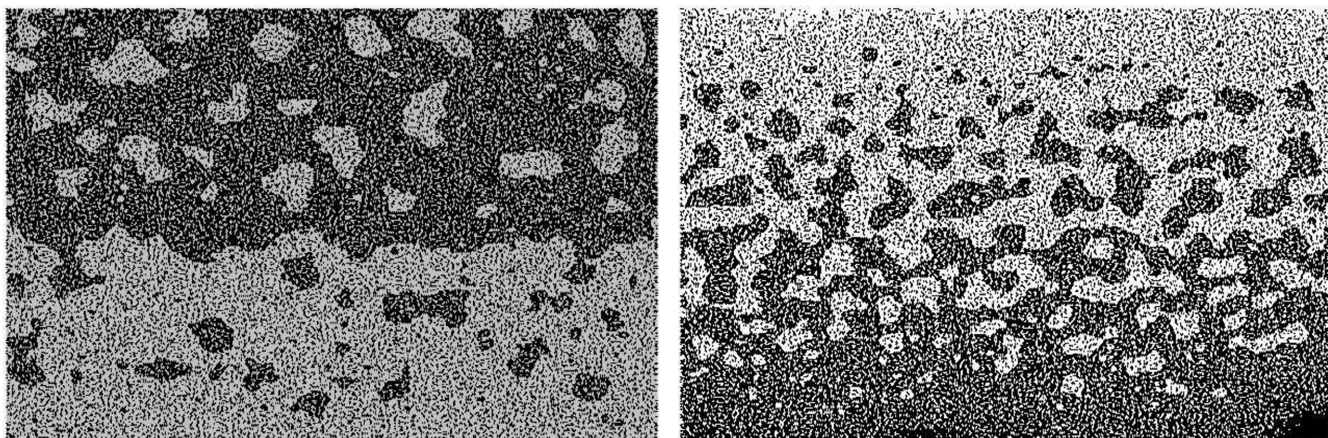

Figure 7: Ω_{12} = 8.4 kJ/mole (left) and Ω_{12} = 8.5 kJ/mol (right).

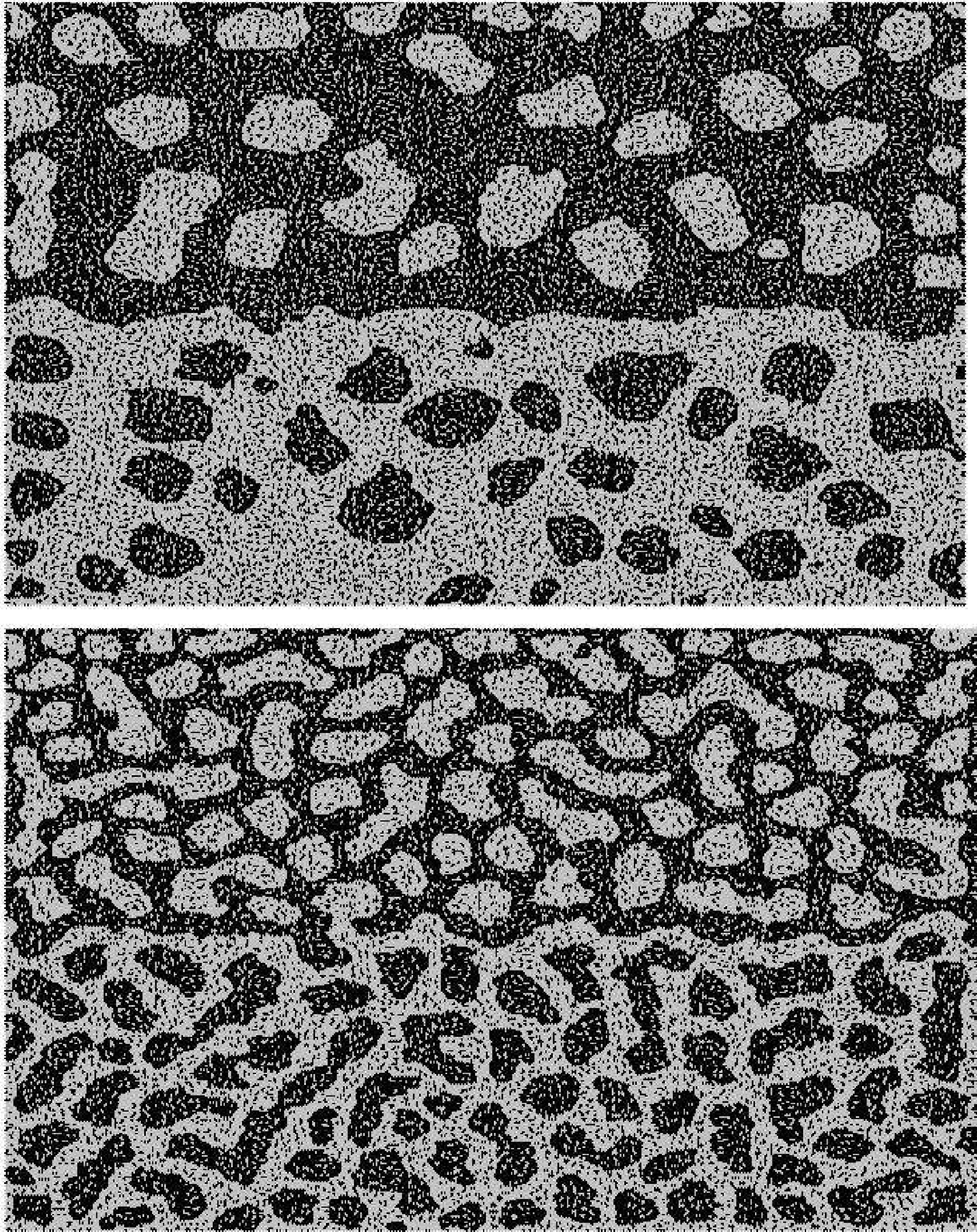

Figure 8: Ω_{12} = 9 kJ/mole (top) and Ω_{12} = 9.5 kJ/mole (bottom).

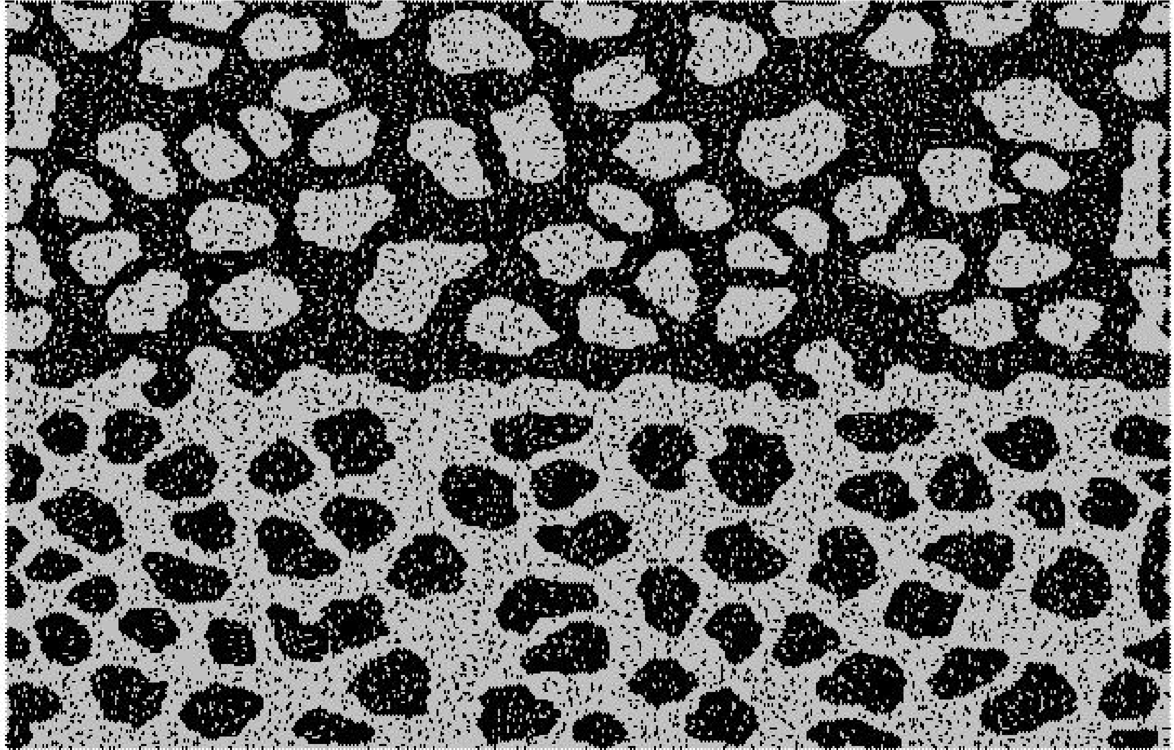

Figure 9: Ω_{12} = 10.5 kJ/mole.

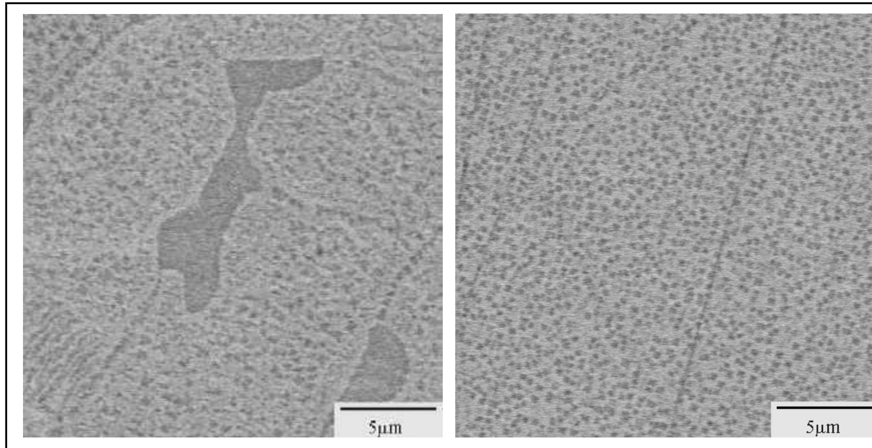

Figure 10: SEM micrographs, in back-scattered electron (BSE) mode, of two types of two-phase alloys. (Left) With primary Pt_3Al (dark contrast) in a fine micture of (Pt) and Pt_3Al; (Right) Fine mixture of (Pt) and Pt_3Al [4].

This was compared to the Scanning Electron Micrographs for the $Pt_{81.5}$:$Al_{11.5}$:$Ru_{2.5}$:$Cr_{4.5}$ (left) and Pt_{84}:Al_{11}:Ru_{2}:Cr_{3}(right) as shown in Figure 10 [4]. It is concluded that an interaction energy value between 8 kJ/mole and 9.5 kJ/mole compares well with the measured results.

The focus now turns to the PVD-prepared thin films. A comparison between the simulated depth profile and microstructure is made with the experimental measured profiles and structures. It was one of the aims of this study to create a model to predict how the microstructure of the thin films (under various annealing times and temperatures) would change during diffusion. A comparison between the simulated depth profile and microstructure is therefore made with the experimental measured profiles and structures to test the validity of the simulated model.

Figure 11 shows a screenshot of the software that was designed. The red colour depicts Pt and the blue colour depicts Al. This simulation was done for a binary thin film of 25 at.% Pt and 75 at.% Al. In this case the red colour represents Pt and the blue colour represents Al. A simulated depth profile can be seen in the top right hand corner of the screenshot. The red line represents Pt and the blue line Al. The x-axis represents matrix depth and the y-axis represents the element concentration. It is important to note that the simulation does not include any substrate effects. Therefore (since there is only a Pt and Al layer) the concentration of Al goes to 100% when the depth profile at the bottom of the matrix is calculated. Likewise the Pt concentration goes to 0% when the depth profile at the bottom of the matrix is calculated.

Figures 12 and 13 are the measured depth profiles, without the impurities, for an experimentally prepared thin film of the same composition (prepared at 400 °C for 16 minutes). If the general shape of the predicted depth profile and the experimental profiles in Figures 12 and 13 are compared the following is noteworthy: although the predicted and measured results to not correlate perfectly, a similar trend can clearly be seen. In both cases (the simulation and the experiment) the top Pt layer has a concentration of about 70 at.%. It then crosses over to about 25 to 20 at.% Pt. At this point in the thin-film system the Al concentration has increased to about 75 at.% to 80 at.%. It should be pointed out again that this is not an absolute comparison being made, but the general trend of the depth profile is compared with the simulation.

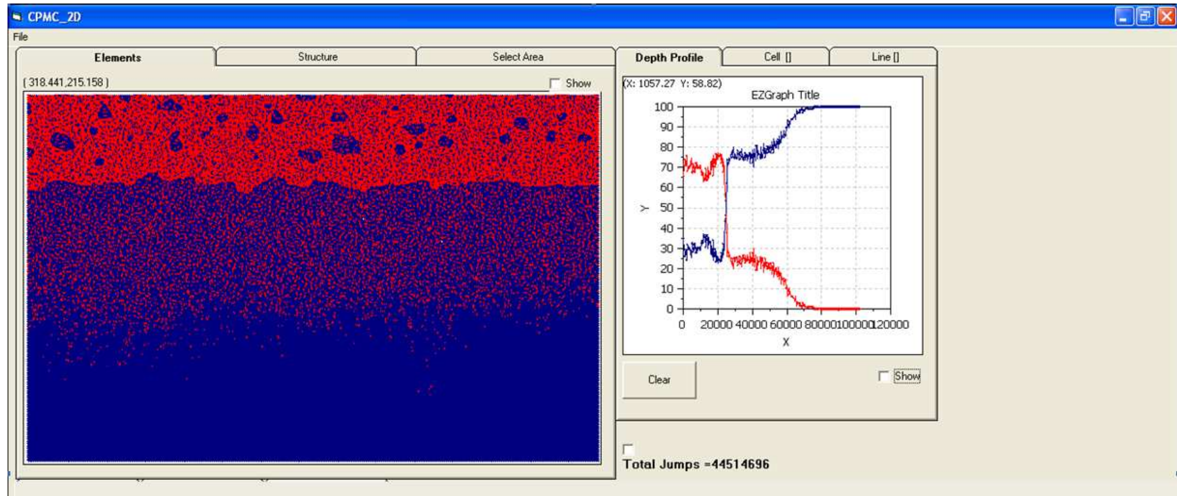

Figure 11: A screenshot of the designed software program showing the predicted microstructure and depth profile for Pt 25 at.% and Al 75 at.%. Red represents Pt and blue represents Al.

From Figure 13 the influence of the oxide layer (after 25 minutes on the depth profile) on the above lying Al layer can be seen. Some of the Al diffused into the Si - oxide layer, decreasing the amount of Al available for Pt to diffuse and interact with in the Pt-Al-thin film system. Thus, the originally prepared composition changed during the annealing process as some of the Al was lost to this oxide layer. This left the composition as presented here: $Pt_{25}Al_{75}$. (This concentration ratio was obtained by comparing the experimentally measured depth profiles and elemental maps with the simulated profiles and maps. Since the simulated concentration ratio was known (the concentration is an input parameter in the model) it is concluded that if a correlation between measured data and theoretical data exist, the concentration ratios must be the same.) The oxide played a detrimental role in all the prepared samples.

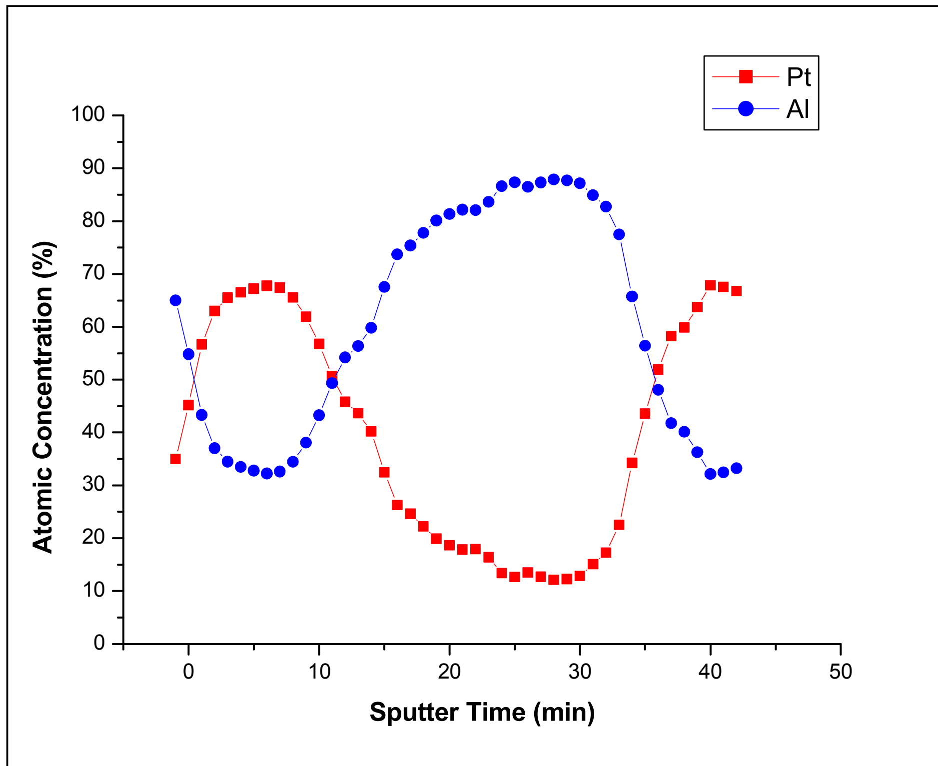

Figure 12: Pt and Al depth profile for $Pt_{25}Al_{75}$ thin film annealed at 400 °C for 16 min.

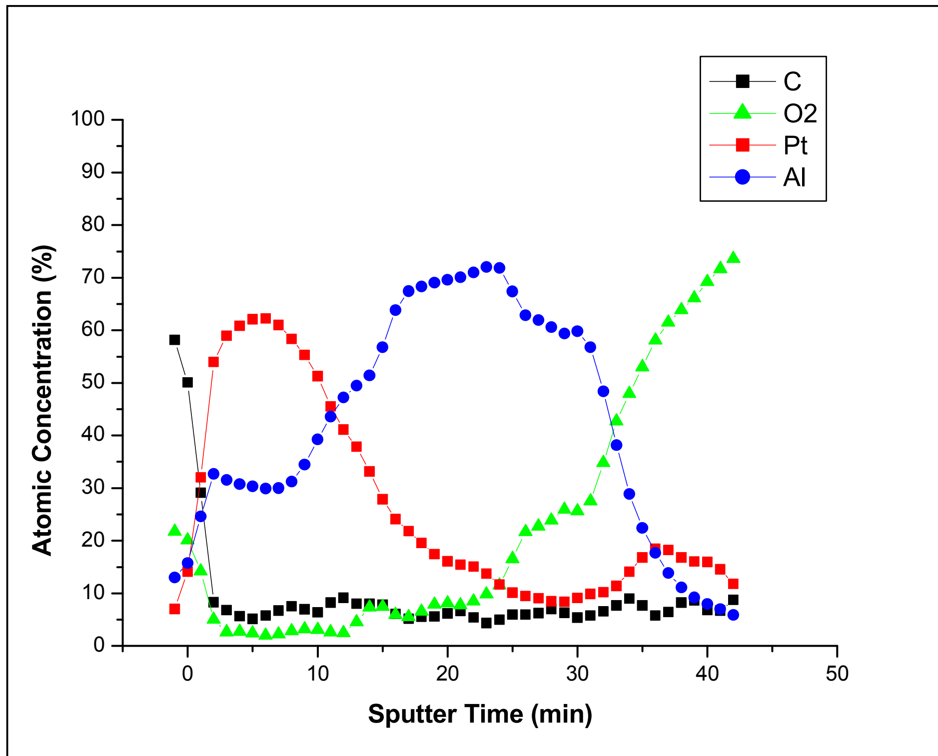

Figure 13: Depth profile for $Pt_{25}Al_{75}$ thin film including impurities annealed at 400 °C for 16 min.

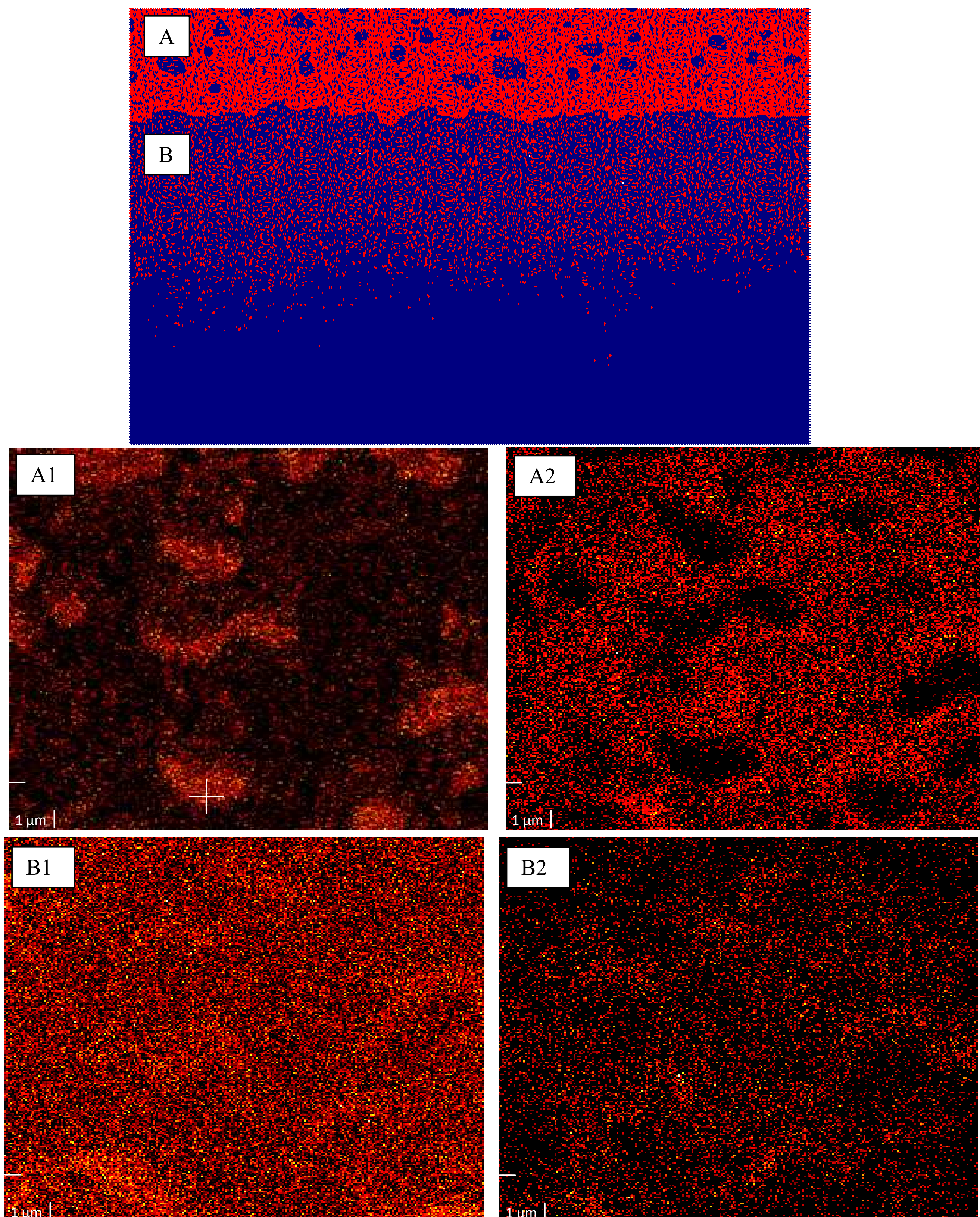

Figure 14: $Pt_{25}Al_{75}$. The top image shows the predicted structure. A1 and B1 are Al elemental maps. A2 and B2 are Pt elemental maps. The elemental maps A and B correspond to the areas A and B on the simulation. Pt is represented by the colour red and Al by the colour blue.

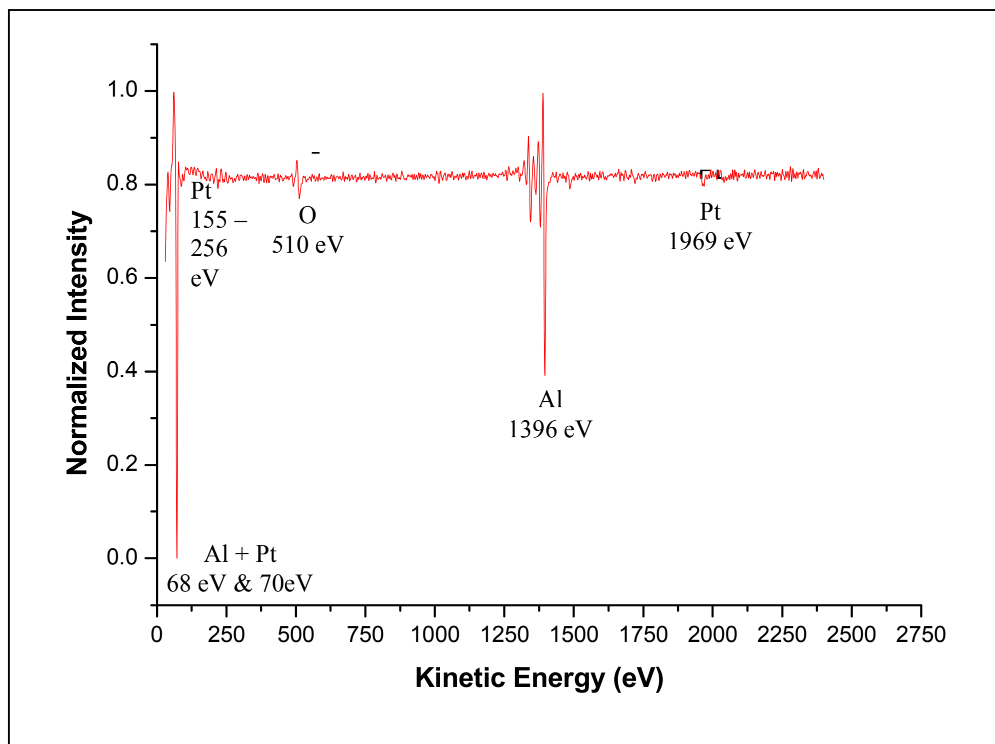

Figure 15: AES spectrum of one of the Al-rich particulates. The white cross-hair in Figure 14 shows the position of the nanometer electron beam for the AES spectrum.

Figure 14 shows a comparison between the predicted structure and the elemental maps. For the $Pt_{25}Al_{75}$ sample it was observed that Al-particulates in the order of a few micrometers (1 to 6 µm) nucleate in the top part of the prepared sample (A form Figure 14). Figure 15 shows an AES spectrum of one such *Al-rich particulate*. In Figure 15 two large peaks at 1396 eV and 68 eV can be seen as well as a smaller one at around 510 eV. Smaller peaks from 70 eV to 275 eV as well as at 1969 eV is also visible. The two large peaks at 1396 eV and 68 eV are both Al peaks. The peak at 510 eV is an O peak. The smaller peaks from 70 eV to 275 eV are Pt. The smaller peak at 1969 eV is also a Pt peak Pt has an Auger peak at 70 eV also. For this reason the possibility exists that the peak at around 68 eV can be an overlapping peak (overlapping with the Pt - 70 eV peak). This means there is a possibility that both Al and Pt can contribute to the intensity of that particular peak (the electron count). However Al is the only contributor to the peak at 1396 eV. Since the Pt peak at 1969 eV is extremely small (barely visible in Figure 15) it is concluded that the **major** contributor to the peak at 68 eV on the spectrum in Figure 15 is Al (although there would be some Pt contribution to that peak also).

On average these particulates have the same composition as the fine mixture of Pt and Al in the B part of Figure 14. This can be seen more clearly when the time-evolution of this system is considered (which will be done in the next section). At a later stage (in the evolution of this system) it is observed that these particulates grow in size until only a thin network of a Pt matrix surrounds it (Figures 18 an 22 of section 8.3 and Figure 38 of section 8.4). This composition can be seen from a 20 minute sputter time - spectrum (Figure 16). (In this spectrum the Al peaks are still at 70 eV (overlapping with Pt) and at 1396 eV. But for 20 minutes sputter time Pt is also present and can be seen from the small peaks at 1969 eV and 2048 eV). This is so because the system tends to evolve to a state where its energy is minimized and this happens when a homogeneous composition for each subsystem (as described in chapter 6) is reached. This in turn allows for the entire crystal to have a homogenous composition. However it is interesting to note what happens to the system *before* this state (of minimization of energy) is reached. That is: what happens if the thin films are not annealed for an *indefinite* period of time, but the annealing, and hence the diffusion, is *interrupted*? Figures 14 and 22 show two such interruptions in the diffusion process. The nucleation of the Al particulates is seen in Figure 14. The increase in size and thus the growth of these Al particulates are seen in Figure 22.

Figure 17 shows an Auger spectrum after 25 minutes of sputtering. The presence of the O peak clearly indicates the presence of the detrimental oxide layer. The increase in the intensity of the oxygen 510 eV peak (compared to the previous Auger spectrum of Figure 15) is clearly visible. Also note the decrease in the amount of Pt present (the decrease in intensity in the Pt peaks around 1969 eV and 2048 eV). This shows that SiO_2 is not the ideal substrate to use for these experiments and an alternative should be found in the future. However, by taking this into account, a comparison can still be made between the simulated results and the measured results. It should just be carefully noted what the exact composition of the experimentally measured thin films are because it would differ from the PVD – prepared composition.

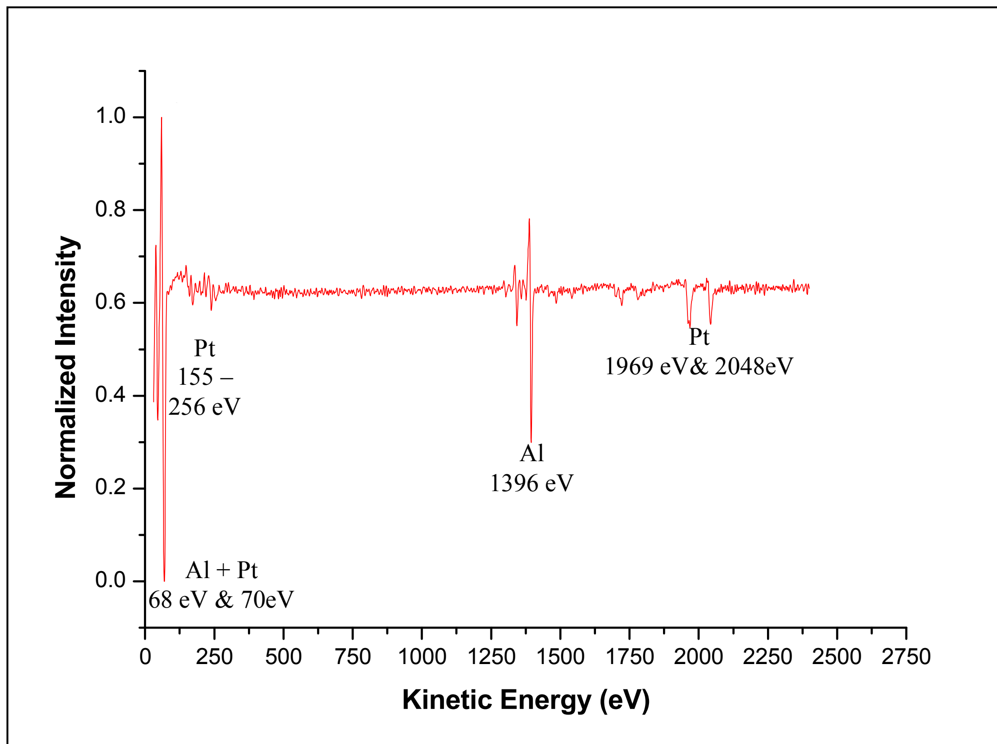

Figure 16: 20 minute sputter time, corresponding to area B of Figure 20.

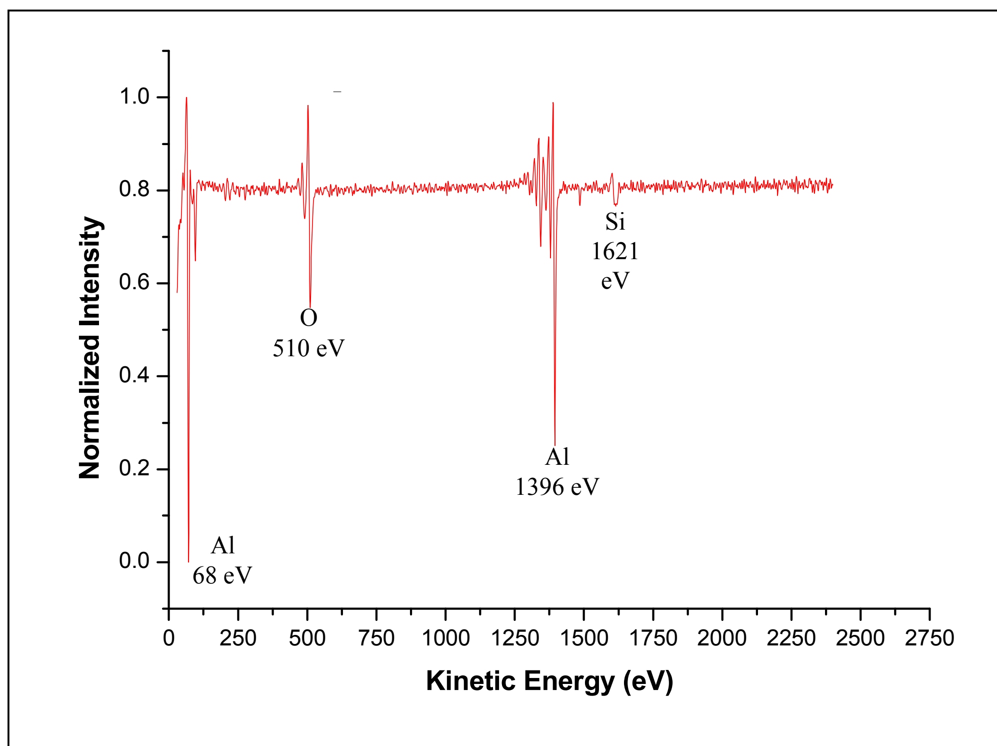

Figure 17: 25 minute sputter time. The presence of the detrimental aluminium oxide can be seen.

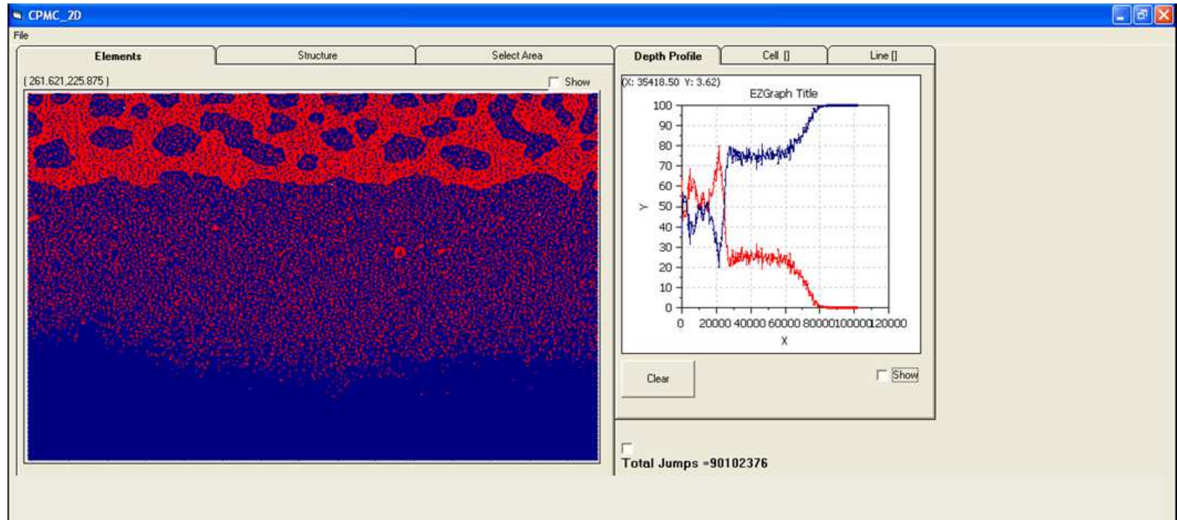

Figure 18: A screenshot of the designed software program showing the predicted microstructure and depth profile for Pt 25 % and Al 75%. This was for a later stage in the time-evolution of the system than that of Figure 2. Red represents Pt and blue represents Al.

From Figure 18 a time lapse (compared to the system discussed above) for a Pt 25 at.%, Al 75 at.% sample can be seen. This time lapse is quantified in terms of "total jumps" which indicate the total amount of Monte Carlo jumps that have occurred. The growth in size of the Al-particles is clearly observable. From this it is clear that as the system tends to form a homogenous composition, more of the surrounding Pt-rich areas are being diffused into the surrounding Al. This would lead to a solid solution of the Pt into the Al. Figures 20 and 21 show the measured depth profiles for the sample heated at 400 °C for 49 minutes. Compare this to the simulated depth profile (top right hand graph in Figure 18). This time the correlation is not as clearly seen as is desired. None the less a similar trend can be observed: the simulation predicts a Pt concentration percentage of about 60 at.% which should diminish to 25 at.% in the Al layer. The Al is 25 to 30 at.% in the Pt-layer and then increase to 70 at. %. This is very general and thus the comparison here is not absolute.

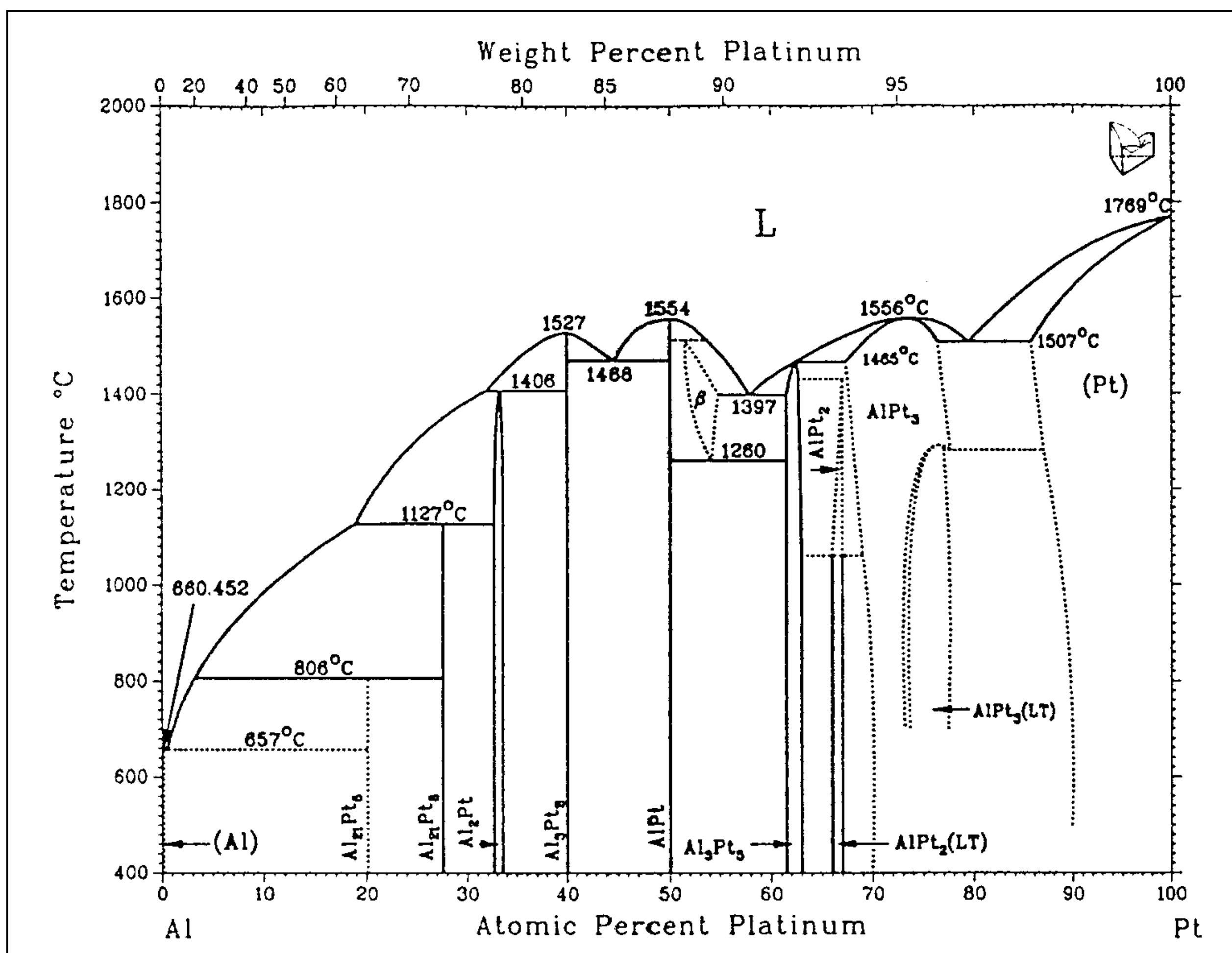

Figure 19: Pt-Al phase diagram. Notice the Pt_8Al_{21}- phase that forms between 20 and 27 at.% Pt.

The effect of the oxide can, once again, clearly be seen as a large percentage of Al diffused into the oxide (Figure 21). Figure 22 shows a comparison between the predicted structure and the experimentally measured elemental maps. The increase in size (compared to the previous system) of the nucleated Al-particulates are seen. Also the elemental maps and the predicted structure compare well and thus a good correlation can be seen.

Figure 23 shows a XRD spectrum for the thin film discussed above, after the background has been subtracted. The positions of the peaks have been labelled on the spectrum. For comparison, the peak positions of Pt_8Al_{21} are also shown (as found in the literature). On the Pt-Al phase diagram (Figure 19) it is clear that the phase Pt_8Al_{21} should form between Pt 20 at.% and Pt 27 at.%. Thus for the composition of this thin film ($Pt_{25}Al_{75}$) it is concluded that the phase Pt_8Al_{21} has formed.

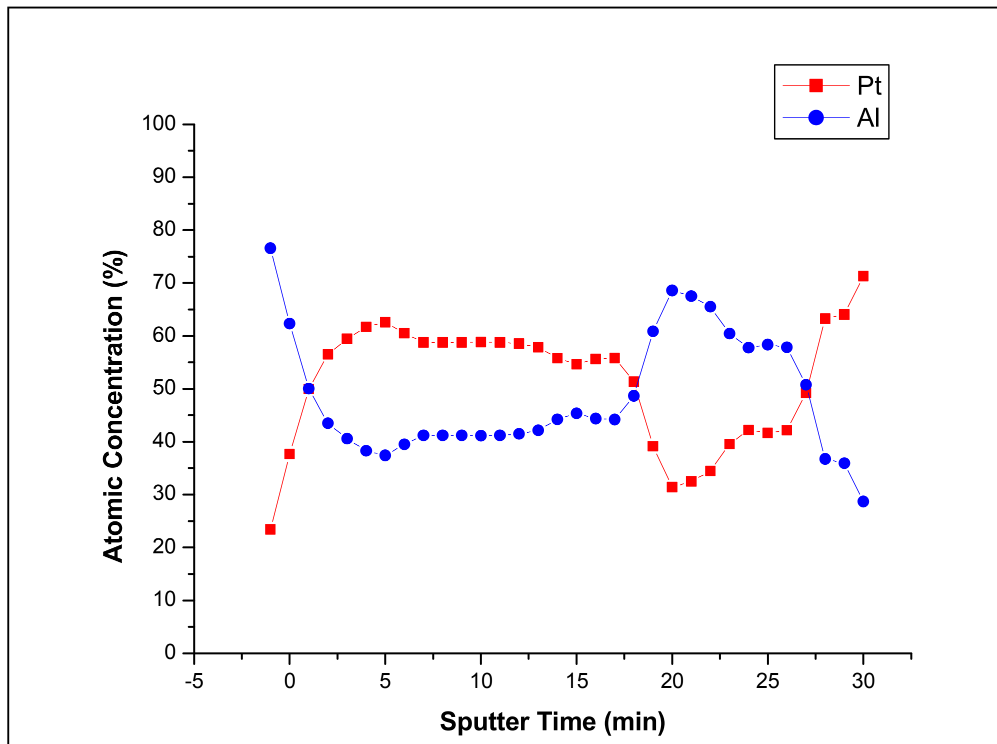

Figure 20: Pt and Al depth profile for $Pt_{25}Al_{75}$ thin film annealed at 400 °C for 49 min.

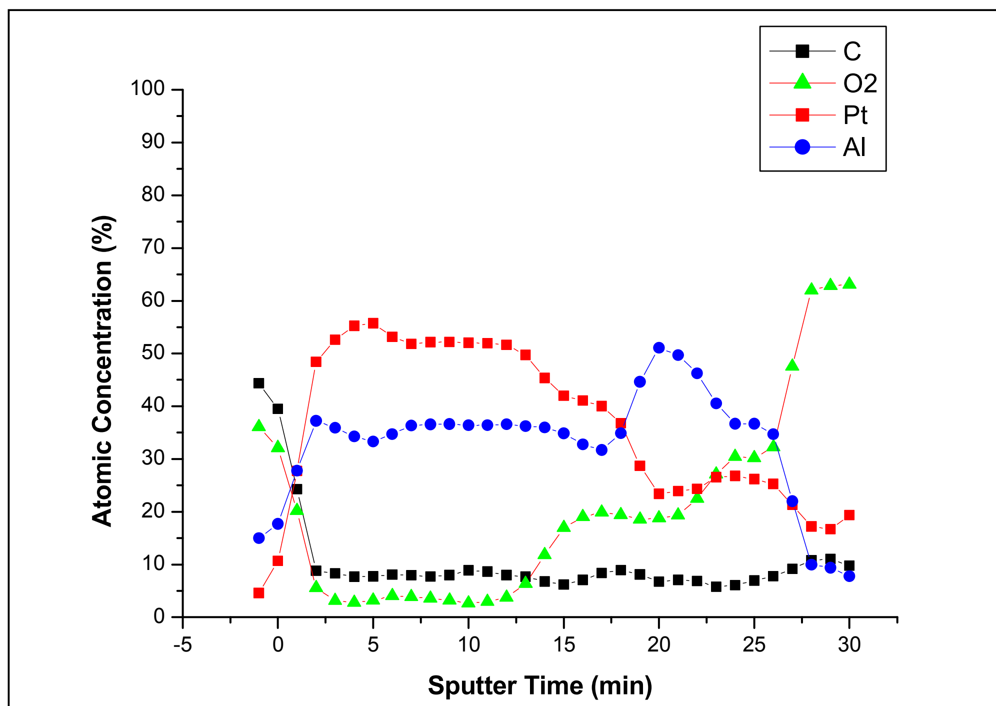

Figure 21: Depth profile for $Pt_{25}Al_{75}$ thin film including impurities annealed at 400 °C for 49 min.

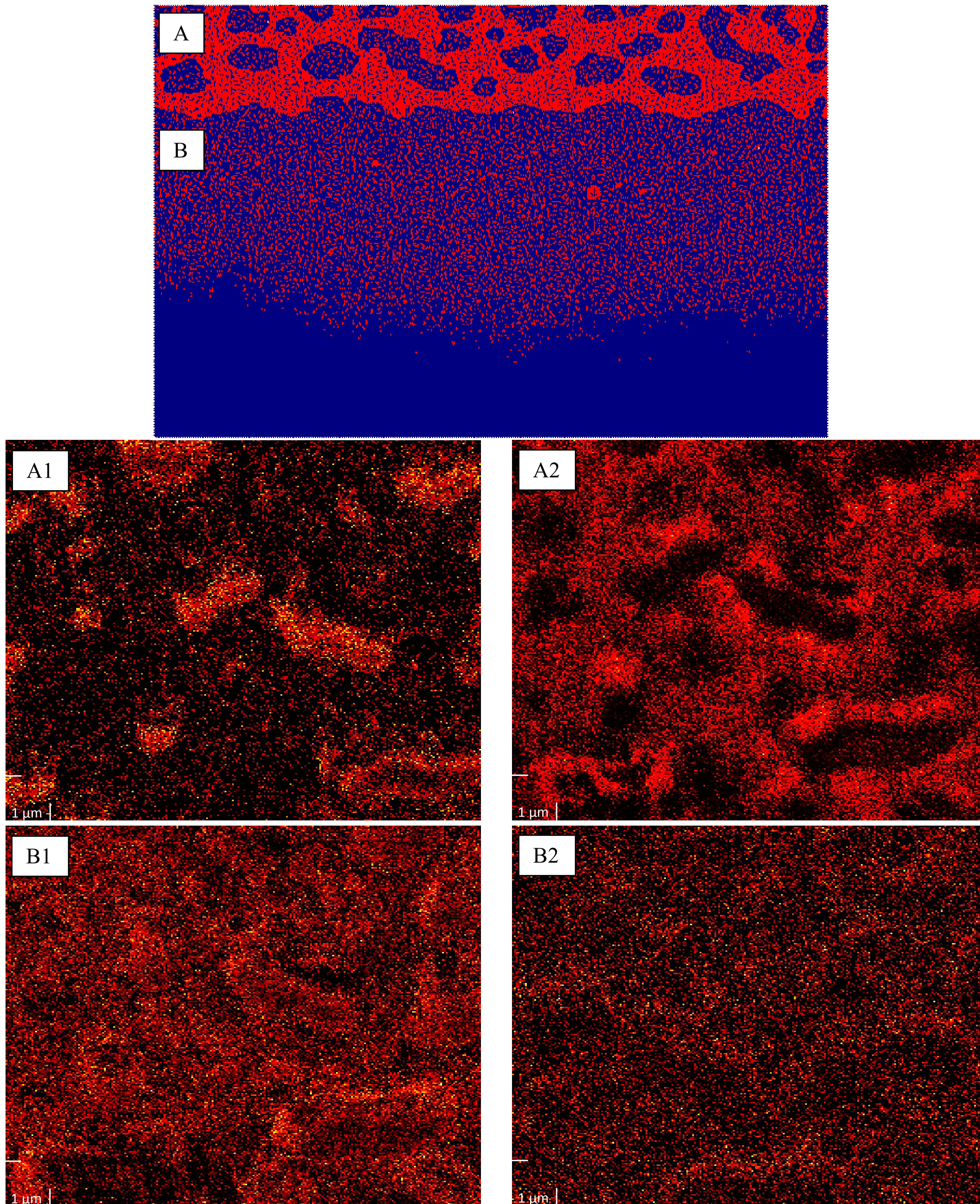

Figure 22: $Pt_{25}Al_{75}$. The top image shows the predicted structure. A1, B1 are Al elemental maps. A2, B2 are Pt elemental maps. The elemental maps A and B correspond to the areas A, B on the simulation. This system was for a later stage in the time evolution than the previous one.

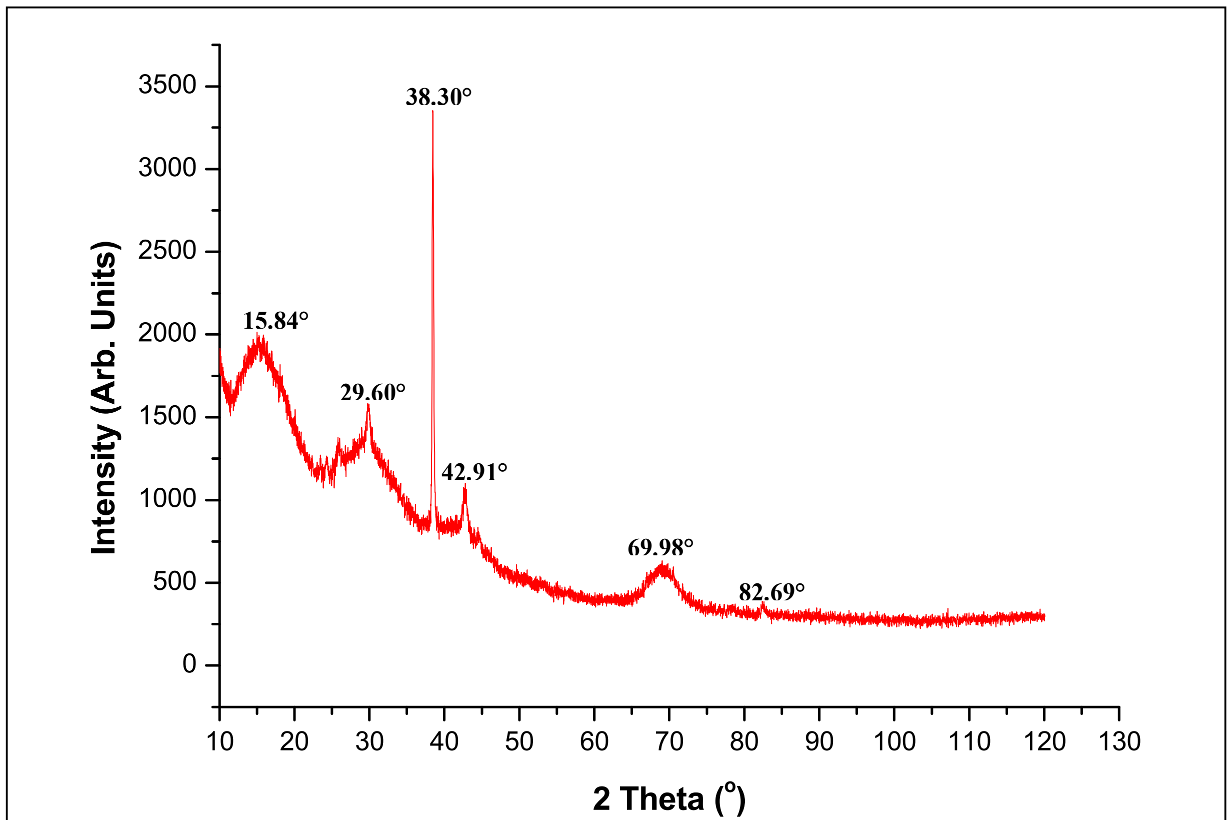

Pt8 Al21
Aluminum Platinum
Ref: Range, K.-J., Universitat Regensburg, Universitatsstrasse, West Germany, Private Communication, (1988)

Fixed Slit Intensity ->
74.78
0 15 30 45 60 2θ°

2θ	Int-f	h	k	l	2θ	Int-f	h	k	l	2θ	Int-f	h	k	l
17.398	31	2	1	1	41.791	136	6	0	0	53.353	44	2	0	6
19.366	53	2	2	0	42.919	57	4	4	2	53.621	86	5	3	4
22.189	173	3	0	1	43.134	287	4	3	3	53.761	50	6	4	2
25.611	590	2	2	2	43.249	47	6	1	1	53.943	95	6	3	3
25.955	432	1	0	3	43.914	91	4	0	4	55.744	24	4	3	5
26.132	999	3	2	1	44.168	148	6	2	0	57.962	41	7	4	1
27.416	402	3	1	2	45.073	231	3	3	4	59.186	19	4	0	6
29.432	179	2	1	3	45.227	308	2	1	5	59.586	20	8	0	2
29.609	222	4	1	1	45.462	106	5	2	3	61.449	48	8	2	2
30.836	24	4	2	0	45.592	352	5	4	1	63.452	52	7	4	3
32.304	43	4	0	2	46.207	109	4	2	4	64.951	38	7	3	4
32.559	51	3	0	3	47.487	65	6	2	2	68.590	49	7	2	5
35.476	51	3	2	3	47.812	58	6	3	1	69.987	36	6	2	6
35.636	27	4	3	1	49.849	52	6	1	3	71.768	52	4	3	7
36.386	31	2	0	4	50.761	49	6	4	0	72.211	67	7	6	3
38.159	75	4	1	3	51.726	35	4	1	5	72.947	101	8	6	0
38.304	76	5	2	1	52.041	59	7	2	1	73.741	127	7	4	5
39.223	176	5	1	2	52.611	29	4	4	4	74.780	68	3	1	8
40.297	64	3	1	4	52.754	117	5	5	2					

Figure 23: XRD spectrum for the $Pt_{25}Al_{75}$ thin film. Below is shown the peak positions for the Pt_8Al_{21} phase. The corresponding peaks for the thin film XRD spectra are circled in red.

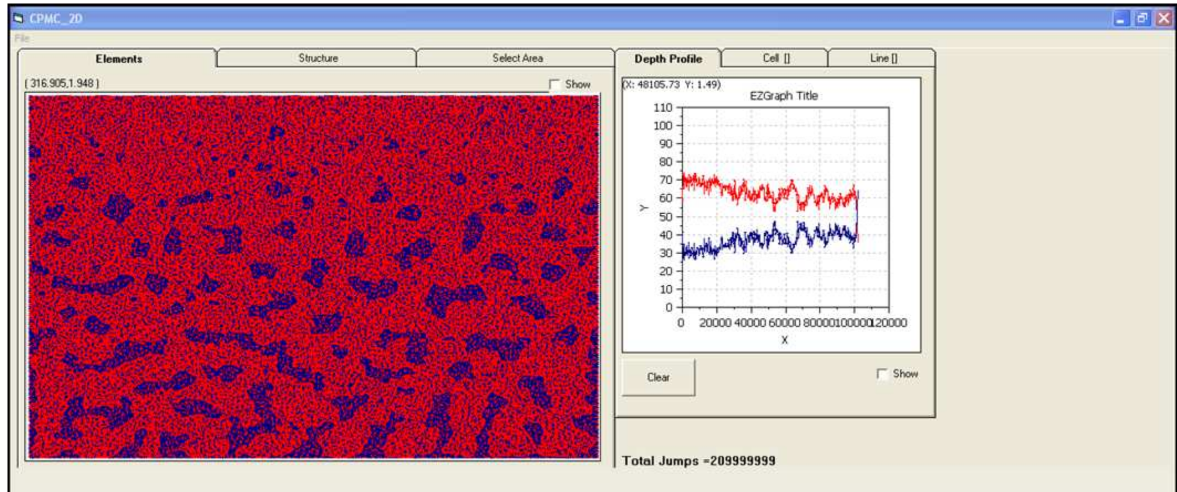

Figure 24: A screenshot of the designed software program showing the predicted microstructure and depth profile for Pt 63 at.% and Al at.37%. Red represents Pt and blue represents Al.

For the $Pt_{63}Al_{37}$ simulation elongated Al-rich areas inside a Pt-rich matrix was observed after some diffusion time. This can be seen from Figures 24 and 27. Unlike in the previous two examples (for the $Pt_{25}Al_{75}$ system) no clear diffusion interface between the Pt and Al could be observed. It is difficult to make a direct comparison between the $Pt_{25}Al_{75}$ samples and the $Pt_{63}Al_{37}$ sample in term of time lapse, since the loss of Al in all these samples into the oxide layer was not quantified. Consider the simulated depth profile (top right hand corner of Figure 24) and the measured one (Figure 25). The Pt and Al are diffused throughout the entire matrix in both these depth profiles. For the simulation the Pt concentration averages around 63 at.% whereas for the measured depth profile the Pt concentration averages to 63 at.% as well. The Al concentration is about 37 at.% in the simulated depth profile and the same holds for the measured one. Figure 26 shows the presence of the oxide layer.

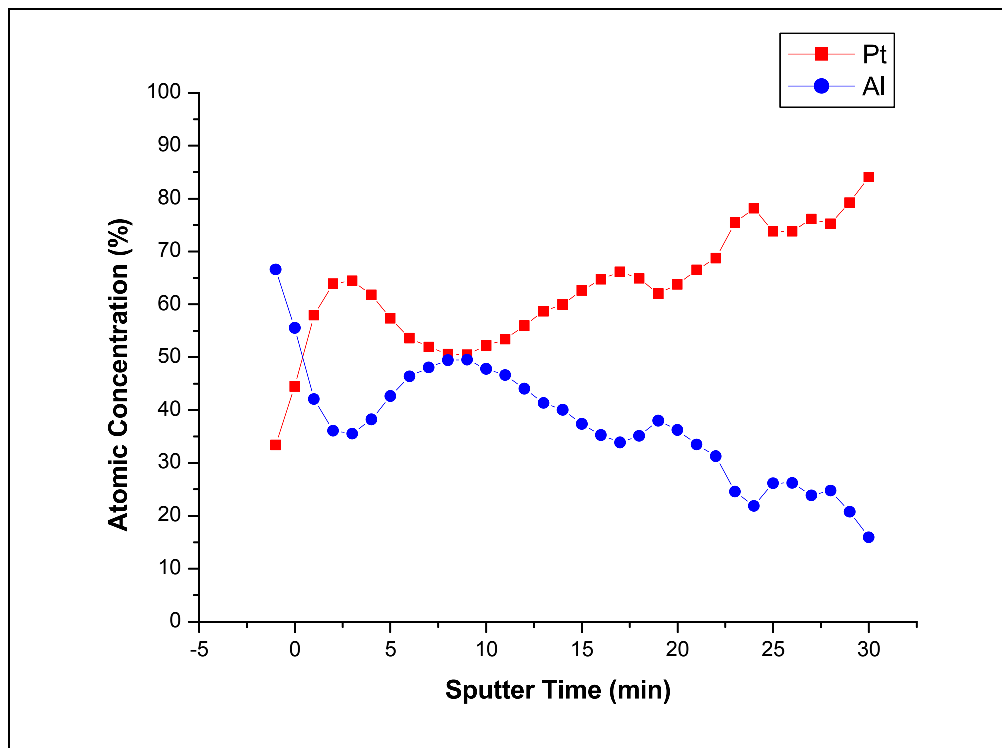

Figure 25: Pt and Al depth profile for $Pt_{63}Al_{37}$ thin film annealed at 400 °C for 16 min.

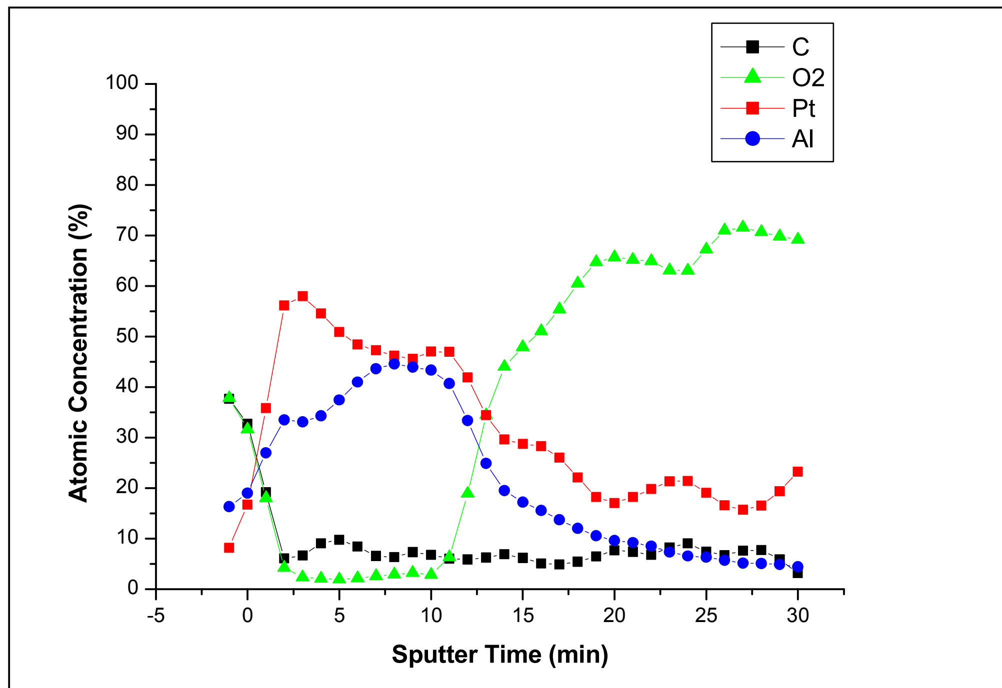

Figure 26: Depth profile for $Pt_{63}Al_{37}$ thin film including impurities annealed at 400 °C for 16 min.

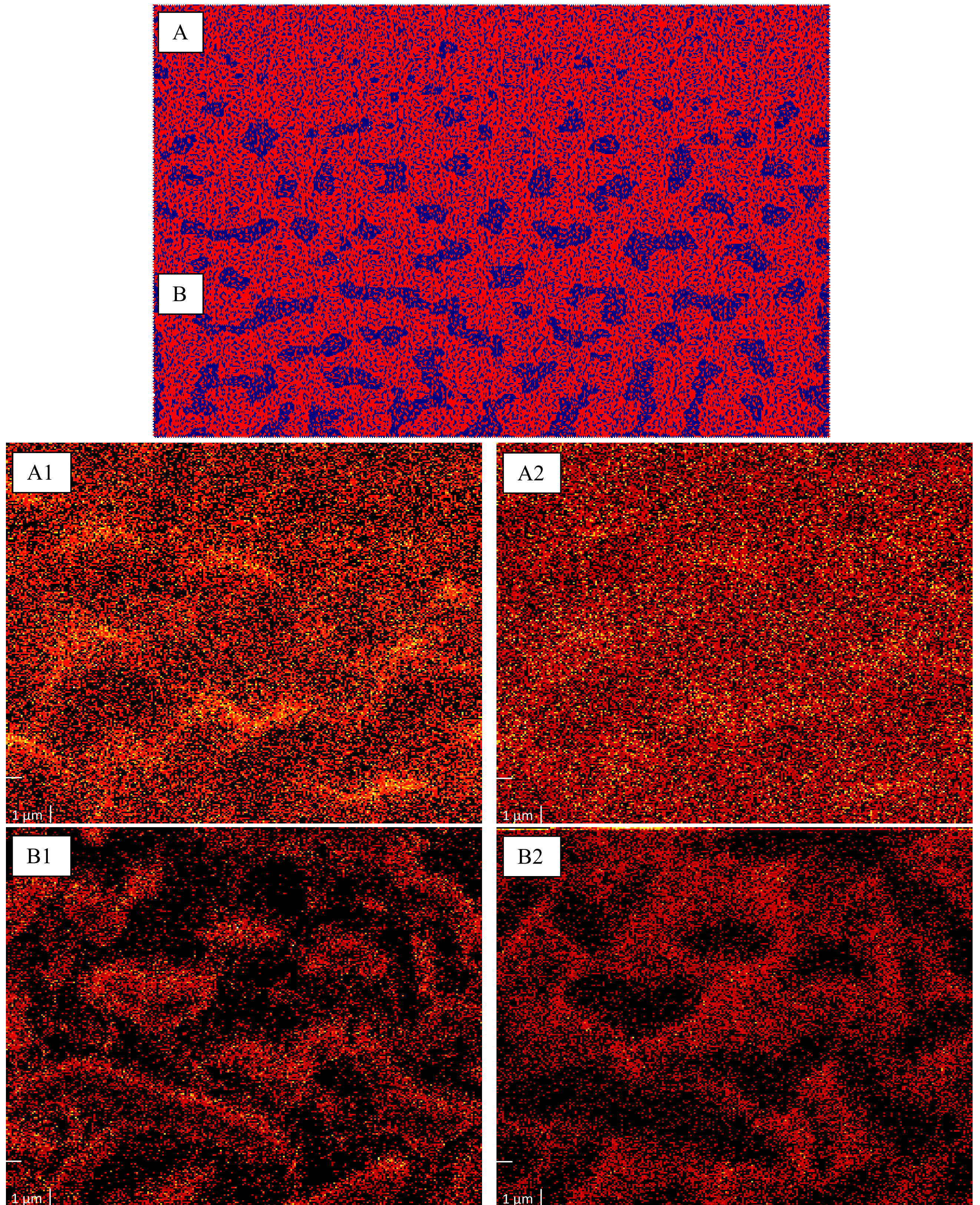

Figure 27: $Pt_{63}Al_{37}$. The top image shows the predicted structure. A1 and B1 are Al elemental maps. A2 and B2 are Pt elemental maps. The elemental maps A and B correspond to the areas A and B on the simulation. Red represents Pt and blue represents Al.

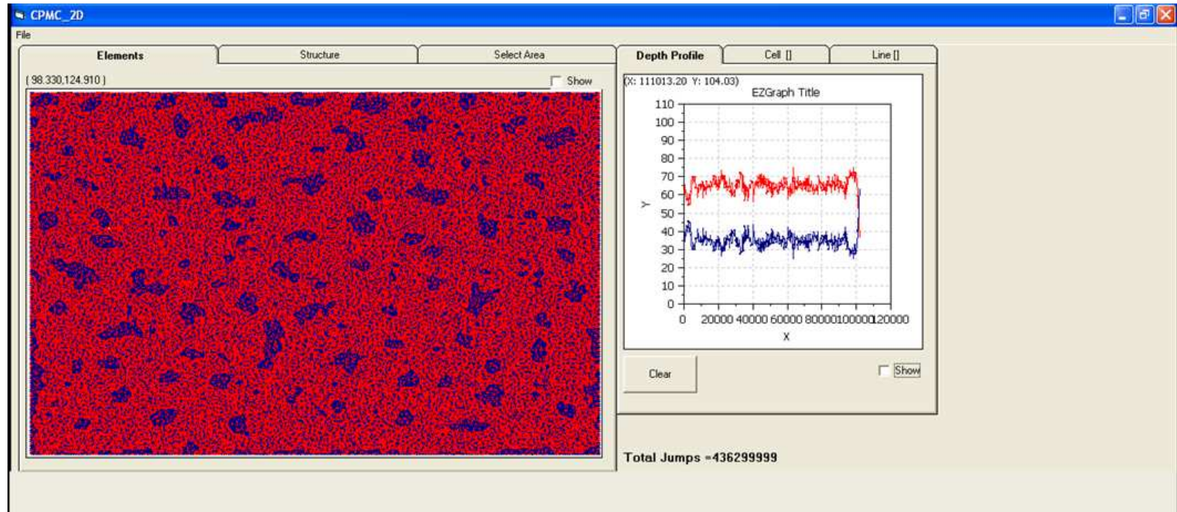

Figure 28: A screenshot of the designed software program showing the predicted microstructure and depth profile for Pt 63% and Al 37%. Red represents Pt and blue represents Al.

Figure 28 gives a screenshot example of the Pt 63 at.% and Al 37 at.% simulation at a later stage. This is quantified in terms of Monte Carlo jumps: thus after 436 million Monte Carlo jumps. It can be seen that some of the longer (elongated) Al-particulates have dissolved into the surrounding Pt-rich area. Therefore these particulates have increased in number and decreased in size. Figure 31 shows the comparison between the simulated results and the elemental maps. Compare the predicted depth profile with the experimentally measured profiles in Figures 29 and 30. It is clear the Pt and Al are almost diffused through the entire sample.

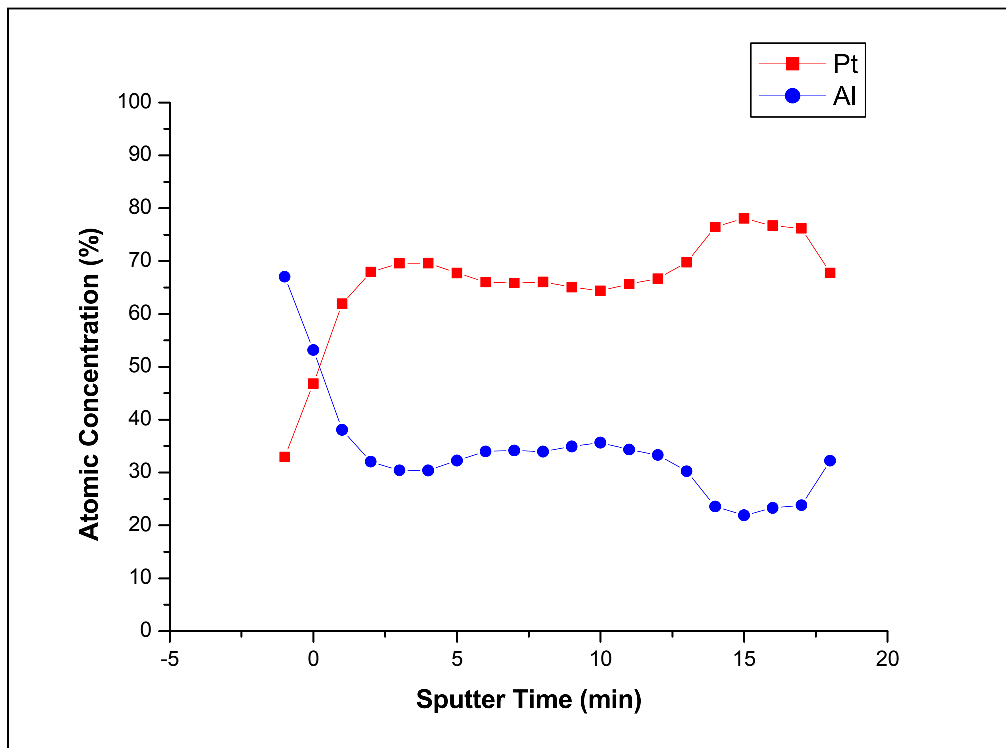

Figure 29: Pt and Al depth profile for $Pt_{63}Al_{37}$ thin film annealed at 400 °C for 49 min.

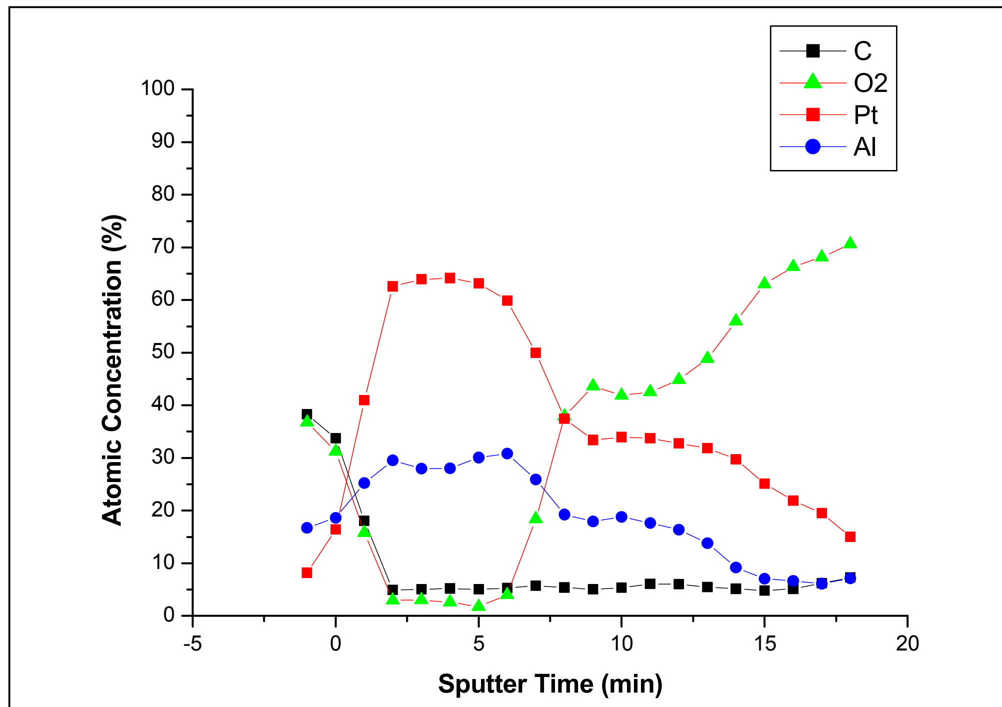

Figure 30: Depth profile for $Pt_{63}Al_{37}$ thin film including impurities annealed at 400 °C for 49 min.

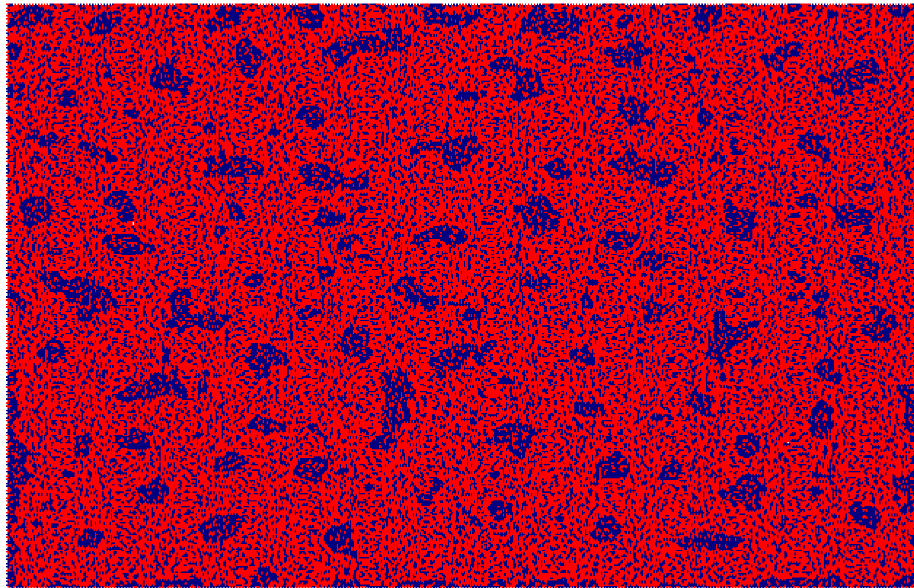

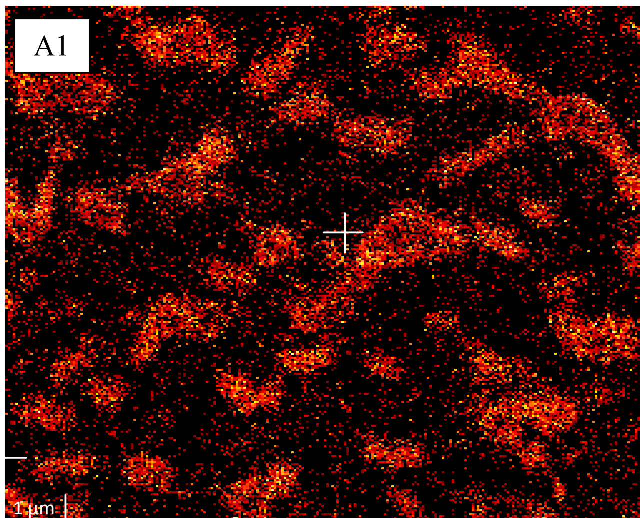

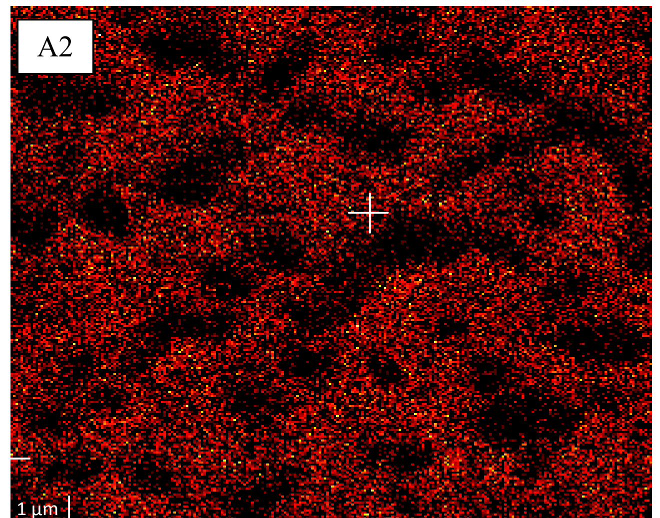

Figure 31: $Pt_{63}Al_{37}$. The top image shows the predicted structure. A1is an Al elemental map. A2 is a Pt elemental map. This system was for a later stage in the time evolution than the previous one. The white cross shows the position of the nanometer electron beam for the AES spectrum. Red represents Pt and blue represents Al.

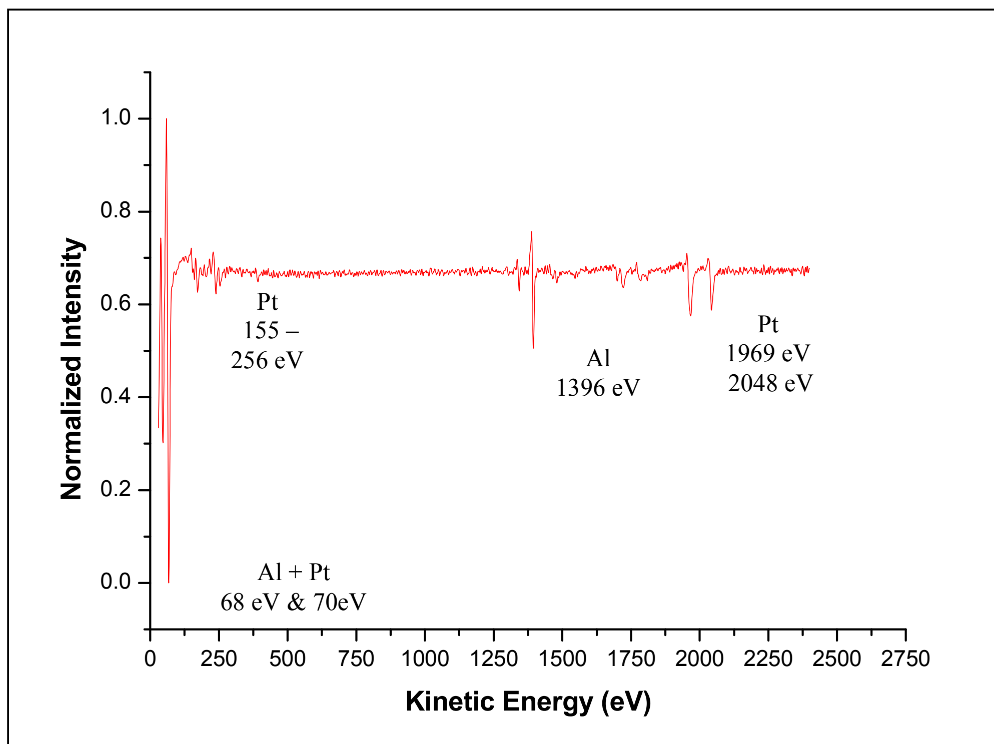

Figure 32: 4 minute sputter time, corresponding to area A of Figure 31. This was taken on the border of one of these particulates (see the white crosshair in Figure 31) in the Pt-rich area.

Figure 31 shows the composition of the thin film on the border of one of the particulates. It was thus taken in the Pt-rich area of the thin film. The white crosshair in Figure 30 shows the position of the nanometer-sized electron beam used for generating the Auger electrons. Both Al and Pt are present in the specific area measured. However it is important to notice the signal strength for the Pt (±12 units) and the Al (±77 units) in this area. Compare this to the Pt-rich area of sample of Figure 35, which will be discussed shortly.

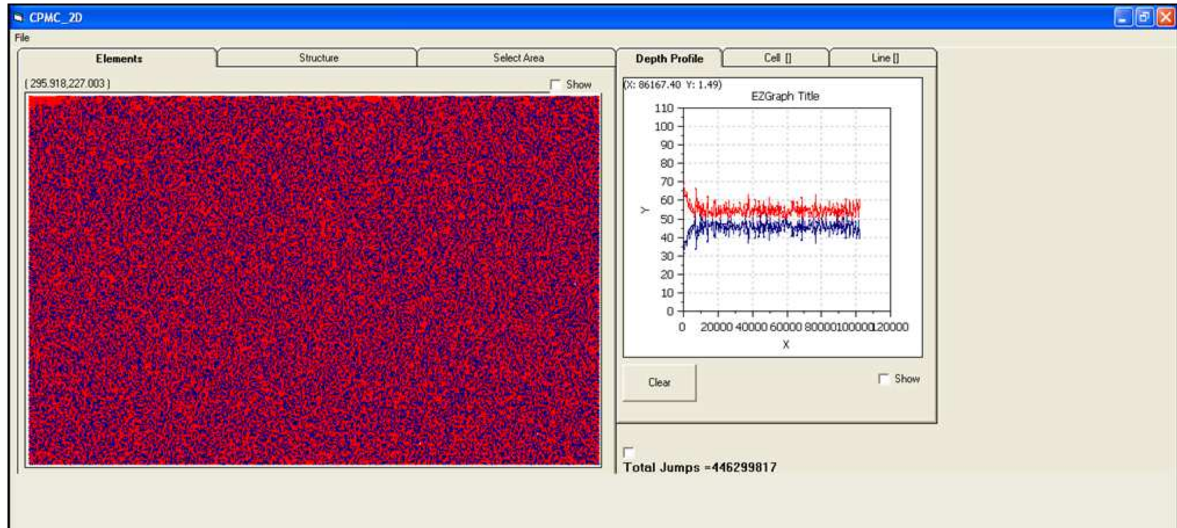

Figure 33: A screenshot of the designed software program showing the predicted microstructure and depth profile for Pt 55 % and Al 45%. Red represents Pt and blue represents Al.

The Pt 55 at.%, Al 45 at.% samples showed a homogenous diffusion throughout the entire sample with no particulates forming (Figures 33 and 36). Just a fine mixture of Pt and Al was observed. Figure 34 and 35 shows the measured depth profiles and it is clear that the Pt and Al have diffused homogenously throughout the entire sample.

The AES spectrum in Figure 37 was taken after 12 minutes. Compared to the Pt-rich area from the previous $Pt_{63}Al_{37}$ sample (Figure 32) it can be seen that the Al signal is larger (±37 units) and the Pt signal (±10 units) smaller (for the $Pt_{55}Al_{45}$ sample) as is expected. This just shows the difference in composition for the Pt-rich areas, because (at an eye-glance) the elemental maps for these areas might look the same (even in the simulation) but they are indeed different in composition.

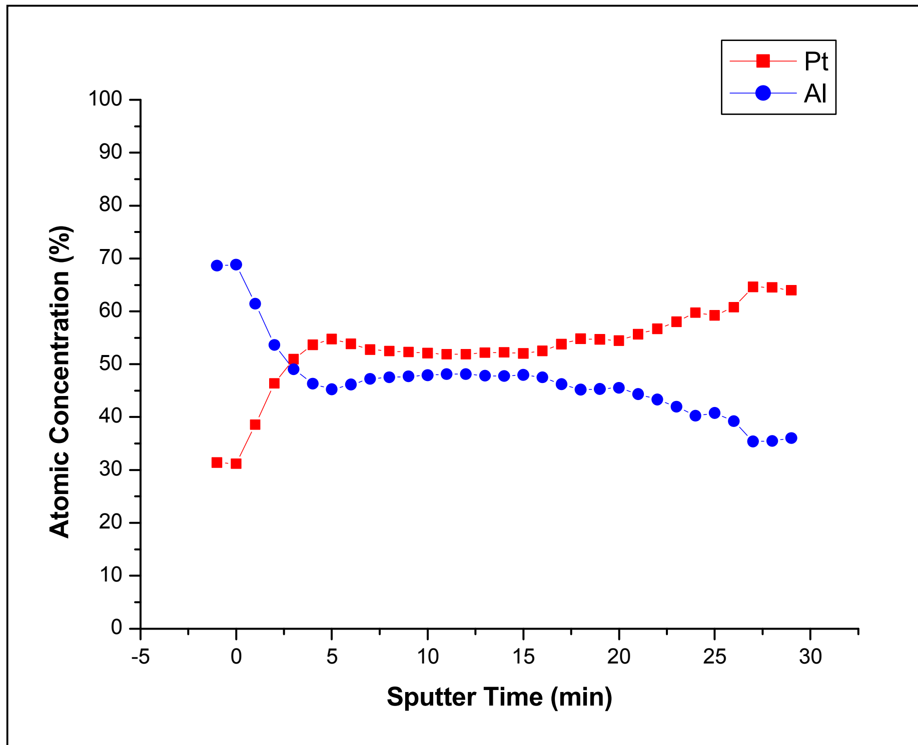

Figure 34: Pt and Al depth profile for $Pt_{55}Al_{45}$ thin film annealed at 400 °C for 49 min.

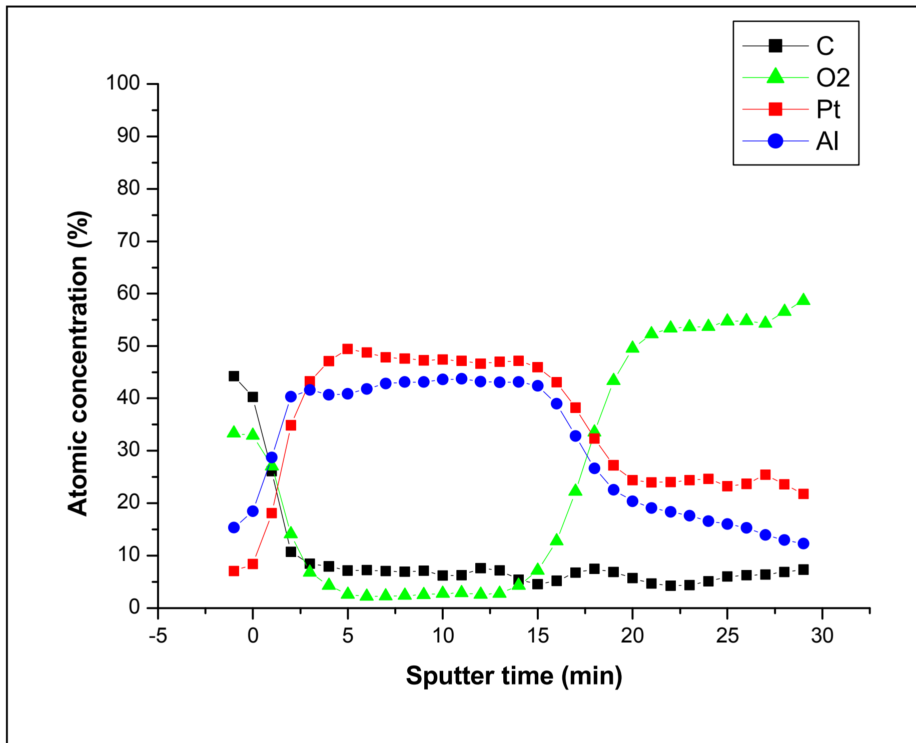

Figure 35: Depth profile for $Pt_{55}Al_{45}$ thin film including impurities annealed at 400 °C for 49 min.

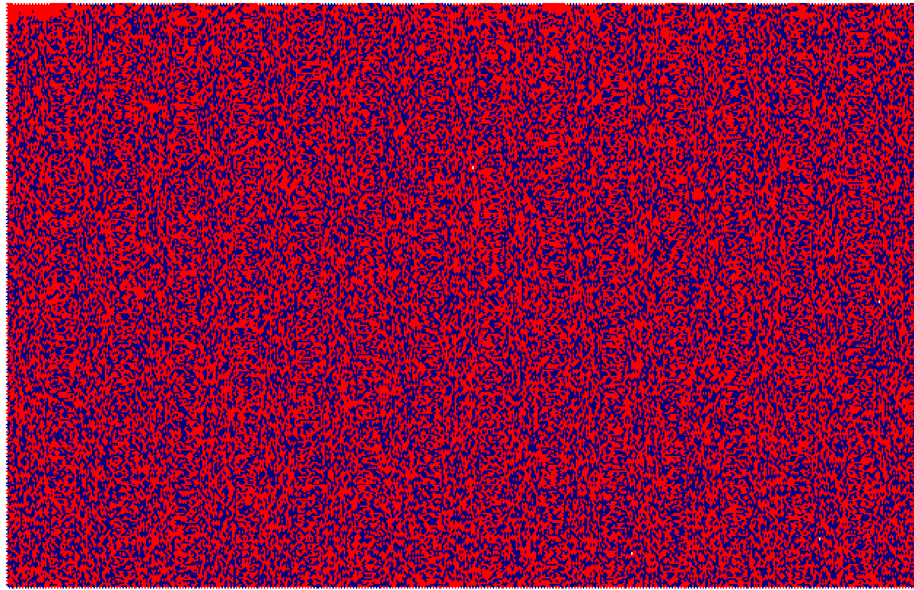

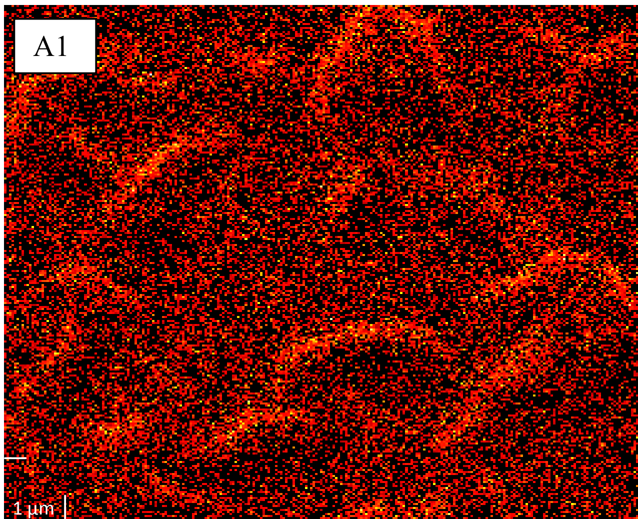

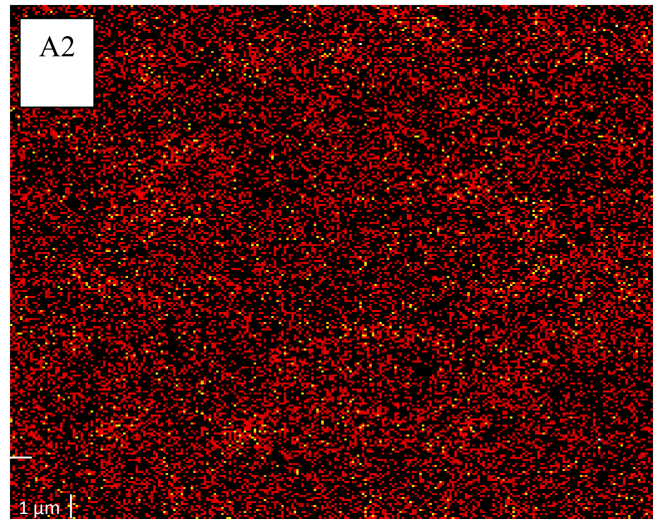

Figure 36: $Pt_{55}Al_{45}$. The top image shows the predicted structure. A1 is an Al elemental map. A2 is a Pt elemental map. Red represents Pt and blue represents Al.

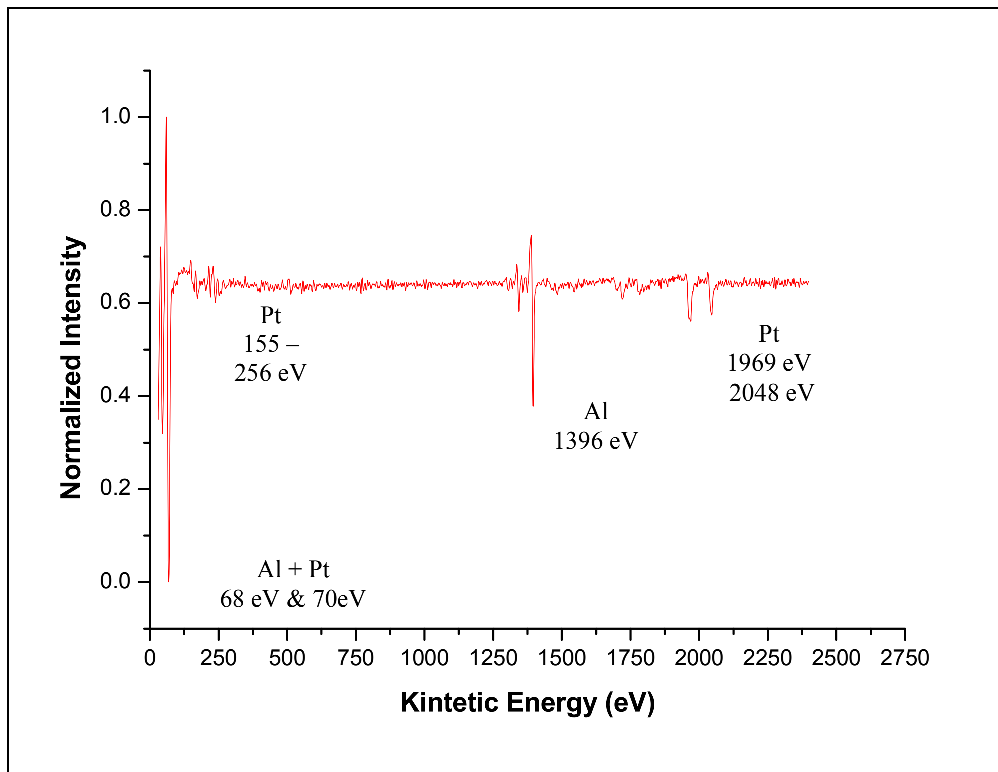

Figure 37: 12 minute sputter time, corresponding to area A of Figure 25.

8.4) Time Evolution

A comparison between the experimentally measured elemental maps and depth profiles of the samples $Pt_{25}Al_{75}$, $Pt_{55}Al_{45}$ and $Pt_{63}Al_{37}$ and the simulated predictions showed a clear correlation between the theoretical results and measured results. With this in mind, a "snapshot" in time can then be taken (with the aid of the simulation) to view the diffusion process in its entirety. From this it is also clear at what stage the aforementioned results fit into this entire process. Figures 38 to 40 shows the time evolution of the $Pt_{25}Al_{75}$, $Pt_{63}Al_{37}$ and $Pt_{55}Al_{45}$ samples respectively. The *number of Monte Carlo jumps* acts as the quantifiable indicator of time evolution.

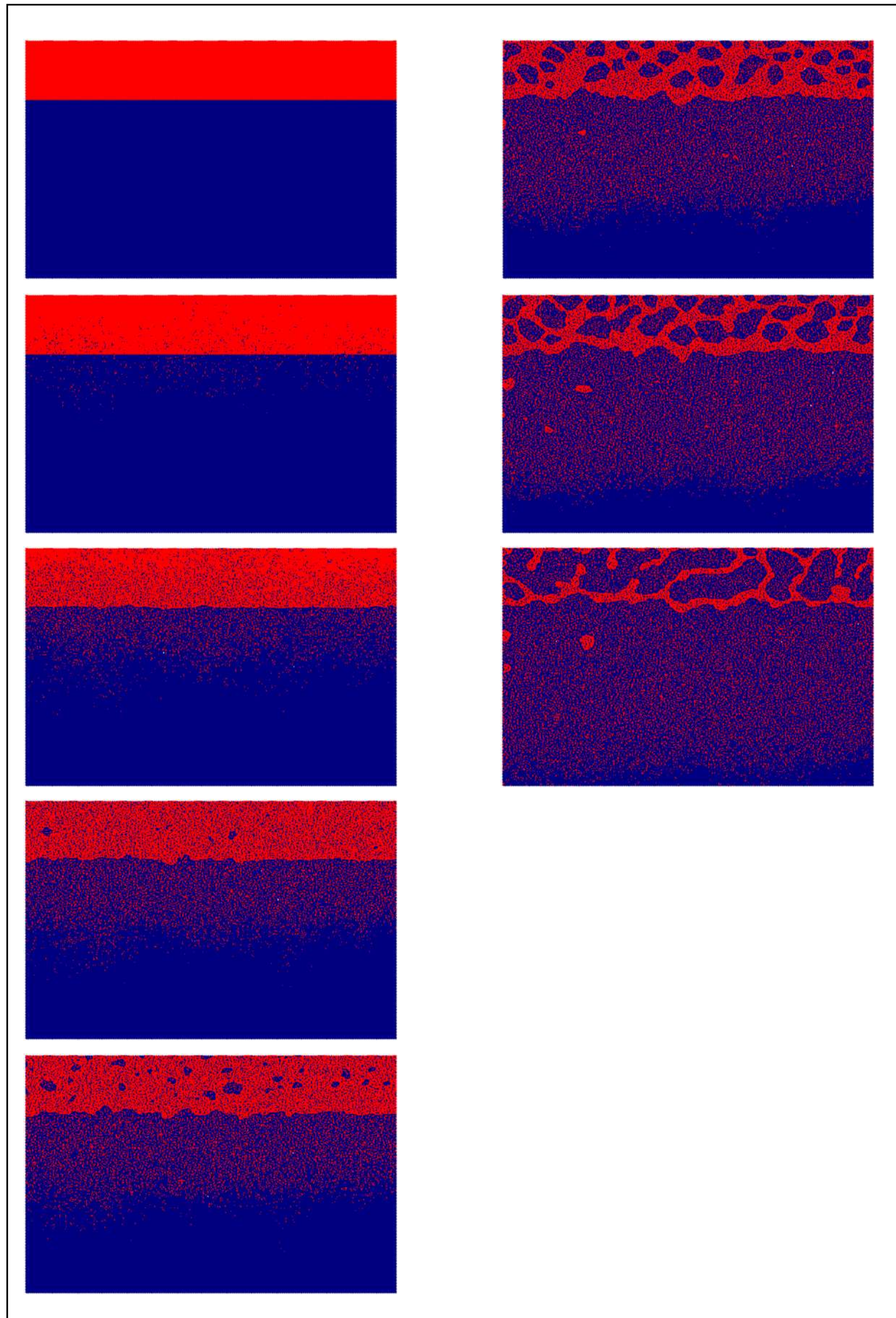

Figure 38: $Pt_{25}Al_{75}$ time evolution. Red represents Pt and blue represents Al.

In Figure 38 an initial Pt:Al ratio of 25:75 was setup into the simulation software. Annealing temperatures ranging from 150 to 650 °C were used for these simulations and input into the simulation software. The results displayed here (in Figure 38) are for 450 °C. The other results look similar. From this the time evolution of the system can clearly be seen. The Pt and Al start to diffuse into each other across the Pt-Al-interface. At some stage Al-particulates nucleate. Compare this to the elemental maps of Figure 14. These particulates start to grow until they grow into each other. Compare this to the elemental maps of Figure 22. At the same time the Pt diffuses into the Al thin film. Finally a "mesh" of Pt with large Al-particulates is the remainder of the original Pt film and a fine mixture of Pt and Al is the remainder of the original Al film. For future work the specific strength, corrosion and oxidation resistance as well as hardness test can be done on each of these particular and unique microstructures to investigate their unique properties. Thus appropriate applications fitting to these properties can be found.

Next consider Figure 39. For this simulation the Pt:Al ratio was 63:37. The results displayed here are for 450 °C. The other annealing temperature results (150 to 650 °C) look similar. At first the Pt and Al start diffusing into each other; the same as the previous system. But this time both Pt and Al particulates start to nucleate. These particulates start to grow and at the same time the clear boundary between the original Pt and Al films disappears. After a while all of the Pt-material and all of the Al-material have diffused into each other and the Pt-Al boundary has disappeared completely. This leaves an extended network of predominantly Pt with a fine mixture of Al in it and with larger Al particulates. These larger Al particulates have a fine mixture of Pt inside. These Al-particulates look like filaments. Compare this to the elemental maps of Figure 17. After a while these Al-filaments begin to dissolve (as the Al and Pt inter-diffuse) leaving only Al particulates but with no definite shape. Compare this to the elemental maps of Figure 22. It would be interesting (as in the previous system) to do hardness tests, specific strength and corrosion/oxidation studies on these individual microstructures to see if the difference in microstructure also leads to a difference in physical properties. If this is the case (as is expected) then the CPMC model can be used to predict beforehand specifically engineered microstructures and hence specifically engineered properties for these thin films.

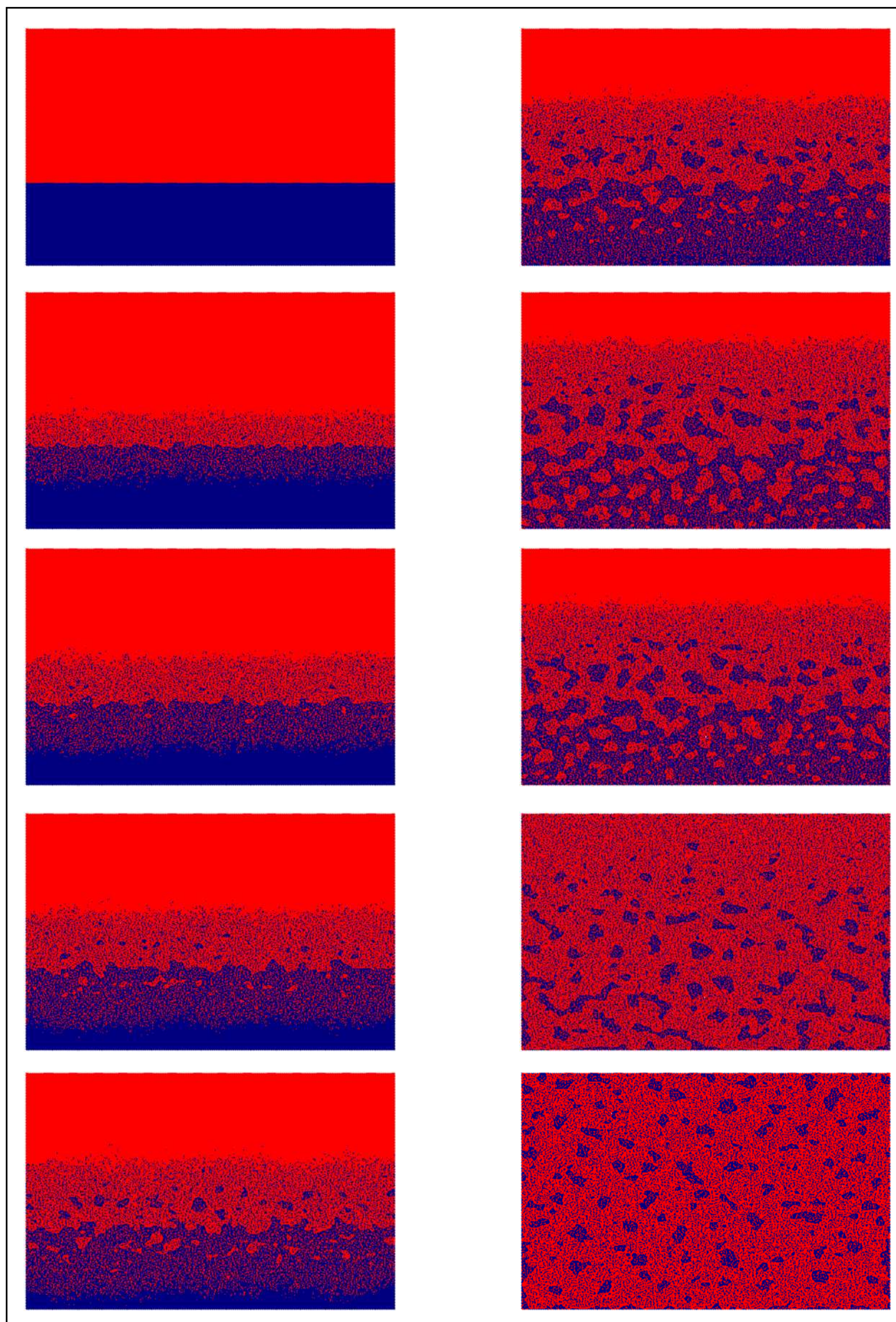

Figure 39: $Pt_{63}Al_{37}$ time evolution. Red represents Pt and blue represents Al.

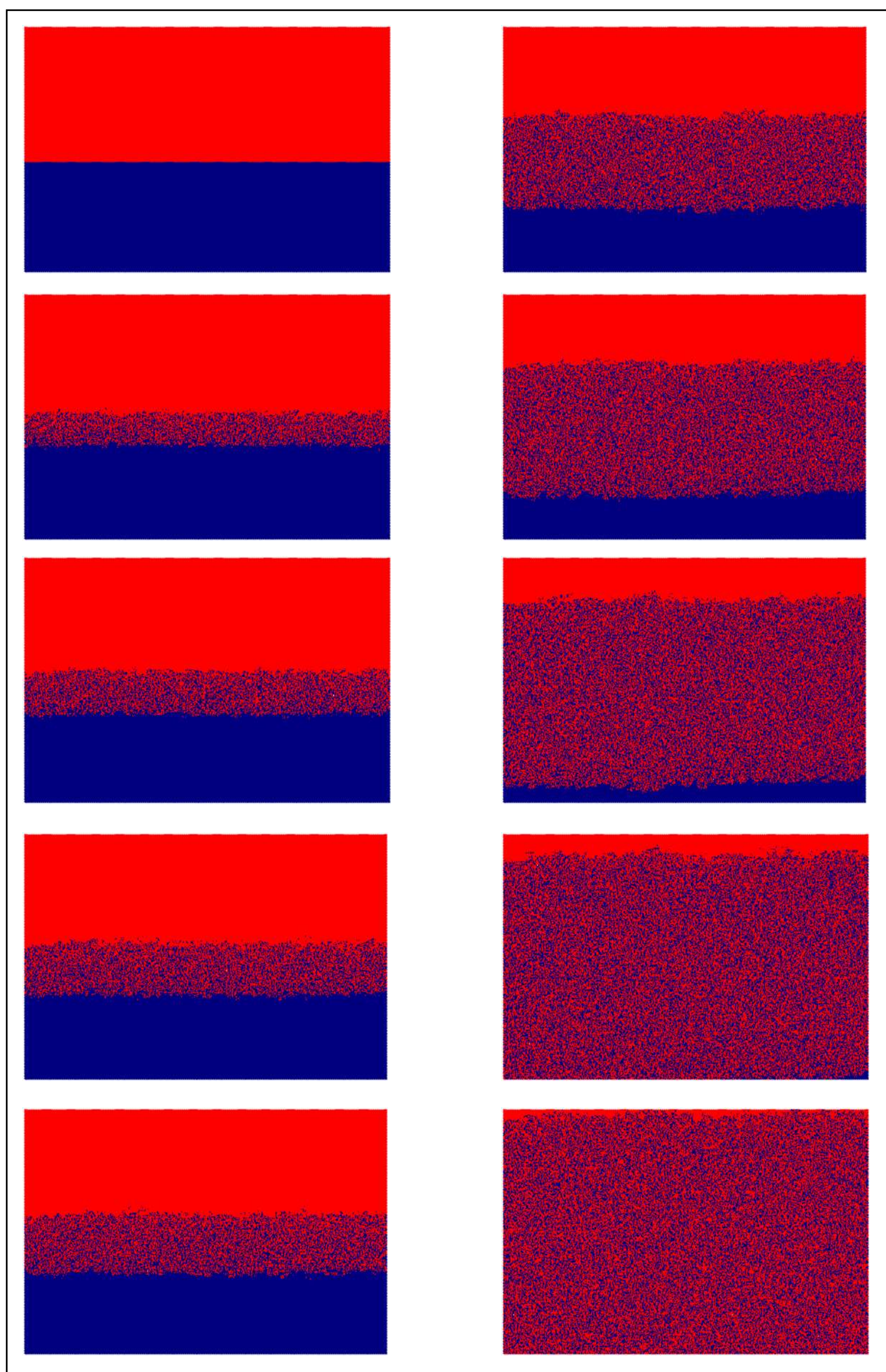

Figure 40: $Pt_{55}Al_{45}$ time evolution. Red represents Pt and blue represents Al.

Figure 40 gives the time evolution for the system $Pt_{55}Al_{45}$. For this system the annealing temperatures that were input into the software ranged from 150 to 650 °C. Here the 450 °C are displayed. The other simulation results look similar. For the $Pt_{55}Al_{45}$ system no particulates formed. The Pt and Al start to inter-diffuse forming a continuous $Pt_{55}Al_{45}$ – phase. Thus the clear boundary between the original Pt film and Al film completely disappears in the early stages of the diffusion process. It is replaced by the $Pt_{55}Al_{45}$ – phase boundaries. This phase then grows in thickness until it consumes all the available Pt and Al material. In the final snapshot only one clear $Pt_{55}Al_{45}$ – phase is left.

From these time-evolutions of the various systems the usefulness of the theoretical model and accompanying simulation results can be seen. For any elemental map of a binary alloy - thin film system, the history and future of that sample can be obtained. If a specific microstructure is required, a correlation between the experimental annealing time and theoretical "snapshot" could be obtained. Thus the required structure can be obtained experimentally. This has some obvious cost saving implications, since the simulation can be run first to determine if the required structure can be obtained at all. The model was specifically developed for Pt and Al systems (a system where both the constituent elements have an FCC crystal structure); however it can easily be extended to any binary alloy. This can be done by simply adjusting the interaction energy values to the appropriate new values for another system. The annealing temperature can then be entered and various time-evolution results can be obtained.

8.5) Summary

In this chapter the preparation of Pt-Al thin films and the comparison of their microstructure with the simulation predicted microstructure was discussed. Si(1 0 0) substrates were oxidized with a wet oxidation technique to form SiO_2 substrates. Pt-Al thin films were deposited onto the SiO_2 substrates by electron beam physical vapor deposition. These films were deposited with different film thicknesses to give Pt-Al alloy thin films with the compositions as listed in table 2: $Pt_{25}Al_{75}$, $Pt_{30}Al_{70}$, $Pt_{35}Al_{65}$ and $Pt_{50}Al_{50}$. The thin films were annealed in a vacuum furnace at temperatures of 350 to 550 °C and at annealing times of 4, 16 and 49 minutes respectively (table 2).

Elemental maps and depth profiles of the microstructures of the annealed Pt-Al thin films were obtained by using Auger electron spectroscopy in conjunction with secondary electron imaging. This was done with the PHI 700 nano-probe. The oxide layer in the SiO_2 substrates had a detrimental effect on the prepared thin films. It consumed some of the Al that was deposited onto the substrate and therefore changed the original composition that was prepared (with EB-PVD). The resulting thin films that were further investigated were: $Pt_{25}Al_{75}$, $Pt_{55}Al_{45}$ and $Pt_{63}Al_{37}$.

Simulations, using the chemical potential Monte Carlo model developed in this study, were run at various compositions, interaction energies and annealing temperatures (Figure 1). From these simulations predicted depth-profiles and microstructures were obtained for the various Pt-Al thin film compositions. A comparison between the predicted and experimentally obtained depth-profiles and elemental maps were made. For the $Pt_{25}Al_{75}$ alloy two systems were investigated: one at 16 minutes annealing time and the other at 49 minutes. This allowed for the evolution of the system to be observed. The theoretically predicted depth-profiles and microstructures compared well to the measured ones. It was observed in both the simulations and the elemental maps how small Al particulates nucleate and grow in size with a lapse of time. For the $Pt_{63}Al_{37}$ alloy two systems were also investigated: one at 16 minutes annealing time and the other at 49 minutes annealing times. This allowed for the evolution of the system to be observed. The theoretically predicted depth-profiles and microstructures compared well to the measured ones. A different microstructure (compared to the $Pt_{25}Al_{75}$ alloy thin films) was observed for the $Pt_{63}Al_{37}$ composition. For the $Pt_{55}Al_{45}$ only one system was investigated and the theoretically predicted depth-profile and microstructure compared well to the experimentally obtained results. The conclusion can therefore be made that the proposed chemical potential Monte Carlo model can satisfactorily predict the depth-profiles and microstructure of the Pt-Al binary alloy thin film system. Therefore the model was used to obtain a visual representation of the evolution of the microstructure (with time) of the three systems discussed above. This can be used by an material engineer to find the different microstructures of these alloys at various annealing times and thus tailor make Pt-Al alloy thin films to specific applications.

References

1. ***Siliconfareast.com***, Available Online May 2010 at http://www.siliconfareast.com /dielectric.htm.
2. **Pliskin W., Conrad E.,** *IBM Journal of Research and Development*, Volume 1, (1964), pg. 43.
3. **Askeland D. R.,** *The Science and Engineering of Materials, Third S.I. Edition*, Stanley Thornes (Publishers) Ltd, (1998).
4. **Cornish L. A., Hohls J., Hill P. J., Prins S. N., Süss R. and Compton D. N., Markovic, Z. S., and Zivkovic, D. T. (Eds.),** The Development of Platinum-based Alloys and their Thermodynamic Database. *Proc. 34th International October conference on Mining and Metallurgy*, (2002), pp. 545-550.

Chapter 9

Comparison to other models

Introduction

In the same time period during which this study was conducted (2006 to 2010) so-called phase- field modelling has been developed and expanded and is becoming quite popular [1 - 4]. It is therefore necessary to put the CPMC model proposed in this study into the proper perspective compared to phase-field modelling developed and expanded by mainly Nele Moelans et.al. [e.g. 1, 2]

9.1) Introduction to phase-field modelling

Over the last couple of years phase-field modelling is increasing in popularity and is becoming a versatile tool for simulating microstructural evolution phenomena, specifically at the mesoscale. Processes such as solidification [5 - 7], precipitation [8, 9], and grain growth [10-12] are being investigated through phase-field simulations. It can predict the evolution of complex morphologies considering different thermodynamic driving forces. Parameters such as interfacial energy, bulk energy, elastic energy and different transport processes (such as heat and mass diffusion) are used to do these calculations.

By using the diffuse-interface approach the study of the evolution of arbitrary complex grain morphologies can be carried out without any prior presumption on their shape or distribution. It can also account for different thermodynamic driving forces for microstructure evolution, such as bulk and interfacial energy, elastic energy and electric or magnetic energy as well as the effect of different transport processes

(like mass diffusion, heat conduction and convection). During phase-field modelling many concepts are introduced. These include diffuse interfaces, the phase-field variables, the thermodynamic driving force for microstructure evolution and the kinetic phase-field equations.

Phase-field theory has been applied to processes such as solidification, precipitate growth and coarsening, martensitic transformations and grain growth. The CPMC model proposed in this study was developed to predict precipitate growth and in solid-state particular in thin films. More recently, phase-field modelling has also been applied to other solid-state phase transformations like the austenite to ferrite transformation in steels, dislocation dynamics, crack propagation and nucleation. A rapid increase in the achievements of phase-field modelling has been observed in the last few years due to improved modelling and implementation techniques and growing computer capacities.

9.2) Phase-field modelling of microstructure evolution

In the phase-field method, a microstructure is represented by means of a set of conserved and non-conserved phase-field variables [1, 3-7]. These variables are continuous functions of spatial and temporal coordinates. An example of a conserved phase-field variable is the molar fraction fields of the constituting components. Non-conserved phase-field variables, such as order parameter fields and phase-fields, contain information on the local structure and orientation. Within domains the phase-field variables have nearly constant values, and *at the interface* they vary continuously over a narrow region between their values in the neighbouring domains. This results in the interfaces having a finite width and the variations in properties at interfaces are continuous. This is the so-called diffuse-interface description [1].

The main advantage of diffuse interfaces is that *no boundary conditions* must be specified at the *moving* **interfaces**. This allows for phase-field models to be able to predict complex morphological evolutions. Also no prior assumptions on the (non-) equilibrium conditions at the moving interfaces are required [13].

The free energy in phase-field models is expressed as a function of the phase-field variables at their spatial gradients. This is the difference between phase-field theory and classical thermodynamics. Since interfaces are characterized by a steep gradient in properties, the gradient term automatically gives rise to interfacial tension. For solid-state applications, the elastic strain energy (due to transformation strains) or an externally applied stress is formulated as a function of the phase-field variables using a continuum micro-elasticity approach. A set of kinetic equations is solved numerically to obtain the temporal evolution of the phase-field variables. It is straightforward to include into a phase-field model the effect of different transport processes, such as diffusive mass and heat (conduction) transport, fluid flow and electric current, on the morphological evolution of the grains [1]. Nucleation, instabilities in a metastable structure or steady-state growth morphology can all be simulated by introducing **stochastic noise terms.** However nucleation is usually incorporated into phase-field simulations using **separate analytical nucleation models** [1, 3, 6].

A **large number of parameters** are used in phase-field models [1]. These parameters have to be determined in order to obtain *quantitative* results for real alloys. The parameters are related to

(1) thermodynamic properties,
(2) equilibrium composition of the coexisting phases,
(3) the interfacial energy,
(4) the interfacial width and mobility,
(5) the diffusion properties of the solute elements and
(6) the elastic properties of all coexisting phases.

This large number of parameters (some of them are related to properties that are difficult to measure) makes **it complicated to determine all the parameters in a phase-field model**. Different methodologies have been proposed to make parameter assessment more efficient and to reduce the dependence on experimental measurements. For example assessed databases (such as the Thermo-Calc and DICTRA databases developed using the CALPHAD approach [1]) are useful for phase-field simulations for multicomponent alloys. It is also found that atomistic simulations can provide information on difficult-to-measure properties, such as the

interfacial energy, mobility and anisotropy. **However, parameter assessment is still a major problem in phase-field modelling** [1 - 5]. The numerical solution and implementation of phase-field equations is, in principle, relatively simple and straightforward, because there is no need to track the interfaces. However, the resolution of the numerical technique must be very fine to catch the steep transitions of the phase-field variables at interfaces. Thus by using ordinary numerical techniques **simulations for realistic system sizes and time scales are not feasible.** This is so **because of excessive computation times and insufficient computer memory**.

To simulate crystal growth during solidification a finite volume or finite element discretization using an adaptive mesh is often applied. This mesh is taken to be

- extremely fine at the *solid–liquid interface*, to resolve the transition of the phase-field variables and
- course within the bulk domains, for describing the mass and heat transfer over macroscopic distances.

A Fourier-spectral method with semi-implicit time stepping and uniform mesh is usually used for solid-state phase transformations. This technique is usually more appropriate than a technique based on adaptive meshing because of the large number of grains or precipitates involved. To increase the system size towards relevant dimensions, the width of the diffuse interface must be taken artificially large [1]. Therefore, it is important to develop phase-field formulations that allows for a change of the interface width without affecting the interfacial energy and mobility or introducing spurious effects.

Much progress is being made in controlling the interfacial profiles of the phase-field variables and suppressing artificial kinetic and non-equilibrium effects*, although a general solution has not yet been found and all strategies are still under debate* [1].

9.3) The CPMC model in its proper perspective

Phase-field modelling has proven to be a versatile tool for simulating microstructural evolution phenomena specifically targeting grain growth such as grain growth in polycrystalline materials. However, the computing time and computing memory requirements of a phase-field model pose severe limitations on ***the number of phase-field variables*** that can be taken into account in a practical implementation. Therefore, to get any realistic results, methods are currently being investigated (such as *the Bounding box algorithm for three-dimensional phase-field simulations* [2]**)** to allows the use of a large number of phase-field variables without excessive memory usage or computational requirements. Only then can grain growth simulations be carried out. The development and optimization of these algorithms is an ongoing process to date.

One of the main differences between the CPMC model and phase-field modelling is that CPMD only provides for diffusion and precipitations forming in the *solid-state*, whereas phase-field modelling allows for a *solid-liquid interface* [1,6]. The CPMC model is very simplistic compared to phase-field modelling. The reason for this is because the main physical process and driving force to predict the microstructure and microstructural-evolution during the annealing of a two-component thin film system, is diffusion. This leads to a reduction in the amount of parameters that are used to do the simulation calculations.

The minimization of the Gibbs free energy through the minimization of the chemical potential of the thin film system acts as the driving mechanism during diffusion of atoms. This in turn leads to the clustering of atoms (of different compositions) into various shapes and sizes. In particular it predicts clustering of atoms during diffusion, either into precipitate-like or ribbon-like structures and the correlation with real microstructures is quite good.

Parameters such as interfacial energy, bulk energy, and elastic energy, and different transport processes, such as heat and mass diffusion has NOT been included in the CPMC model (as is the case in phase-field modelling). However the CPMC model DOES give a good ***first approximation*** solution to the investigation of the formation of these ribbon-like or precipitate-like structures based on concentration-,

temperature-, and interaction energy-parameters alone. In the phase-field model, the *large number of parameters* (where some of the parameters are related to properties that are difficult to measure) makes it complicated and difficult to determine all the parameters.

Therefore, even though only a few parameters are considered in the CPMC model, this lack of complexity, gives it a slight advantage as a first order solution to predict the formation of structures (phases) of various shapes in a thin film system. However where quantitative and more detailed information is required (e.g. grain size, grain growth in polycrystalline materials, pinning effect of small incoherent particles on grain growth in two-dimensional polycrystalline systems, grain growth in materials containing small incoherent second-phase particles etc.) phase-field calculations would be the more appropriate tool to use.

Another important difference between these two approaches is the simulating of crystal growth during solidification. In phase-field modelling *solid–liquid interfaces* are modelled. As was explained in Chapter 8, this is not the case in the CPMC model. It was not the aim of this study to develop a model to predict crystal growth from liquid to solid (as for bulk materials), but rather to predict the interdiffusion of solids *only* comprising of different elements. In particular the goal was to predict the interdiffusion for thin films evaporated onto a substrate in a binary- or multilayer-fashion.

The main advantage of diffuse interfaces is that *no boundary conditions* must be specified at the moving **interfaces** [1]. This is also the case for the CPMC model. Therefore, both phase-field models and CPMC modelling are able to predict complex morphological evolutions. **Stochastic noise terms** can be added to phase-field modelling equations to simulate nucleation or to induce instabilities in a metastable structure or steady-state growth morphology, although nucleation is usually incorporated into phase-field simulations using **separate analytical nucleation models**. The CPMC model does NOT require the addition of these stochastic noise terms since the Monte Carlo technique simulates this stochastic nature during the nucleation of precipitates. Therefore neither stochastic noise terms nor nucleation models need to be added to CPMC modelling in order to simulate morphological evolution.

9.4) Summary

When quantitative solutions pertaining to grain growth in bulk alloys at solid-liquid interfaces and solid-state grain boundaries want to be obtained, phase-field modelling can predict the morphological evolution and allow for obtaining quantitative solutions of various parameters. However the trade of is extensive computer memory and time. Also various complicated algorithms need to be developed for complicated numerical techniques in order to have a fine enough resolution to catch the steep transitions of the phase-field variables at interfaces.The CMPC-model can predict the morphological evolution of thin film alloy systems, without the use of a large number of variables. This allows for a decrease in computer memory and time since straightforward numerical techniques can be used to solve the set of equations. There is therefore no need for further expansion of these algorithms to fine-tune them. The trade of here is in the amount of information that can be obtained from CPMC modelling. CPMC models only predict morphological evolution in solid-state thin films (in particular the precipitate-like or ribbon-like structures that form). Therefore CPMC modelling can be used as a tool to predict morphological evolution as a function of only three parameters: thin film alloy composition, annealing temperature and interaction energy of the atoms.In conclusion: Figure 1(a) and 1(b) show a typical phase-field simulation. A nonlinear multigrid solver is used to solve the phase-field model. The goal of the solver is to perform *grain growth simulations* in two dimensions in an efficient way. Grains are single-phase crystals *being identical except in orientation*. Therefore two adjacent grains have the same phases but different crystallographic orientations. Grain boundaries are interfaces where crystals of different *orientations* meet. A grain boundary is a single-phase interface, with crystals on each side of the boundary being identical except in orientation. Figure 1(c) shows a typical CPMC model simulation. The goal is to perform *phase growth simulations* in order to predict the precipitate-like or ribbon-like phases that are seen in experimentally measured microstructure. A phase is a region of space (in a thermodynamic system), throughout which all physical properties of a material are essentially uniform. Thus the boundaries observed in these simulations are not caused by different crystallographic orientations but by different phases that have formed.

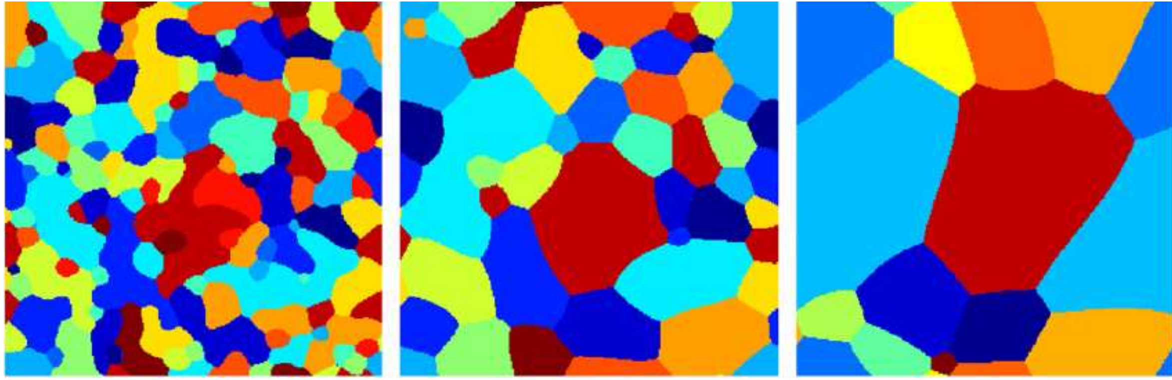

(a)

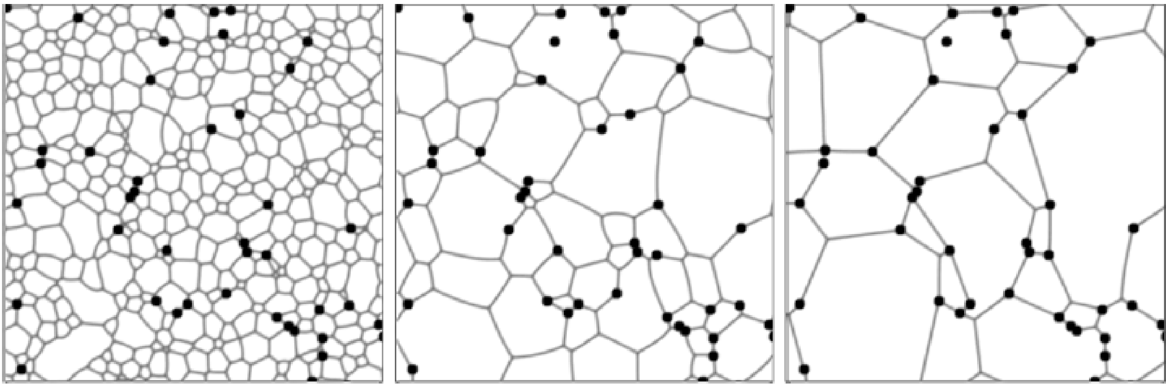

(b)

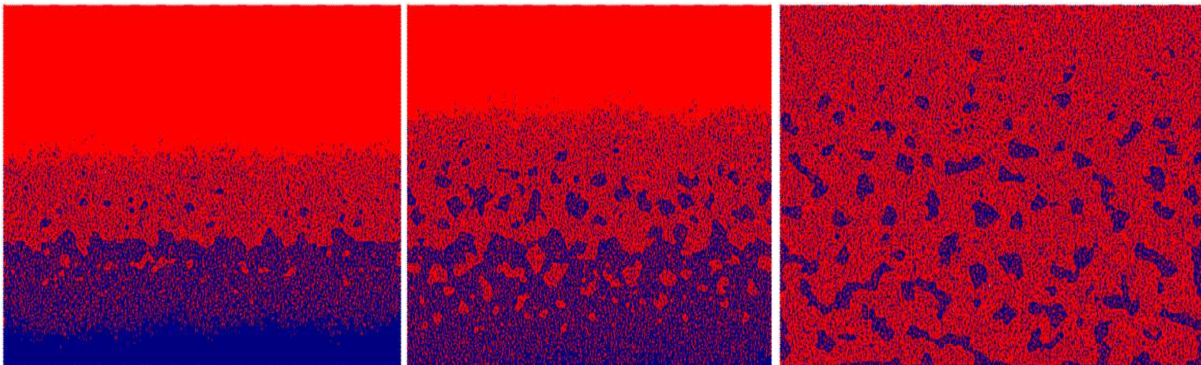

(c)

Figure 1: (a) Phase-field simulation: Grains at t = 2, 20 and 160 time-units respectively (from left to right) [14]; (b) Phase-field simulation: evolution of a polycrystalline system containing second-phase particles (shown at t = 200, 3000 and 30 000 time-units respectively (from left to right) [15]; (c) CPMC simulation: evolution of Pt_{63}:Al_{37} thin film system at t = 50 000, 700 000 and 22 000 000 Monte Carlo-jumps respectively (from left to right). The formation and growth of both ribbon-like and precipitate-like phases can be seen.

References

1. **Moelans N., Blanpain B., Wollants P.**, *Computer Coupling of Phase Diagrams and Thermochemistry*, Volume 32, (2008), pg. 268 – 294.
2. **Vanherpe L., Moelans N., Blanpain B., Vandewalle S.**, *Physical Review E*, Volume 76, (2007), 056702, pg. 1 – 11.
3. **Vanherpe L., Moelans N., Blanpain B., Vandewalle S.**, *Proceedings of Applied Mathematics and Mechanics*, Volume 7, (2007), pg. 2020001–2020002.
4. **Moelens N., Serbruyns A., Heulens J., Blanpain B., Wollants P., Leuven K.U.**, *Discovery and Optimization of Materials through Computational Design*, Materials Science and Technology, Pittsburgh, Pennsylvania, (2008).
5. **Danilov D and Nestler B.**, *Acta Materiala,* Volume 54, (2006), pg. 4659.
6. **Plapp M., Cryst J.**, *Growth,* Volume 303, (2007) pg. 49.
7. **Böttger B., Eiken J., Steinbach I.**, *Acta Materiala*, Volume 54, (2006), pg. 2697.
8. **Bronchard Q., Bouar Y.L., Finel A.**, *Advanced Engineerig of Materials*, Volume 8, (2006), pg. 1245.
9. **Wen Y., Wang B., Simmons J., Wang Y.**, *Acta Materiala*, Volume 54, (2006), pg. 2087.
10. **Fan D. and. Chen L.Q.**, *Acta Materiala*, Volume 45, (1997) pg. 611.
11. **Krill III C. E. and Chen L.Q.**, *Acta Materiala*, Volume 50, (2002) pg. 3057.
12. **Ma N., Kazaryan A., Dregia S. A., Wang Y.**, *Acta Materiala*, Volume 52, (2004), pg. 3869.
13. **Moelans N., Blanpain B., Wollants P.**, *Acta Materialia*, Volume 53, (2005), pg. 1771–1781.
14. Vanherpe L., Wendler F., Nestler B., Vandewalle S., *Mathematics and Computers in Simulation*, Volume 80, (2010), pg. 1438–1448.
15. **Moelans N., Blanpain B., Wollants P.**, *Acta Materialia*, Volume 54, (2006, pg. 1175 – 1184.

Chapter 10

Conclusion

The aim of this study was to investigate Pt-based alloy thin film coatings, i.e. how to grow these films to have tailored microstructures (and resulting properties). Therefore two techniques for growing Pt-based alloy thin films were studied: pulsed laser deposition (PLD) and electron-beam physical vapour deposition (EB-PVD). A chemical potential Monte Carlo model (CPMC) was developed to predict the resulting structure of the EB-PVD prepared films when they are allowed to diffuse during annealing.

Two Pt_{84}:Al_{11}:Cr_3:Ru_2 alloys were prepared to make PLD targets. One target was given a heat treatment at 1350 °C for 96 hours. The other target was left unannealed. With pulsed laser deposition, the Pt_{84}:Al_{11}:Cr_3:Ru_2 alloys were laser ablated and thin films of these material were grown. It was found that microscopic droplets are the dominant feature on these thin films. The influence of the surrounding ambient gas on the formation of these droplets was investigated to see if the size and number density of these droplets could be minimized by varying the ambient gas as well as the ambient gas pressure. Argon gave the smoothest thin film surfaces minimizing the appearance of droplets on the films. It was found that a large percentage of the alloy-target material forms droplets resulting in less material to grow the actual thin films with. This in turn results in very thin films (less than one micrometer). In order to increase the thickness of these films, longer ablation times would be required, which would require larger target samples.

The stoichiometric transfer of target material to substrate surface was also investigated. It was found that no direct stoichiometric transfer could be achieved. The reason for this was the influence the laser beam had in heating the alloy-target, thus giving the prepared targets an unwanted (extra) heat treatment. This property was used advantageously by allowing the laser beam to give the unannealed Pt_{84}:Al_{11}:Cr_3:Ru_2 alloy the required heat treatment (to have a very specific engineered microstructure) during the laser ablation process. This resulted in the thin films

(ablated in this manner) having the specifically engineered properties that was sought after. Thus, in this manner, thin films with the same stoichiometry and structure as the tailor-made Pt-based superalloy, could be grown.

In the second part of this study binary layer - thin films were grown from the pure elements (instead of the prepared alloy-target) with specific compositions. Electron beam-physical vapour deposition was used to evaporate Pt and Al onto a SiO_2 substrate. The Pt to Al ratios that were deposited onto the substrates was varied to give different Pt-Al binary alloy thin film compositions. These samples were annealed in a vacuum furnace at annealing temperatures ranging between 350 and 550 °C and annealing times of 4, 16 and 49 minutes respectively. Elemental maps and depth-profiles of the prepared thin film samples were obtained by using a combination of Auger electron spectroscopy and secondary electron imaging. This was done with the PHI 700 nanoprobe. It was observed that the oxide layer of the SiO_2 substrates had a detrimental effect because of the affinity of Al for oxygen. The composition of the thin films that were measured was therefore different from the thin films that were deposited *via* EB-PVD.

A chemical potential Monte Carlo (CPMC) model was developed to predict the diffusion process and the resulting microstructure of these thin films. The model was developed for a binary Pt-Al alloy thin film system. Simulations were run for various different Pt-Al thin film compositions, interaction energies and annealing temperatures. A comparison between the measured depth profiles and microstructures and the simulated depth profiles and microstructures were made. It was found that the resulting EB-PVD grown thin film microstructure and the CPMC-model predicted microstructure correlate well. The influence of using different compositions of Pt and Al when growing the thin films, and the resulting inter-diffused thin film microstructure (after annealing) was observed in three of the investigated systems ($Pt_{25}Al_{75}$, $Pt_{55}Al_{45}$ and $Pt_{63}Al_{37}$). In the $Pt_{25}Al_{75}$ system small particulates could be formed and in the $Pt_{55}Al_{45}$ system a homogenous composition could be formed. Thus these thin films can be tailored to have very specific properties, depending on the applications a material engineer might have. The CPMC-model can be used to predict these structures.

Future Work

The following should be considered for future projects:

- By using larger Pt_{84}:Al_{11}:Cr_3:Ru_2 alloy targets thicker PLD thin films (in the order of micrometers) can be grown. Hardness tests can then also be included.
- The results of this study (the ambient gas and gas-pressure) should be used to reduce the appearance of droplets to grow smoother PLD thin films.

The CPMC model can be refined by considering the following:

- Interaction energies should be more accurately determined by investigating experimentally measured ablation energies.
- The CPMC model can be extended to ternary- and even quaternary-alloys in order to ultimately predict the material transfer in a Pt/Al/Cr/Ru alloy.
- Different crystallographic orientation can be considered in the model.
- Different atomic sizes can be considered.
- Different bonding directions can be considered.
- Different bonding lengths can be considered.
- Grain boundary effects after nucleation can be considered.
- Any inherent effects of the measuring instrument itself (like different sputtering yields) can be considered to refine to model and make the final depth profile predictions more realistic.
- The model could be expanded to a three dimensional model.
- In this model only kinetics was considered. A more quantifiable approach to the temporal aspect (other than Monte Carlo jumps) can be investigated.
- Multi-layer thin film systems, i.e. Pt/Al/Pt/Substrate, Pt/Al/Au/Substrate, Pt/Al/Pt/Al/Substrate can be considered for future work.

- Scale up from nm thick films to μm thick films.

Appendix A: Computer Code

A.1) Model setup and crystal packing

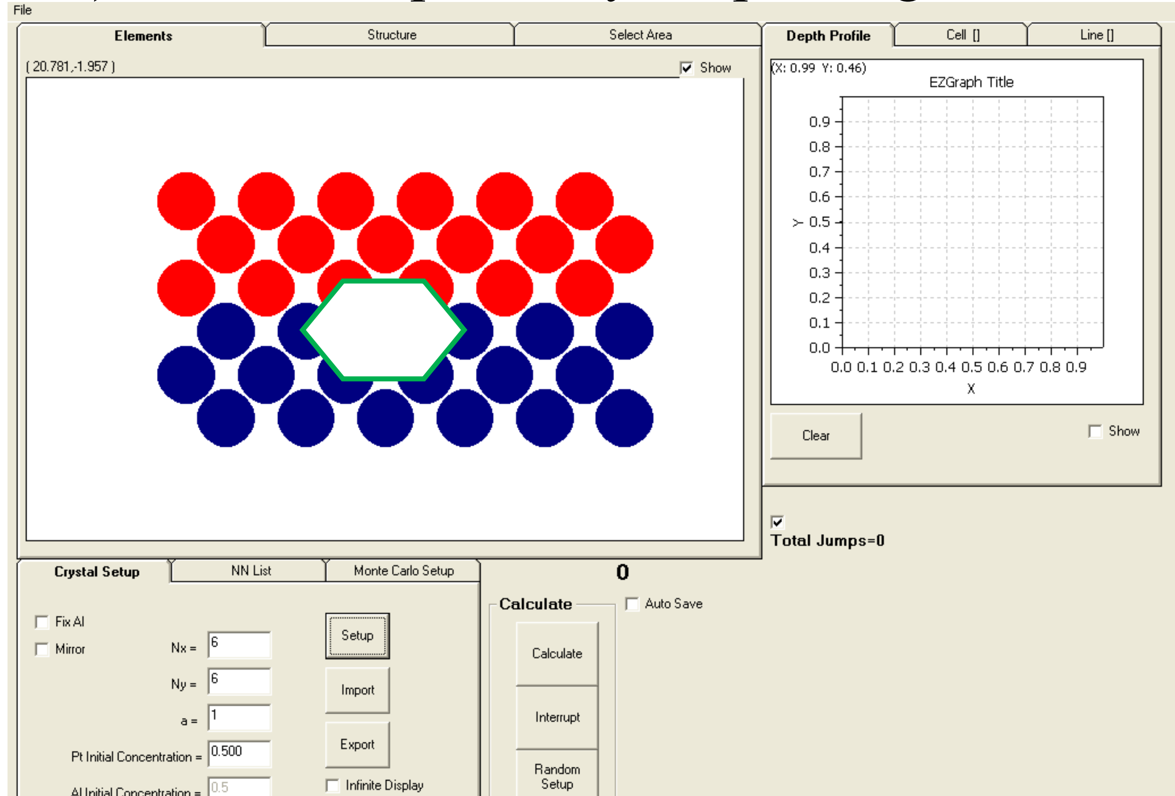

Figure A.1: Screenshot of the crystal-packing showing the relevant nearest neighbours for a random atom A.

The two dimensional FCC packing makes this software setup ***specific*** for ***FCC-crystals***, like Pt and Al. Therefore in order to include other crystal structure the module "Crystal Setup" has to be adapted from FCC to the specific system's crystal structure. This will affect the number of nearest- and next-nearest-neighbours.

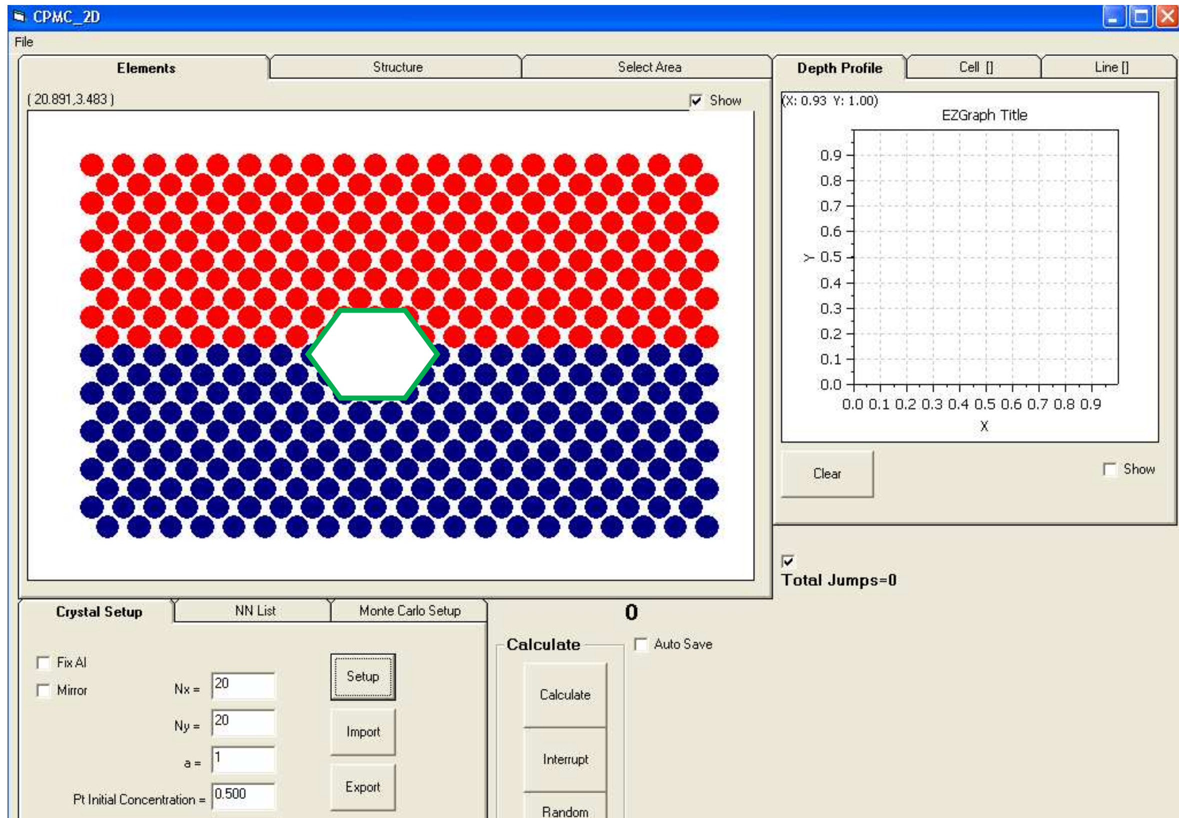

Figure A.2: Screenshot of the crystal-packing showing the relevant nearest-neighbours and next- nearest-neighbours for a random atom A.

A.2) Modules

Module1: Crystal Setup

```
' *************************************************************
' Module        ModuleCrystalSetup
'
' Filename      ModuleCrystalSetup.bas
'
' Author     RA Harris
'            University of the Free State
'            Bloemfontein, South Africa
'
' Description
'
' This module sets up a custom crystal,extends is to "infinity",
' calculates the Nearest Neighbours, as well as the
' NNN (Next Nearest Neighbours) for the FCC crystal
' *************************************************************
Option Explicit
'Create Index for Atom_Matrix
Type ElIndxXY_Type
   El As Double
   Starting_Index As Double
   x As Double
   y As Double
End Type
'Atom Matrix Setup
Global Atom() As ElIndxXY_Type        'Unknown number of Atoms
Global MatrixSize As Double
Global Nx As Double              'Global Nx
Global Ny As Double              'Global Ny
Global a As Double              'Global a (crystal parameter)
```

```
'NN- and NNN- Lists
Global NNList() As Double
Global NNNList() As Double
Global Progress As Double
```

Public Sub FillMatrix(ByRef Nx As Double, ByRef Ny As Double, ByVal a As Double)

```
'Fill Matrix with Similar Atoms

Dim i As Double
        Dim j As Double
        Dim Counter As Double
        Dim x As Double
        Dim y As Double
        Dim Shift As Integer
        'Initialize
        Counter = 1
        x = 0
        y = 0
        Shift = 0
        'Check if X and Y are Even Number:  If Not, make them Even
        If Nx Mod 2 <> 0 Then Nx = Nx + 1   'If Nx is not even, make it even by
        adding 1 to its current value
        If Ny Mod 2 <> 0 Then Ny = Ny + 1   'If Ny is not even, make it even by
        adding 1 to its current value

        'Display New Nx and Ny
        frmCPMC_2D.txtCrystalSetup.Item(0).Text = Nx
        frmCPMC_2D.txtCrystalSetup.Item(1).Text = Ny

        'Reset MatrixSize and AtomMatrixSize
        MatrixSize = (Nx * Ny)
        ReDim Atom(MatrixSize)
```

```
'Pack Matrix with EMPTY Atoms
For j = 1 To Ny
   For i = 1 To Nx
      Atom(Counter).Starting_Index = Counter
      Atom(Counter).x = Format(x, "0.000")
      Atom(Counter).y = Format(y, "0.000")
     Counter = Counter + 1
    x = x + a
 Next i
   y = y + Sqr((0.5 * (a ^ 2)))   '(0.5a)^2+y^2 = a^2
   If Shift = 0 Then
      Shift = 1
      x = 0.5 * a
   Else
     Shift = 0
    x = 0
   End If
Next j

Call BendMatrix
Call ConcentrationFill(Val(frmCPMC_2D.txtCrystalSetup.Item(3).Text))
```

End Sub

Private Sub BendMatrix()

```
' Mirror Matrix 8 Times  to create infinite Crystal

Dim i As Double
Dim Major_X As Double
Dim Major_Y As Double
Dim Starting_Index As Double
ReDim Preserve Atom(9 * MatrixSize)
```

```
'Initial Values
Major_X = (Nx) * a
Major_Y = (Ny) * (Sqr(0.5 * a ^ 2))

'Input Coordinates for 8 Mirror Matrices
'1
For i = 1 To MatrixSize
        Starting_Index = (1 * MatrixSize) + i
        Atom(Starting_Index).Starting_Index = Starting_Index
        Atom(Starting_Index).x = Atom(i).x - Major_X
        Atom(Starting_Index).y = Atom(i).y + Major_Y
Next i

'2
For i = 1 To MatrixSize
        Starting_Index = (2 * MatrixSize) + i
        Atom(Starting_Index).Starting_Index = Starting_Index
        Atom(Starting_Index).x = Atom(i).x - Major_X
        Atom(Starting_Index).y = Atom(i).y
Next i

'3
For i = 1 To MatrixSize
        Starting_Index = (3 * MatrixSize) + i
        Atom(Starting_Index).Starting_Index = Starting_Index
        Atom(Starting_Index).x = Atom(i).x - Major_X
        Atom(Starting_Index).y = Atom(i).y - Major_Y
Next i


'4
For i = 1 To MatrixSize
        Starting_Index = (4 * MatrixSize) + i
        Atom(Starting_Index).Starting_Index = Starting_Index
```

```
        Atom(Starting_Index).x = Atom(i).x
        Atom(Starting_Index).y = Atom(i).y + Major_Y
Next i

'5
For i = 1 To MatrixSize
        Starting_Index = (5 * MatrixSize) + i
        Atom(Starting_Index).Starting_Index = Starting_Index
        Atom(Starting_Index).x = Atom(i).x
        Atom(Starting_Index).y = Atom(i).y - Major_Y
Next i

'6
For i = 1 To MatrixSize
        Starting_Index = (6 * MatrixSize) + i
        Atom(Starting_Index).Starting_Index = Starting_Index
        Atom(Starting_Index).x = Atom(i).x + Major_X
        Atom(Starting_Index).y = Atom(i).y + Major_Y
Next i

'7
For i = 1 To MatrixSize
        Starting_Index = (7 * MatrixSize) + i
        Atom(Starting_Index).Starting_Index = Starting_Index
        Atom(Starting_Index).x = Atom(i).x + Major_X
        Atom(Starting_Index).y = Atom(i).y
Next i

'8
For i = 1 To MatrixSize
        Starting_Index = (8 * MatrixSize) + i
        Atom(Starting_Index).Starting_Index = Starting_Index
        Atom(Starting_Index).x = Atom(i).x + Major_X
        Atom(Starting_Index).y = Atom(i).y - Major_Y
```

```
        Next i

End Sub

Private Sub ConcentrationFill(ByRef IXA As Double)

' Check Initial Concentration Percentages and distribute Elements into Matrix accordingly

Dim i As Double
Dim Element1 As Double
Dim Element2 As Double
Dim IntegerPart As Double
Dim DecimalPart As Double
Dim Nr_Of_Atoms As Double
Dim Starting_Index As Double



CalculateConcentration:  'Of Pt where IXA = Initial Concentration of Pt
Element1 = IXA * MatrixSize
IntegerPart = Fix(Element1)   'Get Integer part
DecimalPart = Element1 - IntegerPart     'Get Decimal part
If DecimalPart < 0.5 Then
        IXA = IntegerPart / MatrixSize
        Nr_Of_Atoms = IntegerPart   'Nr of Atoms that should be Pt
Else
        IXA = (IntegerPart + 1) / MatrixSize
        Nr_Of_Atoms = IntegerPart + 1
End If

 For i = 1 To Nr_Of_Atoms
        Atom(i).El = 1  'Pt
 Next
```

```
  For i = (Nr_Of_Atoms + 1) To MatrixSize
            Atom(i).El = 2  'Al
  Next
'Copy Original Matrix into the other 8 matrices
  Call Copy_Matrix
 'Display New Initial Platinum Concentration
  frmCPMC_2D.txtCrystalSetup.Item(3).Text = Format(IXA, "0.000")
  Call Draw
```

End Sub

Public Sub Copy_Matrix()

```
'Copy Original Matrix into the other 8 matrices

Dim i As Double
Dim Starting_Index As Double

'1
For i = 1 To MatrixSize
          Starting_Index = (1 * MatrixSize) + i
          Atom(Starting_Index).El = 2   'Al
Next i

'2
For i = 1 To MatrixSize
          Starting_Index = (2 * MatrixSize) + i
          Atom(Starting_Index).El = Atom(i).El   'Reflect Original Matrix
Next i

'3
For i = 1 To MatrixSize
          Starting_Index = (3 * MatrixSize) + i
           Atom(Starting_Index).El = 1  'Pt
Next i

'4
```

```
For i = 1 To MatrixSize
     Starting_Index = (4 * MatrixSize) + i
     Atom(Starting_Index).El = 2  'Al
Next i

'5
For i = 1 To MatrixSize
     Starting_Index = (5 * MatrixSize) + i
    Atom(Starting_Index).El = 1   'Pt
Next i

'6
For i = 1 To MatrixSize
    Starting_Index = (6 * MatrixSize) + i
     Atom(Starting_Index).El = 2  'Al
Next i

'7
For i = 1 To MatrixSize
    Starting_Index = (7 * MatrixSize) + i
    Atom(Starting_Index).El = Atom(i).El  'Reflect Original Matrix
Next i

'8
For i = 1 To MatrixSize
     Starting_Index = (8 * MatrixSize) + i
     Atom(Starting_Index).El = 1 'Pt
Next i
```

End Sub

Public Sub NN()

```
'Calculate NN and NNN for Atom A starting from 1 to Matrix Size
```

```
'Pack these NN and NNN into a SubMatrix
 'Search through LargerMatrix at atom(A) NN1,NN2,NN3,NN4,NN5 and NN6 for
empty   index
 'Start packing SubMatrix into the Larger one from THAT index

    Dim i As Double
    Dim j As Double
    Dim g As Double
    Dim Step As Double
    Dim AtomA As Double
    Dim AtomB As Double
    Dim AtomC As Double
    Dim r As Double
    Dim CounterOne As Double
    Dim CounterTwo As Double
    ReDim NNList(MatrixSize, 6)
    ReDim NNNList(MatrixSize, 12)

'Deactivate button
frmCPMC_2D.cmdNN.Enabled = False

For j = 1 To MatrixSize
    DoEvents
    Progress = j
    g = 1

    '   Now search through NNList and NNNList to know where to begin packing
        For Step = 1 To 6
            'If Line is Empty then this is where we should start filling
            If NNList(j, Step) = 0 Then
                CounterOne = Step
                Exit For
            End If
        Next
```

```
        For Step = 1 To 12
          'If Line is Empty then this is where we should start filling
          If NNNList(j, Step) = 0 Then
            CounterTwo = Step
            Exit For
          End If
        Next

    '   Now Search for NN and NNN and pack into SubMatrices
        For i = (j + 1) To (9 * MatrixSize)
          If CounterOne = 7 And CounterTwo = 13 Then Exit For
          AtomA = j
          AtomB = i
          r = Distance(AtomA, AtomB)
          If r <= a And AtomA <> AtomB Then
            'SubMatrix_NN(1, CounterOne) = AtomB      'Nearest Neighbour
            NNList(AtomA, CounterOne) = AtomB
            CounterOne = CounterOne + 1
          ElseIf r > 1.4 And r <= (2 * a) Then
            'SubMatrix_NNN(1, CounterTwo) = AtomB     'Next Nearest Neigbour
            NNNList(AtomA, CounterTwo) = AtomB
            CounterTwo = CounterTwo + 1
          End If
        Next i


        g = 1
    '   Search through LargerMatrix for empty positions
        For Step = 1 To 6
          AtomC = NNList(AtomA, Step)
          If AtomC > MatrixSize Then Exit For   'Falls outside the Crystal that we are
looking at
           For g = 1 To 6
             If NNList(AtomC, g) = 0 Then   'It is EMPTY, fill it with Atom A
                NNList(AtomC, g) = AtomA
```

```
            Exit For
         End If
       Next g
    Next Step
    For Step = 1 To 12
      AtomC = NNNList(AtomA, Step)
      If AtomC > MatrixSize Then Exit For  'Falls outside the Crystal that we are
looking at
      For g = 1 To 12
         If NNNList(AtomC, g) = 0 Then
            NNNList(AtomC, g) = AtomA 'It is EMPTY, fill it with Atom A
            Exit For
         End If
      Next g
    Next Step

  Next j
'Enable Button Again
frmCPMC_2D.cmdExportNN.Enabled = True

'Dim i As Double

'Open "c:\Documents and Settings\Physics\Desktop\NN1.dat" For Output As #1

'For i = 1 To MatrixSize
'Write #1, NNList(i, 1), NNList(i, 2), NNList(i, 3), NNList(i, 4), NNList(i, 5),
NNList(i, 6)
'Next

'Enable Button Again
frmCPMC_2D.cmdExportNN.Enabled = True
Close #1
End Sub
```

```
Private Function Distance(ByVal BB As Double, ByVal AA As Double)
    'Calculating the distance between atom A and B.

    Dim Delta_x As Single
    Dim Delta_y As Single

    Delta_x = Atom(AA).x - Atom(BB).x
    Delta_y = Atom(AA).y - Atom(BB).y

   Distance = Format((Delta_x ^ 2 + Delta_y ^ 2) ^ 0.5, "0.000")
   End Function
```

Module 2: Module Monte Carlo

```
' ************************************************************
' Module          ModuleMonteCarlo
'
' Filename        ModuleMonteCarlo.bas
'
' Author     RA Harris
'            University of the Free State
'            Bloemfontein, South Africa
'
' Description
'
' This module Calculates the Chemical Potential for a random
' atom inside an area consisting out of 19 atoms and decides
' wheter the atom should move or not
' ************************************************************

'Get RandomAtom ->MayJump(Determine if it may jump)
'Get Atomic% for AreaA and AreaB Concentration ->Get_X ->Swop

Option Explicit
Global Eindig As Boolean
```

```
Global TotaleSpronge As Double
Global DepthProfilePt() As Double
Global CrystalSizeChange As Boolean
Global SaveClick As Boolean
'Input Parameters
 Global Dpt As Single
 Global Dal As Single
 Global u0Pt As Single
 Global u0Al As Single
 Global Omega As Single
 Global T As Single
 Global TSpronge As Double
 Const r = 8.314

'Get RandomAtom
Global RandomAtom As Double

'JumpRate
Type Jumps_Type
   NrOfJumps As Double
End Type
Global TotalJumps As Double
Global Jump(2) As Jumps_Type
Global WhatElement As Integer  '1=Pt,2=Al

'Atomic_Percentages
Global AreaA(2) As Double
Global AreaB(2) As Double

'Calculate_U = Chemical Potential
Global UABef(2) As Double
Global UBBef(2) As Double
Global UAAft(2) As Double
Global UBAft(2) As Double
```

```
Global DeltaU1Bef As Double
Global DeltaU2Bef As Double
Global DeltaU1Aft As Double
Global DeltaU2Aft As Double
Global DELTASBef(2, 6) As Double
Global DELTASAft(2, 6) As Double
Global JumpOK(2, 6) As Double

'Probability and NNtoJump
Global Prob(6, 5) As Double
Global SwopAtom As Double
'Global AtomToSwop1 As Integer
'Global AtomToSwop2 As Integer

Public Sub RandomAtomGenerator()
NO:
    Randomize
    If Eindig = False Then
     DoEvents
     RandomAtom = SelectRNumber(MatrixSize, 1)
    If MayJump(RandomAtom, Dpt, Dal) = 0 Then GoTo NO
    End If
End Sub

Public Function MayJump(ByVal Number As Double, ByVal D1 As Single, ByVal D2 As Single)
    'Determine wheter an atom may jump or not according to its Diff. Coefficient
    'It outputs "1" if it may jump or "0" if not.

    Dim NrOfJumps As Single
    Dim Fraction As Single
    Dim f As Single
```

```
    WhatElement = Atom(RandomAtom).El

    'Calculate f
    f = (D1) / (D1 + D2)

    'Determine wheter it may jump or not
    If WhatElement = 2 Then f = 1 - f

    'In the Beginning
    If TotalJumps = 0 Then
        TotalJumps = 1
        Jump(WhatElement).NrOfJumps = 1
        MayJump = "YES"

        NrOfJumps = Jump(WhatElement).NrOfJumps
        Fraction = NrOfJumps / TotalJumps
    ElseIf Fraction <= f Then
        MayJump = "YES"
        Jump(WhatElement).NrOfJumps = Jump(WhatElement).NrOfJumps + 1
        TotalJumps = TotalJumps + 1
    ElseIf Fraction > f Then
        MayJump = "NO"
    End If
End Function

Public Sub Calculate U()
Dim i As Integer
For i = 1 To 6  'Repeat this for the 6 Nearest Neighbours
    Call Atomic_Percentages(RandomAtom, NNList(RandomAtom, i))
    Call U_Before
    Call Swop(RandomAtom, NNList(RandomAtom, i))   'Swop A and B
    Call Atomic_Percentages(NNList(RandomAtom, i), RandomAtom)
    Call U_After
    Call Swop(RandomAtom, NNList(RandomAtom, i)) 'Swop A and B back
```

```
    Call Delta_U
    DELTASBef(1, i) = DeltaU1Bef
    DELTASBef(2, i) = DeltaU2Bef
    DELTASAft(1, i) = DeltaU1Aft
    DELTASAft(2, i) = DeltaU2Aft
Next
Call Equilibrium
Call Probability

End Sub
Private Sub Atomic_Percentages(ByVal AtomA As Double, ByVal AtomB As Double)
'Calculates the Atomic Percentages of AreaA and AreaB

    Dim i As Integer

    'Atomic % for Original Area A
     AreaA(1) = Get_X(AtomA)          'Pt[ ]

    'Atomic % for Area B
     AreaB(1) = Get_X(AtomB)          'Pt[]
End Sub

Private Function Get_X(ByVal AtomNr As Double)
'This Sub Inputs an Atom, and Outputs the PLATINUM Concentration for its 6 NN
'and 12 NNN - area

    Dim i As Integer
    Dim Index As Double
    Dim Counter As Integer
    Dim AtomNN As Integer
    Dim NeighbourArea(18) As String
    Dim NrOfElementA As Integer
    Dim NrOfElementB As Integer
```

```
    'Initialize
    Counter = 1
    If Atom(AtomNr).El = "1" Then
        NrOfElementA = 1
        NrOfElementB = 0
    Else
        NrOfElementB = 1
        NrOfElementA = 0
    End If


'Get NN
For i = 1 To 6
    Index = NNList(RandomAtom, i)
    NeighbourArea(Counter) = Atom(Index).El
    Counter = Counter + 1
Next

'Get NNN
For i = 1 To 12
    Index = NNNList(RandomAtom, i)
    NeighbourArea(Counter) = Atom(Index).El
    Counter = Counter + 1
Next

'Count Nr Of Elements in Area
For i = 1 To 18
    If NeighbourArea(i) = "1" Then
        NrOfElementA = NrOfElementA + 1
Else
        NrOfElementB = NrOfElementB + 1
End If
Next
```

Get_X = Format((NrOfElementA / 19), "0.000")

End Function

Private Sub U_Before()

'Make Sure the math will work
If AreaA(1) = 0 Then AreaA(1) = 0.0000001 Else If AreaA(1) = 1 Then AreaA(1) = 0.9999
If AreaB(1) = 0 Then AreaB(1) = 0.0000001 Else If AreaB(1) = 1 Then AreaB(1) = 0.9999

'AreaA
UABef(1) = u0Pt + Omega * (1 - AreaA(1)) ^ 2 + r * T * Log(AreaA(1))   'Pt
UABef(2) = u0Al + Omega * (AreaA(1)) ^ 2 + r * T * Log(1 - AreaA(1))   'Al
'AreaB
UBBef(1) = u0Pt + Omega * (1 - AreaB(1)) ^ 2 + r * T * Log(AreaB(1))   'Pt
UBBef(2) = u0Al + Omega * (AreaB(1)) ^ 2 + r * T * Log(1 - AreaB(1))   'Al
End Sub

Private Sub U_After()

'Make Sure the math will work
If AreaA(1) = 0 Then AreaA(1) = 0.0000001 Else If AreaA(1) = 1 Then AreaA(1) = 0.9999
If AreaB(1) = 0 Then AreaB(1) = 0.0000001 Else If AreaB(1) = 1 Then AreaB(1) = 0.9999

'AreaA
UAAft(1) = u0Pt + Omega * (1 - AreaA(1)) ^ 2 + r * T * Log(AreaA(1))   'Pt
UAAft(2) = u0Al + Omega * (AreaA(1)) ^ 2 + r * T * Log(1 - AreaA(1))   'Al
'AreaB
UBAft(1) = u0Pt + Omega * (1 - AreaB(1)) ^ 2 + r * T * Log(AreaB(1))   'Pt

```
    UBAft(2) = u0Al + Omega * (AreaB(1)) ^ 2 + r * T * Log(1 - AreaB(1))    'Al
End Sub

Private Sub Delta_U()

'Delta_U_Before
DeltaU1Bef = Abs(UABef(1) - UBBef(1))
DeltaU2Bef = Abs(UABef(2) - UBBef(2))

'Delta_U_After
DeltaU1Aft = Abs(UAAft(1) - UBAft(1))
DeltaU2Aft = Abs(UAAft(2) - UBAft(2))

End Sub

Private Sub Equilibrium()

Dim i As Integer

For i = 1 To 6
   'If DELTASAft(1, i) + DELTASAft(2, 1) > DELTASBef(1, i) + DELTASBef(2, i)
Then ' And DELTASAft(2, i) > DELTASBef(2, i) Then
    If DELTASAft(1, i) > DELTASBef(1, i) And DELTASAft(2, i) > DELTASBef(2,
i) Then
       JumpOK(1, i) = i
       JumpOK(2, i) = 1
   Else
       JumpOK(1, i) = i
       JumpOK(2, i) = 0
   End If
Next

End Sub
```

Private Sub Probability()

```
'Scan through JumpOK-list.  Those atoms that may
'jump have a probability connected to them.  Get that Prob.

Dim i As Integer
Dim Sum As Single
Dim Yes As Boolean

For i = 1 To 6
    If JumpOK(2, i) = 1 Then
        Prob(i, 1) = JumpOK(1, i)
        Prob(i, 2) = DELTASAft(1, i)
        Prob(i, 3) = DELTASAft(2, i)
        If Prob(i, 3) = 0 Then Prob(i, 3) = 0.00001
        If Prob(i, 2) = 0 Then Prob(i, 2) = 0.00001
        Prob(i, 4) = ((1 / Prob(i, 2)) + (1 / Prob(i, 3)))
        If Prob(i, 4) = 0 Then Prob(i, 4) = 0.00000001
        Yes = True
    End If
Next

Dim PlaceHolder As Double

If Yes = True Then
    DoEvents
    TotaleSpronge = TotaleSpronge + 1
    Call NNtoJump
    PlaceHolder = (NNList(RandomAtom, SwopAtom))
    Call Swop(RandomAtom, PlaceHolder)
    If frmCPMC_2D.chkAutoSave.Value = 1 Then Call CheckForSave
        If frmCPMC_2D.chkTotalJumps.Value = Checked Then
            frmCPMC_2D.lblTotalJumps.Caption = "Total Jumps =" & Format(TotaleSpronge, "0") '& Format(TotalJumps, "0") 'Val(Get_X(RandomAtom) / TotalJumps)
```

```
        End If

    If frmCPMC_2D.chkFix_Al.Value = 1 Then Call Fix_Al
    If frmCPMC_2D.chkMirror.Value = 1 Then Call Copy_Matrix

    DrawFlag = True
    Call Plot_XY_Solid(frmCPMC_2D.Pic(0), Nx, Ny, a, 12, (1 Mod 15))
    If Structure = True Then
        Call Draw
        Call Plot_XY_Solid(frmCPMC_2D.Pic(1), Nx, Ny, a, (COLOR + 8), (COLOR +
8))
    End If
        Yes = False
End If
```

End Sub

Private Function NNtoJump()

```
'Draw probability scale
'Gives the Index of the NN that Atom A should jump to

Dim i As Integer
Dim p(6) As Single
Dim Norm As Single
Dim NN As Integer
Dim NormScale(100) As Single
Dim Range1 As Integer
Dim Range2 As Integer
Dim Range3 As Integer
Dim Range4 As Integer
Dim Range5 As Integer
Dim Range6 As Integer
Dim RandomNumber As Integer
```

```
' Get Normalization Value
For i = 1 To 6
   Norm = Norm + Prob(i, 4)
Next

'Get Normalization Scale
For i = 1 To 6
   p(i) = Format(Prob(i, 4) / Norm, "0.00")
Next

Range1 = p(1) * 100
Range2 = Range1 + p(2) * 100
Range3 = Range2 + p(3) * 100
Range4 = Range3 + p(4) * 100
Range5 = Range4 + p(5) * 100
Range6 = Range5 + p(6) * 100

For i = 1 To 100
If i <= Range1 Then
NormScale(i) = 1
   ElseIf i <= Range2 Then
NormScale(i) = 2
   ElseIf i <= Range3 Then
NormScale(i) = 3
   ElseIf i <= Range4 Then
NormScale(i) = 4
   ElseIf i <= Range5 Then
NormScale(i) = 5
ElseIf i <= Range6 Then
NormScale(i) = 6
End If
Next
'Call Random Number and Determine which direction jump will be in
```

```
RandomNumber = SelectRNumber(1, 100)
NNtoJump = NormScale(RandomNumber)
SwopAtom = NNtoJump
```

End Function

Public Sub Swop(ByVal AtomOne As Double, ByVal AtomTwo As Double)

```
    'Swop AtomOne and AtomTwo

    Dim PlaceHolderText As String
    Dim PlaceHolderInteger As Double

    PlaceHolderText = Atom(AtomOne).El
    PlaceHolderInteger = Atom(AtomOne).Starting_Index
    Atom(AtomOne).El = Atom(AtomTwo).El
    Atom(AtomOne).Starting_Index = Atom(AtomTwo).Starting_Index
    Atom(AtomTwo).El = PlaceHolderText
    Atom(AtomTwo).Starting_Index = PlaceHolderInteger
```

End Sub

Public Sub Depth_Profile()

```
Dim x As Double
Dim y As Double
Dim j As Double
Dim i As Double

Dim Sum As Double
Dim PtConc As Single

Dim Size As Double
'Initialize
Size = Ny
```

```
ReDim DepthProfile(MatrixSize) As Double
ReDim DepthProfilePt(MatrixSize)
ReDim DepthProfileAl(MatrixSize)


For j = 1 To MatrixSize Step Nx
PtConc = 0
   For i = 1 To Nx
      If Atom(j + i).El = 1 Then
         PtConc = PtConc + 1
      End If
   Next i
   DepthProfile(j) = (PtConc / Nx) * 100
   DepthProfilePt(j) = DepthProfile(j)
Next j

'Display
For i = 1 To MatrixSize Step Nx
   frmCPMC_2D.EZGraph3.PointGraph 1, i, DepthProfile(i), QBColor(12), 1, 1, 1, 1,
1
   frmCPMC_2D.EZGraph3.PointGraph 2, i, (100 - DepthProfile(i)), QBColor(1 Mod
15), 1, 1, 1, 1, 1
Next
```

End Sub

Public Sub Mirror()

```
On Error GoTo ERROR

Call Copy_Matrix
Dim i As Integer
Dim AtomA As Double
Dim AtomB As Double'
```

```
For i = 1 To 8 * MatrixSize
    Atom(MatrixSize + i).El = Atom(i).El
Next
Call Draw
ERROR:

End Sub

Public Sub Fix_Al()

    Dim i As Double

    For i = ((Nx * Ny) + 1) To ((Nx * Ny) + Nx)
        Atom(i).El = 2
    Next
End Sub
```

Module 3: Module RNG(Random Number Generator)

```
' ***************************************************************
' Module          ModuleRNG
'
' Filename        ModuleRNG.bas
'
' Author          RA Harris
'                 University of the Free State
'                 Bloemfontein, South Africa
'
' Description
'
' This module generates a random number
' ***************************************************************

Option Explicit
```

```
' Declare functions imported from library randomad.dll
' Initialize random number generator with integer seed:
Declare Sub TRandomInit Lib "randomad.dll" (ByVal seed As Integer)

' Get random integer in interval min <= x <= max:
Declare Function TIRandom Lib "randomad.dll" _
   (ByVal Min As Integer, ByVal Max As Integer) As Integer

' Get random double in interval 0 <= x < 1 with a resolution of 32 bits:
Declare Function TRandom Lib "randomad.dll" () As Double

' Get random double in interval 0 <= x < 1 with a resolution of 52 bits:
Declare Function TRandom2 Lib "randomad.dll" () As Double

Public Sub InitializeRNumber()
   'seed the MT rng
   Randomize
   TRandomInit Int(Rnd)
End Sub

Public Function SelectRNumber(ByVal Max As Double, ByVal Min As Double) As
Long
  'generates a random integer in the range min<=rand<=max
  SelectRNumber = Int((Max - Min + 1) * TRandom + Min)
  'trandom on its own generates a random number between 0 and 1

End Function
```

Conference contributions, papers published and reports delivered from this study.

2007

- **Harris R.A., Swart H.C. & Terblans J.J.**
  Report on growth of Pt86:Al11:Cr3:Ru2 –
  super alloy thin films via Pulse Laser Deposition (PLD).
  Report to Mintek,
  Johannesburg, South Africa,
  March 2007

- **Harris R.A., Swart H.C. & Terblans J.J.**
  Pulsed laser deposition of Platinum-based alloys.
  Poster presentation at the 52nd annual conference of the
  South African Institute of Physics,
  Johannesburg, South-Africa
  July 2007

- **Harris R.A., Swart H.C. & Terblans J.J.**
  Report (II) on growth of Pt86:Al11:Cr3:Ru2 –
  super alloy thin films via Pulse Laser Deposition (PLD)
  Report to Mintek,
  Johannesburg, South Africa
  October 2007

- **Harris R.A., Swart H.C. & Terblans J.J.**
  Pulsed laser deposition of Platinum-based alloys.
  Oral presentation at "Suid Afrikaanse instituut vir Wetenskap en Kuns"
  Potchefstroom, South-Africa.
  October 2007

2008

- **Harris R.A., Swart H.C. & Terblans J.J.**
  Report on the Characteristics of Pulsed Laser Deposition (PLD) used to grow Pt_{86}:Al_{11}:Cr_3:Ru_2 – thin films
  Report to Mintek,
  Johannesburg, South Africa,
  March 2008

- **Harris R.A., Swart H.C. & Terblans J.J.**
  Progress report on the Characteristics of Pulsed Laser Deposition (PLD) used to grow $Pt_{86}:Al_{11}:Cr_3:Ru_2$ – thin films, EB-PVD Pt/Al binary thin films and Monte Carlo Modeling of Phase Formation in the Pt/Al Binary alloy system.
  Report to Mintek,
  Johannesburg, South Africa,
  October 2008

- **Harris R.A., Swart H.C. & Terblans J.J.**
  Pt-Al thin film diffusion and phase formation
  Oral presentation at the
  Advanced Metals Initiative Seminar
  Johannesburg, South Africa,
  November 2008

2009

- **Harris R.A., Swart H.C. & Terblans J.J.**
  Progress report on the Monte Carlo Modeling of Phase Formation in the Pt/Al Binary alloy system
  Report to Mintek,
  Johannesburg, South Africa
  April 2009

- **Harris R.A., Swart H.C. & Terblans J.J.**
  The theoretical simulation and characterization of Pt/Al thin films
  Oral presentation at the 54th annual conference of the
  South African Institute of Physics
  Durban, South Africa
  July 2009

- **Harris R.A., Swart H.C. & Terblans J.J.**
  Pt-Al thin film diffusion and phase formation
  Advanced Metals Initiative Seminar
  Johannesburg, South Africa
  July 2009

- **Harris R.A., Swart H.C. & Terblans, J.J.**
  Monte Carlo simulation and AES characterisation of phase formation in Pt-Al thin films.
  Report to Mintek,
  Johannesburg, South Africa
  August 2009

- **Harris R.A., Swart H.C. & Terblans J.J.**
  Monte Carlo simulation and AES characterisation of phase formation in Pt-Al thin films
  Poster presentation
  Ecasia 2009, 13th European conference on Applications of Surface and Interface Analysis
  Antalya, Turkey
  October 2009

- **Harris R.A., Swart H.C. & Terblans J.J.**
  Monte Carlo Simulasie en AES karakterisering van fase forming in Pt-Al dun films
  Oral presentation at "Suid Afrikaanse instituut vir Wetenskap en Kuns"
  Bloemfontein, South-Africa
  November 2009

- **Harris R.A., Van der Lingen E, Paul D.F., Swart H.C., Terblans J.J.**
  Monte Carlo simulation and AES characterisation of phase formation in Pt-Al thin films
  Paper published in scientific journal:
  Surface and Interface Analysis, Vol. 42, Issue 6-7, (January 2010), pg. 1180 – 1183.

2010

- **Harris R.A., Van der Lingen E., Swart H.C. and Terblans J.J.**
  Monte Carlo simulation of Pt-Al binary alloy thin films
  Oral presentation at the 55th annual conference of the
  South African Institute of Physics
  Pretoria, South Africa
  October 2010 (Abstract accepted)

- **Harris R.A., Van der Lingen E., Swart H.C. & Terblans J.J.**
  Monte Carlo simulation of Pt-Al thin film diffusion
  Oral presentation at the Light Metals Conference
  Muldersdrift, South Africa
  October 2010 (Abstract accepted)

.